



Classification of defects for non-destructive inspection using contact sensors and data analysis

David I. Gillespie

Centre for Intelligent Dynamic Communication
Department of Electronic and Electrical Engineering
University of Strathclyde

A thesis submitted for the degree of

Doctor of Philosophy

28/04/2021

Declaration of Authenticity and Author's Rights

This thesis is the result of the author's original research. It has been composed by the author and has not been previously submitted for examination which has led to the award of a degree.

The copyright of this thesis belongs to the author under the terms of the United Kingdom Copyright Acts as qualified by University of Strathclyde Regulation 3.50. Due acknowledgement must always be made of the use of any material contained in, or derived from, this thesis.

Signed:

A handwritten signature in black ink, appearing to be 'D. Gillespie', written over a horizontal line.

David I. Gillespie

Date: 28/04/2021

Dedicated to my Wife Jessica and Daughter Mae
for agreeing to let me complete this insanity

Acknowledgements

To my Wife Jessica and Daughter Mae, I would like to thank you for supporting me through the last three years. I would never have completed this without your help.

I would like to thank Dr Christos Tachtatzis for his endless patience as my supervisor. Your guidance and grounding during my regularly scheduled breakdowns saw me through this.

I would also like to thank Professor Ivan Andonovic for always being the voice of reason without making it feel like my blue sky ideas were ridiculous (they mostly were), and for your unrelenting encouragement in my professional development.

Darci Tachtatzis, thanks for keeping Christos on his toes during our meetings and your occasional creative input into the writing process.

Brian Neilson, thank you for taking this big risk on me and fighting my corner.

Dr Andrew W. Hamilton for talking me into doing this, you are dead to me.

Paul McCubbin, told you I could do it.

I would like to acknowledge the contribution of Collins Aerospace, a Raytheon Technologies company and thank them for their support in the research.

Abstract

The requirement for Non Destructive Testing of composite structures is paramount in Aerospace to maintain structural integrity. There are several established Non Destructive Testing and Inspection methods available dependant on the individual requirements of the structure and situation. Most established non contact methods require an uninterrupted line of sight to the structure to produce an accurate report of the underlying condition. Methods using contact sensors, such as ultrasound, require some form of surface preparation or a couplant to provide accurate readings. Within the Maintenance Repair and Overhaul (MRO) environment, such requirements results in the removal of a component from the maintenance and repair processes, as well as surface preparation to conduct an inspection. This additional time results in a detrimental impact in regards to both financial costs and the time taken to conduct the full maintenance and repair processes. This thesis will focus on the development and application of a tooling system utilising contact temperature sensors which is compatible with the MRO environment, requires minimal surface preparation and is unaffected by line of sight issues created due to the repair process (such as bagging films and breather materials). Once thermal data has been captured, data analysis should be conducted in order to indicate areas of interest (e.g. delaminations and disbonds) as well as to infer useful material properties (i.e. fibre orientation). The indications will be presented in such a manner visually, so as to require minimal training for operators to adopt.

Representative composite structures are thermally profiled within simulations and experimentally, to produce library data of expected ther-

mal responses as well as for use in training Machine Learning algorithms for classification of defects. The methods developed are then tested using data previously unseen by trained algorithms or within the library data, to score their performance.

The thesis presents a two part tool capable of heating a composite sample and record the resultant thermal response, without impact from the vacuum bagging process or a requirement for special surface preparation. It is shown to successfully present impact damage within composite sandwich structures in an areal form familiar to existing inspectors. The tooling in conjunction with an experimentally captured Mean Temperature profile library successfully indicates fibre orientation of biaxial 5 harness satin weave carbon fibre reinforced polymer laminates common within aerospace. This method is performed with an overall accuracy of 87-93% on samples with artificially introduced Gaussian noise. The analysis of transient thermal conductivity profile within a sample is demonstrated to successfully indicate delaminations of maximum acceptable tolerances within composite structures. This method utilises machine learning algorithms in the form of Support Vector Machine (SVM), and Random Forest (RF), achieving overall accuracy of 90% with SVM. Existing methods of tap testing produce accuracy between 73-81%.

The main contributions of this Thesis can be summarised as: the design and creation of a versatile contact-based thermography tool that can be used for a variety of NDI tasks; the development of a contact-based thermography technique that utilises contact temperature sensors to assess impact damage; the creation and validation of a mean temperature response library capable of identifying the fibre orientation within a composite laminate panel based on its thermal response; the development of a contact temperature sensor based thermography method to indicate delaminations within a composite laminate utilising step heating and machine learning.

Contents

1	Introduction	1
1.1	Overview	1
1.2	Aims, Objectives and Challenges within the MRO	4
1.3	Automatic Non Destructive Inspection Economic Benefit	6
1.3.1	Summary	13
1.4	Original contribution to knowledge	14
1.5	Methodology	16
1.6	Thesis Structure	17
1.7	Publications related to Thesis research	17
2	Background	19
2.1	Ultrasonic Non Destructive Testing / Inspection	20
2.2	Broadband Terahertz Spectroscopy	24
2.3	Heat Transfer	26
2.4	Thermal NDT	29
2.5	Heat source, considerations	35
2.5.1	Heat lamps	36
2.5.2	Laser	37
2.5.3	Induction heating	37
2.5.4	Microwave	38
2.5.5	Vibration/Acoustic	38
2.5.6	Heater mats	39
2.6	Contact sensors for thermal detection	39
2.6.1	Thermistors	40
2.6.2	Thermocouples	41
2.6.3	Resistance Temperature Detectors	42
2.6.4	Fibre Bragg grating	44
2.6.5	Rayleigh backscatter in optical fibre as a high resolution temperature sensor	45
2.7	Machine learning applications in Non Destructive Inspection and Testing	45
2.8	Summary	49

3	Tool Design and Validation	52
3.1	Heated Tooling Surface	53
3.1.1	Heat Lamps	53
3.1.2	Laser heating	54
3.1.3	Inducion Heating	54
3.1.4	Resistance heating	55
3.1.5	Microwave heating	55
3.1.6	Mechanical heating	56
3.1.7	Heater mats	56
3.2	Heater mat tooling surface	57
3.3	Sensing Tooling Surface	63
3.3.1	Hybrid Airpad and Carbon Fibre Tooling Design	64
3.3.2	Printed Circuit Board Tooling Design	69
3.4	Final Tool Lay Up	72
3.5	Data capture and Control	73
3.6	Validation of Proposed Tool	75
3.7	User Interface	89
3.7.1	Data Capture via GUI	91
3.7.2	GUI Reports	92
3.7.2.1	Impact Damage Detection	92
3.8	Summary	94
4	Fibre Orientation Through Analysis of Thermal Transfer	96
4.1	Fibre Orientation, Weave and Weaving Patterns	97
4.2	Finite Element Modelling of heat transfer through composite lam- inate structures	98
4.3	Finite Element Analysis Temperature Against Time Results	101
4.4	Comparison of FEA and Experimental Results	106
4.5	Transient Thermal Conduction due to Structural Dissipation As a Fibre Orientation Indication	111
4.5.1	Analysis of Results	113
4.5.2	Automatic Fibre Orientation Detection Method	117
4.6	GUI report presentation	123
4.7	Summary	124
5	Delamination Detection Through Transient Thermal Analysis	126
5.1	Experimental Set up	127
5.2	Methodology	131
5.2.1	Data Exploration	131
5.2.2	Pre-processing	134
5.2.3	Feature Extraction	137
5.2.3.1	Knowledge Based Feature Engineering	138
5.2.3.2	Generic Time Series Feature Extraction	139
5.2.4	Feature Selection	140
5.3	Machine Learning Models	143
5.3.1	Support Vector Machine	143
5.3.2	Random Forest Classification	145

5.4	Application of ML	146
5.4.1	Results for Knowledge-Based Feature	148
5.4.2	Results for Generic Time Series Features	151
5.5	GUI report presentation	156
5.6	Summary	158
6	Conclusion	160
6.1	Thesis Summary	160
6.2	Thesis Contributions	162
6.3	Further Work	163
	Bibliography	166
A	RTD Airpad Array creation curing data	194
B	Temperature against time thermal profiles for Sample D8	200

List of Figures

1.1	(a) Transmission set up thermography. (b) Reflection set up thermography.	2
1.2	Nacelle major components breakdown of V2500, image courtesy Collins Aerospace.	3
1.3	Drying cycle lay up of breather on top of composite sandwich structure contained within a vacuum bag upon a tool surface.	4
1.4	IR images of carbon fibre laminate sandwich panel transmission heat 80°C applied to back surface	5
1.5	The oil drying cycle process in steps with time in hours.	11
1.6	The new oil drying cycle process using sensor to detect fluid presence in steps with time in hours.	12
2.1	Pulse Echo ultrasound non destructive inspection method. ToF_h and ToF_d as time of flight homogeneous and time of flight defect, respectively.	20
2.2	Transmission ultrasound non destructive inspection method. Reduction in Attenuation displayed on right in form of reduced pulse.	21
2.3	A scan example of a pulse echo signal.	22
2.4	(a) A scan example of a pulse echo signal rotated 90° for a single y coordinate (b) B scan example displaying composite of 10 A scans displaying y and z axis.	23
2.5	(a) B scan example of a pulse echo signal for a single row of x coordinate 4, displaying a possible defect at y coordinates 3 and 4 (b) C scan example displaying composite of 10 B scans displaying x and y axis for z axis values greater than 3.	24
2.6	Convection heat transfer, through fluid/gas; Conduction heat transfer, through solids; Radiation of electromagnetic waves, example.	27
2.7	Example of FE method for a square space domain with quadrilateral elements.	28
2.8	Waveform of (a) Amplitude Modulated in steady state, Locked in Thermography (b) Short single pulse, Pulse Thermography.	31
2.9	VT generation of heat within a composite laminate sample with inter-ply defect (a) At rest (b) Vibration exciting ply layers (c) Generation of heat due to friction between ply layers.	31

3.1	Proposed setup to capture thermal transmission through a composite structure, sample sandwiched between a heat source and corresponding sensor array, within a vacuum bag setup.	53
3.2	150mm by 150mm heat zones 1-5(Red) and probe locations (Blue x) on 300mm by 300mm laminate panel.	57
3.3	Heated areal requirements for Impact detection only.	58
3.4	Heated areal requirements for fibre orientation indication only.	59
3.5	Heated areal requirements for delamination detection only.	60
3.6	Heated areal requirements for all three methods, overlay.	61
3.7	Heated areal requirements for impact detection, strip heating.	61
3.8	Heated areal requirements for fibre orientation identification, strip heating.	62
3.9	Heated areal requirements for delamination detection, strip heating.	62
3.10	(a) RTD sample side of HTX tool showing connections threaded through separate slits in the HTX. (b) RTD connection side of HTX tool showing connections threaded through separate slits in the HTX.	66
3.11	(a) RTDs placed within uncured airpad HTX material. (b) RTD airpad array reinforced with two ply 0°, 90° CFRP UD tape.	66
3.12	Contact surface of RTD airpad array showing RTD sensor surface flush with HTX airpad material post curing.	67
3.13	Experimental setup of RTD array holding tool and back plate.	68
3.14	Plate temperature against time captured data vs PCB temperature against time captured data for sandwich panel D0	69
3.15	Experimental setup of RTD array contained within the plate tool prototype of Airpad array tool.	70
3.16	Printed Circuit Board (PCB) RTD array tool, displaying RTD probe locations and off sample connection headers to allow for vacuum bagging to tool.	71
3.17	RTD solder connection to surface mount pad on PCB RTD array tooling.	72
3.18	Cross section of the through transmission set-up for sandwich structure using heater mats and the PCB RTD array.	73
3.19	CPE400 GE Controller experimental data capture setup.	75
3.20	Sandwich panel “Quality” sample lay up cross section.	75
3.21	Defect locations for (a) D1: Delamination in red, impact damage blue. (b)D2: Impact damage shown in blue.	77
3.22	Thermal conductivity and resultant impact to thermal energy transmitted through composite sandwich panel (a) Defect free structure (b) Defect present.	77
3.23	Heater mat temperature against time step heating profile.	79
3.24	Heat map of standard deviation between all heating profile runs or each sample, (a) D0 (b) D1 (c) D2.	80
3.25	Heat map of captured RTD sensor data of top surface of sandwich structure sample D0, free of defects, at 80°C and 250 s sample run 001(a) no interpolation (b) Gaussian interpolation applied.	81

3.26	Heat map of captured RTD sensor data of top surface of sandwich structure sample D0, free of defects, at 80°C and 250 s (a) sample run 002, (b) sample run 003.	81
3.27	Heat map of captured RTD sensor data of top surface of sandwich structure sample D1, containing 2 impact damaged areas and one delamination, at 80°C and 250 s (a) sample run 001, (b) sample run 002, (c) sample run 003.	82
3.28	Heat map of $Defect_i = \frac{Defect_{sT}}{Baseline_{sT}}$ at 250 s with sample run 001 of D0 as the baseline and testing test samples (a) sample run 002, (b) sample run 003, (c) sample run 004.	84
3.29	Heat map of $Defect_i = \frac{Defect_{sT}}{Baseline_{sT}}$ at 250 s with sample run 001 of D0 as the baseline and testing test samples (a) sample run 002, (b) sample run 003, (c) sample run 004.	85
3.30	Heat map of $Defect_i = \frac{Defect_{sT}}{Baseline_{sT}}$ with max value set at 1, at 250 s with sample run 001 of D0 as the baseline and testing test samples (a) sample run 002, (b) sample run 003, (c) sample run 004.	86
3.31	Heat map of $Defect_i = \frac{Defect_{sT}}{Baseline_{sT}}$ with max value set at 1, at 250 s with sample run 001 of D0 as the baseline and testing test samples (a) sample run 001, (b) sample run 002, (c) sample run 003.	87
3.32	Tap testing defect map showing known impact damage points in blue and suspected disbanded area within dotted red area, both impact points and disbond inspected and indicated by qualified inspector.	88
3.33	Graphical User Interface for operators.	90
3.34	Graphical User Interface for operators, Running Impact Detection.	91
3.35	Graphical User Interface for operators, Impact Detection complete.	92
3.36	Graphical User Interface for operators, Impact Detection Review screen.	93
4.1	Common fibre orientation in relation to cloth roll direction (0°).	97
4.2	Example of a Biaxial laminate in a 5 harness satin weave.	98
4.3	(a)Sample IR image of heater mat running, displaying bands	100
4.4	Real-time response to ramp rate of heater mat.	100
4.5	Unidirectional 0/0/0/0 4-ply layup FE analysis transient thermal temperature against time plots for probes 1-64, in (a) heater mat position 3. (b) heater mat position 4. (c) heater mat position 5. (d) heater mat position 1. (e) heater mat position 2.	103
4.6	Unidirectional 0/90/90/0 4-ply layup FE analysis transient thermal temperature against time plots for probes 1-64, in (a) heater mat position 3. (b) heater mat position 4. (c) heater mat position 5. (d) heater mat position 1. (e) heater mat position 2.	104
4.7	Biaxial 0/90/90/0 4-ply layup FE analysis transient thermal temperature against time plots for probes 1-64, in (a) heater mat position 3. (b) heater mat position 4. (c) heater mat position 5. (d) heater mat position 1. (e) heater mat position 2.	105

4.8	Unidirectional 0/0/0/0 4-ply layup FE analysis transient thermal and Experimentally captured, temperature against time plots for probes 1-64, in (a) heater mat position 3. (b) heater mat position 4. (c) heater mat position 5. (d) heater mat position 1. (e) heater mat position 2.	107
4.9	Unidirectional 0/90/90/0 4-ply layup FE analysis transient thermal and Experimentally captured, temperature against time plots for probes 1-64, in (a) heater mat position 3. (b) heater mat position 4. (c) heater mat position 5. (d) heater mat position 1. (e) heater mat position 2.	108
4.10	Biaxial 0/90/90/0 4-ply layup FE analysis transient thermal and Experimentally captured, temperature against time plots for probes 1-64, in (a) heater mat position 3. (b) heater mat position 4. (c) heater mat position 5. (d) heater mat position 1. (e) heater mat position 2.	109
4.11	500 × 500mm test sample experimental set up in heat zone 5 (dashed red outline) using 300 × 300mm RTD probe array (dotted black area).	112
4.12	(a) raw temperature heat map for sample BI090090 at 200 s (b) raw temperature heat map for sample BI090900 at 200 s (c) raw temperature heat map for sample BI0904545 at 200 s (d) Gaussian interpolation temperature heat map for sample BI090090 at 200 s (e) Gaussian interpolation heat map for sample BI090900 at 200 s (f) Gaussian interpolation heat map for sample BI0904545 at 200 s.	114
4.13	Temperature against time of heater mat and probes 33-40 of Biaxial sample 0/90/90/0 run 001.	115
4.14	Kernel Density Estimate line plots shown as tri-surface plots for temperature ranges -3°C to 13°C, colour map denotes probability density. Sample run 001 for ply profile lay ups between 150-300 s with histograms (a) Biaxial 0/90/0/90 (b) Biaxial 0/90/+45/-45 (c) Biaxial 0/90/90/0.	116
4.15	Kernel Density Estimate line plots for temperature ranges -3°C to 13°C in sample run 003 for ply profile lay ups between 150-300 s with median line (a) Biaxial 0/90/0/90 (b) Biaxial 0/90/+45/-45 (c) Biaxial 0/90/90/0.	117
4.16	Proposed Methodology to Determine Fibre Orientation.	117
4.17	Confusion matrix for 12 out of 30 test samples compared to Mean Temperature Distribution Profiles generated from remaining 18 samples.	118
4.18	A Biaxial 0/90/0/90 correctly classified via a MSE comparison against (a) Biaxial 0/90/90/0 (b) Biaxial 0/90/+45/-45 (c) Biaxial 0/90/0/90.	119
4.19	A Biaxial 0/90/+45/-45 correctly classified via a MSE comparison against (a) Biaxial 0/90/90/0 (b) Biaxial 0/90/+45/-45 (c) Biaxial 0/90/0/90.	119

4.20	A Biaxial 0/90/90/0 correctly classified via a MSE comparison against (a) Biaxial 0/90/90/0 (b) Biaxial 0/90/+45/-45 (c) Biaxial 0/90/0/90.	119
4.21	Confusion matrix for 1,200 synthetic data sets with Gaussian noise of $\mathcal{N}(0, = 0.4)$	120
4.22	Confusion matrix for synthetic double thickness samples with added Gaussian noise $\sigma=0.1$	123
4.23	Graphical User Interface for operators, Fibre Orientation indication Review screen.	124
5.1	Delaminations locations shown in red for sample panel D8.	127
5.2	Heater mat locations 1-10 for RTD array tool location 1 and 2 for sample D8.	129
5.3	Thermal profile for heater mat and step heating profile.	130
5.4	Structural conditions of probes in relation to a delamination and the centre of a heat source. (a) Homogeneous Area probe (b) Delamination Edge Probe (c) Delamination Centre Probe (d) Homogeneous Area/Delamination probe.	132
5.5	Thermal profile for all probes over the centre of the heated area for sample D8 at x_heat_dist of 0, 18.75 and 37.5 mm (top, middle, bottom respectively).	133
5.6	Thermal profile for probes in D8 at x_heat_dist of 56.25 and 75 mm (top and bottom respectively).	134
5.7	Thermal profile for probes in D8 at x_heat_dist of 93.75 and 112.5 mm (top and bottom respectively).	135
5.8	Condition distribution within sample D8 data set for HA, DE, DC and HA/D.	136
5.9	Condition distribution within sample D8 data set for No Delamination and Delamination.	136
5.10	All conditions distribution within sample D8 data set for x_heat_dist 0-93.75 mm.	137
5.11	Example of k -fold cross-validation with $k = 10$	138
5.12	Feature Selection overview.	140
5.13	Example of an SVM hyperplane between two features in a 2 dimensional space.	144
5.14	Decision Tree example for classification of one of 5 fruit types.	145
5.15	Random Forest Classifier of n Trees.	146
5.16	ML algorithm pipeline for training/validation and classification of unknown temperature profiles.	147
5.17	Average Cross Validation (CV) Accuracy for all combination of C and γ for sample D8 dataset.	149
5.18	SVM Confusion Matrix for the test set for SVM algorithm utilising knowledge based features, $C=20$, $\gamma=0.15$ for sample D8 dataset.	150
5.19	Random Forest training/validation Max Depth against Mean Test score for number of features = [50 to 1050] in Max Features = [2 to 10], for sample D8 data set.	151

5.20	Random Forest training/validation confusion matrix for sample D8 data set, max_depth=8, max_features=4, n_estimators=150, for knowledge based features.	152
5.21	Feature Rank against Mutual Information.	153
5.22	Cross-validation Accuracy for SVM and RF models against number of top-ranked features.	153
5.23	SVM test confusion matrix for sample D8 data set, 505 top-ranked features, C=4, $\gamma=0.15$	154
5.24	RF test confusion matrix for sample D8 data set, (a) 655 top-ranked features, n_estimators=650, max_depth=8, max_features=8, n_estimators=650, (b) 55 top-ranked features, n_estimators=250, max_depth=8, max_features=6.	155
5.25	Graphical User Interface for operators, Delamination Detection indication Review screen.	157
5.26	Graphical User Interface for operators, Delamination Detection indication with scores Review screen.	158
B.1	Thermal profile for probes in D8 at y_heat_dist of ≤ 37.5 mm and x_heat_dist of 131.25 mm	200
B.2	Thermal profile for probes in D8 at y_heat_dist of ≤ 37.5 mm and x_heat_dist of 150 mm	201
B.3	Thermal profile for probes in D8 at y_heat_dist of ≤ 37.5 mm and x_heat_dist of 168.75 mm	202
B.4	Thermal profile for probes in D8 at y_heat_dist of ≤ 37.5 mm and x_heat_dist of 187.5 mm	202
B.5	Thermal profile for probes in D8 at y_heat_dist of ≤ 37.5 mm and x_heat_dist of 206.25 mm	203
B.6	Thermal profile for probes in D8 at y_heat_dist of ≤ 37.5 mm and x_heat_dist of 225 mm	203
B.7	Thermal profile for probes in D8 at y_heat_dist of ≤ 37.5 mm and x_heat_dist of 243.75 mm	204

List of Tables

1.1	Costs and timescales to train operators to NDT Level 2 certification	8
2.1	Contact Temperature sensors benefits and limitations table	40
4.1	Step heating profile for baseline heater mats	99
4.2	Material properties for Unidirectional single ply.	101
4.3	Material properties for Biaxial 5 Harness 0/90 ply.	102
4.4	Step heating profile for heat zone 5 set up.	113
4.5	Classification report for synthetic samples, standard deviations (σ) 0.1 through to 0.6.	121
4.6	Classification report for synthetic double thickness samples, with added Gaussian noise $\sigma=0.1$	123
5.1	Step heating profile for heater mat.	130
5.2	Number of observation in the training/validation and testing sets.	137
5.3	Hyperparameters for SVM.	149
5.4	Classification Report of test data set for SVM algorithm utilising knowledge based features, $C=20$, $\gamma=0.15$ for sample D8 dataset. .	150
5.5	Hyperparameters for Random Forest.	150
5.6	Classification Report of training/validation data set for RF algo- rithm, $\text{max_depth} = 8$, $\text{max_features} = 4$ and $\text{n_estimators} = 150$.	152
5.7	Classification Report of test data set for SVM algorithm, 505 top- ranked features, $C=4$, $\gamma=0.15$	154
5.8	Classification Report of test data set for RF algorithm for 655 top- ranked features $\text{n_estimators}=650$, $\text{max_depth}=8$, $\text{max_features}=8$.	156
5.9	Classification Report of test data set for RF algorithm for 55 top- ranked features $\text{n_estimators}=250$, $\text{max_depth}=8$, $\text{max_features}=6$.	156

Nomenclature

Acronyms

A-Scan	Amplitude Scan
ANN	Artificial Neural Network
B-Scan	Brightness Scan
CAA	Civil Aviation Authority
CSV	Comma Separated Value
DAC	Differentiated Absolute Contrast
DTT	Dynamic Thermal Topography
FD	First Derivative
FPA	Focal Plane Array
FPI	Fluorescent Penetrant Inspection
FRP	Fibre Reinforced Polymer
GFRP	Glass Fibre Reinforced Polymer
GUI	Graphical User Interface
I/O	Input/Output
IEC	International Electrotechnical Commission
IR	Infrared
LT	Lock in Thermography
MRO	Maintenance Repair and Overhaul
MS	Mean Shift
MT	Modulated Thermography

NDI Non-Destructive Inspection
NDT Non-Destructive Testing
NN Neural Network
OEM Original Equipment Manufacturer
PCB Printed Circuit Board
PCT Principal Component Thermography
PPT Pulsed Phase Thermography
PSC Prestwick Service Centre
PT Pulse Thermography
PTE Pulsed Thermal Ellipsometry
PTFE Polytetrafluoroethylene
QA Quality Assurance
RBF Radial Basis Function
ROS Random Orientated Strands
RTD Resistance Temperature Detector
SD Second Derivative
SHTT Step Heating Transient Thermography
SNR Signal to Noise Ratio
SQ-RTM Same Qualified Resin Transfer Moulding
SQL Structured Query Language
SVC Support Vector Clustering
SVM Support Vector Machine
SWI Swept Wavelength Interferometry
SWI Swept-Wavelength Interferometry
TCR Temperature Coefficient of Resistance
TDS Time Domain Spectrometry
THz Terahertz
ToF Time of Flight

TRL Technology Readiness Level

TSR Thermographic Signal Reconstruction

V2500 A two shaft high by-pass turbofan engine used to power the A320 Airbus family of aircraft

VOV Variance of Variance

VT Vibrothermography

Symbols

psi Pounds per Square Inch

α Temperature Coefficient of Resistance

\mathcal{E} Electromotive Force

Baseline_{sT} Baseline Sample Temperature

Defect_{sT} Defect Sample Temperature

Q Heat flux

Chapter 1

Introduction

1.1 Overview

The use of thermography within the aerospace industry on composite laminates to identify defects and inter-ply delaminations has proven attractive due to its ability to scan large surface areas quickly without the need of physical contact or a couplant between the sensors and the scanned surface. The established techniques for performing thermography of composite structures within the aerospace industry, such as Modulated Thermography [1] - MT also known as “Locked-in”, Pulse Thermography - PT and Step Heating Transient Thermography - SHTT, rely on the heating the part under test and then analysing the thermal response obtained via an Infrared (IR) camera [2]. These methods can be conducted in-situ using reflection or transmission of heat through the component (Figure 1.1) and analysing the part heat conduction [3]. There are benefits and limitations for each of these techniques. For transmission inspection techniques, the ability to identify deep delamination defects due to a thermal profile generated from the entire thickness of the sample under inspection is achievable. However, these do not provide high resolution clarity of defects for the same reason, as the temperature response contains the effects of the complete thickness of the structure. In contrast reflective thermography provides high resolution of surface defects due to

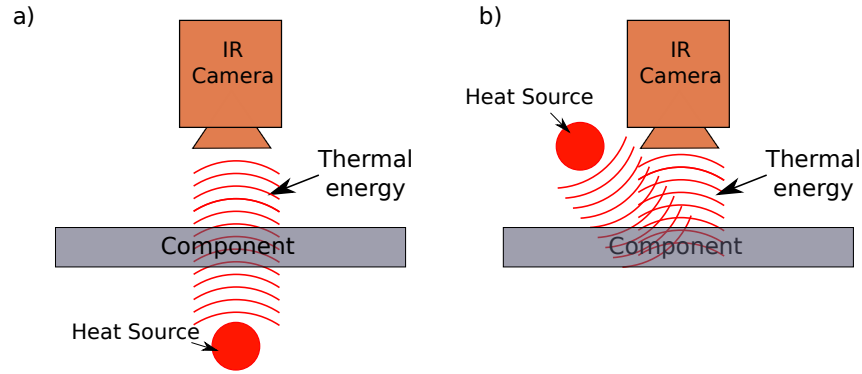


Figure 1.1: (a) Transmission set up thermography. (b) Reflection set up thermography.

the returned temperature profile being generated only by structural components within a sub surface depth. This does however trade resolution for the ability to detect deep delaminations. It has been demonstrated that detecting delaminations in samples thicker than 3mm using reflection can prove difficult [3], whereas transmission methods detected most lateral sized defects in thick panels (up to 5.9mm [3]). As weight is one of the main considerations when constructing an aircraft [4], laminates rarely exceed 3mm in thickness, if a thicker stiff structure is required a sandwich structure consisting of two laminates separated by a core is the currently accepted method [5]. Such sandwich structures are commonly used where a covering is required, this thesis will examine the sandwich structures inspected as part of the Maintenance Repair and Overhaul (MRO) process of a V2500 nacelle as it enters Collins Aerospace PSC MRO. The major components (Figure 1.2) of the nacelle consist of the thrust reverser, the inlet and the fan cowls, these components are separated from the nacelle and delivered to mechanic inspector cells. Each of these cells specialises in a component type (i.e., thrust reverser cell; fan cowl cell; inlet cell). For the purposes of this thesis the major component that will be concentrated on is the fan cowl of a V2500.

It has been demonstrated that reflective PT is able to penetrate into the structure and is capable of detecting fluid ingress and disbonds between the laminate skin and core as well as glue infiltration [6]. Reflective PT and MT methods provide the ability to detect the main defects that are of importance to the aerospace

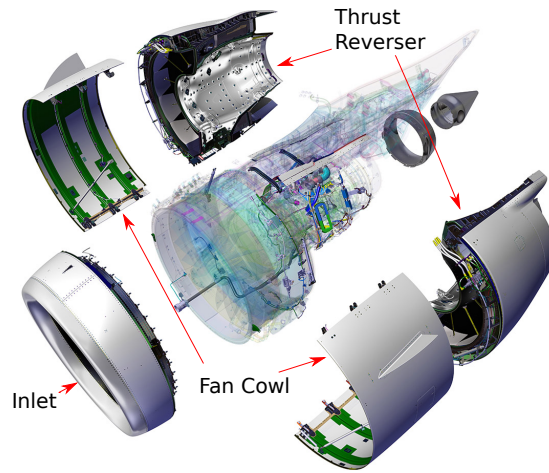


Figure 1.2: Nacelle major components breakdown of V2500, image courtesy Collins Aerospace.

industry. Ongoing development of automated classification and characterisation algorithms for specific use with these techniques provides several options in regard to algorithms which can be used to successfully indicate and even classify defects, as will be discussed further in Chapter 2.

As a stand alone inspection method being carried out by an operator IR vision-based PT is a well developed and widely supported method. It does however rely on an unobstructed surface, emissivity and reflection conditions to be controlled. In order to have such conditions within an active MRO environment a component under inspection will require preparation and a controlled environment to obtain the best results. It can also be time consuming with scan areas being limited to the resolution achievable from the IR capture device. To address these bottlenecks, this work aims to investigate and develop a system which can be utilised within the current MRO environment. It will also address the time aspect associated with inspection by proposing an automated method to capture and analyse the data generated using the transmission inspection method. The aim of this research is to achieve this by adopting the principles of traditional image based IR thermography, replacing the sensing modality from contact free pixels of IR images with contact temperature sensors.

1.2 Aims, Objectives and Challenges within the MRO

As will be explored within this thesis thermography as an inspection technique requires a method of thermal transmission/reflection and a method of capturing the thermal data from the structure being inspected. Currently, the accepted capture method for this technique is that of an infrared camera. This method works well as high resolution images capable of recording the change in thermal profile of the inspected component are now readily available from off the shelf IR cameras, which are able to connect with most available computers. As part of the maintenance or repair process, the fan cowl will undergo a drying cycle in order to remove any fluid ingress by means of heat (80°C) and vacuum, a thermal profile can be captured during this stage. However, the use of the existing thermal

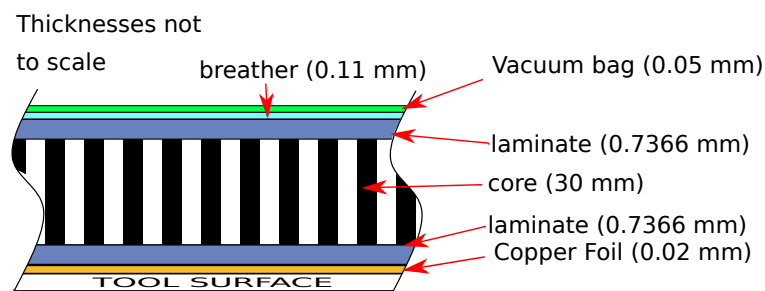


Figure 1.3: Drying cycle lay up of breather on top of composite sandwich structure contained within a vacuum bag upon a tool surface.

transmission within the drying cycle aspect of the maintenance process proves problematic if we are to utilise an infrared camera as this part of the maintenance process requires the application of consumables on the surface of the component as seen in Figure 1.3. A breather cloth material, which is highly porous with a high strength in compression, provides the main barrier to IR cameras obtaining surface temperatures of the fan cowl. This is due to the high volume of air within the breather material acting as a thermal insulation layer. The introduction of a breather material is required for two reasons, firstly, to provide an air-path across the surface of the fan cowl within a vacuum bag and secondly to provide a medium to absorb any fluid within the fan cowl. On top of the breather, a vacuum bag is

applied to create an airtight seal around the component to produce the vacuum when suction from a pump is introduced.

These layers of consumables can overlap and crease during application resulting in a non uniform layer of thermal insulation. To demonstrate the effect of the breather material upon the captured IR images (Figure 1.4), 3 transmission heated set-ups of the same composite sandwich panel were created:

- Position (a): No breather Material was present.
- Position (b): Two layers of breather material present on the right hand side of the sandwich panel, the left hand side free of breather material.
- Position (c): Surface completely covered in breather material.

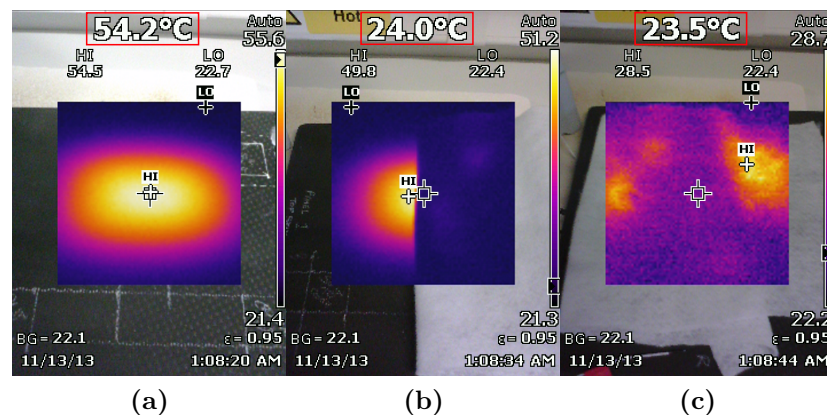


Figure 1.4: IR images of carbon fibre laminate sandwich panel transmission heat 80°C applied to back surface. Top central temperature reading (indicated by red box) from centre of image, minimum and maximum temperature readings annotated 'LO' and 'HI' respectively

(a) Sandwich panel top surface free of consumables, (b) Sandwich panel showing half of top surface free of consumable and half covered in two layers of breather cloth, (c) Sandwich panel showing full top surface covered in breather cloth.

All 3 transmission heated set-ups were heated by a heater mat set to 80°C. A Fluke Ti95 IR Camera recorded a maximum temperature reading from the Carbon Fibre Reinforced Polymer (CFRP) composite sandwich panel in Position (a) 54.2°C (Figure 1.4(a)). As seen in Figure 1.4(b), Position (b) demonstrates the impact of two layers of breather cloth, representing an overlap of the consumable, to the surface the IR camera reading. It is immediately apparent that the

Fluke Ti95 IR is unable to capture the thermal profile or temperature changes on the surface of the composite in the right hand half of the sandwich panel. This is due to the contrast between the insulated surface of the right hand half and the left hand half which is free of breather material. In Position (c) where the surface is completely covered (Figure 1.4(c)), the thermal profile has changed completely and become non-uniformed in its thermal spread when compared to the surface temperature of the sandwich structure beneath the breather material (Figure 1.4(a)).

A further barrier to obtaining thermal imaging data using IR cameras comes from the environment that the drying cycle takes place. The fan cowls, once prepared with the consumable lay up described in Figure 1.3 are placed within an industrial oven, where heat is introduced to the component via air convection at a temperature of 80°C for a 2 hour dwell period. As the accuracies of IR cameras are influenced by the temperature of the environment in which it is situated in [7] the reliability of temperature readings obtained from placing such a device within the industrial oven during a drying cycle can not be assured.

It is proposed that thermal readings will be obtained from the surface of the fan cowl during the drying cycle process via contact temperature sensors applied directly to the surface of the fan cowl. The readings from the contact sensor can then be used as a part of a feedback loop to maintain the temperature of a transmission heat source during the drying cycle. Contact sensors will be arranged within an array reflective of the array of pixels produced by IR thermography images used in established methods. With an array of temperature readings, captured examination and data analysis can be conducted, based on established methods to infer the material properties of the component.

1.3 Automatic Non Destructive Inspection Economic Benefit

In the production of composite structures for aerospace, rigorous testing and quality assurance must be performed. The same level of certification and standard

requirements are applicable for maintenance and repair processes [8, 9]. This applies to Non-Destructive Testing (NDT) of composite structures, however Non-Destructive Inspection (NDI) methods do not require qualification in accordance with Civil Aviation Authority (CAA) [10, 11]. This interpretation of the CAA's definitions and regulations of Testing and Inspection allows for the use of NDI to indicate the presence of defects within an aerospace structure, provided that any qualifications of the defect are carried out by a qualified NDT method in accordance with BS EN 4179 [9]. This requires a qualified and certified NDT technician to conduct the testing. EN 473 "Non-destructive testing - Qualification and certification of NDT personnel - General principles" [12] describes the 3 levels of NDT qualifications that a technician may obtain along with the duties and responsibilities associated with each level.

- The initial certification, level 1, is that of a competent person whom is able to perform testing and record the results under the supervision of a Level 2 or Level 3 operator.
- A Level 2 operator may select NDT techniques, set up and verify NDT equipment, perform and supervise tests, as well as interpret and evaluate results according to applicable standards, codes, or specifications.
- A Level 3 operator is authorised to carry out all of the responsibilities of a Level 2 operator as well as establish and validate NDT instructions and procedures.

For an aerospace facility to carry out NDT in accordance with the legislation and standards [9, 10, 11, 12] it requires the minimum of a level 2 operator on site or access to one. In order for the same aerospace facility to carry out NDI on aerospace components it must have a competent person trained in the NDI method, however they do not require a qualification [11].

In order to train up to Level 2 an operator must have between 40 and 152 hours of training along with 640 to 1920 hours of industrial experience [12]. As shown in Table 1.1, depending on the NDT technique an aerospace facility wishes to use, the costs for simply covering the hourly wage of the inspector (£10.75 [13])

Table 1.1: Costs and timescales to train operators to NDT Level 2 certification, created from data obtained in UK National Aerospace NDT board [10] and PayScale.com [13] 2018.

NDT Technique	Training (hours)	Industrial Experience (hours)	Hourly Wage (£GBP)	Total Cost (£GBP)
Acoustic Emission Testing	128	1920	10.75	22,016
Eddy Current Testing	80	1920	10.75	21,500
Leak Testing (Pressure and Tracer Gas methods)	104	1920	10.75	21,758
Magnetic Particle Testing	40	640	10.75	7,310
Penetrant Testing	40	640	10.75	7,310
Radiographic Testing	152	1920	10.75	22,274
Ultrasonic Testing	144	1920	10.75	22,188
Visual Testing	40	640	10.75	7,310

range from £7,310 to £22,278. Based on a 40 hour work week, it would also take 17 - 52 weeks to train personnel for each technique. If a company were to train only one individual up to Level 2, they introduce a single point of failure should that person become unavailable due to illness, holidays, or new employment. In this scenario, workload and shifts would also generate a bottle neck for NDT. Qualifying employees for Level 1 certification would reduce the time and costing, however, a Level 2 would still be required to supervise ultimately until level 1 employees achieved Level 2 certification. At a cost of £22,188 and one year of time to certify to a Level 2 qualification in Ultrasonic testing, a site such as Collins Aerospace Prestwick Service Centre (PSC) MRO where 162 mechanic inspectors conduct inspection of the nacelles and nacelle components across six business unit cells, over a two shift rota a minimum of twelve mechanic inspectors would be required to provide one qualified and certified NDT Level 2 tester at each cell per shift. However, as each cell requires more than one NDT method, for example, a composite cell could require ultrasonic testing and visual testing to verify the successful completion of a patch repair, and if the nacelle component is part of the acoustic lining, it will also require acoustic emission testing making the number of qualified testers required three per shift. With the consideration of

employee turn over and costs associated with certifying mechanic inspectors with level 2 NDT qualification, it creates an economic business challenge to use NDT methods for all repairs and evaluations of damage at an MRO. Therefore, with the development of an inspection method which provides the necessary information required to select a certified repair method or to declare a component damaged beyond repair, which can be quickly adopted by operators, it would make sense as a business case to utilise this method.

A full nacelle or individual components will arrive at PSC MRO either as part of scheduled maintenance or as a drop in piece of work after either suspected damage or verified damage has occurred. Once the component is accepted and work begins, an inspection of the component will occur, and this consists of a visual inspection and an impact resonance inspection in the form of the coin tap test. Using this form of impact resonance, an experienced inspector can indicate the presence of defects within a composite sandwich structure depending on depth and stiffness of the structure [14], however, this is a subjective and non-quantifiable inspection. It has been observed that impact resonance (tap testing) could detect defects with a circumference as low as 8 mm in diameter in a perspex test, increasing in size to 10 mm for an aluminium test piece [15]. It was concluded that this increase in the minimum detectable defect corresponded to the increase in stiffness between the two materials [15]. When comparing the stiffness of Aluminium to that of CFRP the latter is more than twice as stiff (69 GPa Aluminium, 150 GPa CFRP) suggesting that the minimum defect circumference that can be reliably detected is larger than 10 mm. The largest allowable defects within some areas of laminate for a fan cowl on the V2500 are 5.1 mm [16]. As this is smaller than the diameter for which the impact resonance inspection method has been shown to reliably detect in structures with a lower stiffness, it can be assumed that there is a likelihood that defects out of the allowable limit are not being detected using this inspection method. A result of this is that within these areas certified NDT methods must be carried out to provide assurance that defects out of the allowable size are not present. This again requires removal of the component from the maintenance and repair process and

surface preparation of the component, as well as waiting for access to an operator qualified to the appropriate level and of the desired testing method.

Tap testing as an inspection method requires the inspector to inspect single points and is subjective to individual interpretation when using a manual tap test hammer. It has been demonstrated with transmission set-up thermography, using flash (pulse thermography), that defects down to 4 mm^2 can be detected within laminates up to 5.9mm in thickness [3]. As an inspection technique, PT in the transmission set up provides indications of smaller areas, 4 mm^2 compared to 10.18 mm^2 tap testing, of damage. Thermography as an inspection method, unlike the manual tap testing method, is not subjective to the individual inspector interpretation but rather the calibration of the equipment and condition of the sensors. Two inspectors should arguably come to the same conclusion regarding a defect using the same thermography equipment and method, whereas two inspectors may return different results using the same tap testing hammer. As the maintenance process of the V2500 includes the drying cycle which requires heat transmission into the component, there is the opportunity to utilise this heat transmission to form part of the inspection using transmission-based thermography. Doing so would remove the subjectivity of the current inspection method as well as an opportunity to use signal analysis and machine learning to automate the classification of the indicated areas of defects and damage.

Currently, no sensor data is utilised in the monitoring of the fluid levels within the drying cycle process, the progress of this is monitored visually by removing the component from the oven, stripping it down of consumables and visually inspecting the breather material for signs of fluids. This requires operators to prepare the component in vacuum bagging with consumables, move the component into the oven, run a drying cycle, then remove the component from the oven, strip it of consumables and visually inspect the breather cloth. This process is conducted on average 3 times with a V2500 fan cowl within the PSC MRO facility. As seen in Figure 1.5 the operator hours required to perform a single drying cycle is 0.66 hours, the chargeable hourly rate for an operator as of 2018 is \$140 US Dollars, resulting in a cost of \$92.40 US Dollars. Should the component require three full

drying cycles this increases to 1.98 hours and a cost of \$277.20 US Dollars.

As the component requires removal from the oven to remove the consumables and perform the visual inspection of the breather material, the component requires a cool-down period within the oven to allow for safe handling. Should the process require repeating a new ramp up, dwell and cool down are all required within the oven totalling 3.5 hours. In the typical 3 drying cycle process, this

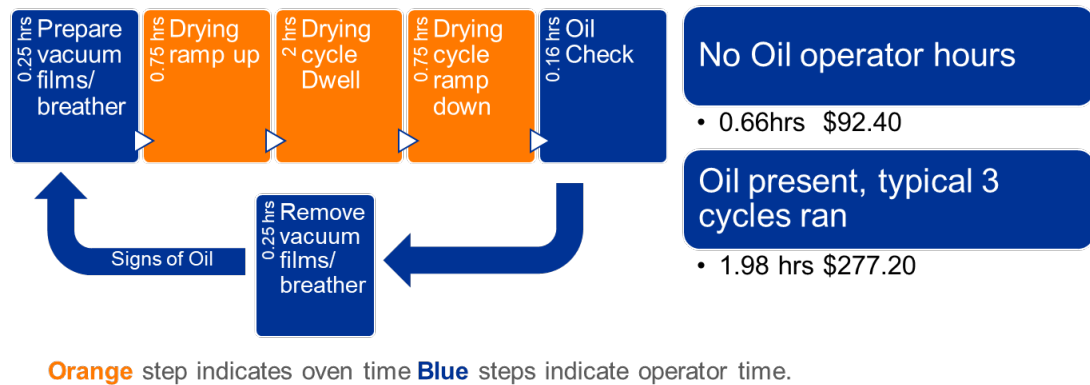


Figure 1.5: The oil drying cycle process in steps with time in hours.

results in an oven time of 10.5 hours, consisting of 6 hours of dwell heating, 2.25 of ramping up to dwell temperature, and 2.25 of cooling. If fluid levels within the component could be monitored during the drying cycle processes, it would be possible to continue the drying cycle until the fluid levels are reduced to an acceptable level. This would remove the need to run consecutive drying cycles and thus only a single ramp up, dwell and cool down periods would be required per complete removal of fluid. This would reduce the full process time within the oven from 10.5 hours to 9 hours, with a reduction of resource use of 1.5 hours (14.28%). Figure 1.6 shows the process steps and time in hours for a new process with an automated shut-off linked to a fluid level indication within the component. It can be seen here that regardless of the drying cycle dwell time, there is a reduction of operator hours required due to the removal of the repeated vacuum bagging and addition of consumables stage step as well as the visual oil check. This results in a typical cost savings of operator hours of the monetary value of \$207.20 US dollars per drying process per unit. The PSC MRO site during the 2018-2019 period performed the oil drying process on 72 V2500 fan cowls.

Were a new automated fluid detection process, with the cost and time savings described above, to be used during this period, a cost saving of \$14,918.40 US dollars could be realised on operator time alone. The reduction in ramp up and ramp down within the oven would save 108 hours of oven use, increasing capacity by 12 units across the year. Reducing the requirement for separate preparation of drying cycles when more than one cycle is required, also reduces the generated waste of consumables by up to two-thirds. This has not only an economic benefit but also an environmental one.

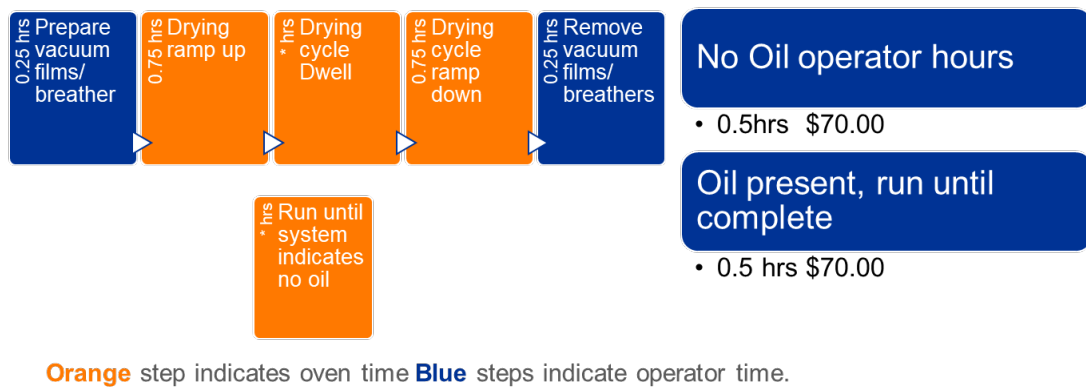


Figure 1.6: The new oil drying cycle process using sensor to detect fluid presence in steps with time in hours.

The V2500 fan cowl surface will take an experienced operator on average approximately 20 minutes to inspect both the inner skin and outer skin. This is conducted prior to the drying process and also again once the drying process has been completed to identify if any damage has occurred during the drying process. There is the possibility in cases of extreme fluid ingress within the sandwich structure, that during the drying cycle that high volumes of trapped fluid within the cells of the core expand under temperature and apply pressure from within the sandwich structure. This pressure can result in weak adhesive bonds between the laminate skin and core to come apart resulting in a disbond between the skin and core. As the coin tap test requires a tapping hammer to make contact with the surface of the component being inspected, it is not possible to carry out the pre-drying cycle inspection nor the post drying cycle inspection for defects of a V2500 fan cowl once it has been prepared within a vacuum bag

for the drying process. This is due to the consumables used in the preparation resulting in a physical barrier preventing impact between the hammer and the surface under inspection.

The proposed inspection method could be performed whilst the V2500 fan cowl was prepared for the drying process within a new heated surface tool which utilised transmission heating through the component alongside an applied vacuum to draw out fluids, which would allow for a more lean process overall. Such a method would allow for the unit to be received, cleaned, bagged, inspected, then dried and inspected again before the bagging material and consumables are removed. Currently, a unit can be received, cleaned, inspected, and then it joins a queue for the drying process. An added benefit of inspection post vacuum bagging is that the bag will act as a barrier to the MRO environment, keeping the unit free from contaminants. There is also the possibility of a mid drying process inspection without removing the component from the vacuum bag. The main benefit would again be seen in the form of operator time, should the component be able to see a reduction in inspection time through an automated method, a cost saving will also be realised. Inspection time of 40 minutes (20 minutes pre and post-drying process) per unit at the \$140.00 per hour rate charged for an operator would cost \$93.33 US Dollars per unit. Over a year, assuming the rate of units maintains at 72, this would result in \$6700.00 worth of chargeable hours used in the inspection of the components. As the inspection method would be automated, the chargeable operator hours would be cut to zero, adding to the previous cost saving, resulting in a new total cost saving of \$21,638.40 over the year.

1.3.1 Summary

A business case analysis has been conducted to consider the benefits to the existing process of preparing a V2500 fan cowl for Maintenance Repair and Overhaul should the introduction of a contact temperature sensor system capable of analysing the thermal profiles in such a way as to indicate defects. It has resulted

in the prediction of a cost saving of \$21,638.40 US Dollars over one year and an increase in capacity for the process by 12 units per year due to time savings. In order for the new method to be successful, it needs to satisfy the following requirements:

- Must be performed using a temperature of 80°C as the heat source to fit seamlessly within the current drying process.
- Must utilise contact temperature sensors to obtain temperature readings directly from the component surface and mitigate interference from consumables.
- Must provide a repeatable inspection method, which is not subjective.

1.4 Original contribution to knowledge

The objective of this thesis is to explore the analysis of the thermal profile from transmission through a contact sensor based capture method which can be applied directly to the surface of the component. The theory of traditional IR image based thermography will be utilised and applied in practice to the proposed contact sensor based thermography. This direct application will allow for more accurate readings of the surface temperature as it is unaffected by the introduction of consumables used during the maintenance and repair process within an MRO. The proposed method of applying the sensors to the surface of the component will also provide the ability of the system to be used for a wider range of applications where thermal data is required, such as the curing of repairs. The particular area of interest for Collins Aerospace from this research is in the indication of poor quality adhesive bonds (disbonds) between laminates and core, previous repair fibre orientation detail, and delaminations within laminates. There is an abundance of knowledge around the use of non-contact thermography using IR imaging. The area which has been identified to explore further is that surrounding the inspection of large aerospace structures of changing geometries with an in-line inspection system that can utilise existing tooling and methods. The major

benefit of such a system is the introduction of a quality assurance method which can be automated as part of the process without a significant impact on the process time, resulting in a significant reduction in operator time and increasing capacity across the same calendar period.

The limitations placed upon MRO environments when compared to an Original Equipment Manufacturer (OEM) in terms of the ability to control processes are far more stringent. This is due to the parts being worked upon already being in existence, so the processes are created around the parts. Within an OEM the production of the part is considered alongside the development of the part allowing for a holistic approach to inspection and production. The MRO environment must accommodate the various parts they receive, flexibility while retaining the use of existing equipment is key. The receipt of new families of components into an MRO requires new methods which can be costly and limited to a single family of components as they are typically physically customised. As a result of this it is difficult to accept ad hoc work if the physical tooling at the existing site is not transferable. By exploring transferable sensors and instead customising a software process inspection method to components, an inline process monitoring/inspection system could be introduced that is transferable to any component entering the MRO.

As the method is that of inspection and not testing, there is also interest surrounding the use of the developed technique within an Aerospace MRO environment due to the strict legislation surrounding such methods for human operators to complete. There is further work which could be conducted surrounding the ethical and legal ramifications of certifying a Machine Learning process to carry out certified testing under various international aviation authority legislation. However, this is not within the scope of this thesis, where only the technical aspects will be investigated.

The thesis contributions can be summarised as follows:

- i Develop a versatile contact-based thermography tool that can be used for a variety of NDI tasks.

- ii Proposed and developed contact-based thermography technique that utilises the tool to assess impact damage [17], by visually displaying areas of interest.
- iii Creation and validation of fibre orientation mean temperature response library, to identify fibre orientation of a part of unknown origin and history by comparing its thermal response to that of the mean temperature response library [18].
- iv Proposed and developed contact-based thermography model to detect delamination utilising incremental step heating [19].

1.5 Methodology

In order to test the hypothesis of producing indications of defects within CFRP aerospace components with a non-destructive inspection method, inspired by image based IR thermography techniques, from temperature data captured from contact temperature sensors this research will progress through Technology Readiness Levels (TRL) 1-6, as dictated by Collins Aerospace policy.

TRL 1-2 will consist of background research as to the feasibility of the use of contact temperature sensors in this manner, and will make up the majority of Chapter 2 in the form of a literature review.

TRL 3 (proof of concept) will take place in the form of experimental capture of temperature readings using contact temperature sensors on a sandwich panel with known damage in the thermal transmission set up to identify if the basic principle of thermography, being that damage results in measurable variations in thermal conductivity within a structure, are identifiable (Chapter 3).

TRL 4-5 (validation) contained in Chapters 4 and 5 will seek to validate and develop the method through data analysis and process development to provide a useful indication as to the characteristics of the CFRP under inspection.

TRL 6 (Prototype Demonstration) is in the form of a physical prototype tooling set up and analysis software which will be developed throughout the

content of this thesis.

1.6 Thesis Structure

The Thesis continues in Chapter 2 with a background of non-destructive testing, which goes on to focus on thermography, temperature contact sensors and the use of machine learning in the classification and identification of defects. Chapter 3 introduces the development of a prototype contact temperature sensor array created to capture the surface temperatures of the samples used to test the proposed thermography methods. The Chapter continues by demonstrating that image-based thermography techniques can be used in association with temperature data captured from contact temperature sensors, and through data analysis impact damage and disbonds between core and laminate skins can be detected using a low temperature thermal transmission set-up. In Chapter 4 the use of transient thermal structural dissipation and data analysis is explored as a form of characterising material properties within CFRP laminate structures. This is continued in Chapter 5 where further investigation is conducted in exploring the application of this method in indicating inter-ply inclusions of laminates in the form of delaminations. The thesis ends with Chapter 6 with the conclusion of the research and a discussion on further work which may result from this research.

1.7 Publications related to Thesis research

The work conducted in Chapter 3 is contained in:

- [M1] **Gillespie DI**, Hamilton AW, Atkinson RC, Bellekens X, Michie C, Andonovic I, Tachtatzis C. Defect Detection in Aerospace Sandwich Composite Panels Using Conductive Thermography and Contact Sensors. *Sensors*. 2020; 20(22):6689.

The methods developed within Chapter 3 were applied and used in:

[M2] Mills JA, Hamilton AW, **Gillespie DI**, Andonovic I, Michie C, Burnham K, Tachtatzis C. Identifying Defects in Aerospace Composite Sandwich Panels Using High-Definition Distributed Optical Fibre Sensors. *Sensors*. 2020; 20(23):6746.

The work conducted in Chapter 4 sections 1-4 is contained in:

[M3] **Gillespie DI**, Hamilton AW, Kruckenberg T, Neilson B, Atkinson RC, Andonovic I, Tachtatzis C. "Geometrical thermal analysis as a form of Finite Element Analysis enhancement". In 17th International Conference on Manufacturing Research 2019 Sep 12 (pp. 187-192).

The work conducted in Chapter 4 section 5 is contained in:

[M4] **Gillespie DI**, Hamilton AW, McKay EJ, Neilson B, Atkinson RC, Andonovic I, Tachtatzis C. Non-Destructive Identification of Fibre Orientation in Multi-Ply Biaxial Laminates Using Contact Temperature Sensors. *Sensors*. 2020; 20(14):3865.

The work conducted in Chapter 5 is contained in:

[M5] **Gillespie DI**, Hamilton AW, Atkinson RC, Bellekens X, Michie C, Andonovic I, Tachtatzis C. Composite Laminate Delamination Detection Using Transient Thermal Conduction Profiles and Machine Learning Based Data Analysis. *Sensors*. 2020; 20(24):7227.

Chapter 2

Background

Non destructive testing of composite structures is a well established area of research. This chapter will examine the literature and state of the art within several non destructive methods, discussing the benefits and limitations of each. As this thesis will explore thermography based inspection methods, this chapter continues with further discussion surrounding consideration of heat sources and their compatibility within the MRO environment for inspection. With the control of the heating methods and their compatibility with both the proposed method of inspection and environment within the the MRO examined, the selection of non silicone rubber heater mats is discussed. This is followed by an overview of the available contact surface temperature sensors available. The benefits and limitations of each sensor type is discussed and the down selection of a contact surface temperature probe in the form of Resistance Temperature Detector is explained. The Chapter concludes with an overview of existing Machine Learning methods and their successful application within existing IR based thermography inspection methods.

2.1 Ultrasonic Non Destructive Testing / Inspection

The most widely used Non Destructive Testing/Inspection (NDT/NDI) technique employed for composite structures is that of Ultrasonic/Ultrasound [20]. This is actually a family of techniques which utilise ultrasound frequencies (above 20 kHz). The most commonly used technique of ultrasound inspection is that of pulse echo. The premise of this technique is described in its name, whereby a pulse of ultrasound is generated by a transducer, typically piezoelectric, and injected into the sample under inspection. The same transducer switches to a receiving mode to ‘listen’ for the echo generated by the pulse from within the sample. Figure 2.1 shows that the amplitude of the echo can then be used to determine the intensity of the echo giving a Time of Flight (ToF) within the structure, which can be used to calculate the thickness [21]. Inspection/Testing of structures with a known thickness and material density will result in the identification of defects within the structure via the setting of gates at the maximum depth of the sample. Readings within the range of this gate would be from a reflection within the sample, which is indicative of a defect. Ultrasound inspection can also be conducted

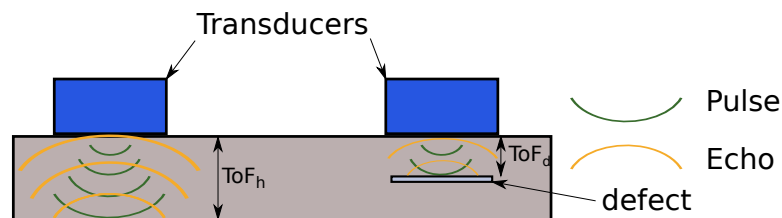


Figure 2.1: Pulse Echo ultrasound non destructive inspection method. ToF_h and ToF_d as time of flight homogeneous and time of flight defect, respectively.

in a transmission set up where the pulse is generated from a transducer on one surface of the sample and a separate receiver is located on the opposite surface. Similar to pulse echo, with a known thickness and known density of the sample, the expected attenuation resulting from the signal travelling through the sample can be calculated. Any discrepancies to attenuation would be produced through some form of inclusion within the sample modifying the acoustic properties [22] as displayed in Figure 2.2. Generation of ultrasound signals has been successfully

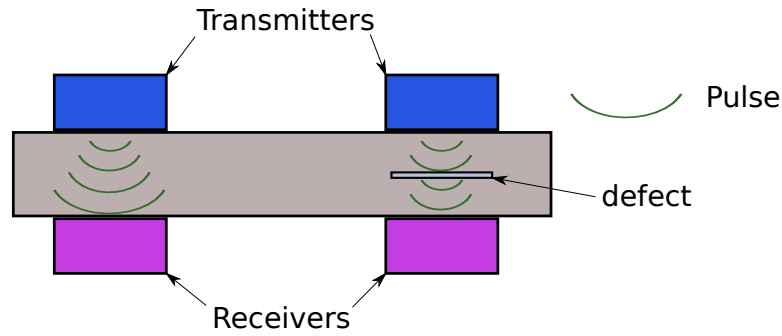


Figure 2.2: Transmission ultrasound non-destructive inspection method. Reduction in Attenuation displayed on right in form of reduced pulse.

achieved and utilised in inspection from several different sources. As a sound wave is a vibration within a medium, ultrasound signals can be generated from any source which can produce a vibration at a frequency above 20 kHz, either internally or externally, which can be transmitted. The most commonly used is a piezoelectric transducer, which will generate a force when an electric charge is applied. This is also true in the opposite, with the piezoelectric material generating a measurable electrical charge proportional to the force applied [23]. This two-way generation of controlled vibration and of sensing a measurable voltage from vibration makes for ideal ultrasound transducers which can operate in both a transmission and receiving capacity.

It has long been known that attenuation within CFRP composites increases in line with frequency [24]. This is also true in regard to voids, the correlation between void content and attenuation can be used to measure the void content within a CFRP sample [25, 26, 27]. However as filler materials in sandwich structures are in essence a layer of voids used to provide stiffness but also be lightweight, these also impact attenuation. Such is the impact of sandwich structures on the attenuation of sound waves that they are commonly used within aerospace structures to provide noise reduction both within the aircraft and to meet the noise level requirements of engines [28]

The ultrasonic frequency ranges typically used within composite structures of between 2 MHz to 10 MHz, experience high attenuation of sound in air resulting in signal loss when an poor contact exists between the sample and transducers. To mitigate the signal loss due to attenuation, a couplant can be used to transmit

the ultrasonic signal. The most reliable methods of coupling the ultrasound transducer to the sample, in order to transfer the mechanical energy, is via full submersion or the use of water jets [29]. For structures where the ingress of moisture will have a negative impact on the structural properties the use of air as a couplant has been investigated with promising results [30, 31, 32]. However an unobstructed line of sight between the transducer and sample under inspection is required, as well as the maintaining of a controlled distance between both.

A non-contact ultrasonic method without the requirement of a physical couplant has been achieved via introducing mechanical excitement within the sample under inspection through the application of lasers [33, 34, 35, 36]. When compared to contact ultrasonic methods, non contact ultrasonic laser methods provide low sensitivity and are heavily affected by environmental noise [37]. As the MRO environment is one of varying workloads and processes, the removal of background noise which would impact the laser ultrasonic method is not feasible without considerable modification to existing processes, which would require significant investment into new processes and infrastructure. When presenting

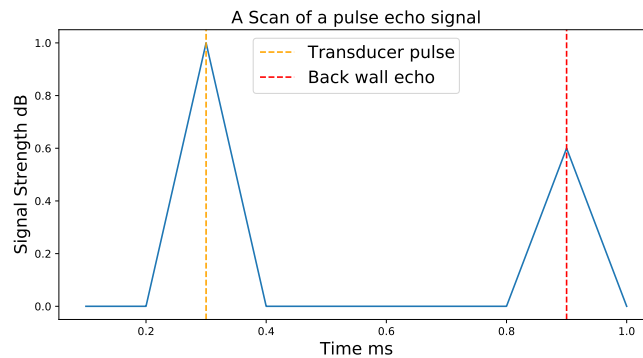


Figure 2.3: A scan example of a pulse echo signal.

the ultrasonic readings captured, there are several options available. For single point inspections, the Amplitude Scan (A-Scan) [38] presents a 1 dimensional line plot of the strength of the echo from the transmitted ultrasonic pulse over time (Figure 2.3). As the speed of sound within the structure under examination can be known, the Time of Flight (ToF) of the pulse can be used to calculate the thickness of the structure. An operator can also use the ToF of the A-Scan to

identify defects within a structure due to the profile of the A-Scan presenting a strong echo generated from defects [39].

For local inspection and testing of structures the A-Scan provides a high level of detail of the underlying structure, however over larger structures it is a time consuming process. By arranging an array of pulse echo transducers, each generating their own A-Scan, the collated A-Scans can be presented together in a top-down view presenting the intensity of the echo generated in a colour palette or a corresponding degree of brightness to intensity of the echo [40]. Such Brightness Scans (B-Scans) provide a report of the echo strength captured by the array along a single dimension (Figure 2.4). Visually, this presentation is more

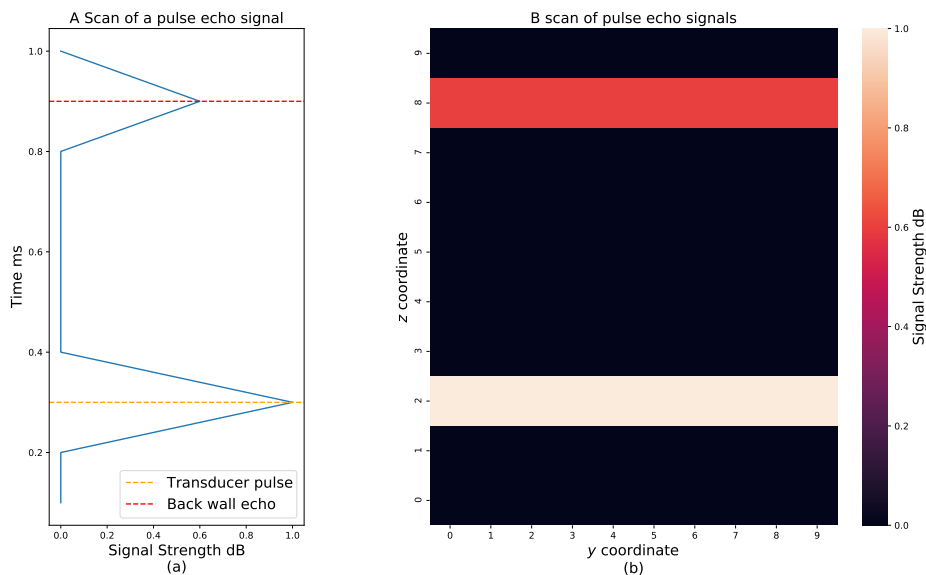


Figure 2.4: (a) A scan example of a pulse echo signal rotated 90° for a single y coordinate (b) B scan example displaying composite of 10 A scans displaying y and z axis.

intuitive to interpret as it can be described as a ‘slice’ of the structure viewed side on. Describing the A-Scan as measurements in the z -axis and the B-Scan as measurements in the z -axis and y -axis, the x -axis can be introduced by capturing a series of B-Scans and their translation in regards to each other. This results in the generation of a C-Scan report (Figure 2.5(b)) which presents a top-down view of the structure under inspection or testing [41, 42, 43]. As the C-Scan produces a

report with known areal dimensions, it allows for a report to be directly compared to the component under inspection or testing.

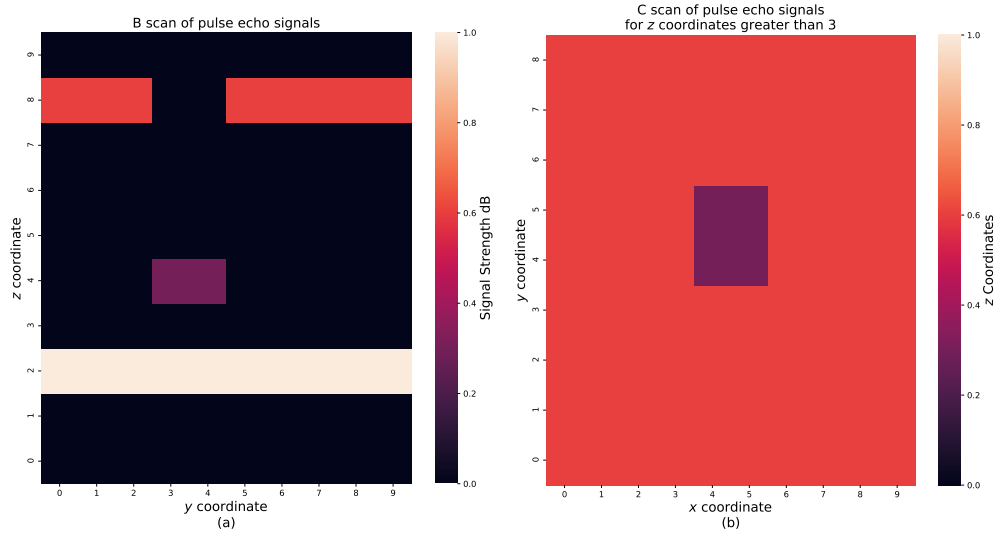


Figure 2.5: (a) B scan example of a pulse echo signal for a single row of x coordinate 4, displaying a possible defect at y coordinates 3 and 4 (b) C scan example displaying composite of 10 B scans displaying x and y axis for z axis values greater than 3.

2.2 Broadband Terahertz Spectroscopy

The Terahertz (THz) spectral range sits between microwave and Infrared (IR) $30 \mu\text{m}$ and 30mm [44]. Due to this it has been possible to utilise some techniques developed for microwave and IR. However systems are still complex, requiring several components to function. THz are a non-ionising radiation allowing for safe use around human operators, unlike X-ray. The three THz generating methods are electronic, laser and optical. Electronic generation and detection as a method is the more mature of the three due to the transfer of similar established methods within microwave. The use of optoelectronic systems allows for greater access to the range above 1 THz, at which point it has been observed that many important spectroscopic features occur [44]. Through generating THz pulses from ultra fast (femtosecond) lasers it is possible to detect from simultaneous broadband spectra and perform THz spectroscopy. This allows for the detection of both amplitude

and phase, providing simultaneous properties for both the absorption and dispersion of the samples under testing. However, the generation of THz pulses from lasers is a costly and complex process currently involving sensitive systems which may not be suitable for some industrial applications, such as mechanical workshops.

The use of THz Time Domain Spectrometry (TDS) in reflection mode has been shown to be successful in detecting multi layer delaminations [45]. That is to say delaminations which are independent of each other within a sample but overlap each other within the z-axis when considering in 3D space. Depth and thickness of these defects were able to be calculated to the μm scale with a 5% margin of error. This level of detail, while impressive, adds no benefit in an environment where a defect area once identified will be removed and replaced in its entirety.

TDS has a strong sensitivity to moisture, which results in precise moisture detection [46]. This is of particular interest within the area of composite sandwich panels within aerospace components, especially those located within areas of the aircraft that come in to contact with fluids (e.g. hydraulics, oils and fuels). As sandwich panels contain voids within the filler area in the form of honeycomb or foam fillers, they are susceptible to trapping moisture within these voids. This can lead to damage to the structure through the shrinking and swelling of the fluids due to significant temperature changes in flight separating the laminate panels from the sandwich filler. As TDS can be used in both reflective and transmission set up for inspection, it is able to detect sub-surface defects within the laminate structure to a high spatial resolution in the reflective method, providing quantitative details of depth. However due to the loss of propagation of the THz pulse when entering the voids of the filler section, this level of detail and ability to detect laminate defects is limited to the front laminate, this being the laminated in the direct line of sight of the reflective transmission and capture set up [46]. Such is the level of detail obtainable through TDS on composite laminate structures that it is possible to detect low impact damage to the skin of composite aircraft components such as bird strikes, hail, or tool damage during maintenance [47].

Due to the nature of low velocity impact damage, they can present without visual indication upon the surface of the composite laminate while subsurface cracks and damage can be extensive [48]. When compared, imaging results produced from Time Domain performed better than that of Frequency Domain, providing qualitative and quantitative detection of defects.

It has been shown that material properties within Carbon Fibre Reinforced Polymers (CFRP) are affected by fibre orientation within the structure [49, 50]. Amongst these is the electrical conductivity of the structures [51]. As such, the quality of readings achievable has been shown to be impacted by the alignment of the THz emitter and the fibre orientation of the sample undergoing inspection [52, 53, 54]. Further to this impact of electrical conductivity of composite laminates on the penetration of THz through the structure, subsurface inspection still requires more development to achieve comparable results to the established NDT/NDI techniques for CFRP [55, 56]

2.3 Heat Transfer

The process of heat transfer within the three basic phases of matter (solid, liquid and gas) has long been understood through Fourier's law of heat conduction [57]. The transfer of heat as energy due to the collision between particles which are excited by a heat source, as seen in Figure 2.6, can be classified as:

- Convection - Energy transfer between a solid and a moving fluid (liquid/gas) which are at differing temperatures. The convection heat flux (q), the rate at which this energy transfer occurs, can be described as:

$$q = h(T_2 - T_1) \quad (2.1)$$

Where h is heat transfer coefficient, T_2 is the fluid temperature, and T_1 is the temperature of the solid.

- Conduction - Energy transfer between solids where there is an imbalance

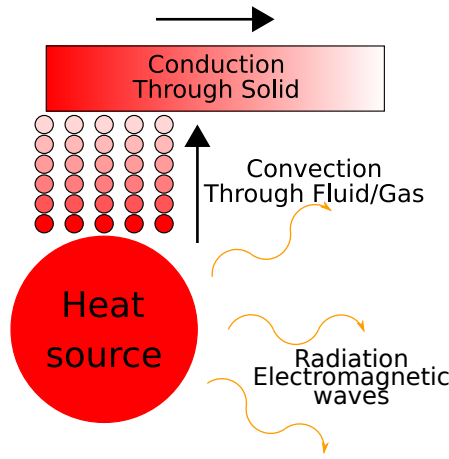


Figure 2.6: Convection heat transfer, through fluid/gas; Conduction heat transfer, through solids; Radiation of electromagnetic waves, example.

in energy, this occurs in the direction from the higher energised particles within the solid to the lower energised particles. Fourier's law describes the conduction heat flux in 1 dimension for the direction of travel (q_x) as:

$$q_x = k \frac{dT}{dx} \quad (2.2)$$

Where k is the thermal conductivity of the solid, dT is the change in temperature, and dx is the distance in 1 dimension.

- Radiation - Is the energy transfer through the emission of electromagnetic waves [58]. This transfer occurs from all bodies which have a temperature above absolute zero, and requires no specific medium to transfer. The Radiated heat flux (q) transferred in this way is described by the Stefan-Boltzmann law:

$$q = \epsilon \sigma T^4 \quad (2.3)$$

Where ϵ is the Emissivity coefficient, σ is the Stefan-Boltzmann constant and T is the surface temperature of the object radiating heat.

Modeling these energy transfers within a known space domain can be calculated through the finite element method. This is achieved by splitting the space domain through Discretization into smaller sub domains, known as finite elements, with nodes associated with each finite element. Figure 2.7 displays the breakdown

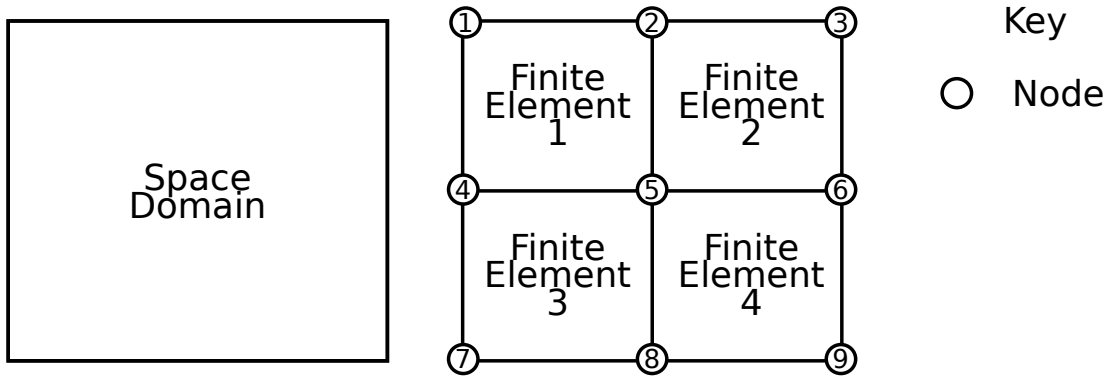


Figure 2.7: Example of FE method for a square space domain with quadrilateral elements.

of a square Space domain into 4 finite elements with 9 nodes. Once the nodes have been created the one dimensional energy transfer equations can be applied between nodes and an approximation calculated for the element described by the nodes through a shape function. For example in the instance of Finite Element 1 in Figure 2.7, described by nodes 1,2,4,5, the approximation heat flux for the finite element can be described as:

$$q = N_1q_1 + N_2q_2 + N_4q_4 + N_5q_5 \quad (2.4)$$

Where N is the shape function and q the heat flux. This finite element method is the basic principles for FE thermal analysis conducted in FE software like ANSYS. It is possible to measure the magnitude of the thermal energy within a material due to the relationship between temperature and electromagnetic waves. For example, in the case of iron ore undergoing a smelting process, where temperatures reach in excess of 1250°C [59], the changes within the electromagnetic spectrum are within the range of visible light and the human eye can perceive the temperature as the metal glowing in a range of colours. Further, the characteristics of the thermal radiation are influenced by surface properties from where it emits, Kirchhoff's law [58]. Of these properties, emissivity coefficient is regarded as how effective the surface can emit thermal radiation. This is described as a ratio (0 to 1) of the thermal radiation emitting from the surface of an object in comparison to that of a perfect black body object [60].

From Planck's equation [61] the spectral radiance (B) of electromagnetic radiation can be used to infer temperature given a black body in thermal equilibrium.

$$B(\nu, T) = \frac{2h\nu^3}{c^2} \frac{1}{e^{\frac{h\nu}{k_B T}} - 1} \quad (2.5)$$

Planck's equation and Fourier's law allow for both the quantification of IR data and its analysis.

2.4 Thermal NDT

The Non Destructive Inspection (NDI) method of thermography has developed from the nature of transient heat flux (Q) changes across a sample when thermal energy is applied [62]. These changes occur due to the changes in the structure (defects) impacting the diffusion of the thermal energy. Technological advancements over the years have made the use of Infra-red image capture of areas of interest the accepted method for Thermography inspection. This has been largely due to the development of of uncooled Focal Plane Array (FPA) [63] resulting in the system being able to capture data without the need of cooling systems. More recently the advances in data analysis and processing have allowed for the use of increasingly more complex algorithms, for example solving inverse heat conduction to characterise defects [62]. Active Thermography models can be classified into three areas:

- Type of thermal stimulation, e.g., electrical, optical, mechanical, etc.
- Arrangement of the sample and the heat source i.e. 'onesided' reflection based thermography and 'two sided' transmission based thermography.
- Size and shape of stimulated area i.e. point-by-point, line scanning and areal.

Processing the temperature data from scanned samples in its most basic form is achieved through calculating the differential in temperature between readings

assumed to be sound and scanned areas. The contrast between these readings can be assumed to indicate areas of interest and are generally visible on standard IR camera equipment. Processing techniques also have an impact on the heating times required to obtain areas of interest. The use of Signal to Noise Ratio (SNR) allows for the analysis of a single IR image that captures at the optimum observation time. This allows for short or pulsed temperatures to be used as heat sources to identify larger defects. A clearer image can also be captured with shorter heating times as it limits the lateral heat diffusion within the sample. With the availability of increasingly more complex data processing algorithms and affordable powerful processing computers [62] along with researchers and engineers who are able to process this data [64], the noise associated with thermal non-destructive inspection can be repressed to allow for sharper images and increasingly more accurate defect identification.

It is possible to apply external sources of heat such as Lock in Thermography (LT) and Pulsed Thermography (PT) as well as the option to generate internal sources of heat within the samples through mechanical excitement such as Vibrothermography (VT) [65]. LT and PT both make use of a heat source which is external to the sample under inspection in order to analyse how the thermal energy diffuses within the sample[66]. Where they differ is in the form that the heat wave takes between the heat source and the sample. LT makes use of an amplitude modulated heat wave in steady state (Figure 2.8(a)), where as PT uses a single pulse to inject heat into the sample (Figure 2.8(b)). Using optical sources for external heat application, such as lamps, can provide a fast non contact method of introducing thermal energy. However due to the nature of the heat source in the rays and the resultant heat profile inferred from emissivity, they are subject to the same restrictions as other forms of light, and as such the emissivity of the inspected sample is heavily impacted by reflection, surface roughness and conditions (e.g. dust) [67, 68]. As VT generates heat from within the sample, using ultrasonic transducers to induce vibrations/excitement (Figure 2.9), this removes the loss of thermal energy into the sample via reflection as can be the case with optically heated samples. However as the source of thermal energy is

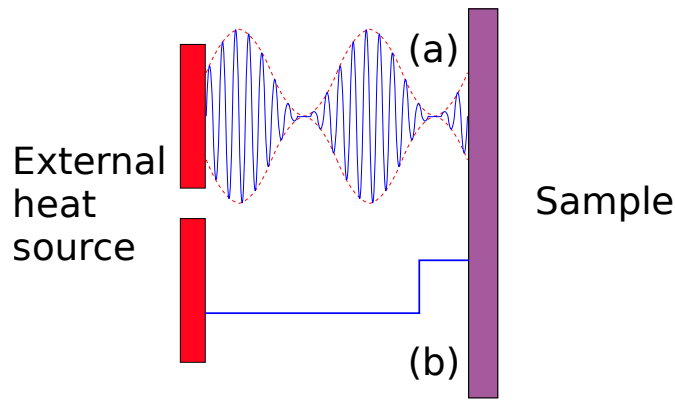


Figure 2.8: Waveform of (a) Amplitude Modulated in steady state, Locked in Thermography (b) Short single pulse, Pulse Thermography.

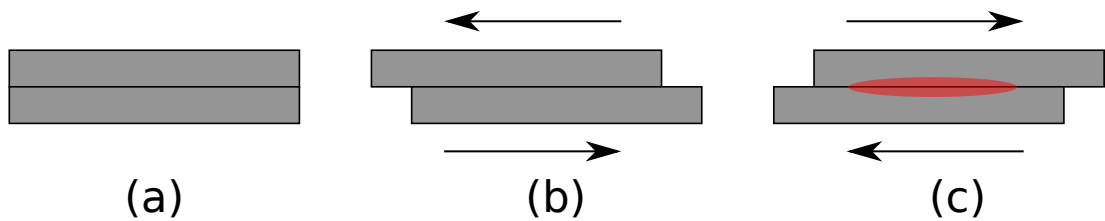


Figure 2.9: VT generation of heat within a composite laminate sample with inter-ply defect (a) At rest (b) Vibration exciting ply layers (c) Generation of heat due to friction between ply layers.

generated through the vibration of the sample, the sample must be immobilised to ensure that the transducer transmitting the ultrasonic wave has good contact. The use of a coupling agent is also required to ensure the transmission of ultrasonic waves and to prevent damage at the injection points due to misalignment of the transducer [65]. Both optical and vibration as forms of thermal energy within thermography require short time periods (a fraction of a s), high energy injections of heat as longer time periods of high energy heat being released into composite samples increase the risk of inducing damaging to the area [69]. The identification of delaminations, disbonds, excess adhesive and crushed core within composite Carbon Fibre Reinforced Polymer (CFRP) sandwich panels, has been compared for two sample panels of thickness 2.5cm and 7.6cm and for two densities of honeycomb utilising X-ray, C-scan ultrasonic, Pulse Thermography PT, LT and VT with varying success in identification [65]. In that study X-ray inspection of the samples was only able to successfully detect the honeycomb walls of the sandwich filler structure as well as disbonds and excess adhesive. The ultrasonic C-scan

inspection could detect all defect types and honeycomb walls. Accompanying ultrasonic C-scan with B-Scan cross sections also allows for a quantification of the defect depth within the samples. To compare PT, LT and VT the same two sandwich structure samples were inspected, for PT, a raw thermogram captured at 2.5s was used as it provided the best thermal contrast of the defects. When three processing methods were applied to the PT raw thermogram, Differentiated Absolute Contrast (DAC) , First Derivative (FD), Thermographic Signal Reconstruction (TSR) and Second Derivative (SD) TSR, FD results produced the clearest indications of all defects with the exception of delaminations, SD clearly indicates the delaminations and honeycomb cells [65]. As these methods use the same raw thermogram it is possible to capture all defects clearly within the sample.

A two-sided transmission based step heating method to accurately predict the thickness of stainless steel samples using an inexpensive halogen bulb with a gradual temperature increase, has been demonstrated to account for the gradual temperature rise from the halogen bulb heating source [70] by utilising a modified one-dimension formula of heat transfer [71] and half the rise time of the Greens' function [72]. Provided that the thermal diffusivity of the sample is known using the modified one-dimensional formula the thickness of the sample can be inferred. Conversely, if the thickness is known, then the thermal diffusivity can be inferred. The presence of a large amount of random errors occur when the sample process times are short, longer processing times provide better results, between 0–+3.7% for all sample thicknesses until the thinnest sample size of 5.09mm where an error percentage of +7.3% is produced [70]. In this work the authors argue that the accuracy of this technique is related to the process duration and not that of the thickness, while the random errors are directly related to the low power of the heating lamp [70]. As the heating source in this instance is a halogen bulb separated from the part by an air gap there will be a loss of heating from the source into the atmosphere due to convective heat transfer.

Similar to the aerospace industry, the wind energy industry are producing larger composite structures more than ever before. The construction of a wind

turbine blade, similar to that of an aerospace wing structure consists of the skin being supported by stiffeners running along length of the structure. The wind turbine blade joins the upper and lower shell via two shear webs via an adhesive bond. The turbine blades can have rotor diameters up to 180 m and weigh no less than 30 tons each [73], such loads apply enormous pressure to the adhesive joints. A method of inspecting the quality of these joints via transmission thermography has been proposed, where heat is transmitted to the back surface of the shear web via heating the air of the internal cavity through electrically heated wires [74]. This then thermally conducts through the structure of shear web, adhesive, and skin structure. Reading the resultant temperature profiles along the structure a quantitative ‘Adhesive Quality’ value analysis algorithm is proposed that can identify the adhesive boundary and predict thickness [74]. This demonstration shows that data obtained through a conduction to convection to conduction heating method can be used to infer the quality of a large composite structure.

There have been several experimental comparisons between MT and PT methods of thermography. Comparisons are required of these techniques on laminate structures to outline the advantages and disadvantages, to make an informed choice as to which method would best suit a particular Quality Assurance (QA) process. MT as a technique uses thermal waves, as such the phase frequency is directly linked to the defect depth. As the amplitude and phase images are not impacted by reflection upon the surface, and the phase image is not impacted by emissivity variations, no surface treatments are required to enhance the testing. As the phase image is created from variances in the phase angle no post-processing to the image is required. Another benefit to the phase angle and not thermal profile creating the phase image is that the inspected part is not required to increase temperature as much as is required by PT. It is noted that as PT uses temperature changes resulting from pulse heating, it should be possible to measure the width of defects, if these are close to the surface [75]. For deeper defects post-capture processing to the image is generally required due to the 2D transfer of heat (in the x and y axis) as it travels through the laminate (z axis).

The emissivity coefficient of the surface of the part being tested is required for PT to quantify any defects found, a surface treatment can be applied in order to improve the emissivity coefficient as well as reducing reflection to and from ambient sources. It has been noted that if quantifying the dimensions of the defect is not a priority and only the indication of a defect, then PT is able to provide indications of defects and greater depths than those achievable by MT [75].

It has been demonstrated that it is possible to apply pre and post-processing procedures that have been developed for pulse thermography in a step heating thermography method [76, 77]. The use of Thermographic Signal Reconstruction (TSR) , and early detection methods can be used with the Step Heating method and compared with PT. Similar to PT, TSR can be applied to Step Heating in order to produce thermograms of the log-log scale. It is noted that PT thermograms can be normalised by one value taken shortly after heat deposition has started to account for the impact of non-uniform heat deposition. This normalisation to a single value can be unreliable in the case of Step Heating due to the very low Signal to Noise Ratio (SNR) at the beginning of a heat deposition, However the logarithmic derivatives are automatically normalised. This method confirms the TSR processing technique used in PT is able to be applied to Step Heating to detect and image artificial delaminations within composite materials.

The time evolution of the contrast created by defects show that for both PT and Step Heating, the influence of thermal resistance decreases as the contrast tends to zero. However this is much more pronounced within PT making it a more accurate method for quantifying the depth of a defect using an early detection approach. Further analysis of this technique suggests that pulse heating provides an accuracy 2.2 times greater than step heating [76, 77]. It is suggested that this is due to the low SNR within the first images captured when the Step Heating method is used, which in turn negatively impacts the normalisation procedure. However, if no data processing is carried out a better image can be seen with Step Heating due to the thermographic sequence persisting within shallower defects better when compared to PT. The method verifies that the theoretical findings of TSR methods developed for PT can be successfully applied to Step Heating

thermography methods with minor alterations and produce accurate indications of defects. Through the monitoring of thermal decay after inducing heat into a laminate it is possible to identify sub-surface defects. This has been demonstrated via an automated detection and classification method by processing the thermal decay, utilising pulsed thermography was in a reflection capture setup [78]. It should be noted that as the laminates were not isotropic materials that traditional simplified models could lead to misleading interpretations of defect depth within finite samples. However, if the defects were larger than their depth this model would give a realistic approximation of thermal propagation and produce accurate defect depth estimates. As the samples were based on laminates common to the aerospace industry where the thickness rarely exceeds 3 mm and the tolerances of classified defects within these laminates are typically several millimetres, a less sensitive model would be suitable. The thinness of aircraft laminates also sits within the limits of penetration of the reflective thermography setup [79].

2.5 Heat source, considerations

In order to examine a sample in the transmission set up a heat source and capture method are required. For transmission of thermal energy several options are available. The use of an industrial oven, while available and the current method of injecting thermal energy into the V2500 fan cowl during the drying process, raises issues when utilising a contact temperature sensor to detect variations in thermal conductivity via surface temperature. This is due to the thermal energy being introduced to the sample via convection within the confined volume of an industrial oven. As this method requires the entire sample structure to be contained in a confined volume of air which is then heated, all surfaces which are exposed to the heated air become thermal injection points. For uniform application of thermal energy this is an ideal solution, however, as the contact surface temperature sensors will provide temperature readings of the temperature that they themselves are experiencing. As the sensing tooling surface would also have to be within the oven, the reading captured by the contact sensors is likely to

be that produced within the sensing tooling surface itself due to convection from the air temperature within the oven. To ensure that only through transmission temperature recordings are collected the heat source must be one which can be controlled and applied to the heated side of the sample only, thus ruling out use of an oven. As the final requirements of this research are for the inspection process to be implemented as part of the drying process, the heat source must also be capable of producing and maintaining a steady 80°C as per the drying cycle requirements.

2.5.1 Heat lamps

The use of heat lamps in composite repairs is commonplace within an MRO due to the ease of mobility and directional heating allowing for their use in a wide range of components. This optical method uses IR radiation generated from a halogen bulb, transferring it from the lamp to the structure via convection. Temperature can be controlled via distance of the lamp from the structure in conjunction with controlling the bulb via a thermocouple providing feedback from the surface of the component. This is achieved by setting a dwell temperature for the surface to reach, allowing for an overshoot within pre-set parameters, typically 5-10°C. Once the surface temperature is within the overshoot range, power to the lamp is cut off until the surface temperature drops to within another pre-set parameter, this time at or just below the dwell temperature. Areal coverage can be controlled via a shutter to limit the diameter of the beam created by the heat lamp as it reaches the surface of the structure being heated [80].

The use of heat lamps in IR thermography is accepted source of introducing thermal energy in both the reflective and transmission set-up [81, 82, 83, 84] however, as discussed within Chapter 1 the line of sight for IR radiation is impeded by consumables within the drying process. This may result in the uneven application of heat to the surface due to the consumables.

2.5.2 Laser

Another optical method of heat transfer, which is now common within several industries, is that of lasers. Due to their ability provide accurate, focused energy to the surface of structures is an rapidly growing research area with promising results. Focused laser radiation will generate heat within the surface at the focal point, such is the intensity of the heat generated within the focal point that it is possible to machine CFRP at high speeds to fractions of a millimetre [85]. Due to this narrow focal points achievable by modern day lasers their use in NDT/NDI allows for indication of defects at the sub millimetre [86, 87]. However, expanding the diameter of the laser to cover larger areas has an obvious impact in that it is no longer focusing the laser radiation, and as such generating heat to the intensity when focused. To cover larger areas with a single laser the use of a line scanning, or flying dot technique is required [88, 89, 90]. Although these techniques can be extremely fast and accurate, as with the heat lamp heated methods of thermography, they rely on a clear line of sight to the structure under inspection.

2.5.3 Induction heating

Induction heating of a structure is achieved through two effects of placing a ferrous structure within an oscillating magnetic field. Firstly, the induction of eddy currents within the structure will occur, as the structure is electrically shorted the eddy currents will generate heat. The secondary heating effect occurs due to hysteresis, where rapidly inverting magnetic fields create electrical resistance within structures that have magnetic properties. It has been shown that induction heating within CFRP composite laminates can generate temperature changes along the length of CFRP fibres [91], however these are considered minimal. Where joins are present between fibres, when comparing parallel fibre orientations to perpendicular fibre joins, it is possible to create a ‘circuit’ within the laminate and generate heat, which concentrates at these joins [92]. This requires for such closed-loop fibre ‘circuits’ to be present in order to generate heat via

induction [93]. As the control of fibre orientation and placement during manufacture involves multiple ply layers of varying fibre orientations, add to this repair patches, the continuity of fibres within a large composite structure is unlikely exist to the extent that could support a uniform controlled application of heat.

2.5.4 Microwave

It is possible to generate thermal energy within a structure through introducing electromagnetic energy to the structure via microwaves. As the thermal energy is converted from the electromagnetic energy, there is no form of convection or conduction resulting in an energy saving when compared to heat transfer methods [94]. This form of heating results in either volumetric or surface heating depending on the material properties. In the instance of dielectric materials, microwaves can produce volumetric heating within the structure due to dielectric loss heating [95]. Carbon is highly microwave absorbent [96] and as such microwave as a heat inducing method of CFRP layered structures such as sandwich structures may result in the thermal energy concentrating within the initial layer of CFRP laminate. The use of microwave heating in thermography has the benefit that as the thermal energy originates within the structure itself, any discontinuity presents as uneven heating, with defects and inclusions showing as cold spots when examined[97, 98, 99].

2.5.5 Vibration/Acoustic

The use of ultrasonic/ultrasound waves in NDI/NDT as a method where the attenuation of the sound wave is used to characterise the condition of the material under inspection has been discussed. Ultrasound waves are vibrations within a medium, this vibration can also be used to induce heat within a structure. The simplest method of this can be seen when two vibrating surfaces meet, the friction at the contact points will generate heat. This generated heat can be detected within defects where the contact surfaces of a defect are close enough so as to

be undetected by other methods [100] where the close contact may present as a solid structure. As the resonance within the material will alter in areas where the structure differs, it is possible to target the resonance frequency of defect areas to enhance their detection[101]. Similar to other heating methods where thermal energy is induced within the structure, the heating of the structure is non-uniform. In this method the thermal energy is concentrated in defective areas and is dependant on the contact areas for the quantity of thermal energy produced. As such, the temperature will be non-uniform across a structure, and theoretically non-existent in a perfect structure.

2.5.6 Heater mats

Composite patch repairs on aerospace structures can be conducted in situ with the use of localised heating to cure the repair area with non-silicon heater mats [102]. Due to the flexibility of the heater mats, they can be applied directly to the surface of curved surfaces and held in place via the vacuum bagging required for the consolidation of the patch repair. A uniform, easily controlled temperature can be produced across the surface of composite structures [103]. A wide range of shapes and sizes of heater mats are available, which allow for targeted, controlled heating of a structure under vacuum and in the presence of consumables associated with the vacuum process.

2.6 Contact sensors for thermal detection

The introduction of sensor systems to the surface of composites during the curing process can have negative impact on the mechanical properties of the cured laminates[104]. There are alternatives in the form of product health monitoring systems which can be cured within the composite systems that have shown negligible and sometimes improved material properties of the cured laminate [105, 106, 107, 108]. However, the introduction of any changes to the material within an aerospace structure has to undergo intensive testing to be certified

Table 2.1: Contact Temperature sensors benefits and limitations table

Sensor	Benefit	Limitation
Thermistors	-Low cost -Fastest response time	-Susceptible to ‘Aging’ -Low Accuracy
Thermocouples	-Simple to produce -Cheap -Large Temperature range -Robust	-Dependant on secondary Temperature sensor -Susceptible to electrical and magnetic interference -If sheathing required poor thermal contact can occur -Cable drift -Replacement time
Resistance Temperature Detectors	-High accuracy -Linear TCR -Interchangeable sensors (Class A and B)	-Self heating (negligible)
Fibre Bragg Grating	-High resolution -Single sensor	-Requires bonding to structure for accurate readings
Rayleigh Back scatter optical fibre	-High resolution -Single sensor -Cheaper than FBG	-Each probe requires calibration Requires bonding to structure for accurate readings

for use on aircraft [109], this is a costly endeavour both financially and in time requirements. An alternative to altering the materials within a component is to modify the method of curing, thus retaining the material certification as in the case of Same Qualified Resin Transfer Moulding (SQ-RTM) [110]. This modification to curing methods while retaining material certification opens up the possibility of inspection tooling which can serve as post curing tooling or as cure tools providing that non obtrusive sensor devices are utilised without impacting material properties.

2.6.1 Thermistors

Thermistors are Thermally sensitive Resistors made of solid semi conducting materials where their electrical resistance value is dependant on temperature, an

increase in temperature results in a non linear decrease in resistance [111]. The changes in resistance against temperature of thermistors can be plotted as a curve of specific resistance versus temperature and as such the temperature of the thermistor can be inferred from a given resistance reading. When compared to other thermal contact sensors, thermistors are the lowest cost and offer the fastest response time [112]. However, thermistors are susceptible to time related changes to their electrical characteristics, known as “Aging” [113] and commercially available thermistors often have an accuracy of $\pm 1^\circ\text{C}$ [114]. When considering the use of thermistors the lower stability of the sensor when compared to other sensors (e.g. RTD) must be considered. In applications where cheap highly responsive temperature sensors are required for short periods of time and accuracy is the least important characteristic, thermistors are the strongest candidate.

2.6.2 Thermocouples

The Seebeck effect results in a measurable voltage or Electromotive Force (\mathcal{E}) being produced between two metals which are joined via a junction point (e.g. a weld). This is produced when a temperature difference is present between the junction point and the free ends of the wiring. As it is the difference in temperature between two points that is being measured and not the absolute temperature at the junction point, a second absolute temperature reading is required to infer the absolute temperature at the junction point. This is achieved through the maintained known temperature of 0°C at the free end. However, as this temperature is unlikely to be 0°C , or maintaining such a temperature within an MRO environment is not practical and the use of cold junction compensation is required. This is achieved through a temperature reading obtained from a secondary temperature sensor at the cold end of the thermocouple, which is used to determine the missing voltage generated within the thermocouple when compared to that of a thermocouple with a cold end at 0°C . Accuracy of thermocouple systems depends on maintaining an accurate temperature sensor for the cold junction compensation.

Thermocouples are simple to produce and thus cheap, robust in nature as well as able to operate in a large temperature range (-270°C to 3000°C [114]). In applications where thermocouples require isolation from the sample being measured (e.g., corrosive chemicals), various sheaths can be used depending on the temperature range required. It is possible that electrical and magnetic fields can interfere with electromotive force through the introduction of external noise [115, 116]. Application of physical shielding from the effects of both electric and magnetic fields as well as environmental conditions can result in a poor thermal contact between the junction point and sample. This can result in temperature disturbance errors.

As this sensor type relies on an uninterrupted wired connection between the heat source and the free ends of the wiring, the wiring itself is part of the sensor. Any damage to the wiring itself results in complete replacement of the thermocouple from end to end. In an environment where the thermocouple is wired through long or complex routes, replacement can be a time consuming process. It also leaves the thermocouple susceptible to cable drift, intermediate junctions, and incorrect cable specifications impacting the readings captured [117].

2.6.3 Resistance Temperature Detectors

Resistance Temperature Detectors (RTD) are able to provide high accuracy temperature readings through the electrical resistance properties of pure metals. The electrical resistances of pure metals, such as platinum, have a linear increase against temperature [118, 119]. By calibrating a recording device with resistance against time for the RTD, the temperature of the RTD can be inferred based on the resistance reading. The relative resistance change per unit of temperature change within an RTD, Temperature Coefficient of Resistance (α or TCR), is calculated as shown in equation 2.6. R denotes resistance and T temperature.

$$\alpha(T) \equiv \frac{1}{R} \frac{dR}{dT} \quad (2.6)$$

RTDs when crafted from pure metal Platinum are able to infer temperatures within the ranges 13.8033 K and 1234.93 K with an accuracy of $\pm 1\text{mK}$ [120]. This is due to the high stability of pure metals used in the production of RTDs and the previously discussed linear increase of electrical resistance against temperature. During fabrication of an RTD it can be calibrated to the International Electrochemical Commission (IEC) standard 60751:2008 [121]. This standard classifies RTDs into either class A or class B.

- Class A RTDs have a temperature range between -200°C and 650°C and
- Class B RTDs a temperature range between -200°C and 850°C .

Under this standard, a TCR of 0.00385^{-1}K is required, leading to RTDs of this standard being referred to as 0.00385 type. By sharing the same TCR it is possible to effectively change out RTDs within a system without calibration provided that they meet IEC Standard 60751:2008.

As the use of a current within the RTD is required, they are susceptible to ‘Self Heating’, which can be calculated as:

$$\text{SelfHeatingError} = \frac{I^2 R}{\delta} \quad (2.7)$$

Where I is the measurement current, R is the measured resistance and δ dissipation constant. Through maintaining a constant measurement current the self heating error can also be accommodated for. Pt100 RTD element temperature sensors produce self heating of less than $0.5^{\circ}\text{C}/\text{mW}$ [122]. This self heating error in the range of and ambient temperature of 22°C to the oil drying cycle steady state temperature of 80°C , would result in a self heating of between $0.00010857^{\circ}\text{C}$ to $0.000130897^{\circ}\text{C}$. Such a low self heating range can be considered negligible for the intended application within this thesis. Additionally in this thesis a dedicated RTD module provides a constant current source to mitigate against self heating effects.

2.6.4 Fibre Bragg grating

Within optical fibres that have been created with Fibre Bragg Grating (FBG), the refractive index within the core is such that it periodically changes, as opposed to within untreated optical fibres where this is uniform. The result of this is that when a light formed of many wavelengths is introduced to the optical fibre, there will be wavelengths that are in phase with the grating and will be reflected back when it reaches the FBG. The light wavelengths that are not in phase will continue to be transmitted along the optical fibre. This produces two spectra of light, the reflected spectrum and the transmitted spectrum. When strain is introduced to the optical fibre, it deforms the fibre and the grating within the core. This deformation to the grating changes the profile of the grating and in turn the spectrum which will be reflected. By examining the reflected spectrum changes against time the strain within the optical fibre can be inferred. As the coefficient of thermal expansion for the optical fibre can be quantified the strain that it will undergo against temperature and time can be calculated. This allows for the calculation of temperature from the strain readings within the optical fibre that has been calculated from the spectrum changes [123, 124, 125].

FBG is a sensor method that uses strain to produce data, it requires bonding to the structure that is undergoing strain in order to undergo the same strain and operate correctly [126]. It is possible to bond FBG directly into or onto the structure which is undergoing inspection, however bonding into the structure requires a material change and as discussed this is a costly process requiring certification within the aerospace industry. Bonding directly onto a sample to record strain can result in damage to the sample and optical fibre during removal of the sensor and adhesive. Bonding to an external tool which sits upon the sample surface would measure the strain which the tool undergoes. FBG does offer a high resolution of temperature readings across a sample when compared to other single point contact sensors due to the ability to apply multiple gratings to a single fibre.

2.6.5 Rayleigh backscatter in optical fibre as a high resolution temperature sensor

Rayleigh backscatter can be measured through Swept Wavelength Interferometry (SW) [127]. Unlike FBG this method does not rely on a material change to the optical fibre and as a result the spatial resolution which can be achieved is not limited to the quantity of gratings which can be created within the fibre. The random fluctuations within the index profile of an optical fibre produce a Rayleigh backscatter that is unique to that optical fibre. This individual Rayleigh backscatter can be mapped at a known temperature/strain to form a calibrated function of the scatter amplitude across the length of the fibre. Swept-Wavelength Interferometry (SWI) can then be utilised to measure the Rayleigh backscatter of an optical fibre as a function of length [128]. Any changes within the length of the optical fibre due to stretching, will result in a measurable change of the Rayleigh backscatter, and therefore the length calculated. As the co-efficient of thermal expansion for the glass fibre is also known, the temperature change can be inferred.

This method as a temperature sensor results in a higher resolution than is achievable with other contact sensors. It is also cheaper to produce sensors than the comparable method of FBG as the optical fibres only require calibration of the Rayleigh backscatter with length and no physical modification. However, it does have the same limitations as FBG regarding bonding the sensor to either tooling or sample under inspection.

Table 2.1 outlines the discussed benefits and limitations of the contact surface temperature sensors within this section.

2.7 Machine learning applications in Non Destructive Inspection and Testing

The coining of the term machine learning is often credited to Arthur Samuel [129] who developed what would become the min-max algorithm. Machine learning can

be used to provide prediction of results or classification into groups based on inputs in the form of features [130]. As a method it can be separated further into sub methods of Supervised, Unsupervised and Reinforcement learning [131]. Supervised algorithms generate models to predict or classify inputs after training on data which has been labelled with the correct classifications or predictions [132]; Unsupervised algorithms are provided with unlabelled data in order to find patterns within the data sets [133]; Reinforcement learning which utilises a trial and error sequence of events, these sequences are rewarded or punished depending on their outcome, producing a model from the highest scoring sequence [134]. Of these sub methods, the supervised algorithms are most commonly used for machine learning applications for Non Destructive Inspection or Testing, as ultimately the objective is to produce classifications of either ‘Defect’ or ‘No Defect’ and data sets obtained for either known manufactured defects or from established NDI/NDT techniques can be produced. The orientation of fibre reinforcement within a Fibre Reinforced Polymer (FRP) component has a substantial impact to the wear rates [135] and strength [136]. The use of Pulsed Thermal Ellipsometry (PTE) combined with an Artificial Neural Network (ANN) has been successful in providing estimates of the fibre orientation of Randomly Orientated Strands (ROS) within the surface of laminates [137]. Through application of image processing techniques [138] this method is also able to assess the fibre orientation of continuous fibres within a laminate with a single point heating source.

Three image post processing techniques: Dynamic Thermal Topography (DTT) [139], Pulsed Phase Thermography (PPT) [140] and Principal Component Thermography (PCT) [141], along with image binarising using an automated threshold selection based on the Otsu method [142] can be used to create a line envelope. Samples undergoing such a process produce numerical features which can be used as inputs in an ANN. The outputs of the ANN provide classification of the samples into one of four classes with a 45° range used to represent the fibre orientations of 0° , -45° , 90° and $+45^\circ$. Demonstration of this method resulted in an output layer of four neurons each responsible for recognising the individual four classes [137].

A strong argument for using ANN in quantifying defects captured in thermo-

graph is their ability to handle non-linear problems from data that is noisy or incomplete [143]. This would include the thermal variations within a material that are not in themselves linked to a defect. This is of interest as it aerospace components within the MRO environment will have thermal variations across the structures due to geometry changes, such as reinforcement for rib structures, or ply variations due to repairs. Training of a neural network (NN) to detect defects within an Aerospace structure, based on training data alone, requires noise addition to the simulation data along with filtering as if it were experimentally captured. However, it has been demonstrated that even with the addition of data sets created via simulation, a poorer performing model will result when compared to that of one trained on experimentally captured data [143]. It has been argued that using NN inputs of raw temperature and contrast data alone will not produce reliable classifications between defect free areas and those which contain defects [144]. The production of clear differences between the classification of defects and defect free areas can be improved when the input data was enhanced by the thermal running contrast data curve [144]. As previously discussed [143], it has been shown that a NN can reliably identify defects within the samples with noisy input data.

As seen above the literature is filled with machine learning for the classification and identification of defects within thermography using IR camera data. The outcome of this research is to establish a non-IR system that can identify defects within a composite structure. In material classification for robotics, there is an abundance of research that uses single point probes in conjunction with heating elements and machine learning to identify and classify materials through thermal profiles [145, 146, 147, 148, 149]

It has been demonstrated that through short duration (0.5 s to 1.5 s), the incidental contact between a single point probe and the resultant transient thermal temperature/time curve, that a ML system can identify materials with a high accuracy (84% at 0.5 s and 98% at 1.5 s) [146]. As the ideal future process for this body of work requires to produce no added time to the current process by utilising existing non image based sensors further exploration of robotic sensors

in this area is of great interest.

Within Non Destructive Inspection methods utilising thermography, it can be difficult to differentiate between defects and temperature artefacts, such as non-uniform densities within a structure, requiring the experience of a trained operator[150]. Semi-Automated techniques such as Signal to Noise Ratio (SNR) algorithms require a known ‘sound’ area to use as a base. Within structures of an unknown condition, it can not be assured which areas are of ‘sound’ condition. SNR is also best used as an evaluation method when some extent of the defect and location data is known. To create a more automated technique based on SNR algorithms, utilisation of a Mean Shift (MS) filtering to tune spatial and range resolutions within samples so as to allow for MS segmentation into areas of interest (defects) and areas not of interest (sound) can be used [150]. This has been achieved through the creation and use of a weighting map of the scanned area, which modulated the MS vector to better detect edges. The improved MS filtering method application to several processing techniques is commonly used within IR thermography. Of the processing techniques tested, First Derivative (FS) has been shown to produce the best results in both laminate and honeycomb sandwich structures [150].

One method of identification of defects within a vision based system is that of a Random Forest (RF) algorithm using Variance of Variance (VOV) features. This feature selection method measures the variance of pixel intensity across the image, due to normal surface conditions, then in turn allows the RF to identify any variations outwith the general variation [151]. Within Aerospace vision based NDT techniques such as Fluorescent Penetrant Inspection (FPI) , require an operator to treat the surface of component with fluorescent penetrant, then visually inspect the surface under ultra violet light. Where surface defects, such as cracks, exist the penetrant dye will pool and produce strong fluorescent results, easily drawing the eye of the operator. Through feature extraction of Peak Brightness, Haar Features, Area of Bright Regions, Average of bright pixels and Standard deviation of bright pixels a RF algorithm can be trained which performs to the standard of a trained and certified human operator[152].

Support Vector Machine (SVM) algorithms make use of hyperplanes which split and cluster data to provide a classification. The SVM is compatible with small data sets [153] and can be applied to both classification and prediction problems. For time series data, the use of SVM algorithms to predict outputs has been shown in some cases to out perform NN when using the Mean Absolute Error as a performance indicator [154].

Of the discussed methods, the literature demonstrates that all are suitable for the classification of defects within composite structures. However, consideration must be given to the certification of the method within a real world environment. The Aerospace industry is a highly regulated area, and as such inspection and testing methods must be fully understood. The use of NN based methods may fail in it's attempts for certification due to the 'Black Box Problem' [155]. This is the problem of the NN not providing a clear description of it's decision making process to achieve the result, as both SVM and RF methods are more transparent in their selection methods they have the ability to be scrutinised. This Thesis will focus on the use of RF and SVM based methods, due to this criteria as the method aims to be applied to a working MRO facility.

2.8 Summary

When considering the selection of an appropriate inspection method to build upon, the environment in which the proposed method is to be applied to and procedures it is to be used in conjunction with are of most importance. The main benefit of using the contact method of Ultrasonic Inspection comes in the form of high resolution areal reports of components. However as this method requires unobstructed access to the component's surface it does not lend itself well to integration into the existing process without adding considerable time and cost.

High levels of detail surrounding the material properties of a sample can be produced through the application of Broadband Terahertz Spectroscopy. However the method is still not an established technique, as of the writing of this thesis,

widespread industrial adoption of the method is still to be realised [156]. As such, most available equipment is in the form of experimental equipment designed for the development of the method.

Thermography as an inspection method within the problem statement is an obvious choice due to its compatibility with the process methods it is to be used in conjunction with already utilising heat. The method is also able to provide high resolution areal reports of the component in the form of IR images, and provide detailed material characteristics through data analysis. Through modification of the capture method used within thermography from an array of temperature data obtained from pixels within an IR image to an array of temperature data obtained from contact temperature sensors, the established data analysis methods can in turn be modified and built upon to produce useful reports.

The main benefit of thermography as an inspection method within the scope of this thesis is realised in the compatibility of transmission-based heating with that of the required oil drying cycle. A suitable heat source that is able to provide the required areal heat coverage for a drying cycle as well as produce the thermal energy profiles necessary for thermography is needed. Of the options discussed, non-contact methods are ruled out again due to the consumables present within the vacuum bag set up on the component resulting in an unpredictable heating profile directly to the surface. The proposed method will make use of a direct contact heat source to assure uniform areal heating to the component when under inspection, as well as providing the opportunity to be used as a heat source for the oil drying cycle.

To make use of the thermal profile generated within the component due to transmission heating, contact temperature sensors are considered. All of the contact temperature sensors considered lend themselves to integration within the proposed methods vacuum set-up, and a high level of resolution can be achieved with both Fibre Bragg grating and Rayleigh back-scatter in an optical fibre. However both of these sensor types are costly and difficult to replace within a tooling surface. The single point contact temperature sensors require placement of each point within an array of known distances to produce the required temperature

array. Consideration has to be given to the environment and application of the method, as such the sensor must be robust and easy to replace whilst also producing accurate temperature readings. As thermistors are susceptible to ‘Aging’ through repeated use, which impacts the accuracy of the readings produced, their consideration as a contact sensor must be done so in the knowledge that calibration of the sensors must be carried out prior to use. Accuracy over time is also an issue with the application of thermocouples due to ‘cable drift’ and possible electrical and magnetic interference from intermediate connections between the sensor and capture device.

The Resistance Temperature Detector provides accurate temperature readings through a linear Temperature Coefficient of Resistance, and this Temperature Coefficient of Resistance is maintained across all RTDs which are manufactured to the same standards. As such, it is possible to replace an RTD with another of the same class without need for calibration. RTDs are a low cost contact temperature sensor which are common to the MRO environment. For these reasons they make an ideal candidate for application in the proposed method as the contact temperature sensor.

Investigation into existing methods of data analysis and machine learning for established IR based thermography suggests that as the methods are based largely on Fourier’s transform equations and the interaction between temperature points at known Cartesian coordinates. Provided that the proposed transmission based method within this thesis utilises both it should be amenable to the application of similar data analysis and Machine Learning methods. As the proposed method will not achieve the same level of resolution of which IR image thermography is capable, investigation into inferring useful indications from between capture points will be required for more complex inspection.

With the selection of heating methods, contact temperature sensors and analysis considered, a method to examine sample with these methods is required. Chapter 3 will discuss the development of a tooling system capable of conducting thermography inspection using contact temperature sensors.

Chapter 3

Tool Design and Validation

Identification of defects through contact-based temperature sensing necessitates the construction of a versatile and flexible apparatus that permits the injection of heat into the components of various geometries and a mechanism to measure the component temperature profile in an accurate and repeatable fashion. Since the intention is to utilise techniques similar to image-based IR thermography, where temperature changes and intensity are recorded as changes in pixel intensity [78], it is proposed that the apparatus should gather temperature measurements from contact temperature sensors in a grid-like fashion similar to that captured IR thermography. The proposed inspection techniques are targeting defects in thick structures often containing honeycomb cores. These target structures are typical for most aerospace components and therefore transmission based thermography techniques are adopted as these have been shown to be more appropriate for this specific class of structures (described in Chapter 1). Taken these constraints in consideration, the developed apparatus consists of a heated surface which is used to inject heat into the component under inspection and a second surface that contains an array of temperature sensors to measure the thermal response of the component as illustrated in Figure 3.1. This chapter proposes the design and testing of two sensor tooling surfaces; Section 3.3.1 provides an overview of the construction and implementation of the hybrid airpad sensor tooling, including

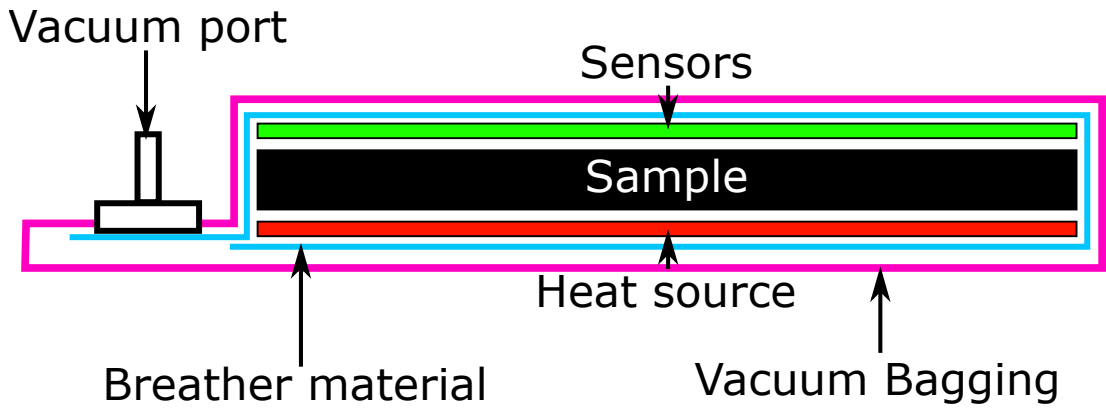


Figure 3.1: Proposed setup to capture thermal transmission through a composite structure, sample sandwiched between a heat source and corresponding sensor array, within a vacuum bag setup.

the issues identified when used. The second surface utilises a Printed Circuit Board (PCB) array which is discussed in Section 3.3.2. The benefits of the PCB array tool over the hybrid airpad array tool resulted in its selection for use in experimental data capture within this thesis.

3.1 Heated Tooling Surface

As the proposed method will require the application of the heated tool directly to the sample, consideration must be given not only the control of temperature within the tool but also the environment in which it is to operate. Due to the cyclic loading which will occur through the application of the heated tool surface to samples, as well as undergoing repeated vacuum loads it is desirable for the tooling itself to remain flexible. Furthermore, the heat source must allow for the setup to be applied directly in the oil drying cycle process without modification following the inspection step.

3.1.1 Heat Lamps

As discussed in Chapter 2 there are several options available for use as a heat source within a transmission setup. Heat lamps directed to the rear surface of the component, however, these would require an increased energy consumption

to overcome the insulation and uneven consumable placement may result in an unknown and uneven thermal application on the component surface.

3.1.2 Laser heating

Excitement via laser provides rapid and accurate heating to the focal point of the laser. This does provide the opportunity for focused inspection at the focal points, however heating of large areas requires either multiple lasers or high energy consumption to power a large diameter focal point.

3.1.3 Inducion Heating

Induction heating within CFRP as a method has been discussed within the background of this thesis, which was discounted as a heating method applied directly to a CFRP sample due to the minimal temperature changes and difficulty in controlling areal temperature zones due to the quasi-homogeneous nature of CFRP. However, within a homogeneous ferrous structure, targeted heating with this method can be achieved through coil design and power control [157, 158, 159]. There is an opportunity to utilise induction heating of ferrous tooling surfaces, such as steel, allowing for a tough heated tooling surface. It should be noted that the coefficient of linear thermal expansion for ferrous metals such as steel, between 10.8 to $12.5 \cdot 10^{-6}m/(m^{\circ}C)$, is high. When compared to the coefficient of linear thermal expansion for CFRP materials, $-0.8 \cdot 10^{-6}m/(m^{\circ}C)$, which are often described as "negligible" [160], a significant difference is observed. Interaction between these vastly different coefficients of linear thermal expansion, especially when considering trapped geometry surfaces within the tooling, has the potential to cause damage to the samples through a mismatch of geometry developing under temperature. Due to the complex nature of induction heating, the associated financial investment to set up the method is high when compared to other methods [161].

3.1.4 Resistance heating

The use of CFRP's electrical resistance to control heating of laminates for curing has been investigated with some success [162, 163, 164]. This is achieved through the application of electrodes to opposite ends of a CFRP laminate and introducing an electrical current. The electrical resistance within the CFRP will produce heat as a by-product of the electrical resistance, the temperature of which can be controlled through changes to the electrical current. Issues arise in producing uniform temperatures across laminates when the fibre orientation is not uniformly parallel within the laminate and the fibres perpendicular to the electrodes [165]. As a heating technique this method also requires that the electrodes be attached directly to the fibres, a requirement which would require some degree of destruction to a cured laminate if it is to be considered as a heating method for the proposed methods. This is due to the resin system providing a barrier to the fibres. As there is requirement for small, controlled areal coverage to allow for compatibility between the 3 inspection methods, as well as the difficulty in producing uniform temperatures in laminate plies of varying orientation, direct resistance heating applied to the laminate under inspection would not appear to be an appropriate heating option. However, with consideration given to the fibre orientation, electrodes could be cured into a CFRP tooling surface in sections which would provide the strip heating required to produce heating profiles which are compatible with all 3 proposed inspection methods within this thesis.

3.1.5 Microwave heating

Microwave energy can be used to generate heat from within the structure through the excitation of the molecules within the structure. CFRP, however, is highly microwave absorbent, applying microwave energy in a transmission setup will result in the back surface of a CFRP sandwich panel absorbing the majority of the microwave energy acting as the heat source for the remaining structure. This unbalanced injection of heat may result in thermal damage. Finally, the components under consideration are heterogeneous with metallic honeycomb structures,

making the heat injection process complex.

3.1.6 Mechanical heating

Mechanical excitation could be applied directly to the surface of a component via a dielectric transducer to generate heat within the structure itself. This is known as Vibration or acoustic heating, the vibrations within the structure generate heat via friction, however, this will result in a concentration of heating within an area of defects where inter-ply interactions exist and hence not suitable for controllable, spatially uniform heating method.

3.1.7 Heater mats

Heater mats are widely available within the MRO environment and commonly used for targeted heating of patch repairs. They are flexible, rubber housed, sectional areas which are compatible with vacuum set ups and resistant to contaminants. A similar ramp response rate to that of industrial oven heating is produced by the heater mats, due to both utilising electrical resistance as the source of heat. Set-up and application of heater mats is achieved quickly through direct application of the heater mat to the area requiring heat, and control is achieved through contact sensor feedback.

Considering that the main objective of the thesis is to investigate the feasibility of detecting defects in carbon fibre parts in the MRO environment, the selection of the heated tool surface is not as critical as long as it provides a spatially uniform heating stimulus. The remainder of the thesis utilises heater mats to provide the heating stimulus and in particular an 100W 150 × 150 mm 240 V RS heater mat, which can reach maximum temperature of 180°C and 150°C in continuous use [166]. The algorithms and analysis proposed in this thesis can be fundamentally transferred to setups with alternative heating sources without loss of their applicability.

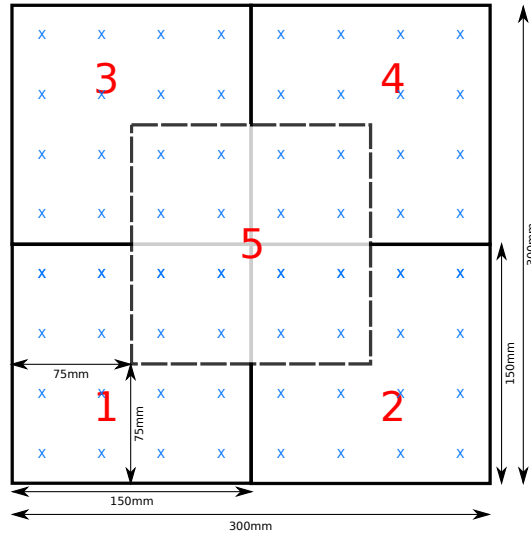


Figure 3.2: 150mm by 150mm heat zones 1-5(Red) and probe locations (Blue x) on 300mm by 300mm laminate panel.

3.2 Heater mat tooling surface

The final heated surface consists of a heated surface that can be arranged in a variety of ways and utilising multiple heater mats to facilitate the experimental needs. In particular:

- Section 3.6 utilised 4 heater mats arranged in a 2×2 array (positions 1-4 as shown in Figure 3.2) and controlled simultaneously to emulate a single heater mat of 300×300 mm.
- Chapter 4 utilise one heater mat which is shifted through positions 1-5 as shown in Figure 3.2.
- Chapter 5 utilise 1 heater mat which slides across the x -axis of the panel surface at 18.75mm increments and more details are given in the chapter.

In all cases, the heater mats are held in contact with the bottom tool surface through vacuum. The Samples sizes fabricated are 300×300 mm and 500×500 mm, these are industry standard sample dimensions based on the areal requirements of testing apparatus. During the validation and testing of the proposed methods within this thesis, the physical placement of heater mats into the correct locations is appropriate due to the limited number of arrangements they can be

situated in upon the samples (300×300 mm and 500×500 mm). However, when considering the final application upon the V2500 fan cowl (approximate dimension 3000×1800 mm) a significant increase in the required heat sources, where by any time savings realised in the use of the proposed inspection methods would be lost during the physical application of the heat sources. A tooling surface with controlled sectional heating requires consideration to realise the time and cost savings associated with the proposed methods. Given that all developed techniques employ fundamentally the same physical heated surface, an alternative heating method could be utilised to provide controlled temperature profiles via modular heat zones and satisfy the requirement of all three NDI methods.

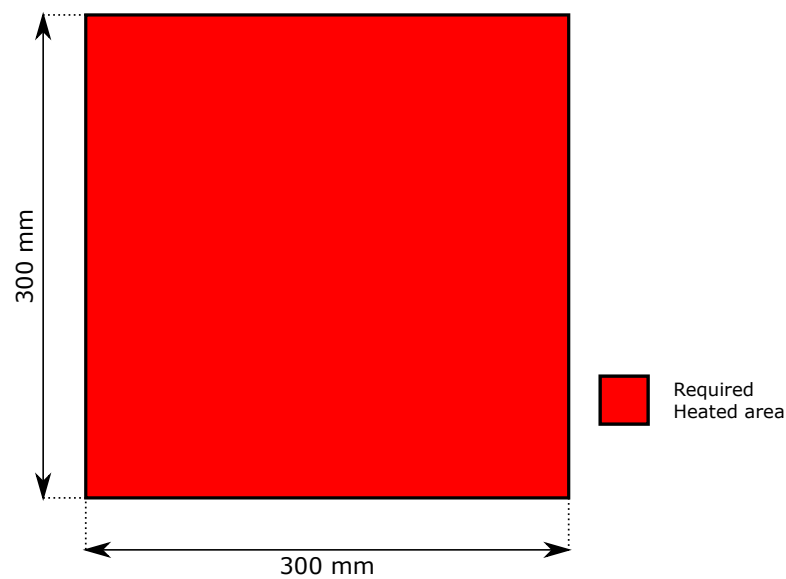


Figure 3.3: Heated areal requirements for Impact detection only.

Of the three proposed methods within this project, the simplest to achieve regarding areal heat coverage is that of impact detection for composite sandwich panels (Section 3.6). Over a 300×300 mm areal surface Figure 3.3 displays the required heated areas, which can be seen to be full coverage of the 300×300 mm area. This could be in the form of a singular heat source with full coverage, or an array of smaller heat sources used in collaboration with each other to produce a single heat source.

In Chapter 4 the requirements for fibre orientation indication are a centrally located heat source to obtain temperature profiles which are indicative of a con-

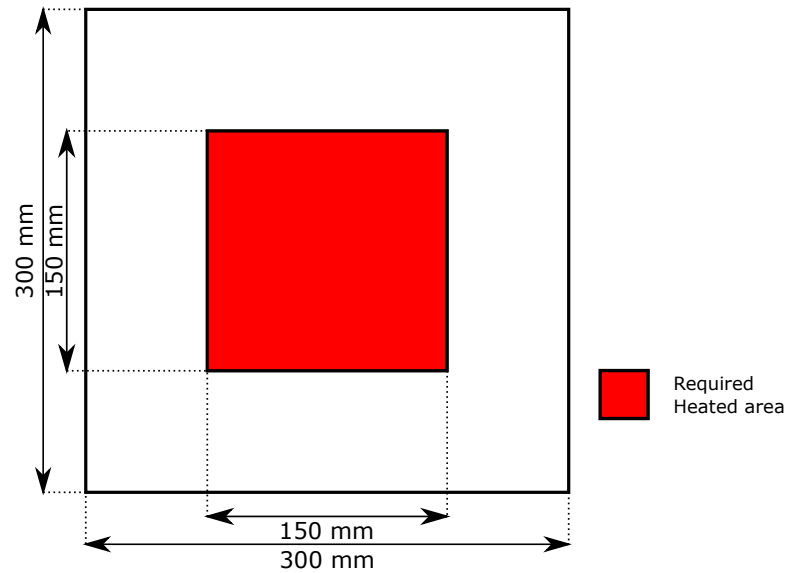


Figure 3.4: Heated areal requirements for fibre orientation indication only.

centration along the x -axis, y -axis or a combination of both and how that profile relates to known ply fibre orientation profiles. As is seen in Figure 3.4 this can be achieved by heating a 150×150 mm square within the centre of the sample.

For the delamination detection method (Chapter 5), the method utilises temperature against time profiles generated as a result of the transient thermal conduction due to structural dissipation within the sample. This has been successfully demonstrated in detecting delaminations from probes located within 93.75 mm of the centre of a 150×150 mm heater mat. Within this 93.75 mm, two separate heating groups exist:

- The transmission group, where the main factor for heating comes in direct transmission of thermal energy through the thickness of the sample via the heat source.
- Conductive group, where the transient thermal conduction due to structural dissipation impacts the temperature profiles of the sample within these areas.

Probes from both heating groups can be described as existing in a 75 mm column within the y -axis relative to the heater mat. To achieve a reading for each probe from both heating groups across the sample and ensure that a delamination of 40

$\times 40$ mm, the minimum allowable, can be identified a 150×150 mm heat source is required to move along the x -axis in 75 mm increments. Figure 3.5 displays this in a 150 mm section in the y -axis and 75 mm strips in the x -axis representing the movement of the heated area.

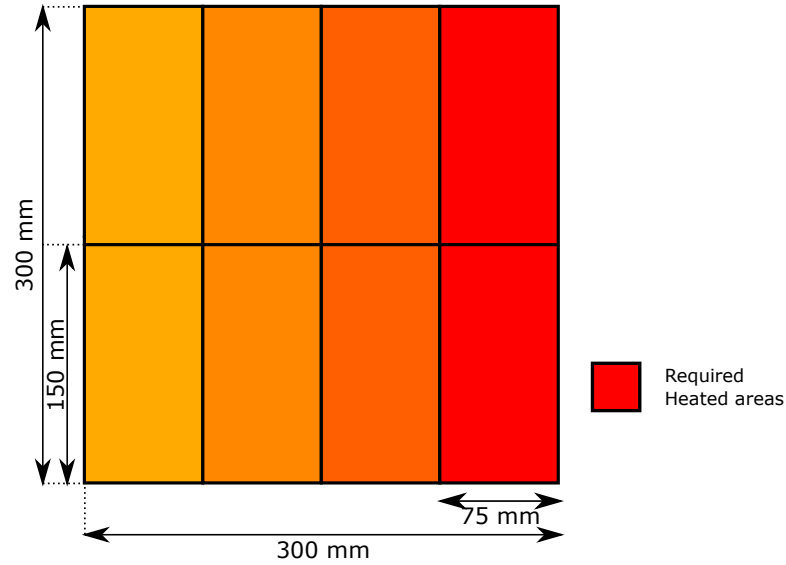


Figure 3.5: Heated areal requirements for delamination detection only.

When the required heated areas for all three methods are overlaid, the result is seen in Figure 3.6. It can be seen that the 75 mm strip sections will fit to the width of both the 150 mm sectional width required for the fibre orientation indication method and the 300 mm width required for the impact damage detection method, when used 2 times and 4 times respectively. Moreover, it is noted that in the y -axis half of the bottom row of 150 mm tall 75 mm wide strip section covers the bottom half of the 150×150 mm fibre orientation indication heated area requirement where they overlap, this is repeated along the top row of the 150 mm tall 75 mm wide strips section in regards to the top half of the 150×150 mm fibre orientation indication heated area requirement. From this it can be reasoned that the smallest dimensions of a shape which when arranged equally across a 300×300 mm area of composite structure which is to undergo any one of the three methods is 75 mm in the y -axis and 75 mm in the x -axis. Figure 3.7 displays this in a 4 row \times 4 column array of heated areas. When all heated areas are under temperature a full 300×300 mm areal heat coverage is achieved as is

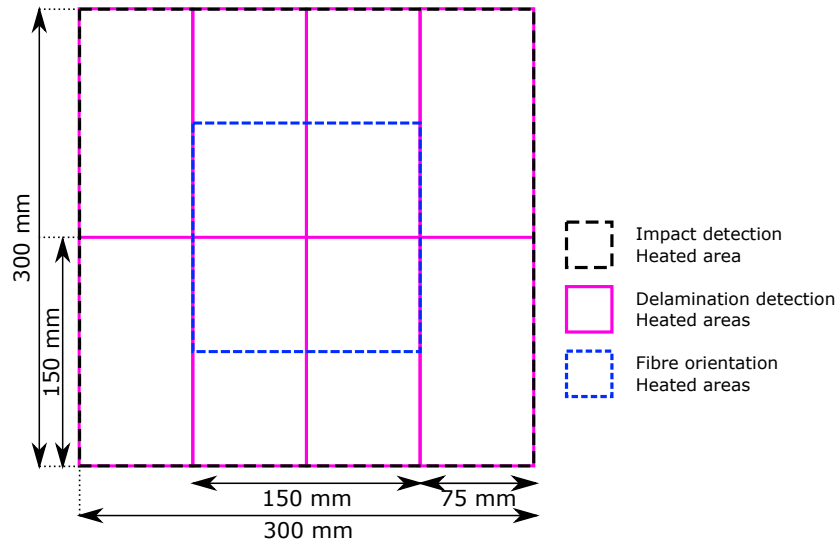


Figure 3.6: Heated areal requirements for all three methods, overlay.

required for the impact detection method. Heating only the heated strips within

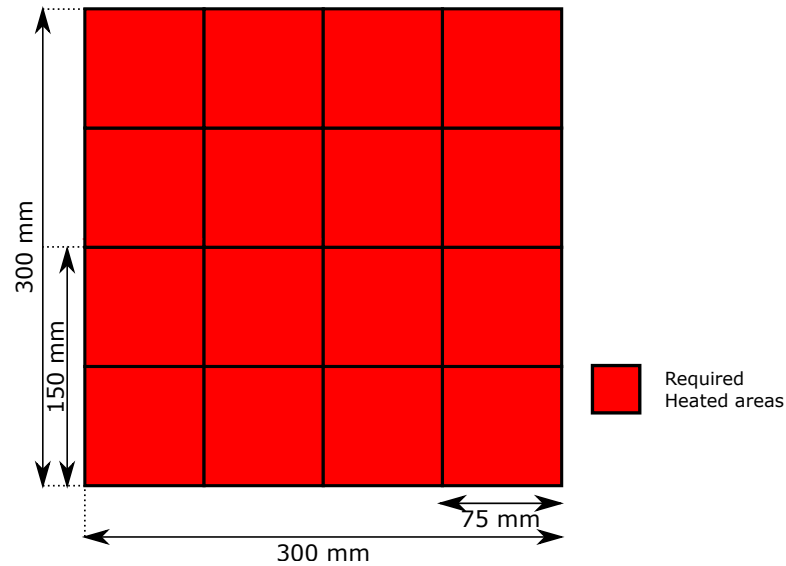


Figure 3.7: Heated areal requirements for impact detection, strip heating.

the 150 mm \times 150 mm section at the centre of the 4 \times 4 array of heated areas, as seen in Figure 3.8, provides the 150 mm \times 150 mm areal heat coverage required in the fibre orientation identification method for the sample.

For the final of the three proposed methods, delamination detection, the required heating areas can be achieved by heating a 150 mm wide section of 2 columns from the 4 \times 4 array of heated areas. This 150 mm wide 2 column section can be incrementally moved along the x -axis by heating an additional

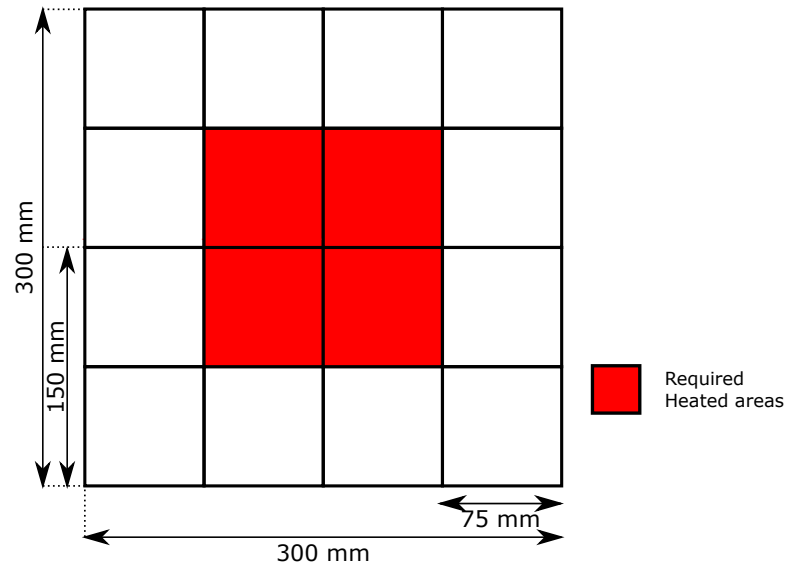


Figure 3.8: Heated areal requirements for fibre orientation identification, strip heating.

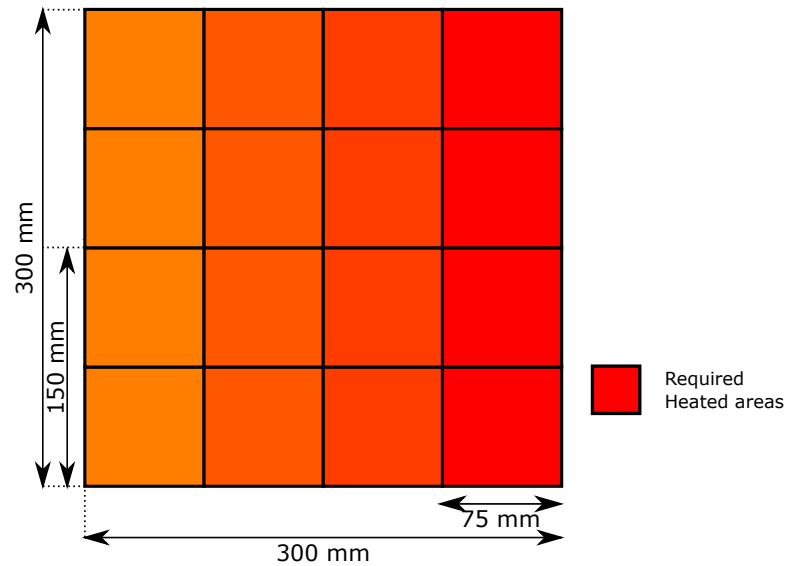


Figure 3.9: Heated areal requirements for delamination detection, strip heating.

column and removing the initial 1st column, maintaining the 2 column width.

Utilising a 4 row \times 4 column of 75 mm wide \times 75 mm tall array of heated areas which can be controlled individually would allow for all three proposed methods to be conducted from a single heated tool. A cooling interval between methods, and in the instance of the delamination detection method between incremental heated area movement along the x -axis, would be required to allow the tooling surface to return to ambient temperature to perform as expected.

3.3 Sensing Tooling Surface

There is a number of considerations which must be taken into account when designing the sensing tooling surface to ensure that the tool is fit for purpose in the MRO environment. The most established IR-thermography techniques [167] rely on Fourier transform, which necessitates prior knowledge of the distance between temperature probe points and accurate profile of temperature versus time. To ensure consistency between inspections and reduce the need to calibrate sensors based on placement, the sensors can be fixed within a tooling surface and their locations relative to each other will be known and measurable. There are multiple options to maintain the temperature sensors in place:

- Manual Placement held in place with adhesive. This approach will result in increased labour in the process, also risks damaging the part surface upon removal, and is prone to human error.
- Template based tooling surface that holds the temperature sensors in position; this approach would be expensive to manufacture and requires bespoke molds for individual parts. There is a number of possible materials to use such as aluminium, plastic, or carbon fibre. Metallic tool surfaces could result in heat absorption, which may increase data processing complexity because the thermal response of the tooling surface must be taken in consideration. Plastic tools could lead to warping through multiple process cycles. On the other hand, carbon fibre tools are more appropriate since the material is thermally stable, however, rigidity remains still an issue.
- One approach for sensor integration is to utilise a hybrid construction combining the strengths of non-silicone rubber materials and carbon fibre. This combination provides a semi-flexible, thermally stable surface which mitigates the before-mentioned issues.
- Glass fibre Printed Circuit Board (PCB) provides a thermally stable tooling surface upon which contact temperature sensors can be mounted. These

are available in a range of thicknesses and dimensions which result in semi-flexible options. As these are printed from design files, the produced PCBs dimensions are the equivalent of any created from the same design. This also allows for the accurate placement of sensors upon the printed mounts.

Initially a hybrid non silicone rubber and carbon fibre construction was trialed as described in Section 3.3.1 however a number of issues were identified. Ultimately, the remainder of the thesis utilises a glass fibre PCB which was constructed and implemented as described in Section 3.3.2.

3.3.1 Hybrid Airpad and Carbon Fibre Tooling Design

Silicone contamination in composites such as graphite/epoxy, during MRO operation has a significant impact during processing, resulting in adhesive related failures [168, 169, 170]. Such contaminants can prevent bonding between laminates or result in areas of weakened bonds. These weak bonds can go undetected during inspection as the differences between weak bonded areas and homogeneous regions are negligible, it is not until a stress is introduced that the bond fails. A non-silicone rubber such as airpad HTX [171], which is typically used in the production of pressure caul sheets, would be appropriate to house the temperature sensor array mitigating the risk of silicone contamination. This material was chosen over other non-silicone rubber options such as airpad FMSC [172] as it eliminates the need to use a permanently bonded release film. Furthermore, the non-silicone requirement is imposed by the clean room facilities used to manufacture the airpad array and prohibits the use of silicone to avoid contamination of adhesives. The airpad array was fabricated and cured within the Collins Aerospace Prestwick Service Center, which is a live MRO facility processing in-flight aerospace components, making it crucial to follow site fabrication guidelines.

A number of possible contact temperature sensors have been considered for the implementation of the tool as described in Section 2.6. For this construction, RTD Tolerance Class A Pt100 thin film sensors [122] were selected as they

provide a linear response in the temperature range that the tool will operate (0-80°C). Additionally, their physical footprint is small but manageable for human handling and integration with the tooling surface. It is anticipated that other contact temperature sensors could have been used in this construction without affecting the results and conclusions drawn in relation to the defect detection and identification, which is investigated in the remainder of the thesis.

The airpad HTX was marked out with the probe positions 1-64 and spaced 37.5mm apart both in the x and y axis. The spacing of 37.5mm was used to reflect the mean spacing between taps performed by an inspection operator when inspecting a component, and this is the established method for tap testing inspection. Within a sample size of 300×300 mm, the available area allows for the fitting of 64 probes whilst maintaining constant spacing. This results in a grid of 8×8 probes. With acceptable defects allowed within the V2500 of 40×40 mm [16] this spacing is the lowest resolution capable of capturing defects outside of tolerances. A higher resolution set up could be created for lower tolerances, however for this application the extra cost associated with construction time and materials justified maintaining the 37.5mm spacing.

Careful consideration must be given when embedding RTD sensors on the airpad array, as the curing process increases the risk of short circuiting the RTD pins. To reduce this risk, at each of the probe locations, two slits were cut and the individual pins threaded through separate slits (Figure 3.10). This was repeated for all of the 64 probe locations as seen in Figure 3.11(a).

The non silicone HTX material provides a non-stick, resilient surface both to thermal loads and Petrol, Oil and Lubricants (POLs). However, airpad HTX will shrink during the curing process affecting the RTD locations. In order to keep the RTDs in the specified locations, the airpad is reinforced with a thermally stable material. The reinforcement utilised consists of CFRP tape strips positioned between the RTD probe locations. Each strip utilised a single ply CFRP unidirectional, arranged in a two ply construction of orientations 0° and 90° (Figure 3.11(b)). The non-symmetrical nature of this lay-up provides a semi-flexible tooling surface which can be deployed in components with curved surfaces.

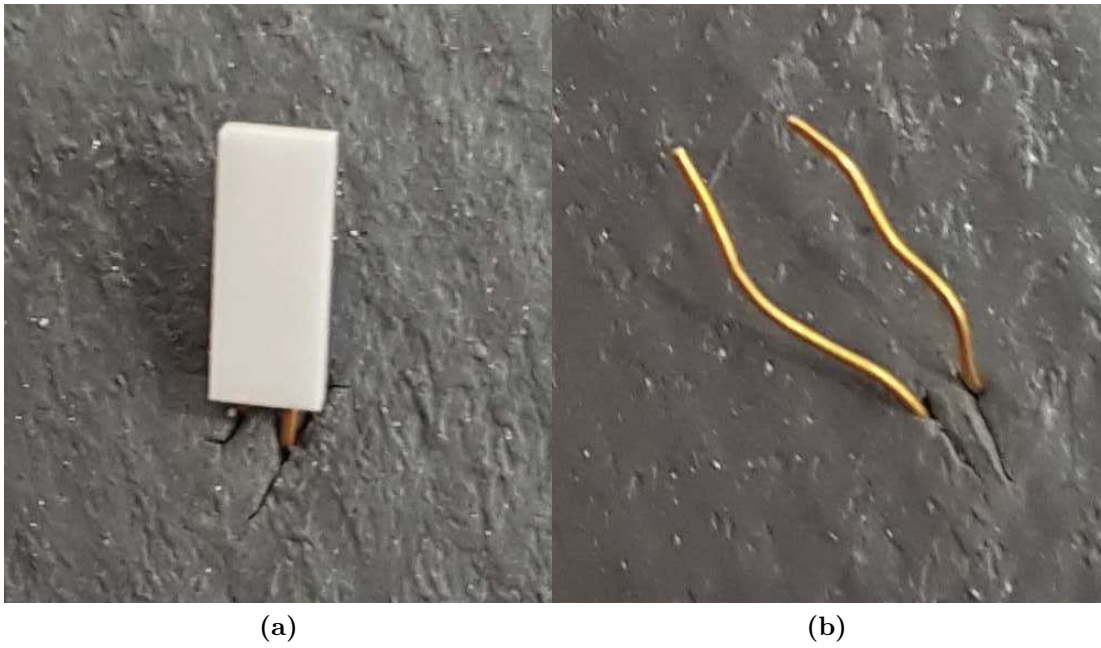


Figure 3.10: (a) RTD sample side of HTX tool showing connections threaded through separate slits in the HTX. (b) RTD connection side of HTX tool showing connections threaded through separate slits in the HTX.

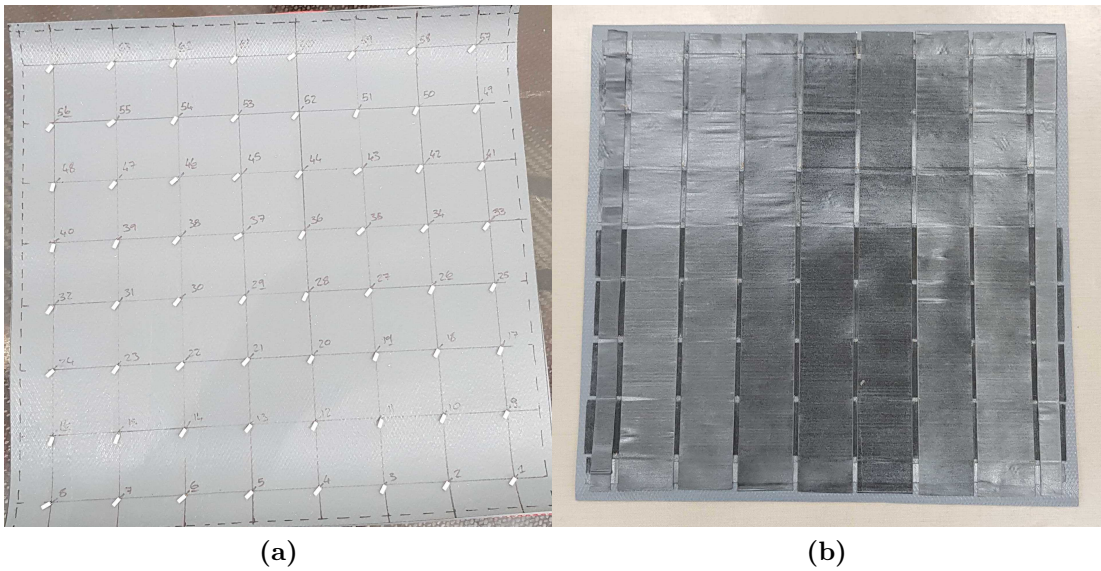


Figure 3.11: (a) RTDs placed within uncured airpad HTX material. (b) RTD airpad array reinforced with two ply 0°, 90° CFRP UD tape.

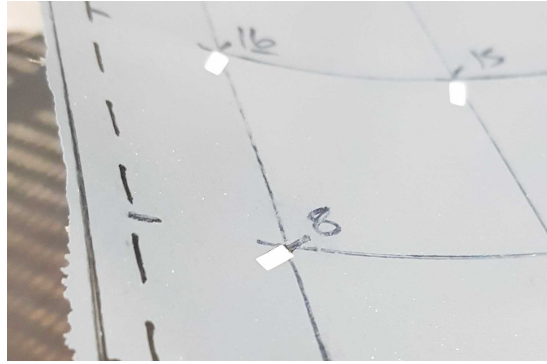


Figure 3.12: Contact surface of RTD airpad array showing RTD sensor surface flush with HTX airpad material post curing.

Once the reinforcement had been applied to the RTD airpad array, a debulking process was carried out to ensure uniform contact across the airpad surface and CFRP unidirectional tape. The RTD airpad array was at this point ready for a curing cycle, and this was conducted at 36 psi , over 257 minutes according to the recommendation from the manufacturer. Complete curing parameters and details are provided in Appendix A. All of the 64 RTD connections were resistance checked to ensure that no damage to the sensors had occurred during the curing process. This was verified by measuring the RTD resistance with a multimeter and converted to temperature according to the device datasheet. The temperature obtained from the measurement was compared to that measured from a laser thermometer, it was found to be within $\pm 0.5^\circ\text{C}$ which is within the accepted tolerances.

The contact surface of the RTD airpad array contained no visible abnormalities and the sensor surfaces of the RTDs were flush with the cured HTX airpad, allowing close contact with the surface of the component under test (Figure 3.12). Each RTD was connected to the corresponding input connection of the industrial controller (described in Section 3.5). The reinforced HTX airpad is designed to provide uniform pressure distribution under 1 bar vacuum bagging pressure, providing a strong contact between the sensors and the component surface.

One of the issues is the routing of the RTD wires through the vacuum bag without introducing air paths that will compromise the vacuum pressure. Routing wires in a bundle increases that risk and for that reason a common approach is to

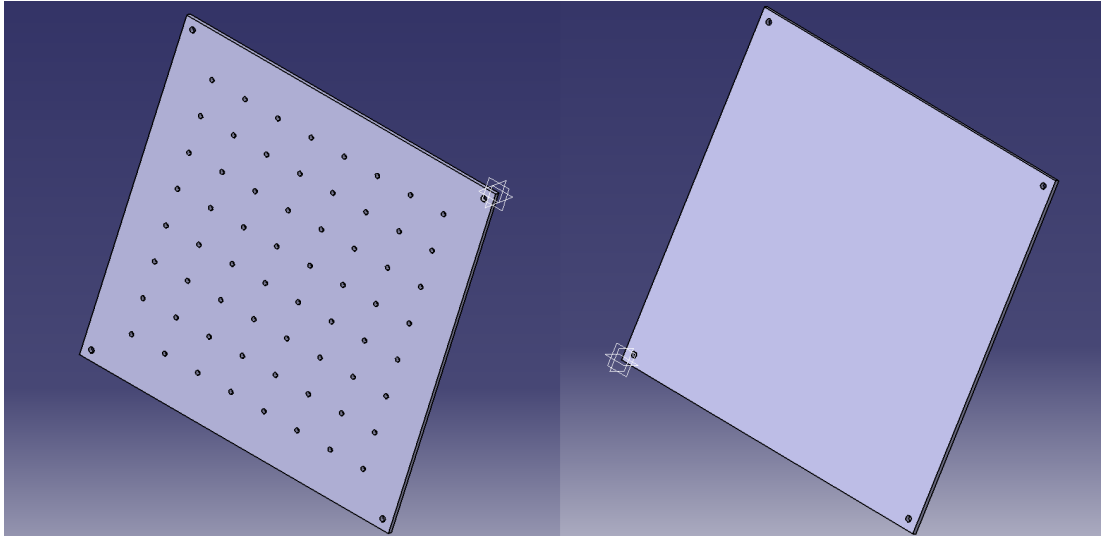


Figure 3.13: Experimental setup of RTD array holding tool and back plate.

route each wire individually through tacky tape. Given the experimental nature of this work, a new single-use vacuum bag was anticipated. Renewing the vacuum bag and tacky tape between experiments increases the risk of wire damage.

An alternative approach trialed to mitigate the burden of the experimental setup while maintaining contact between the sensing surface and component, which was through mechanical force. In principal, this approach should be able to emulate the vacuum pressure. The initial prototype developed consisted of two plates to contain the sample, RTD array and heater mats, and the mechanical force was applied through screw threaded bolts at the corners of the prototype tool (Figures 3.13 and 3.15).

The final setup was trialled with sample laminate panels and CFRP honeycomb sandwich structures and a number of issues were identified:

1. The initial trials provided reasonable results for the laminate less than 1mm thickness, however, for the thicker structures large discrepancies in the data were observed within the central RTD probes located within heater mat location 5. These readings produced results 5-9°C lower than expected, this can be seen when compared to the captured data for the PCB tool in Figure 3.14. After further investigation and through close visual inspection, it was identified that the inconsistency in the temperature data was due to

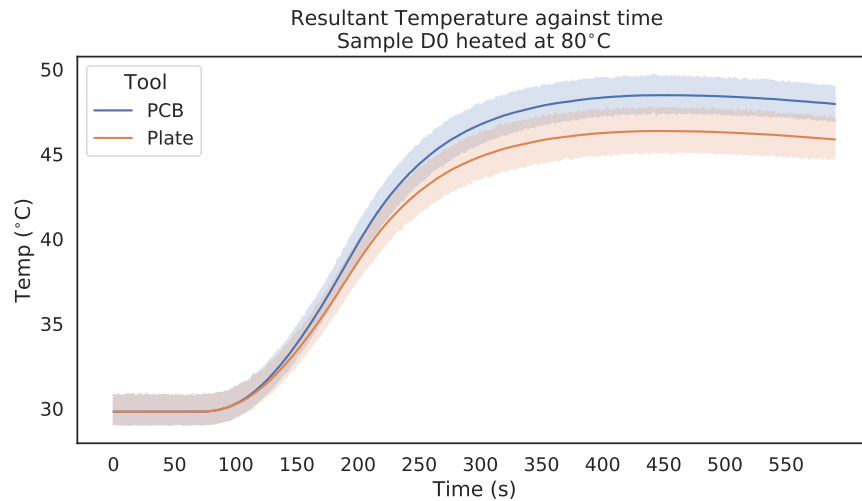


Figure 3.14: Plate temperature against time captured data vs PCB temperature against time captured data for sandwich panel D0

bending of the plate (as it was anchored from the 4 corners) that prevented a uniform application of the probes across the sample surface.

2. During the initial experiments, one of the RTD probes failed. Although the Airpad HTX is designed in such way that it can be patched after replacing the RTD, a full autoclave cycle is required. Given that the majority of the sensing array construction costs is associated with the autoclave curing it is equivalent to constructing a completely new sensing surface.

These issues led to investigating alternative approaches to construct the sensing surface as described in the following section.

3.3.2 Printed Circuit Board Tooling Design

The issues encountered with the HTX airpad array tool required rectifying prior to the cyclic capture of data from the samples to prevent downtime from the experimental capture if one of these issues were to occur. This led to the design of a Printed Circuit Board (PCB) sensing surface that mitigated the before-mentioned issues and in particular:

- Equally spaced, absolute probe locations. For the HTX airpad tooling surface RTD were manually threaded through the material and that creates

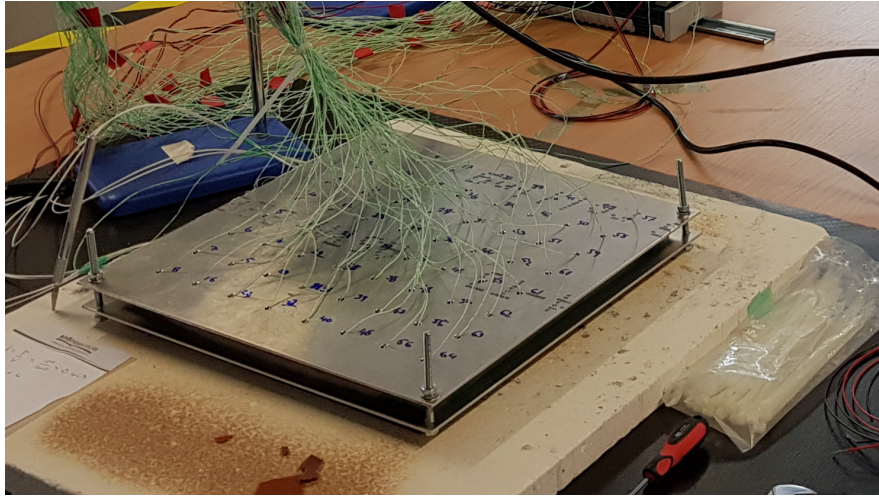


Figure 3.15: Experimental setup of RTD array contained within the plate tool prototype of Airpad array tool.

a small variation on the probe locations. In PCB manufacturing, machine fabrication and placement ensures accurate and repeatable probe placement. Finally, the PCB manufacture supply chain is mature, making it easy to adopt in the Collins Aerospace workflow.

- Withstand strain induced by vacuum pressure. The PCB substrate material is a Glass Fibre Reinforced Polymer (GFRP) composite laminate. Composites, such as GFRP structures, are widely used across industries for their structural properties, the most notable of which is their high strength to weight ratio [173, 174, 175, 176] making them a strong candidate to withstand vacuum pressures. This is evident in the increasing use of composite tooling surfaces used within the manufacturing processes for other composite structures [177], requiring the use of vacuum and autoclave pressures.
- Quick and cost-effective RTD/probe replacement. Replacing damaged RTD sensors on the previously proposed HTX airpad array is cumbersome, requiring cut-outs, patching and threading. In contrast, utilising the PCB sensing surface, RTD replacement can occur in situ using basic soldering equipment. When multiple probes fail, complete board replacement is more economically efficient compared to the remanufacture of the HTX Airpad array.

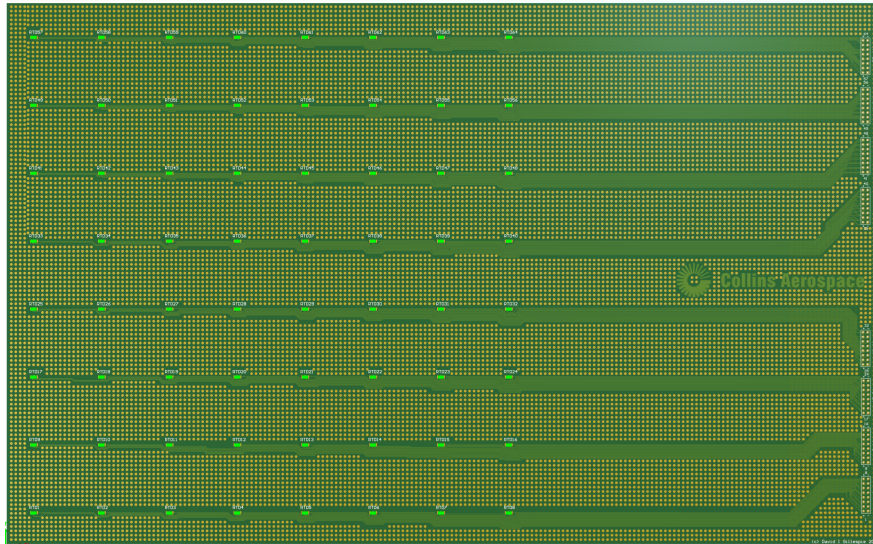


Figure 3.16: Printed Circuit Board (PCB) RTD array tool, displaying RTD probe locations and off sample connection headers to allow for vacuum bagging to tool.

- Vacuum sealing without applying tacky tape to wiring. An epoxy solder mask is used as a protective layer to the underlying copper traces which form the connections within the PCB. This combination of epoxy and copper traces allows for a connection between the RTD sensors and external connection headers without the need of a cables like those used within the HTX airpad array. If necessary, tacky tape can be directly applied to the board surface to partially vacuum bag the tool and the sample under test eliminating air paths between the RTD array section of the tool that is under vacuum and the external connection headers.
- Contact surface flush with sample to provide uniform sensor contact. A flush contact between the tool and sample surface is realised by a combination of applying vacuum pressure and the bending strength of the PCB to ensure strong contact between the tooling and sample surfaces.

The PCB schematic and layout was designed using Altium Designer. The RTD sensors were placed on 8×8 surface mount pads using the same spacing configuration as used previously for the HTX airpad surface (37.5mm grid spacing between sensors). The surface mount pads were then routed to 8×8 external headers (which are kept outside the vacuum area as shown in Figure 3.16). The

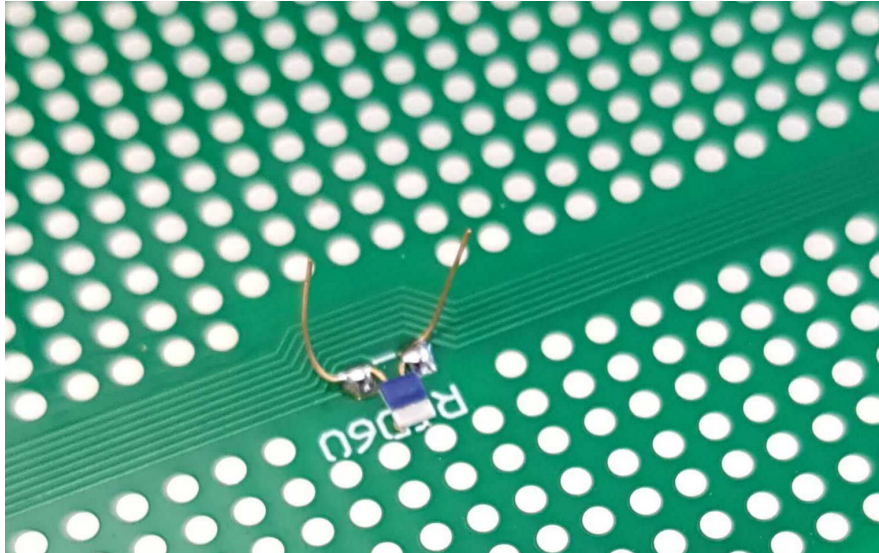


Figure 3.17: RTD solder connection to surface mount pad on PCB RTD array tooling.

header connections are grouped by RTD sensor rows and labelled on the board to allow easy identification to the controller. A gap of 180 mm between the outermost RTD pads and the header connections was introduced to provide an area upon the tooling surface to apply vacuum sealing tape (tacky), vacuum ports, and other required consumables. The project files were processed and manufactured by Newbury Electronics. After PCB manufacturing 64 Pt100 RTDs were soldered to the surface mount pads oriented flush to the PCB surface as shown in Figure 3.17. Subsequently, each RTD resistance was checked across its corresponding header terminals to ensure good connection and verify the resistance and ensure it is appropriate for the room ambient temperature.

The final PCB sensing surface can then be applied as illustrated in Figure 3.1.

3.4 Final Tool Lay Up

The final tool lay-up utilises heater mats and the PCB sensing surface to enclose the component under test as shown in Figure 3.18. Furthermore, the overall lay up is enclosed in an airbag and the associated vacuum set up can be attached to ensure flush uniform contact between the heater mats, sample and PCB RTD

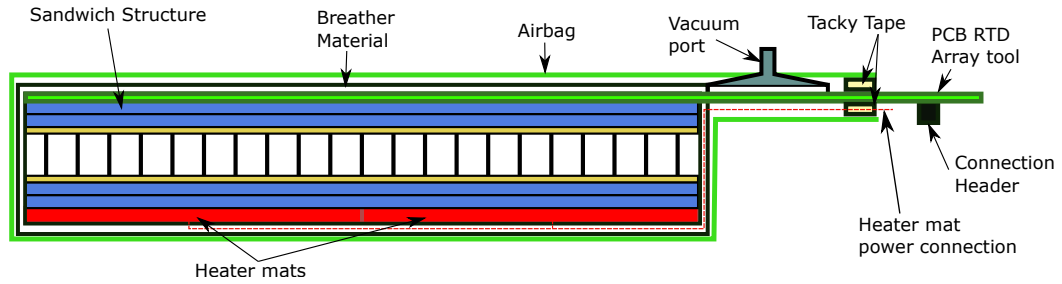


Figure 3.18: Cross section of the through transmission set-up for sandwich structure using heater mats and the PCB RTD array.

array tool.

Practical use of this tool verified the hypothesis that the PCB design will reduce the air paths due to RTD wiring. However, the heater mat power cables remain an issue since their insulation is not vacuum certified. To eliminate the air paths, cables were stripped and attached to two solid copper bus bars which are in turn sealed with tacky tape. The connection from the bus bars outside of the vacuum seal are then reconnected to insulated wire.

3.5 Data capture and Control

The heated and sensing surface have to simultaneously control and capture the data to permit thermographic analysis of the components under test. For data capture, this requires the ability to simultaneously record temperature data from the 64 RTDs of the PCB array sensing surface. The heat is injected in the component using the 4 heater mats on the bottom surface, however, to ensure the injected heat is controlled and does not damage the component due to overheating, 4 additional RTD sensors are placed on the heater mats. These 4 RTD sensors are used as a feedback loop to the Proportional-Integral-Derivative (PID) controller and provide the ability to control the temperature ramp rate.

For the controller hardware, multiple platforms were considered. Electronic control systems such as the Raspberry Pi or Arduino allow for custom control systems to be designed and implemented at relatively low cost. The systems are

able to utilise common programming languages such as Embedded C and Python which have access to a large number of open source libraries to help rapidly prototype up a working system. However, the application for the developed method requires use within an active MRO facility, which dictates the use of an industrial grade controller certified to operate in harsh environments. The use of an off-the-shelf controller allows for the developed system to be easily duplicated at any location and permit scale-up if more sensing and heating zones are required.

A General Electric (GE) controller that has been used to control other out-of-autoclave tools, has been made available for the purposes of this research. The complete control system consists of a CPE400 controller, an RSTi EP modular remote I/O (Input/Output) system that can facilitate up to 64 modules. The operation of the tool requires 4 outputs to provide heater mat actuation and 68 inputs for the RTD probes (64 for the sensing surface array and 4 that provide feedback stimuli to control the heater mats). This requirements lead to $1 \times$ EP-2814 Solid-State Relay Output Module with 4 channels and $17 \times$ EP-3704 Analog Input modules with 4 RTD Channels each. The EP-3704 channel analog inputs operate with 16 bits resolution in a temperature range of -200°C to $+850^{\circ}\text{C}$, providing a step of 0.016°C . As will be discussed in Section 3.6, the ramp rate of the heated tooling surface over 120 seconds from ambient to 80°C is 0.426°C/s , a capture step of 0.016°C per s provides an acceptable resolution. Figure 3.19 shows the controller setup as configured for data capture.

The controller was configured to control the ramp rate of the 4 heater mats and record the temperature data from the 68 RTDs. The controller software allows a maximum sampling and actuation rate of 1 Hz.

The controller software stores the live data from the sensor array and heater mat feedback RTDs within an Structured Query Language (SQL) database and can be exported to Comma Separated Value (CSV) files. The CSV files are easily read by most data analysis software and programming environments, however this can be changed if required.

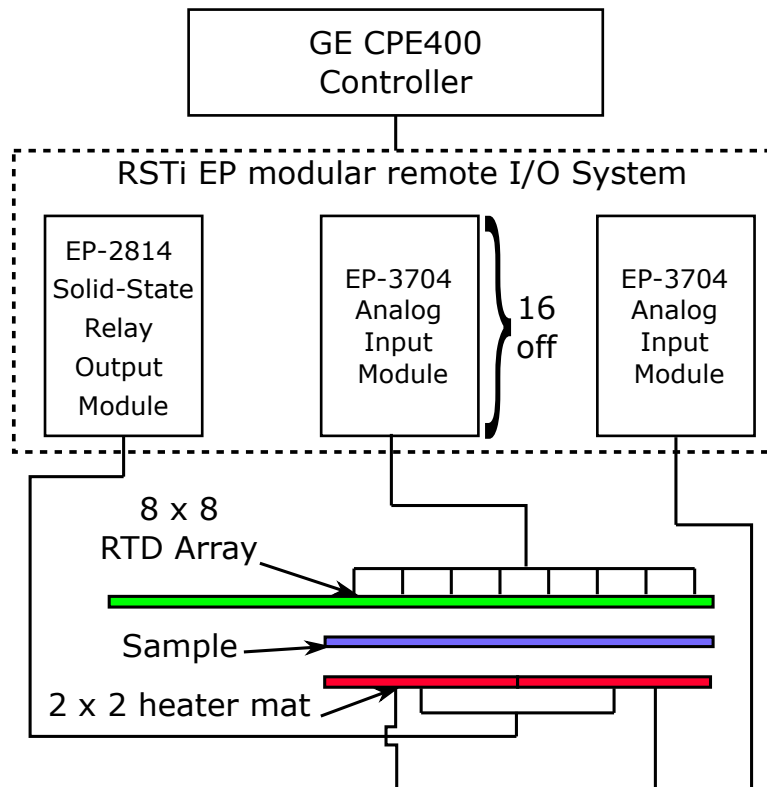


Figure 3.19: CPE400 GE Controller experimental data capture setup.

3.6 Validation of Proposed Tool

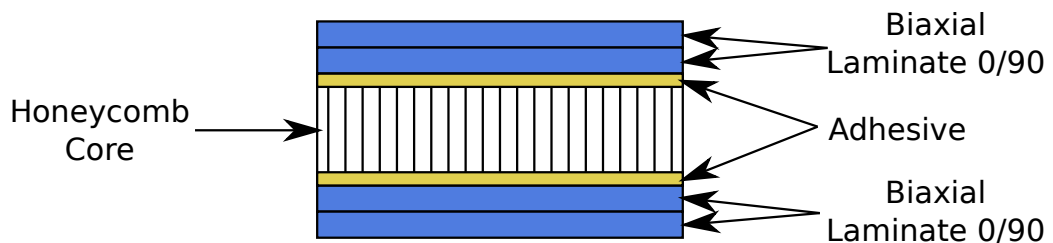


Figure 3.20: Sandwich panel “Quality” sample lay up cross section.

It is important for the proposed thermography methods to be evaluated on structures which are as representative as possible of in-service components. Each of the proposed defect detection techniques is evaluated on sample panels which mimic the construction and lay up typically found within the V2500 fan cowl. In this chapter, the aim was to identify defects within the main body of the fan cowl and the sample panels created consisted of two 5 harness biaxial 0/90/0/90

laminates cured to an aluminium honeycomb core via adhesive layers as shown in Figure 3.20. The only difference of this panel lay up, in comparison to the fan cowl, is the absence of the the copper foil lightening strike layer typically found on the outer skin of the fan cowl but bonded within the resin system. Given that the proposed method is based on the comparison of thermal profiles between parts of known quality and test panels, the structure with the lightening strike layer will require new reference profiles and does not change the validity of the approach. Furthermore, the lighting strike layer is copper based, which provides high thermal conductivity essentially becoming transparent under the proposed transmission thermography approach.

To demonstrate discernible variations to the expected temperature within a sandwich structure, 3 sample panels were manufactured as follows:

- Sample D0: a 300×300 mm defect-free sandwich structure to obtain thermal profiles of a quality panel.
- Sample D1: a 300×300 mm sandwich structure with a single delamination located within the upper right quadrant of the the top laminate and two impact damage points also within the top laminate (Figure 3.21(a)).
- Sample D2: a 300×300 mm sandwich structure with 4 impact damage points, one in each quadrant of the panel, all on the top laminate (Figure 3.21(b)).

The defects were introduced to the panels using the following methods:

- the delamination within sample D1 was manufactured during the fabrication of the sandwich panel by including two 25×25 mm square Polytetrafluoroethylene (PTFE) sheets laid on top of each other between the two plies that constitute the top laminate. The PTFE acts as a barrier between the plies preventing crosslink and hence curing of the plies together, known as structure delamination; this defect was verified on the final panel through tap testing.

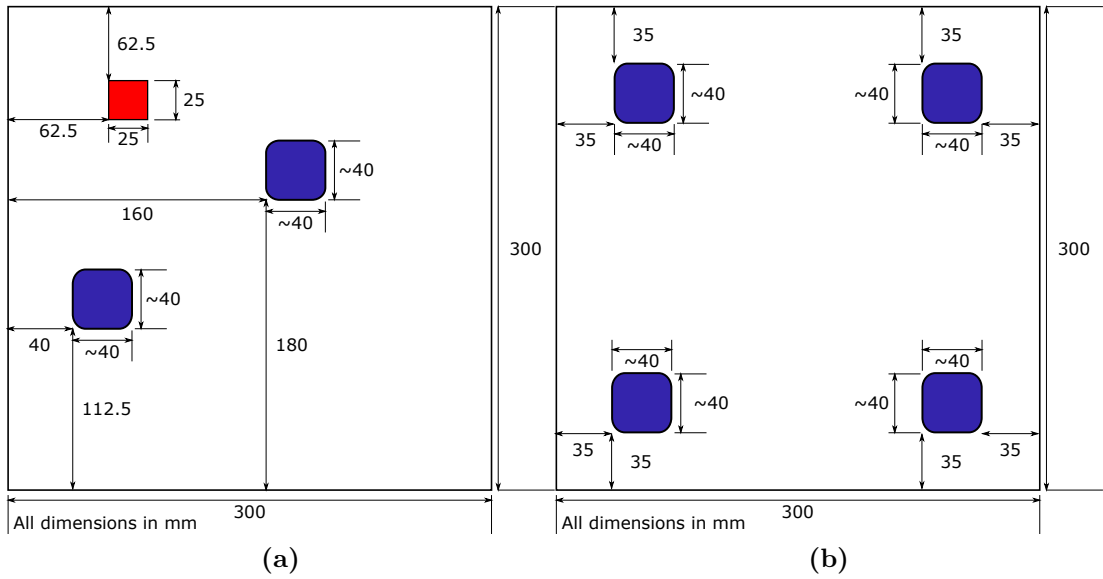


Figure 3.21: Defect locations for (a) D1: Delamination in red, impact damage blue. (b) D2: Impact damage shown in blue.

- The impact damage for both samples D1 and D2 were introduced post fabrication by means of impact with a ball peen hammer. To create the defects, the samples were struck once at each defect designated location, shown in blue in Figures 3.21(a) and (b). Subsequently, defects were verified through tap testing to ensure that measurable damage had occurred.

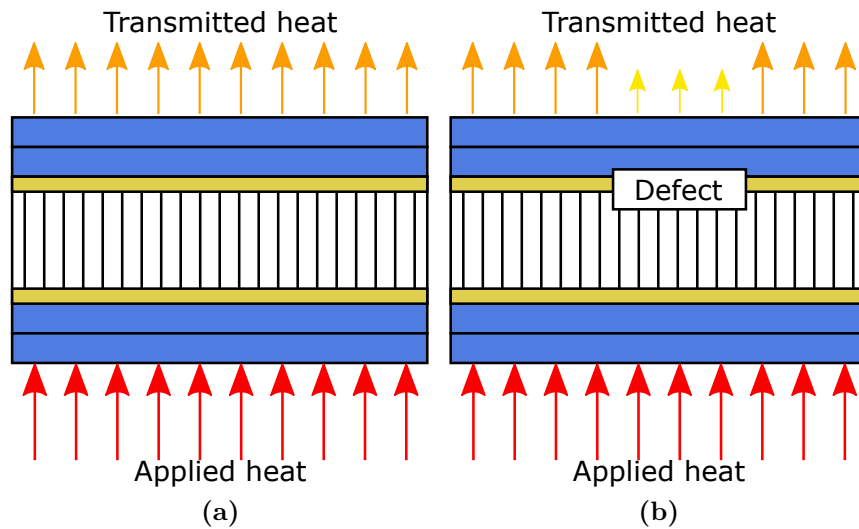


Figure 3.22: Thermal conductivity and resultant impact to thermal energy transmitted through composite sandwich panel (a) Defect free structure (b) Defect present.

The principle of active thermography is that a known thermal energy is introduced into the structure under inspection and the resultant surface temperatures are measured and compared with that of the expected result based on the structures thermal conductive properties. In the transmission method this thermal energy is introduced on the opposite surface of the sample than that where the temperatures are recorded, as is seen in Figure 3.22(a). As the sandwich structure sample is comprised of materials which are uniformly distributed across the sample the material thermal properties should also be uniformly distributed. The result of this is a constant thermal conductivity across a sample with uniform material distribution through its thickness. Should an area of the sample differ in its material properties within the structure this would result in a differing thermal conductivity (either decreasing or increasing) to that of the surrounding area and will be extrapolated to temperature deviations on the top surface, for example, as shown in Figure 3.22 (b). Such a reduction in recorded transmitted heat will be present in heat maps such as those produced by IR thermographic images and extrapolated as cold spots. Defects, such as inclusions, delaminations, disbonds or fluid ingress in the structure cause variation to the thermal conductivity of the component [62, 65, 178, 179].

Typically components are dried in multiples of 2 hour cycles at 80°C. A component initially enters a 2 hour drying cycle and any oil ingress in the component will bleed into the breather material. Personnel inspect the breather material and if liquid is present, the component is stripped and re-bagged to enter a subsequent drying cycle. The process is repeated until the breather material remains clean at the end of the drying cycle. The intention is to utilise the inspection techniques proposed for the drying cycle process and consequently, the heating stimulus should mimic closely the temperate profile used in the drying cycle. It is less important to emulate the full dwell time for defect detection as the intention is to detect defects as soon as possible in the drying cycle process. The remainder of this section shows that defects can be detected within 250 s within the drying cycle.

Taking these aspects in consideration a drying cycle was emulated which has

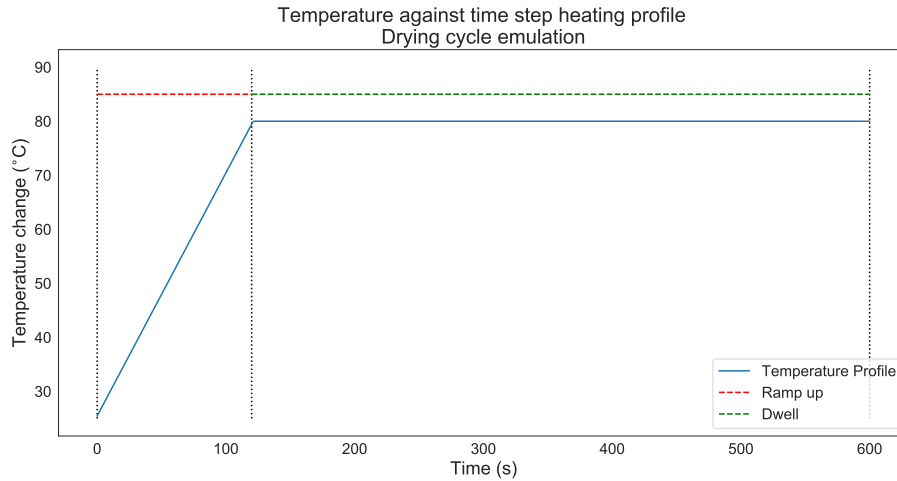


Figure 3.23: Heater mat temperature against time step heating profile.

total duration of 10 minutes (600 s). The temperature profile is shown in Figure 3.23 and consists of a ramp-up section at which the heater mats are turned on at full power and ramp-up temperature until 80°C is reached. After that point, the heater mat power is modulated to maintain the temperature at 80°C for the remainder of the 10 minutes cycle. This leads to a ramp-up rate of approximately 0.45°C per s assuming an ambient temperature of 25°C. This heating profile was applied to all sample panels D0, D1 and D2 and the measurements were repeated 3 times to ensure repeatability. The standard deviation for all probes across these runs can be seen for each sample in Figure 3.24.

The resultant data from the 64 RTD sensors within the PCB RTD array was presented in an 8×8 grid heat map generated using the `imshow` function of Python library `matplotlib`, one heat map per s of capture was generated (Figure 3.25(a)). These heat maps are of lower resolution to the IR images generated in IR image based thermography. As many of the developed IR thermography methods utilise pixel comparison, it is common for operators to expect a higher resolution image than a 8×8 pixel grid. Within the Python `matplotlib` library function `imshow`, an interpolation argument can be passed which allows for interpolation of values between the points plotted. The Gaussian argument was utilised to produce a higher resolution image more familiar to C scan type images commonplace within NDI/NDT (Figure 3.25(b)). At this stage within the re-

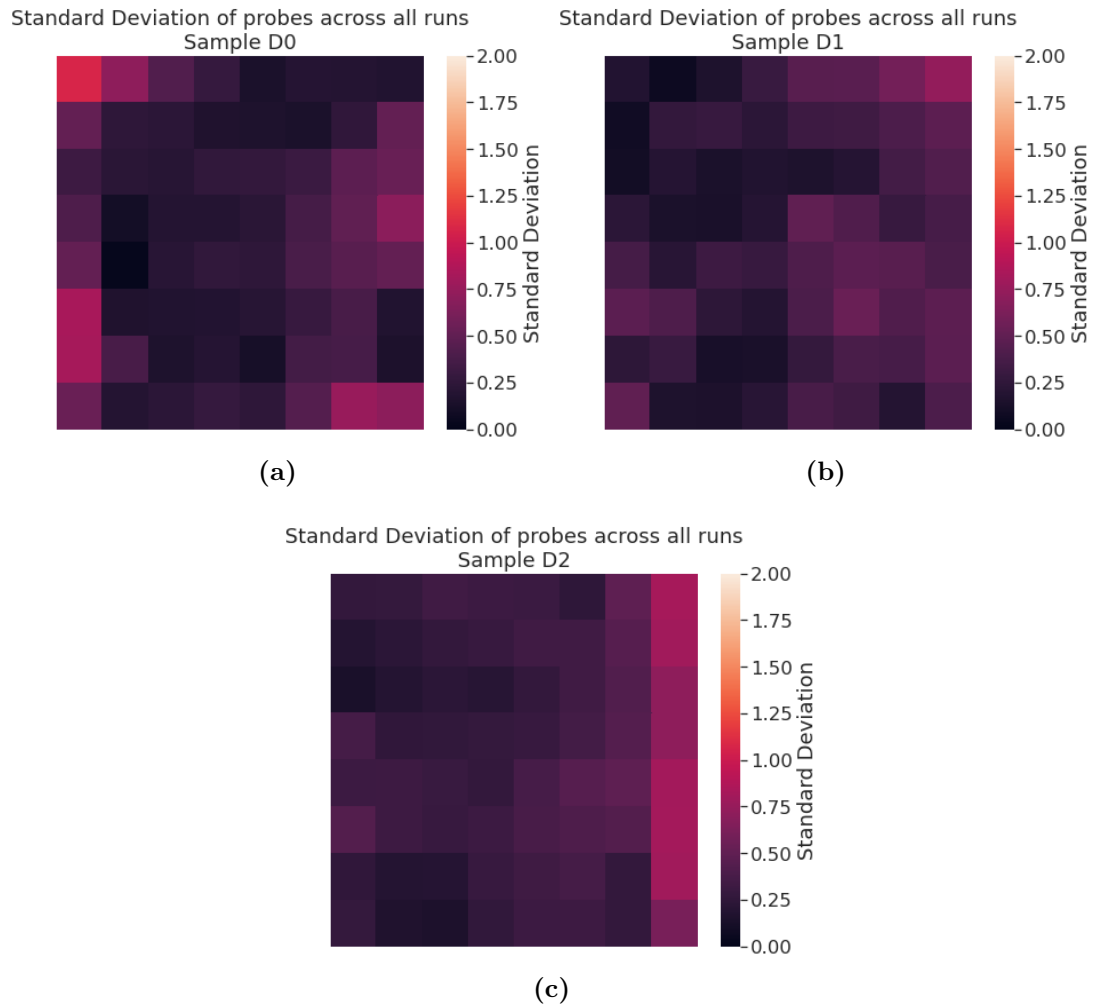


Figure 3.24: Heat map of standard deviation between all heating profile runs or each sample, (a) D0 (b) D1 (c) D2.

search, the Gaussian interpolation is purely aesthetic for demonstration purposes to industrial partners and stakeholders.

In Figure 3.26(a)-(b) sample runs 002-003 are shown, respectively, using this heat map presentation method. It can be seen here that there is a concentration of heat within the centre of the of the sample, which as it reaches the edges of the sample reduces by up to 14°C. This reduction in temperature is more obvious at the corner points of the sample. When compared against the heat maps obtained using the same set up and heater mat step heating profile for sample D1 (Figure 3.27 (a)-(c)), there is visually differences between the two sample panels However the reasons for these differences are not presented in

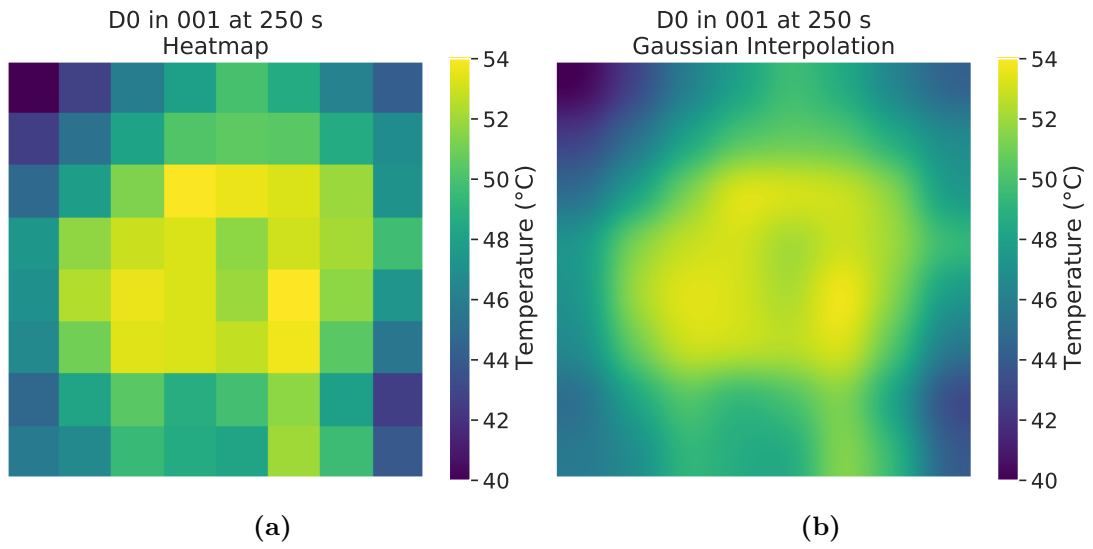


Figure 3.25: Heat map of captured RTD sensor data of top surface of sandwich structure sample D0, free of defects, at 80°C and 250 s sample run 001(a) no interpolation (b) Gaussian interpolation applied.

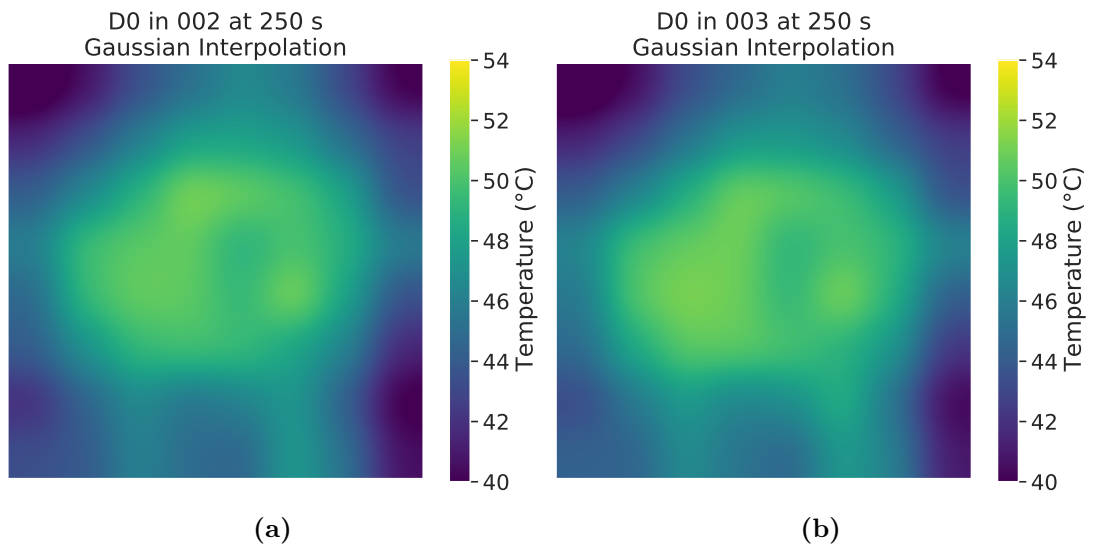


Figure 3.26: Heat map of captured RTD sensor data of top surface of sandwich structure sample D0, free of defects, at 80°C and 250 s (a) sample run 002, (b) sample run 003.

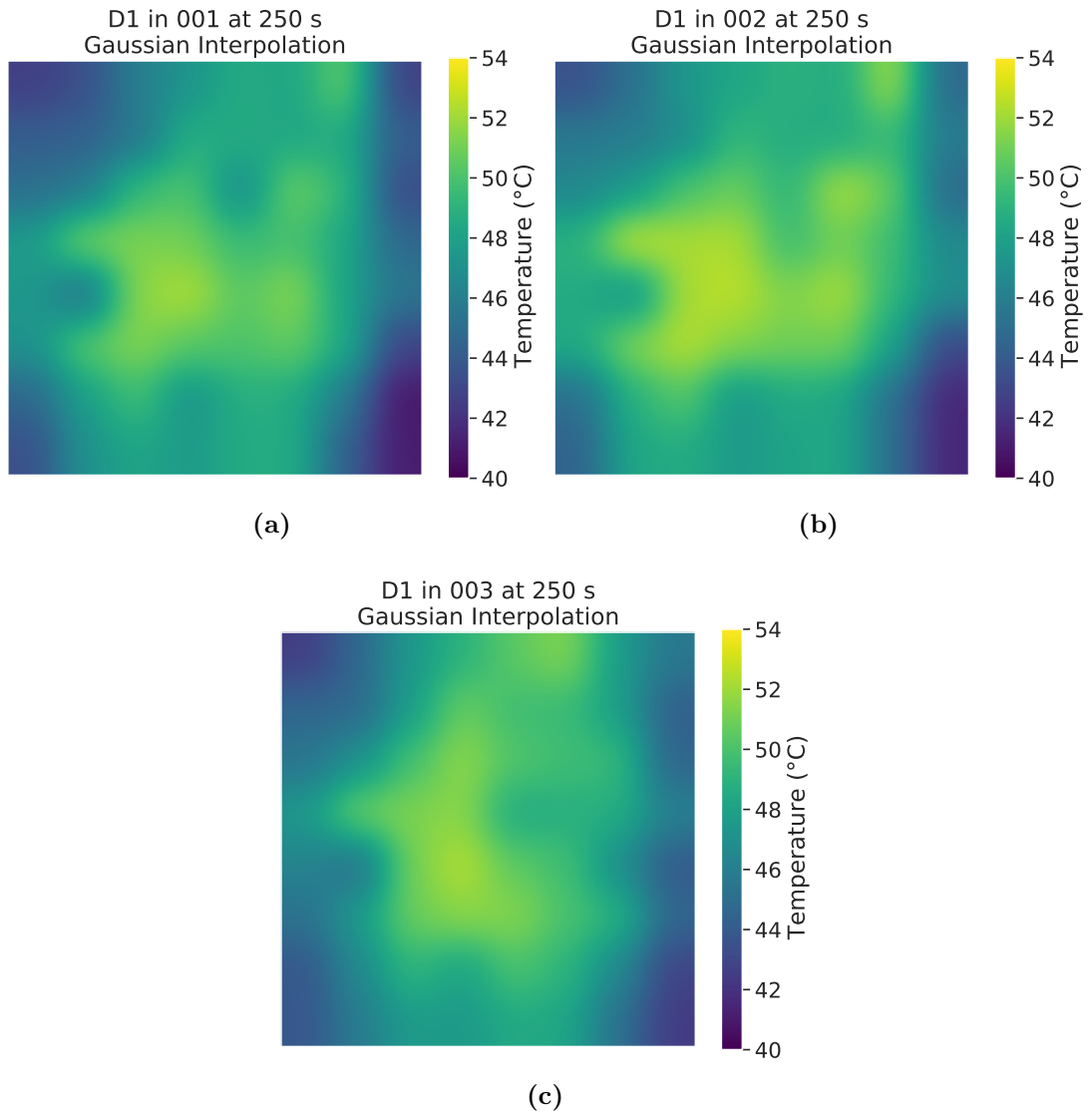


Figure 3.27: Heat map of captured RTD sensor data of top surface of sandwich structure sample D1, containing 2 impact damaged areas and one delamination, at 80°C and 250 s (a) sample run 001, (b) sample run 002, (c) sample run 003.

such a way that they are visually obvious to an observer without knowledge of the make up of the samples. What is obvious in both samples is that the heat transferred to the PCB RTD array tool is not uniform across the surface of the sandwich structure. Due to the thickness of the sandwich structures, there is structural dissipation along the edges of the sandwich structure as the heat flows through. To produce an image which is capable of easily presenting areas of interest regarding temperature, a method of generating a ‘flattened’ heat map when the sample is regarded as having no areas of interest is needed. This can be achieved through a simple comparison of a heat map of a sample under inspection with that of a heat map of a known quality sandwich structure. A value of (or near to) 1 will be produced when two values which are (or close to) identical are presented as a ratio. The resultant value will further deviate from 1 the more significant the difference between the two values being compared. In the instance of comparing two sandwich panels temperature profiles where one is of a quality homogeneous structure and the other contains a defect which reduces thermal conductivity, if the quality structure or the baseline sample temperature ($Baseline_{sT}$) is used as the denominator and the defective sample temperature ($Defect_{sT}$) as the numerator as seen in equation 3.1, a defect index ($Defect_i$) less than 1 will be produced where the thermal conductivity of the $Defect_{sT}$ has been reduced due to a defect within the structure.

$$Defect_i = \frac{Defect_{sT}}{Baseline_{sT}} \quad (3.1)$$

Conducting this ratio comparison for each corresponding sensor of two generated heat maps at the same time in s within the step heating profile will generate a new 8×8 array which can be displayed as a heat map.

The expected result for a sample without any thermal conduction reducing defects within it would be the generation of a uniform heat map. This hypotheses was tested using the D0 samples runs and comparing them against each other with sample run 001 used as the baseline and sample runs 002-004 as the test samples. As seen in Figure 3.28 (a)-(c) this results in a significantly more uniform

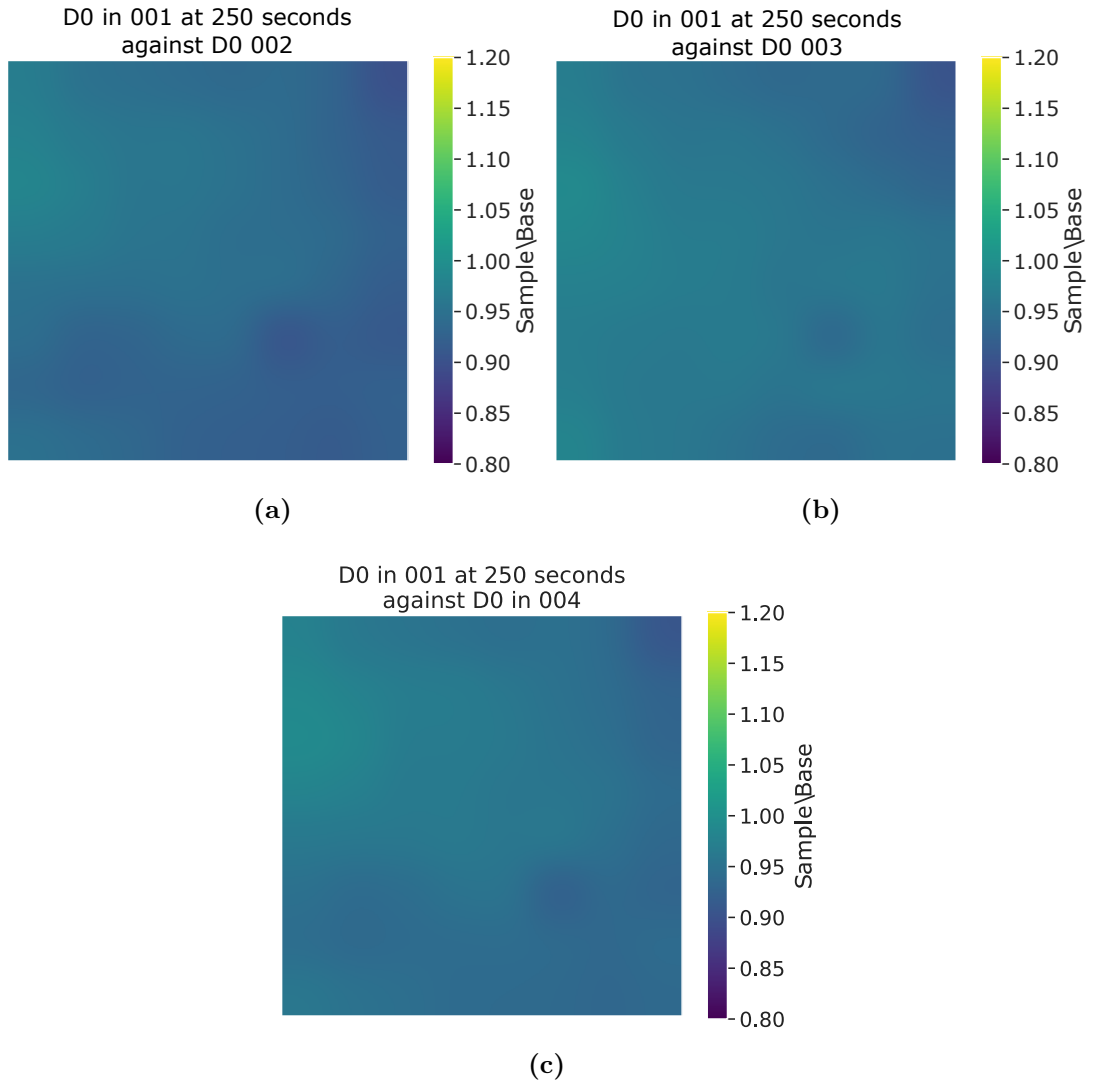


Figure 3.28: Heat map of $Defect_i = \frac{Defect_{sT}}{Baseline_{sT}}$ at 250 s with sample run 001 of D0 as the baseline and testing test samples (a) sample run 002, (b) sample run 003, (c) sample run 004.

presentation within the generated heat maps. Applying this same comparison method to the D1 samples with known defects as the test samples to provide $Defect_{sT}$ data at the 250 s point within the step heating profile produces heat maps which do not display the same uniformity as the D0 samples. As seen in Figure 3.29 (a)-(c) there are two circular darker areas of interest generated. Comparing these darker circular areas to that of the known defect locations produced by impact damage (Figure 3.21(a)) indicates that these are cold spots directly over the impact damaged areas. As impact damage defects reduce thermal con-

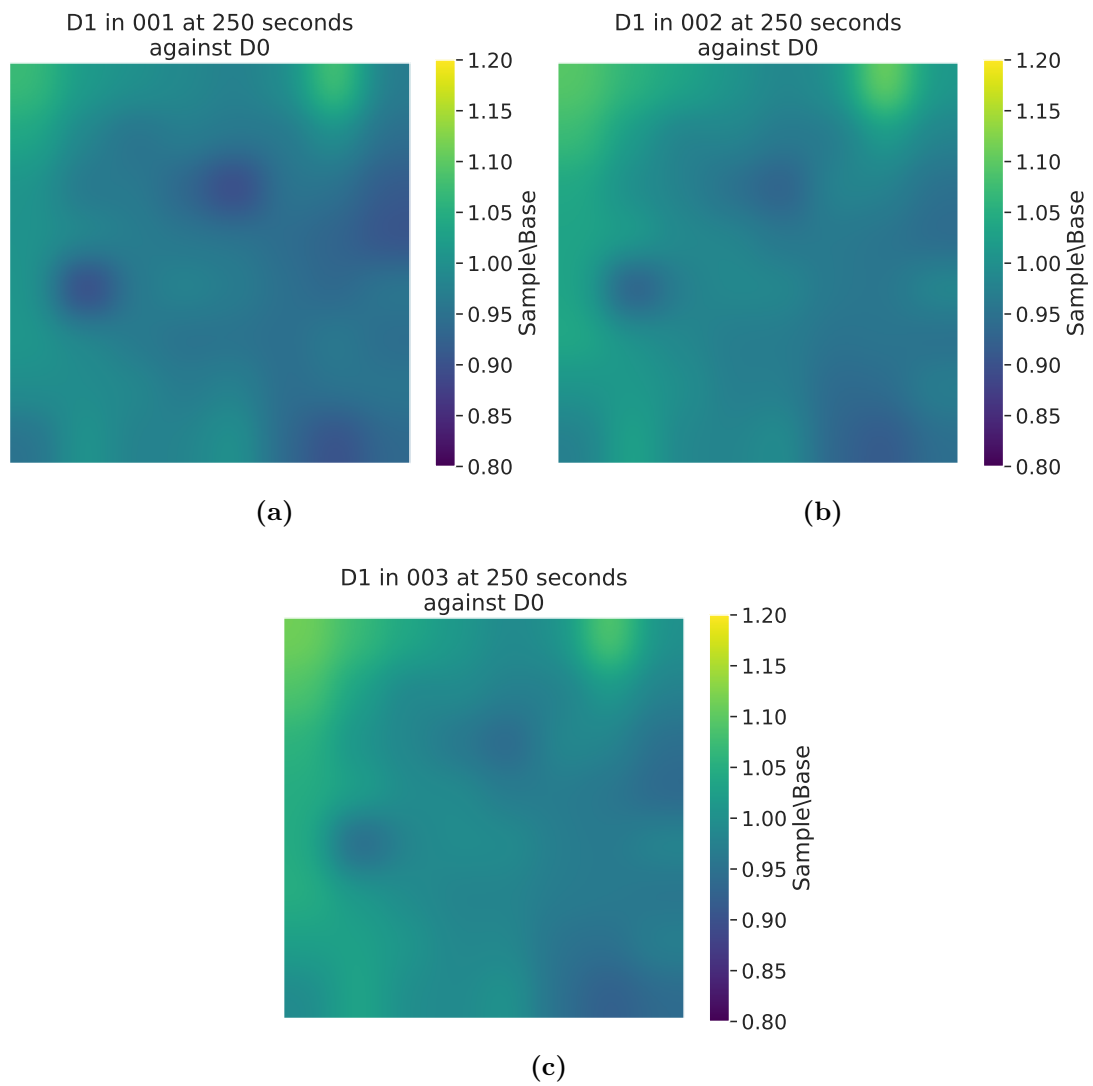


Figure 3.29: Heat map of $Defect_i = \frac{Defect_{sT}}{Baseline_{sT}}$ at 250 s with sample run 001 of D0 as the baseline and testing test samples (a) sample run 002, (b) sample run 003, (c) sample run 004.

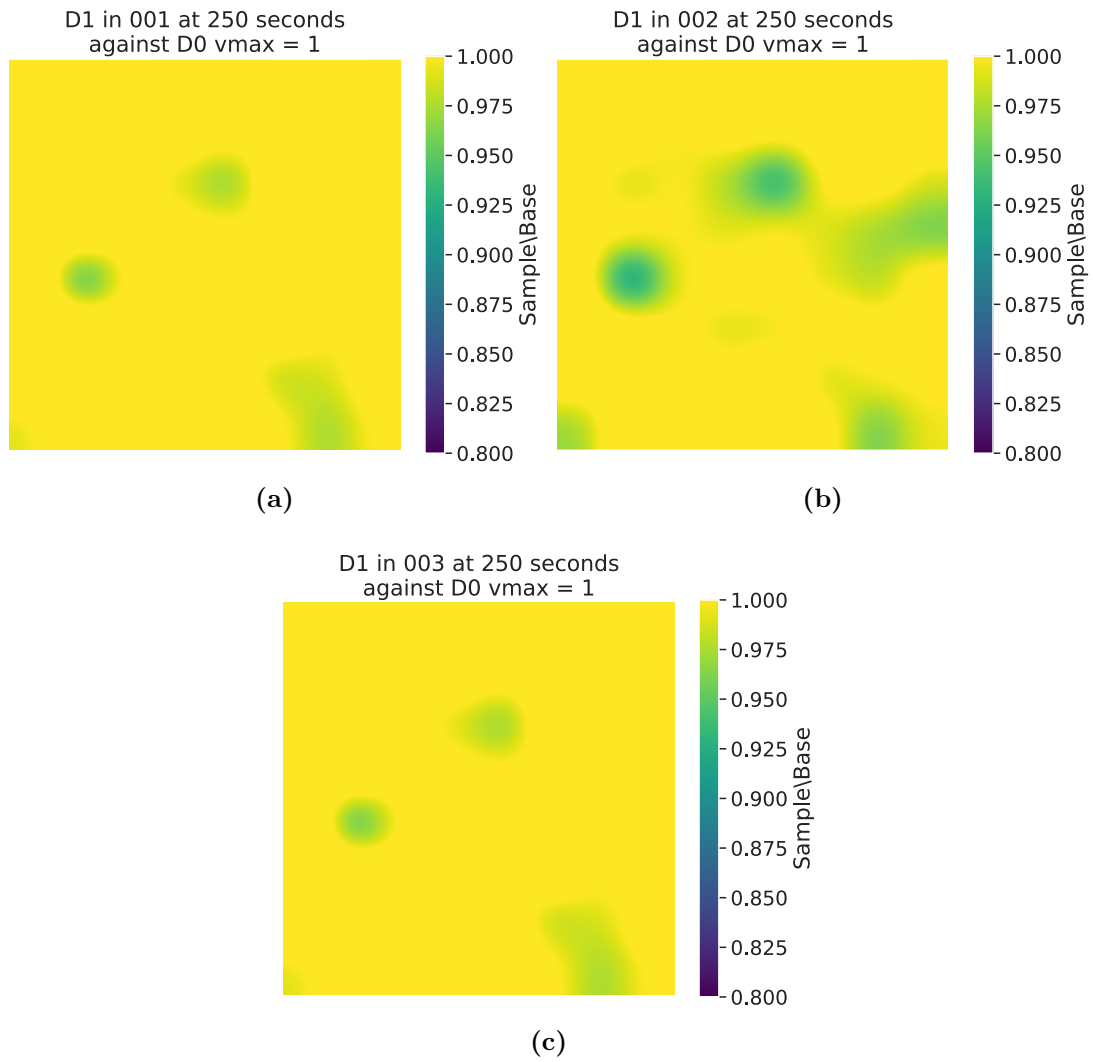


Figure 3.30: Heat map of $Defect_i = \frac{Defect_{sT}}{Baseline_{sT}}$ with max value set at 1, at 250 s with sample run 001 of D0 as the baseline and testing test samples (a) sample run 002, (b) sample run 003, (c) sample run 004.

ductivity, and as described in equation 3.1 a reduced thermal conductivity will present itself as a value less than 1, these defects can be further highlighted by limiting the range of values presented within the heat maps to a maximum of 1. This limiting of the maximum values displayed does produce clearer indications of areas with reduced thermal conductivity and again correlates with the locations of known impact damage within the sample (Figure 3.30). To verify that the indications captured with sample D1 are due to reduced thermal conduction caused by impact damage, sample D2 was examined using the same method and compared with the same baseline data. As seen in Figures 3.31(a) and (b), the 4

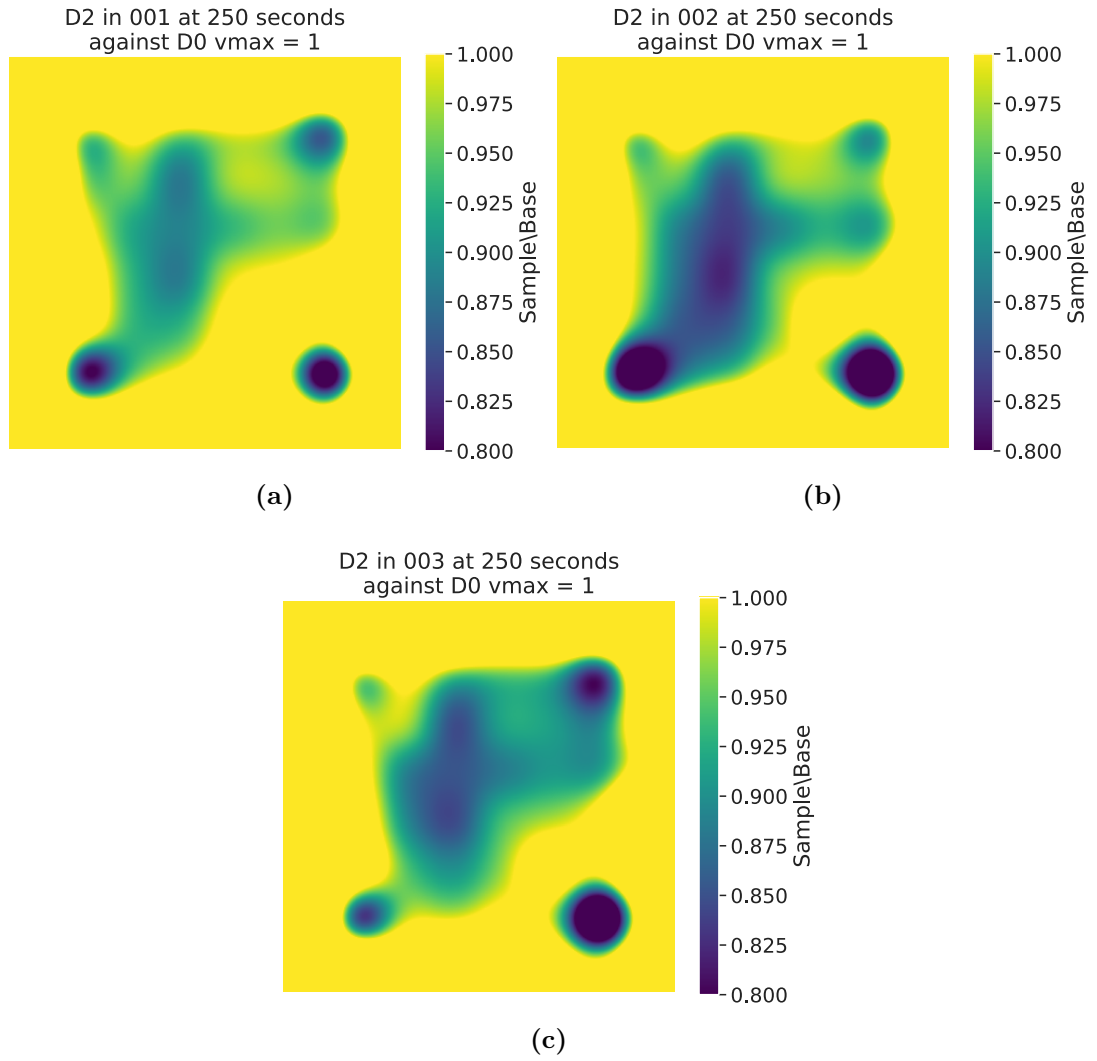


Figure 3.31: Heat map of $Defect_i = \frac{Defect_{sT}}{Baseline_{sT}}$ with max value set at 1, at 250 s with sample run 001 of D0 as the baseline and testing test samples (a) sample run 001, (b) sample run 002, (c) sample run 003.

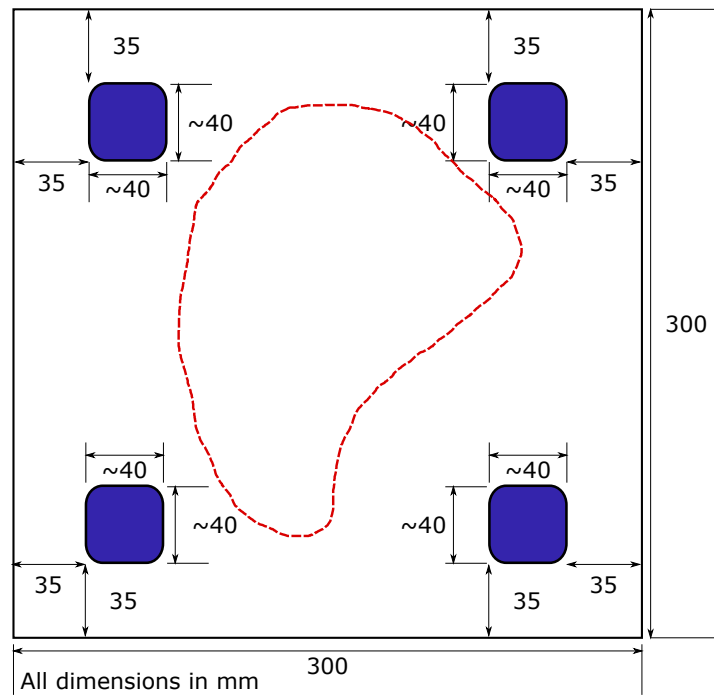


Figure 3.32: Tap testing defect map showing known impact damage points in blue and suspected disbonded area within dotted red area, both impact points and disbond inspected and indicated by qualified inspector.

corner points that correlate to the impact damage areas shown in Figure 3.21(b). It can also be seen in the captured images in Figures 3.31(a) and (b) that between the four corner points there is also an indication of reduced thermal conductivity. The sample D2 was inspected via the tap testing method by a qualified aerospace engineer and a defect map was produced, shown in Figure 3.32, it can be seen here that a large suspected disbond area was indicated during this inspection. It is suspected that the disbond was induced during the creation of the impact damage to sample D2. It is known that sub surface defects within composite structures created during impact damage will cover a larger area than the impact point [180, 181, 182]. In this instance, at least three of these subsurface defects created by the impact have spread far enough to come into contact with one another and have resulted in a larger subsurface defect.

It has been demonstrated using the developed PCB RTD array tool and heater mat set up that it is possible to detect defects within a composite sandwich structure which result in a reduction to the thermal conductivity of the sample. The method is robust enough to capture defects within a sample that, until verified by

an established alternative inspection method, were unknown. However, it should be noted that there are no immediately apparent indications of the delamination defect within sample D1. Unlike impact damage, that can result in several defect types occurring from a single impact, a delamination does not have as large an effect on the thermal conductivity of the sample. This is largely due to defects caused by impact damage presenting at several layers through the sample and the fabricated delaminations only creating a defect between the two plies. This is not to say that delaminations can not be detected via thermal analysis, in fact the opposite is true. As shown in the literature, techniques have been developed that can not only indicate delaminations through thermography but also quantify them in terms of dimension and depth [2, 3, 78, 79, 183]. We know that changes to a material will change the material properties, in the case of delamination, this changes the thermal conductivity within the laminate [184]. The result of this is that the thermal energy contained within an area of the material with a delamination does not conduct away from the surface of the material at the same rate as the surrounding quality area. When thermal energy is introduced to the sample and a uniform temperature is reached within the sample, if the source of the thermal energy is stopped the resultant thermal profile of the sample cooling would produce a slower cool-down rate within a delamination. As a method of defect detection, thermal through transmission using the PCB RTD array and this heater mat combination are not suitable for detecting complex inter-laminate thermal properties such as delaminations due to operating principally in a 1 dimensional capacity. With the limitations of defect detection in transmission mode from data considered only in a 1 dimensional sense, an exploration of how the experimental setup can be modified to capture and analyse the resultant thermal profiles in 2 or 3 dimensions must be conducted.

3.7 User Interface

For this method, and those described later within the thesis, to be utilised within an MRO environment by operators, a user interface is required. This needs to

provide both presentation of the results produced from the proposed method to an operator as well as a control system for conducting the proposed method. A proposed Graphical User Interface (GUI) can be seen in Figure 3.33.

Within the GUI the Operator is presented with:

- A large UI display area labelled ‘Thermal Profile’.
- 2 numerical indicators for Time in s and Temperature in °C.
- ‘Run Inspection’ button.
- A state indicator displaying ‘NOT RUNNING’.
- 3 button options under ‘Method Selection’ of Fibre Orientation, Impact Detection and Delamination Detection
- 2 button options under ‘Report’ of ‘Review’ or ‘Print’.

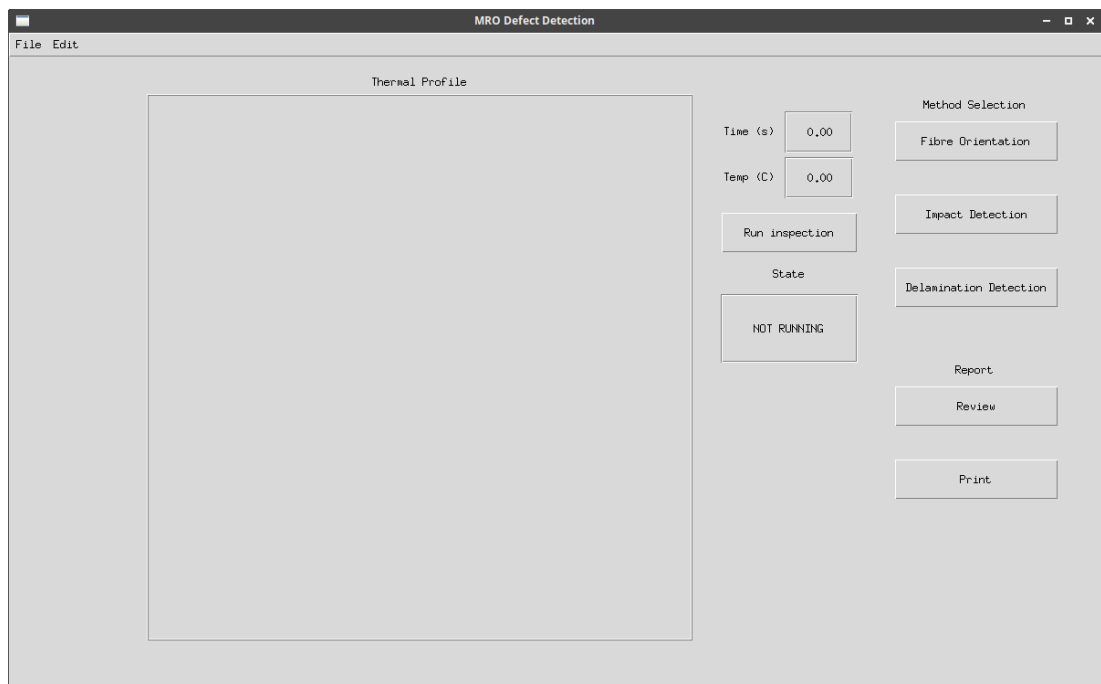


Figure 3.33: Graphical User Interface for operators.

The intention is to provide the least number of steps from starting the GUI to obtaining the desired output. With a sample connected to the control system, the GUI effectively instructs the control system which heat profile to use and how to interpret the resultant data once captured.

3.7.1 Data Capture via GUI

Using the proposed method for Impact Detection (Section 3.6) as an example, with the Method Selection button ‘Impact Detection’ selected the operator then instructs the system to run the inspection by clicking the ‘Run inspection’ button. At which point the ‘State’ indicator will change in colour to red and display the text ‘RUNNING’ to indicate that the system is active (Figure 3.34).

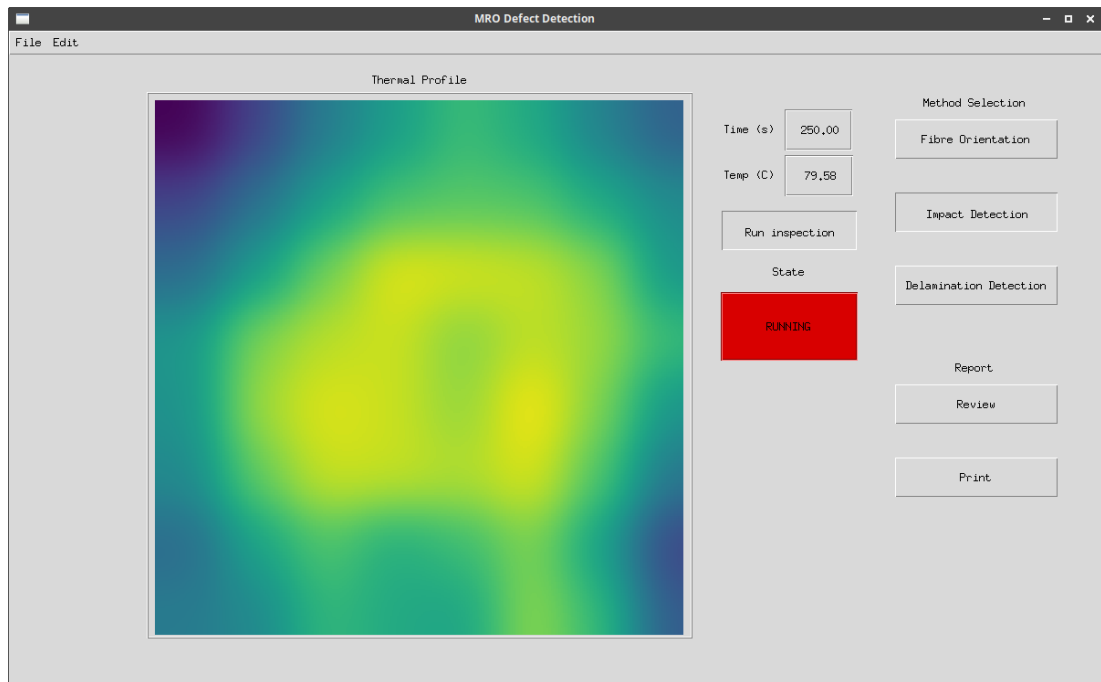


Figure 3.34: Graphical User Interface for operators, Running Impact Detection.

Once the data capture is running, the temperature readings captured by the control RTD for the heater mats are displayed within the ‘Temp (C)’ indicator to allow for the operator to ensure the system is operating within the temperature range expected, the ‘Time (s)’ indicator will provide the time passed in s. The previously blank ‘Thermal Profile’ section now displays a Gaussian interpolation representation of the RTD array tool readings, this will be the raw temperature data as no analysis has occurred at this point. However, it is expected, as the operator becomes more familiar with the system that this raw data may provide useful information as to the performance of the inspection in real time.

Once the heating profile for the selected inspection method has concluded, the GUI will indicate the completion with ‘State’ indicator colour of green and a

text of ‘COMPLETE’ (Figure 3.35). At this point, the inspection has captured the required data set for the selected method to conduct the analysis to provide a report. All three proposed method’s data capture via the GUI is conducted in the same way, the only difference being which selection is made under ‘Method Selection’ i.e., ‘Fibre Orientation’ for Fibre Orientation indication, ‘Impact Detection’ for Impact Damage detection and ‘Delamination Detection’ to capture data for Delamination Detection via transient thermal analysis.

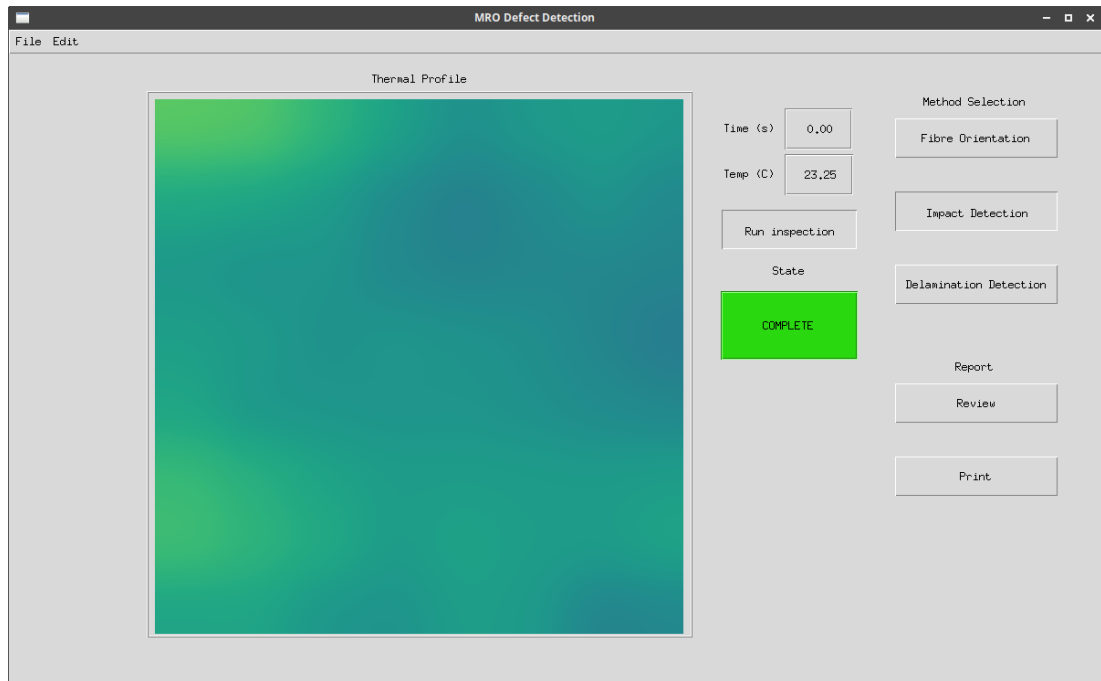


Figure 3.35: Graphical User Interface for operators, Impact Detection complete.

3.7.2 GUI Reports

3.7.2.1 Impact Damage Detection

With the data captured and the method previously selected, a report can be generated through use of the proposed methods discussed within Chapters 3, 4 and 5. Continuing with the Impact Detection method example, after selection of the ‘Review’ button from the ‘Report’ options, the GUI view will change to the Report Review layout as seen in Figure 3.36. The Thermal Profile display features the resultant image generated from the comparison of a calibrated homogeneous

as discussed within Section 3.6. As this method results in a visual areal display of the structure, the review screen layout is similar to that of the initial GUI screen, the notable differences are the removal of the option to run the inspection and its corresponding ‘State’ indicator. The time in s, from which the compared images are generated during the inspection is displayed within the ‘Time (s)’ indicator, as is the ‘Temperature (C)’. A ‘Step’ sliding bar is available for the operator to progress through the generated reports in s to provide a full indication of the evolution of the report. The presentation of the generated reports will vary

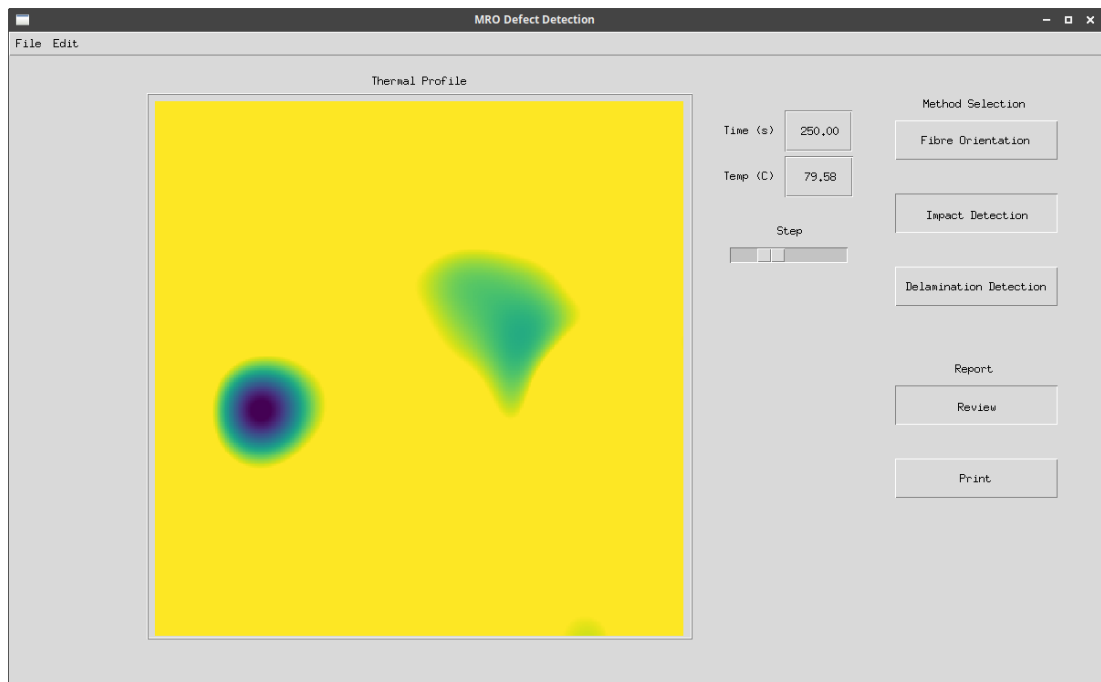


Figure 3.36: Graphical User Interface for operators, Impact Detection Review screen.

depending on the methods used, and these are discussed within the relevant chapters. For all reports, a print out can be produced by selecting ‘Print’ from the ‘Reports’ options, the report printed will be as discussed within the ‘Review’ option descriptions for each method.

3.8 Summary

The chapter introduces the design of a tool which can be utilised for the experiments presented in this thesis, to conduct thermographic defect detection analysis. The tool consists of a heated and a sensing surface. Careful consideration was given to the design of both surfaces to satisfy the requirements for accurate data capture and constraints for adoption in the MRO environment.

The heated surface utilises readily available heater mats and their flexibility allows uniform contact under vacuum. The sensing surface comprises of contact temperature sensors in the form of RTDs, that are capable of withstanding the vacuum pressures, liquid contaminants and provide a uniform flush contact with the sample under inspection. The first iteration of the sensing surface used non-silicone HTX airpad, however a number of practical issues have been identified, mitigated through the an alternative construction of glass fibre reinforced polymer - PCB. An industry standard controller has been used to actuate and capture data which makes it easily integrated with the Collins MRO workflow. The remainder of this thesis utilises the heated and sensing surfaces in conjunction with the proposed controller for data acquisition and control.

It has been demonstrated within this chapter that the principles of established IR transmission thermography, Fourier's law of heat transfer, can be applied successfully to the proposed contact sensor tooling capture method. Utilising an array of contact sensors in place of an array of pixels within an IR camera, the location and temperature data over time are recorded. The proposed method is able to indicate the location of defects which impact the 1 dimensional thermal characteristics of a composite sandwich structure, such as impact damage and disbonds, as well as infer the area of the defects through Gaussian interpolation. The findings of this chapter have been presented in the Journal Sensors [17]. More complex thermal interactions within 2 and 3 dimensions, which are required to infer interlaminar defects such as delamination, are not measured within the proposed method. However Chapter 4 explores the use of the contact sensor tooling in conjunction with transient thermal conduction to infer material properties of

CFRP laminate structures. This is expanded in Chapter 5 where inter ply delamination detection is explored through data analysis and machine learning of transient thermal conduction profiles.

The proposed GUI is also discussed to allow easy integration of the proposed inspection methods into an active MRO environment. The GUI provides control of the data capture required to perform the inspection methods, as well as a function to display the results in a visual manner which is familiar to operators.

Chapter 4

Fibre Orientation Through Analysis of Thermal Transfer

Within the MRO environment parts that arrive at the facility are not always accompanied with a repair history (or repair details are lacking) and consequently the laminate fibre orientation is not always known for any areas that have been repaired. Thermal analysis can be used to infer the fibre orientation which provides insight to the operator to decide appropriate repair strategies. The principal to infer the fibre orientation is based on comparing the thermal response of the part under test with the thermal response of part with known fibre orientation.

The thermal response of a part with known fibre orientation could be obtained either through Finite Element Analysis (FEA) simulations or through experimental data collection. Each of these approaches present their own challenges. On the one hand, simulations offer fast route to obtain the part thermal response, however, to obtain this with high accuracy requires a model of high fidelity encompassing the interaction between plies, effects of fibre weaving and consumables [185, 186, 187, 188] all of which result in anisotropic heat transfer. Even then, variability between components in the manufacturing process is challenging to capture with physics-based simulation models. On the other hand, experimental measurements provide an accurate thermal response as these complex interactions because these physically extrapolate in the measurement

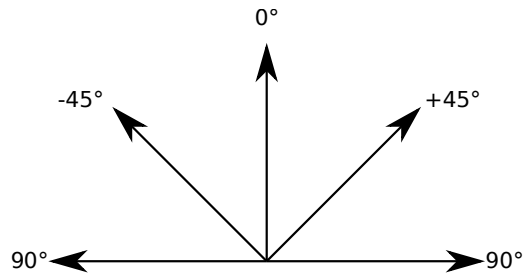


Figure 4.1: Common fibre orientation in relation to cloth roll direction (0°).

campaigns, but it is time consuming and expensive to manufacture specimen parts to characterise them thermally. Considering Collins Aerospace operates an OEM facility, access to multiple specimen parts is relatively easy to obtain, mitigating the challenges of the experimental data collection approach. This chapter starts by examining FE simulations and shows that the assumptions that model the layers as solid structures instead of individual fibres and the effect of weaving do not produce accurate results. Such assumptions are common when simulating thicker structures, however, since the laminates in the V2500 fan cowl are relatively thin, FE modelling requires significantly higher complexity. The chapter then examines capturing thermal response data experimentally which are then used to predict the fibre orientation of the lay-ups.

4.1 Fibre Orientation, Weave and Weaving Patterns

There are multiple options for the lay up of a laminate sheet which affect its structure and consequently its thermal properties. Firstly the number of plies, their fibre orientation of each ply, their weave and their weaving pattern.

Ply fibre orientation can be described in the format of the angle of the fibre when compared to the roll direction (0°), as seen in Figure 4.1 the most common fibre orientations (and those considered in this thesis) are 0° , $+45^\circ$, -45° and 90° . Weave and weave pattern refers to the direction fibres are woven within a ply. Weaves can vary significantly from basic to more exotic. Typical weaves are: (a) unidirectional, where all fibres are oriented in the same direction, (b) biaxial

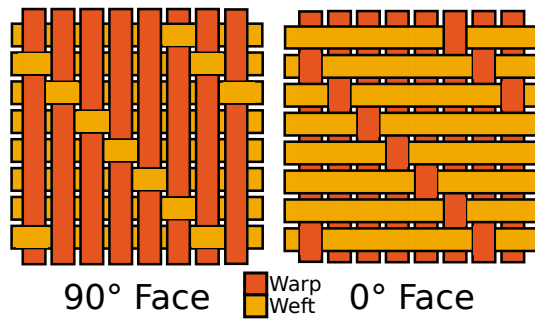


Figure 4.2: Example of a Biaxial laminate in a 5 harness satin weave.

where fibres are woven in two directions relative to the ply plane for instance, perpendicular weaving, (c) tri-axial weave where fibres are oriented in 3 directions. Furthermore, there are variations in the weave pattern of the plies which dictate the frequency of warp and weft. For example, the 5 harness satin weave is shown Figure 4.2. Other patterns are possible, but in this study this pattern has been selected to mimic that typically used for V2500 fan cowl manufacture and repair.

Since the aim here is to infer the fibre orientation, the following panel structures were considered:

- Panel 1 0/0/0/0 - Unidirectional
- Panel 2 0/90/90/0 - Unidirectional
- Panel 3 0/90/90/0 - Biaxial 5 harness satin weave

The two Unidirectional fibre laminates have density of 1625 kg m^{-1} while the biaxial fibre laminate panel is of density 1589 kg m^{-1} .

4.2 Finite Element Modelling of heat transfer through composite laminate structures

The software suite used for the Finite Element Analysis model was ANSYS 17.1 mechanical workbench with Composite PrePost environment and Transient Thermal toolbox. The panel structures 1 and 2 had a constant uniform thickness of 0.508 mm and $300 \times 300 \text{ mm}$. The third panel structure had identical dimensions

Table 4.1: Step heating profile for baseline heater mats.

Stage	Time Step(secs)	Start temperature (C)	End temperature (C)	Ramp rate (C/s)
Ramp	0-60	Ambient	80	≈ 0.9
Dwell	60-120	80	80	0.00

except for the thickness which was 0.7366 mm caused by the different cure ply thickness due to the weave, while sustaining the same volume fraction across all panels. These thickness are representative of the skin thickness within the V2500 fan cowl, with the majority being 0.7366 mm of Biaxal 5 harness material.

A heater mat, with dimensions 150×150 mm was also modelled within ANSYS to reflect the geometry of the real world equivalent. To ensure that the transient thermal simulation and experimental validation are both reacting to the same thermal input, the physical heater mat thermal profile was captured using a two-minute step heating profile divided into two parts, the ramp and dwell according the schedule shown in Table 4.1.

In order to obtain a realistic temperature rise profile for the simulation, the heater mat was visually inspected using an Fluke Ti 95 IR camera [189], with a thermal sensitivity of ≤ 100 mK, and accuracy of $\pm 2^\circ\text{C}$. Experiments were conducted to capture actual temperature data on the heater mat surface. From the visual inspection, four bands were observed as shown in Figure 4.3 (note: Figure 4.3(a) is an example image of the heater mat set at 120°C). To capture the temperature data, the ramp and dwell cycle was conducted thirty times to capture the temperature output across the heater mat with statistical confidence. Given that the visual observation identified 4 distinct bands on the heater mat surface, the temperature data was captured using four RTDs (Resistance Temperature Detector) each located in the middle of each band. Furthermore, temperature data were collected from an RTD off the heater mat surface for acquiring ambient temperature and a sixth RTD was located at the centre of the heat mat surface to provide the feedback loop for the PID controller.

Using the knowledge acquired from the visual inspection and the experimental

data obtained, the heater mat was simulated in ANSYS as four distinct bands (elements), while the temperature profile; ramp and dwell mimic the mean temperature responses obtained from the thirty experimentally captured data across all four bands (mean of 120 thermal responses). The final profile simulated is shown in Figure 4.4 along with the corresponding setpoint programmed in the controller.

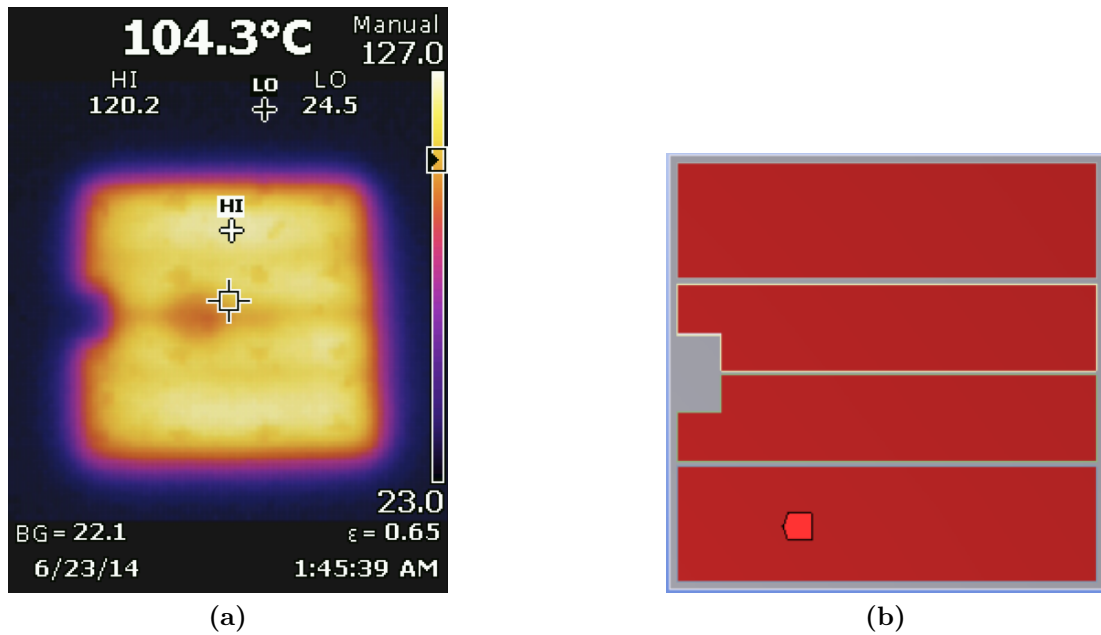


Figure 4.3: (a) Sample IR image of heater mat running, displaying bands
(b) Ansys 17.1 FE model of heater mat with bands in red.

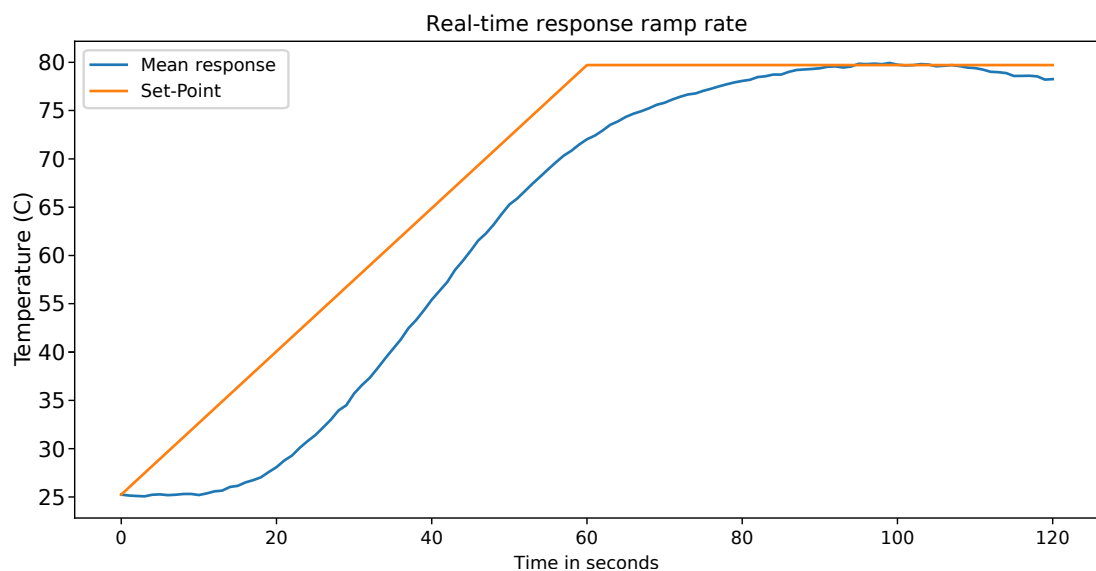


Figure 4.4: Real-time response to ramp rate of heater mat.

Table 4.2: Material properties for Unidirectional single ply.

Description	Units	-55°C	23°C	121°C
CTE 0°	10 ⁻⁶ mm/mm/°C	–	1.27	1.75
CTE 90°	10 ⁻⁶ mm/mm/°C	–	10.80	22.50
CTE thickness	10 ⁻⁶ mm/mm/°C	–	40.5	40.5
k 0°	W/m-°K	9.11	10.98	13.02
k 90°	W/m-°K	0.75	0.91	1.08
Specific Heat	J/kg-°K	678	904	1185

The Transient Thermal toolbox system was used to calculate the temperature against time profiles resultant of the structural dissipation within the FE model.

Heat zones 1-5 of the heated surface tool options discussed within Chapter 3 (Figure 3.2) were modeled within the simulation as heat injection points for the simulated panels. 64 simulated temperature probes were taken from the top surface of the simulated component in a 8×8 array evenly spaced at 37.5 mm in x and y axes and in 18.75 mm offset from the bottom left corner of the panel; location (0,0); in a fashion identical to the sensing surface designed in Chapter 3 (Figure 3.2).

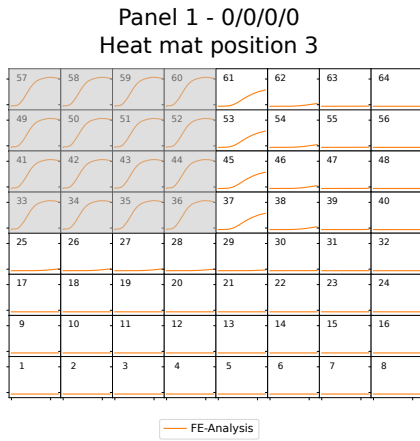
4.3 Finite Element Analysis Temperature Against Time Results

The FE analysis simulation for the 3 panels was conducted for all 5 heater mat locations and the temperature against time plot for each of the 64 corresponding probe points was plotted within an 8 × 8 grid representative of their location within the array to provide a visual indication to the dissipation due to transient thermal conduction within the samples. For the purposes of this section, the 0° orientation is aligned parallel to x -axis. The material properties used within the FE analysis for Unidirectional are shown in Table 4.2 and the biaxial 5 harness in Table 4.3. These were obtained from the manufacturer data sheet, where CTE is the coefficient of thermal expansion, k is thermal conductivity and the direction is noted relative to the fibre orientation. The results from the transient thermal FE

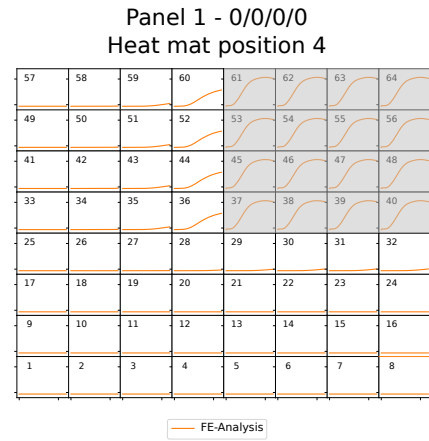
Table 4.3: Material properties for Biaxial 5 Harness 0/90 ply.

Description	Units	-55°C	23°C	121°C
CTE 0°	10 ⁻⁶ mm/mm/°C	–	1.8	2.16
CTE 90°	10 ⁻⁶ mm/mm/°C	–	1.8	2.16
CTE thickness	10 ⁻⁶ mm/mm/°C	–	18.8	31.9
<i>k</i> 0°	W/m-°K	9.32	11.2	12.98
<i>k</i> 90°	W/m-°K	0.70	0.93	1.03
Specific Heat	J/kg-°K	678	904	1185

analysis in panel 1, shown in Figure 4.5 (a)-(e), displays the discussed temperature against time plots for each heater mat location within the unidirectional 0/0/0/0 panel. It can be observed that within all 5 heater mat locations, when comparing the thermal spread within the panel in the x -axis and y -axis directions, that a higher degree of transient thermal conduction due to structural dissipation is occurring along the x -axis. As within panel 1 the fibres are parallel to each other along the x -axis so too is the concentration of thermal conduction along the carbon fibres within the plies. The produced FE analysis transient thermal temperature against time plots for panel 2, shown in Figure 4.6 (a)-(e), differs from that of panel 1. It can be seen that in this instance, the transient thermal conduction due to structural dissipation within panel 2 results in a balance of thermal conduction in the x -axis and y -axis. As panel 2 consists of a ply lay up which is both symmetrical and contains a balanced fibre orientation of 0° and 90° it is expected that so too shall the fibres within these plies balance the thermal spread as they progress through the ply layers. Figure 4.7 (a)-(e), similar to panel 2 (Figure 4.6 (a)-(e)) again displays a balanced thermal spread within the panel at all 5 heater mat locations for the x -axis and y -axis. Once again, this panel is both symmetrical and balanced in its ply lay up and as such should produce a balanced thermal conduction.

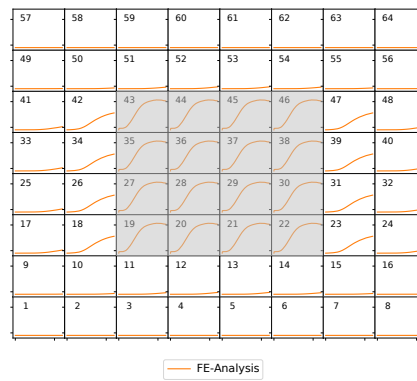


(a)



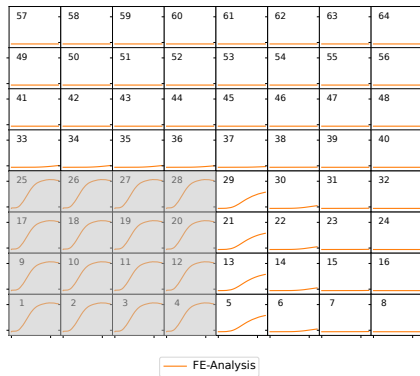
(b)

Panel 1 - 0/0/0/0
Heat mat position 5



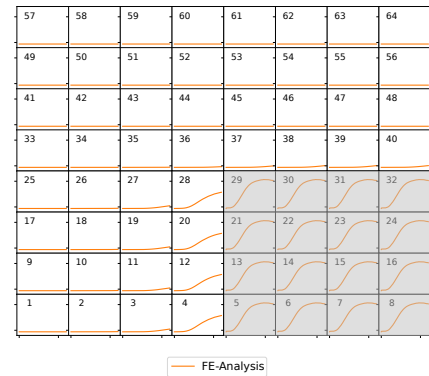
(c)

Panel 1 - 0/0/0/0
Heat mat position 1



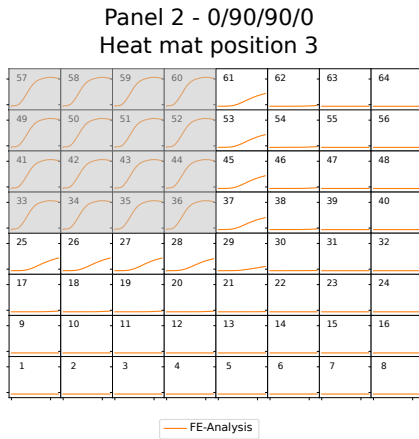
(d)

Panel 1 - 0/0/0/0
Heat mat position 2

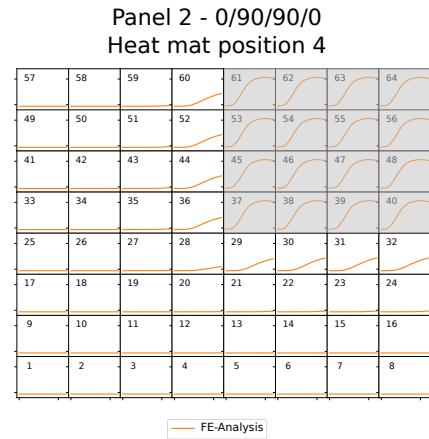


(e)

Figure 4.5: Unidirectional 0/0/0/0 4-ply layup FE analysis transient thermal temperature against time plots for probes 1-64, in (a) heater mat position 3. (b) heater mat position 4. (c) heater mat position 5. (d) heater mat position 1. (e) heater mat position 2.

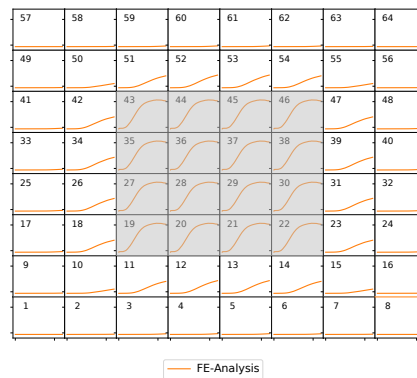


(a)



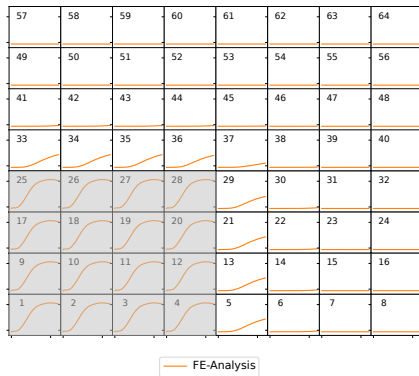
(b)

Panel 2 - 0/90/90/0
Heat mat position 5



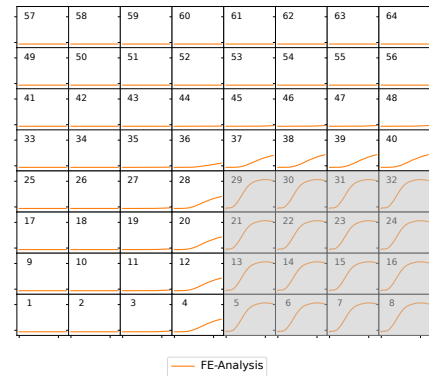
(c)

Panel 2 - 0/90/90/0
Heat mat position 1



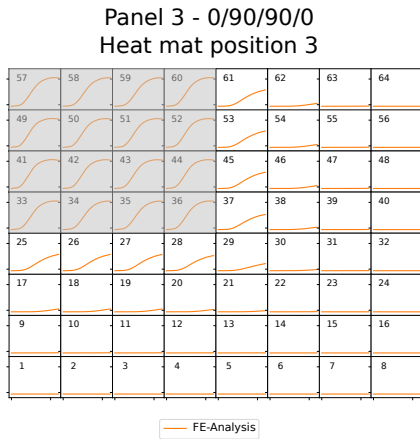
(d)

Panel 2 - 0/90/90/0
Heat mat position 2

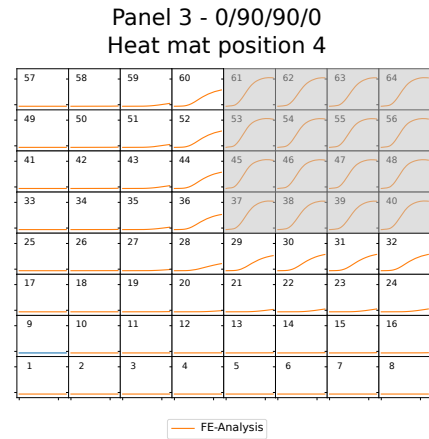


(e)

Figure 4.6: Unidirectional 0/90/90/0 4-ply layup FE analysis transient thermal temperature against time plots for probes 1-64, in (a) heater mat position 3. (b) heater mat position 4. (c) heater mat position 5. (d) heater mat position 1. (e) heater mat position 2.

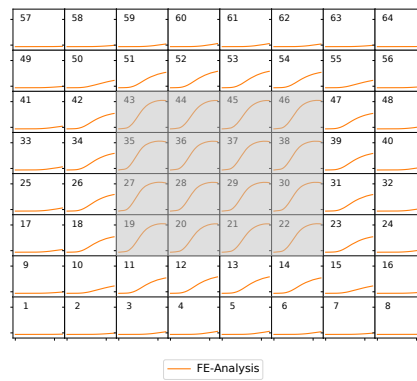


(a)



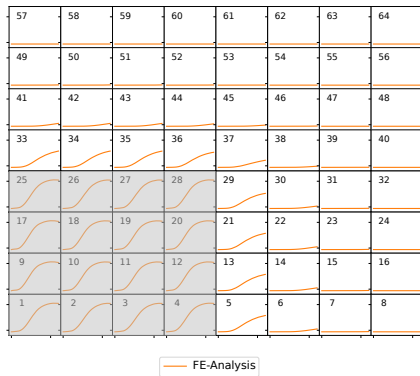
(b)

Panel 3 - 0/90/90/0
Heat mat position 5



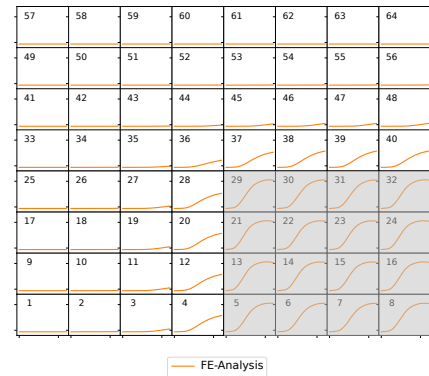
(c)

Panel 3 - 0/90/90/0
Heat mat position 1



(d)

Panel 3 - 0/90/90/0
Heat mat position 2



(e)

Figure 4.7: Biaxial 0/90/90/0 4-ply layup FE analysis transient thermal temperature against time plots for probes 1-64, in (a) heater mat position 3. (b) heater mat position 4. (c) heater mat position 5. (d) heater mat position 1. (e) heater mat position 2.

4.4 Comparison of FEA and Experimental Results

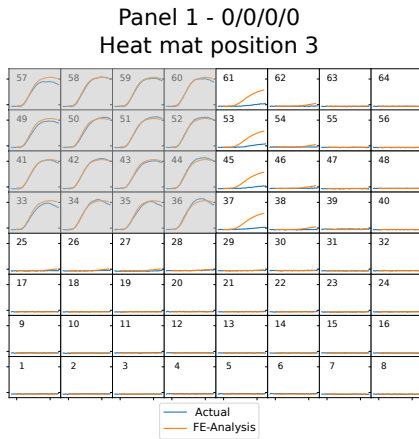
The Experimental set-up, of which the FE analysis is representative of, was conducted on three physical panels created using the same fibre orientation and weave as those within the FE analysis. The panels underwent the same step heating profile as within the FE analysis, with RTD probes spaced at corresponding locations to those within the FE analysis, allowing for a direct comparison of the captured temperature against time profiles to those generated by FE analysis.

The simulated and experimental thermal profiles are shown in Figures 4.8 (a)-(e), 4.9 (a)-(e), and 4.10 (a)-(e). These figures display all five heater mat position resultant temperature changes over the 2 minute period. Probes immediately above the heater mat are shaded gray.

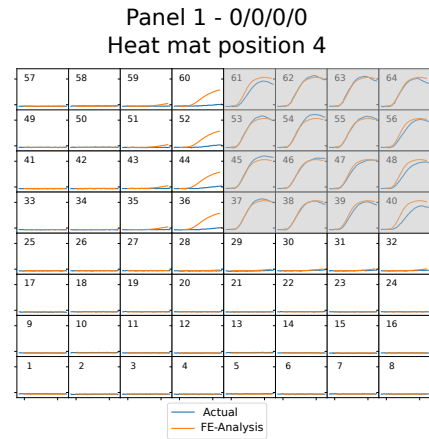
Experimentally obtained results from the unidirectional 0/0/0/0 laminate sample (Panel 1) were compared to the FE analysis as shown in Figure 4.8. The figures illustrate that the temperature profile between the simulation model and experimental results follow the same trend for the location directly above the heater mat; for instance, Figure 4.8 (c) the heater mat is located at the centre of the panel (locations 19-22, 27-30, 35-38, 43-46).

However, it can be seen that the lateral thermal conduction due to structural dissipation within the x -axis of the experimentally captured profiles (blue) has significantly lower amplitude compared to that obtained by the FE analysis (orange). The difference highlights the difficulty in designing an accurate FE model and it is likely to inappropriate modelling of the thermal propagation in the direction of the fibre. It should be noted that the thermal coefficient used for the FEA simulation is that provided by the material manufacturer (typically given for 1 ply), however, when multiple plies are laid up, complex interactions between the layers, resin system and fibre, shift significantly the thermal behaviour of the panel.

For the second and third panel unidirectional 0/90/90/0 and biaxial 0/90/90/0, the FEA results show equal and balanced thermal spread in both the x and y axes,

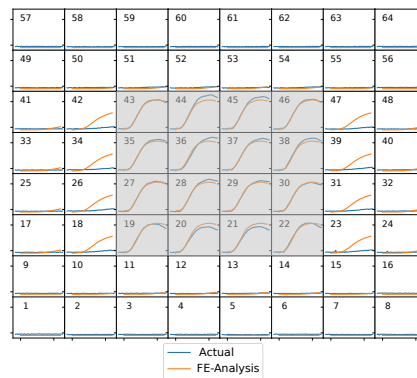


(a)



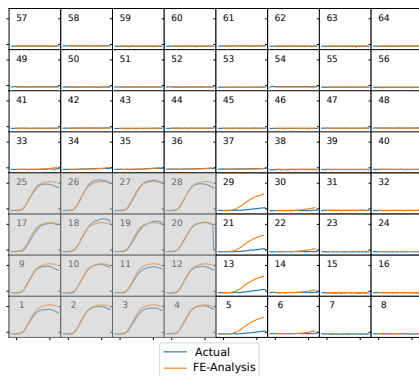
(b)

Panel 1 - 0/0/0/0
Heat mat position 5



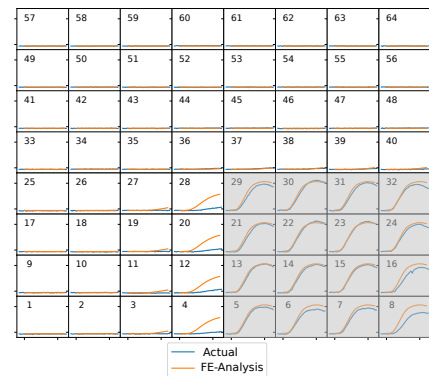
(c)

Panel 1 - 0/0/0/0
Heat mat position 1



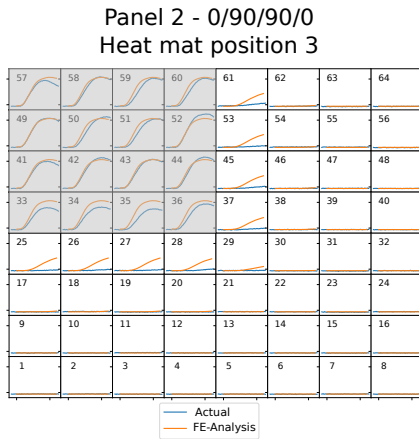
(d)

Panel 1 - 0/0/0/0
Heat mat position 2

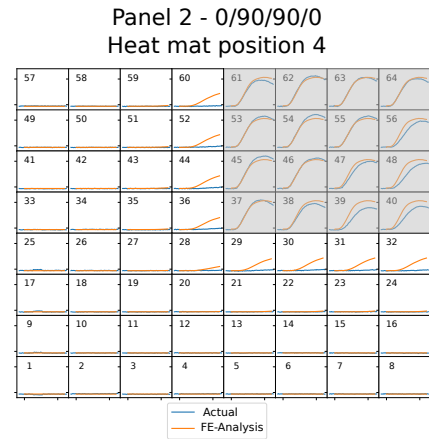


(e)

Figure 4.8: Unidirectional 0/0/0/0 4-ply layup FE analysis transient thermal and Experimentally captured, temperature against time plots for probes 1-64, in (a) heater mat position 3. (b) heater mat position 4. (c) heater mat position 5. (d) heater mat position 1. (e) heater mat position 2.

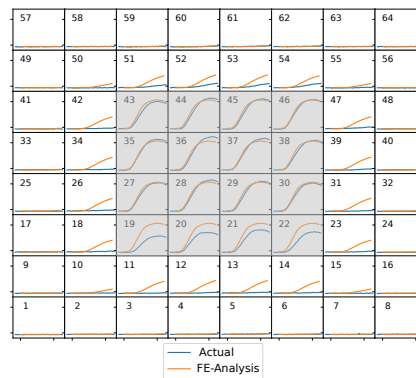


(a)



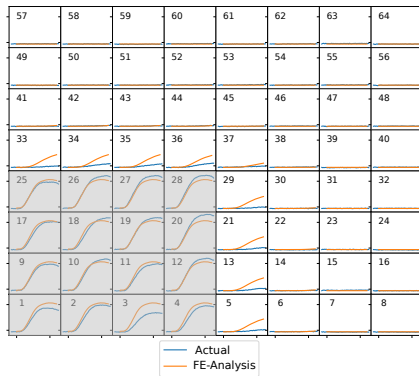
(b)

Panel 2 - 0/90/90/0
Heat mat position 5



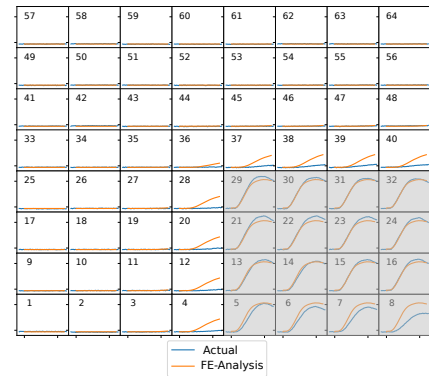
(c)

Panel 2 - 0/90/90/0
Heat mat position 1



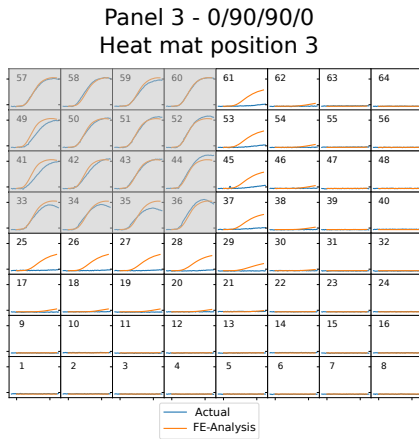
(d)

Panel 2 - 0/90/90/0
Heat mat position 2

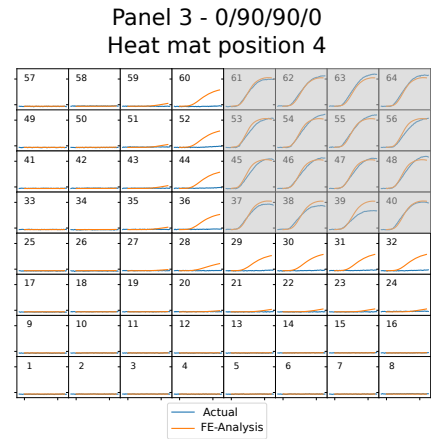


(e)

Figure 4.9: Unidirectional 0/90/90/0 4-ply layup FE analysis transient thermal and Experimentally captured, temperature against time plots for probes 1-64, in (a) heater mat position 3. (b) heater mat position 4. (c) heater mat position 5. (d) heater mat position 1. (e) heater mat position 2.

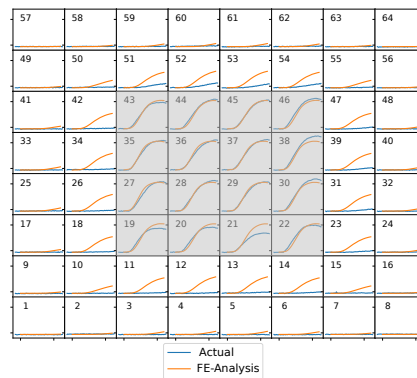


(a)



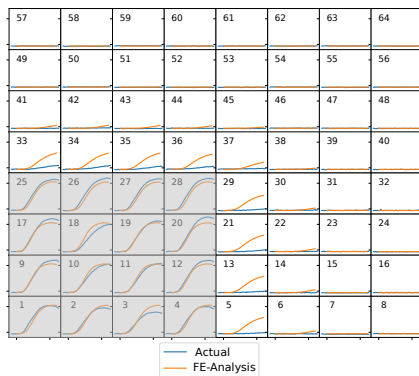
(b)

Panel 3 - 0/90/90/0
Heat mat position 5



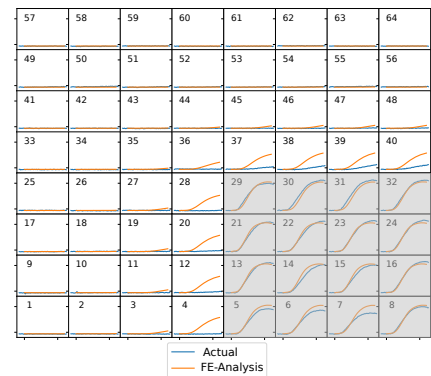
(c)

Panel 3 - 0/90/90/0
Heat mat position 1



(d)

Panel 3 - 0/90/90/0
Heat mat position 2



(e)

Figure 4.10: Biaxial 0/90/90/0 4-ply layup FE analysis transient thermal and Experimentally captured, temperature against time plots for probes 1-64, in (a) heater mat position 3. (b) heater mat position 4. (c) heater mat position 5. (d) heater mat position 1. (e) heater mat position 2.

however, experiments show only a very slight thermal spread in the y direction, Figure 4.9 and Figure 4.10 respectively. Similar to the unidirectional 0/90/90/0 the biaxial woven 0/90/90/0 samples displayed experimentally captured results differed from the FE simulations. Again, the thermal spread and magnitude were very different in the x and y axis, Figure 4.10 displaying no indications of thermal spread reaching the x axis outwith the area of the heater mat. This is not the case in the FE simulation where there is seen to be a uniform thermal spread of the sample around the heater mat area. The possible interference from the control and power connections at the base of the heater mat is also repeated within this sample. Probes 11-14 are showing no thermal spread originating from the heater mat along the 90° fibre orientation but as with the unidirectional 0/90/90/0 sample there is a temperature increase recorded within probes 51-54 on the opposite side of the 90°. This would support the hypothesis that the two 90° fibre orientations meeting is forming a concentration in the plane for heat conduction. As seen in Figure 4.2, the 5 harness composite fabric used exposes the fibres in lengths of five widths on top of fibre bundles before it is woven underneath the sixth. Figure 4.2 also shows that this is the same for both the 90° face and the 0°, which would result in a larger surface area within the 90° fibre orientation ply faces meeting in a similar fashion to the unidirectional 0/90/90/0 sample.

These comparisons between the experimentally captured data and the FEA would suggest that further thermal interactions are occurring within the panels which have not been accurately modeled within the FE analysis.

The discrepancies observed between FEA and experimental results have been identified by other researchers and have been attributed to treating laminates as solids [190] as well as uniform undulation assumptions regarding the drape of the fibres [191].

In the instance of the unidirectional 0/90/90/0 sample the explanation as to the thermal spread concentrated in the 90 degree fibre angle (y axis) may be due to the meeting of two ply layers at 90° acting more as a single thick layer of unidirectional tape than two separate layers as modelled within the FE package. Thermal conductivity will improve along the centre axis of two fibre directions

when the fibre orientation is closer to parallel than perpendicular [192, 193, 145, 194, 195, 196]. A single thicker layer could transmit higher thermal conduction along its fibre direction due to the increased fibre volume distribution in that direction.

4.5 Transient Thermal Conduction due to Structural Dissipation As a Fibre Orientation Indication

It has been demonstrated within this chapter that the fibre orientation within laminate structures results in a measurable difference in the thermal profile of the laminate. This has been observed using a step heating profile which ramps to 80°C within 120 s. This is due to the structural dissipation of thermal energy concentrating along the fibre orientation. Further analysis of the data that is produced in biaxial woven laminate structures is needed to develop techniques that could provide detailed information regarding the fibre orientation of the structures. Initial experimental results conducted for comparison the FEA models identified that when the heater mat was placed on the edge of the panel this resulted in boundary effects which increase the complexity further.

The intention of this chapter is to conduct the feasibility for the detection of fibre orientation in laminate panels by comparing the thermal response of a component under test with a database of thermal responses. To avoid the before-mentioned boundary effects, larger test samples were created that would mitigate thermal energy dissipation from the edges.

Three new samples were created with dimensions of 500 × 500mm. Given that laminates with biaxial lay-up are more representative in the aerospace sector and more challenging to discriminate, this study utilises the following lay ups:

- Bi090900 - Biaxial 0/90/90/0, symmetrical and balanced
- Bi090090 - Biaxial 0/90/0/90, non-symmetrical and balanced
- Bi0904545 - Biaxial 0/90/+45/-45, non symmetrical and unbalanced

This was to provide the best chance of identifying any intermediate changes between the two samples containing only 0/90, 90/0 laminate plies within the 0/90/+45/-45 sample. An intermediate change between the samples may allow for an indication as to the underlying fibre orientation of other samples with a top laminate which can be visually verified as 0/90 but an unknown base laminate.

The same set-up as was utilised with one heater mat and the 64 RTD sensing surface. The complete experimental set up on the $500 \times 500\text{mm}$ panel is shown in Figure 4.11. Both the heater mat (position 5) and sensing surface were placed in the middle of the part.

The ramp up and dwell period were kept the same as in previous experiments and an additional cooling-off period as shown in Table 4.4. The total cycle duration was 400s consisting of 50 s of ramp, 250 s of dwell, and 100 s of cooling-off. It should be noted that analysis of the cooling-off period was not performed but the data was captured for completeness.

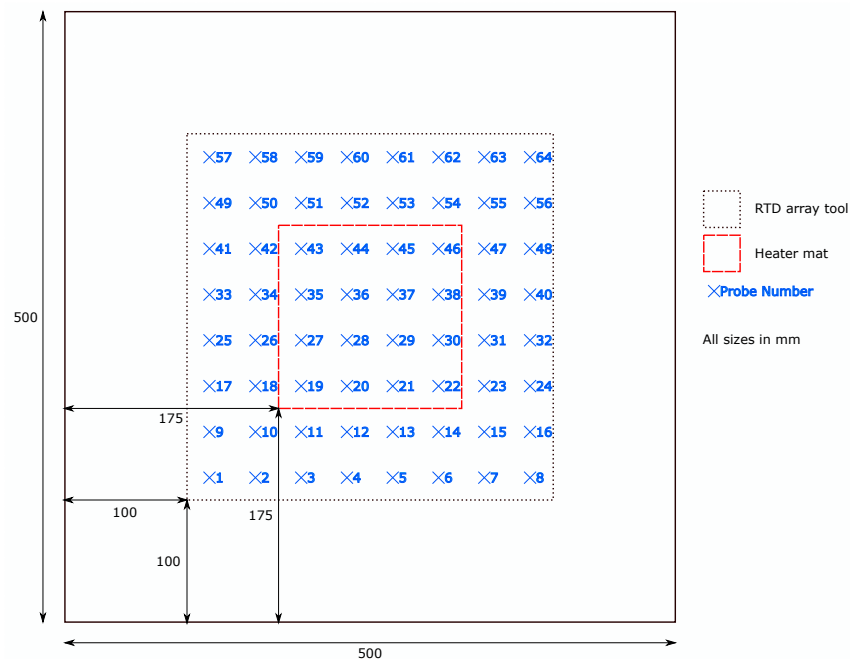


Figure 4.11: $500 \times 500\text{mm}$ test sample experimental set up in heat zone 5 (dashed red outline) using $300 \times 300\text{mm}$ RTD probe array (dotted black area).

Table 4.4: Step heating profile for heat zone 5 set up.

Stage	Time Step (secs)	Start Temperature ($^{\circ}\text{C}$)	End Temperature ($^{\circ}\text{C}$)	Ramp rate ($^{\circ}\text{C}/\text{s}$)
Ramp	0-50	Ambient	80	≈ 0.5
Dwell	50-300	80	80	0.00
Cool off	300-400	80	Ambient	–

4.5.1 Analysis of Results

The initial approach was to visualise the obtained temperature data [197] across the panel surface for various time points in the cycle as shown in Figure 4.12 (a)-(c) for 200 s; however, the low spatial resolution makes these difficult to interpret. One approach is to utilise Gaussian Interpolation [198] to upscale the raw data and obtain smoother visualisations. This approach generate images which are easier to understand (Figure 4.12 (d)-(f)), i.e., it is clear that there is a thermal spread in both the x and y directions as expected, however, differences between the three panels are not easily discernible. This method is therefore open to interpretation by the person examining the samples.

Investigating at the temporal profiles of probes 33-40, all of which are located on the same horizontal line in the middle of the part, reveals that the probes which are directly above the heater mat follow closely the heater mat temperature (Figure 4.13). On the other hand probes 33, 34, 39, and 40 are located off the heater mat and any temperature change can be attributed solely to lateral conduction. These probes reach a steady state temperature significantly lower than the heater mat temperature, 29.0°C , 33.7°C , 34.3°C and 29.4°C respectively and the temperature reduction is proportional to the distance of the probes from the heated area. Furthermore, even after the heater mat power is removed (cooling-off period) at 300 s, the temperature continues rise and this is attributed to the heat that is stored on the region above the heater mat (probes 35-38) which have a temperature greater than 60° until 350 s, approximately. Finally, the probes do not feature the ripple swing during the steady state, which is observable for the probes directly above the heat mat (35-38). The ripples during the dwell period are is expected and caused by oscillations of the PID controller with an

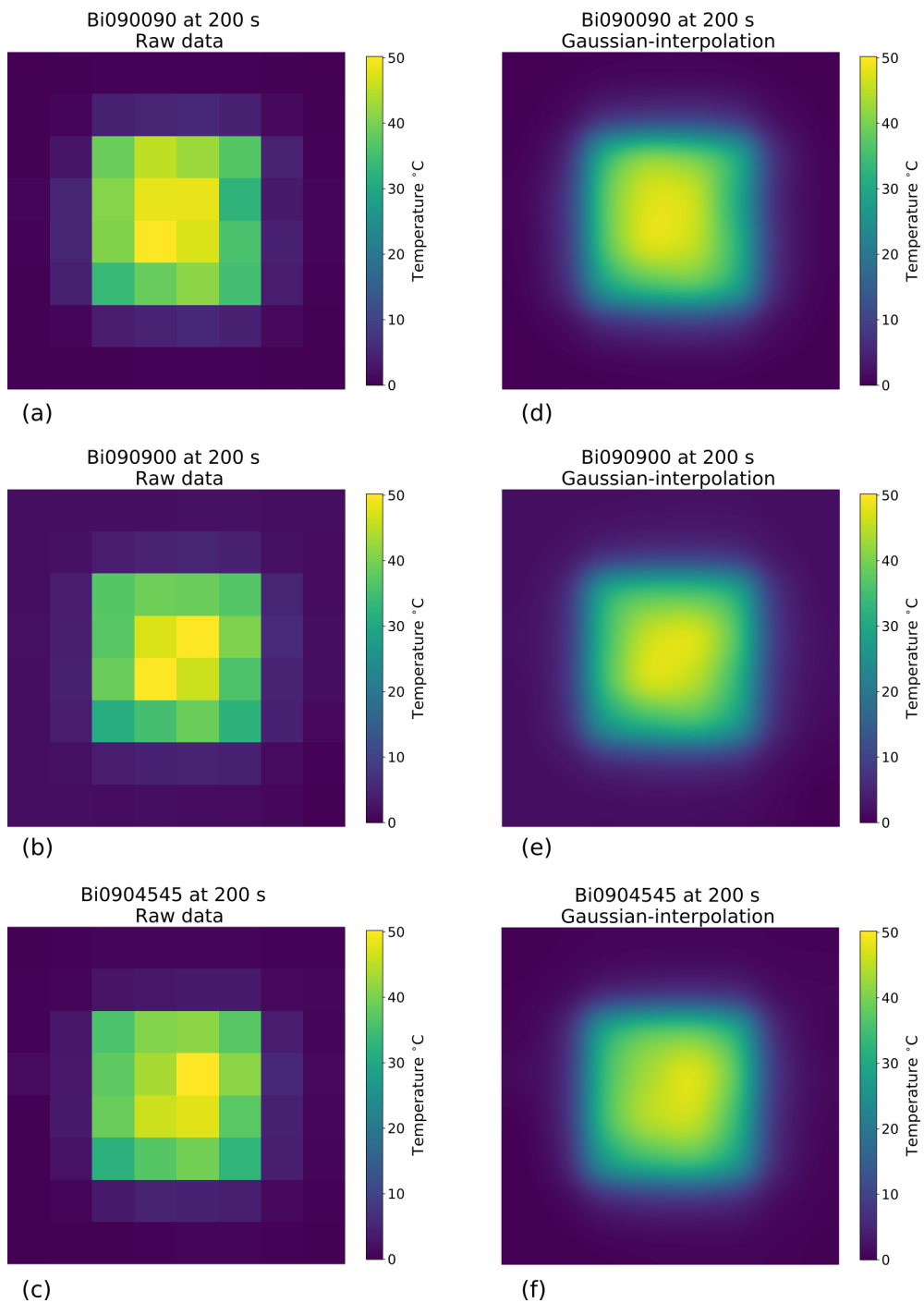


Figure 4.12: (a) raw temperature heat map for sample BI090090 at 200 s (b) raw temperature heat map for sample BI090900 at 200 s (c) raw temperature heat map for sample BI0904545 at 200 s (d) Gaussian interpolation temperature heat map for sample BI090090 at 200 s (e) Gaussian interpolation heat map for sample BI090900 at 200 s (f) Gaussian interpolation heat map for sample BI0904545 at 200 s.

amplitude of $\pm 0.7^{\circ}\text{C}$.

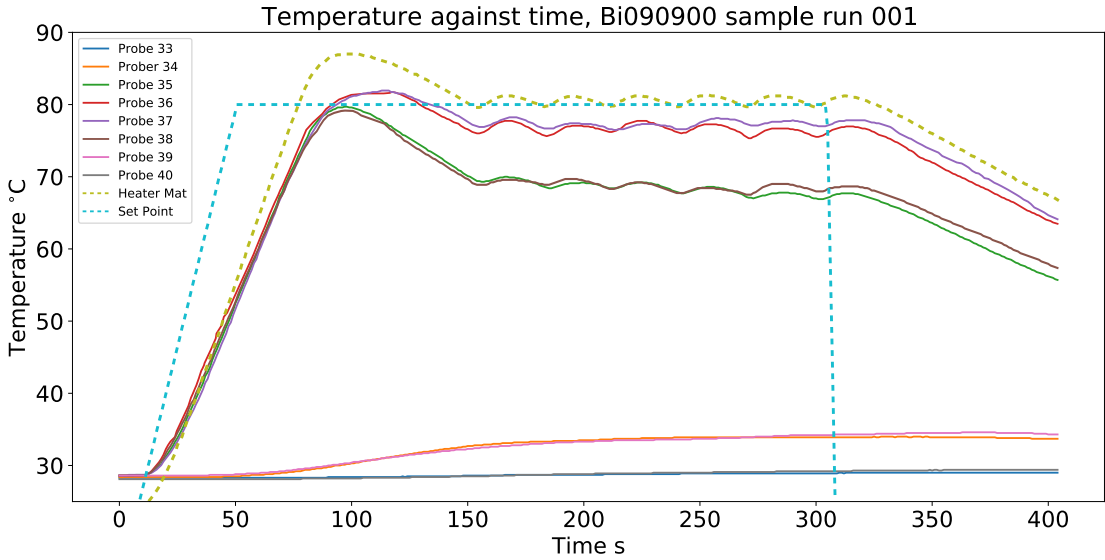


Figure 4.13: Temperature against time of heater mat and probes 33-40 of Biaxial sample 0/90/90/0 run 001.

Interpretation of the time series signals (such as those presented in Figure 4.13) by inspectors is challenging owing to the large number of probes and their correlation with the distance from the heated area. An alternative visualisation is obtaining the temperature difference distribution of the sensing surface with time as shown in Figure 4.14. More formally, the temperature difference $\Delta T_k(t)$ for probe k at time t is given by

$$\Delta T_k(t) = T_k(t) - T_k(t_{ref}) \forall k \in [1, 64] \text{ and } t_{ref} \leq t \leq 300 \quad (4.1)$$

where $T_k(t)$ represents the temperature of probe k at time t and $T_k(t_{ref})$ represents the probe temperature at time t_{ref} . To select the time t_{ref} , stability analysis was used for all the probes 1-64 and it was determined that all have researched steady state at the point of $t_{ref} = 150s$, which is used throughout the rest of the analysis. Then the temperature difference distribution across all probes $k \in [0, 64]$ at time t is denoted as $f_{\Delta T(t)}(x)$ which is essentially the histogram of the temperature differences across all times in the dwell period.

To reduce noise in the visualisation and quickly present quantitative data in a way that is easily interpreted visually, the data were presented in histogram format, the histograms were subsequently smoothed through Kernel Density Estima-

tion [199] with a bandwidth of 1, which was determined experimentally through visual observation.

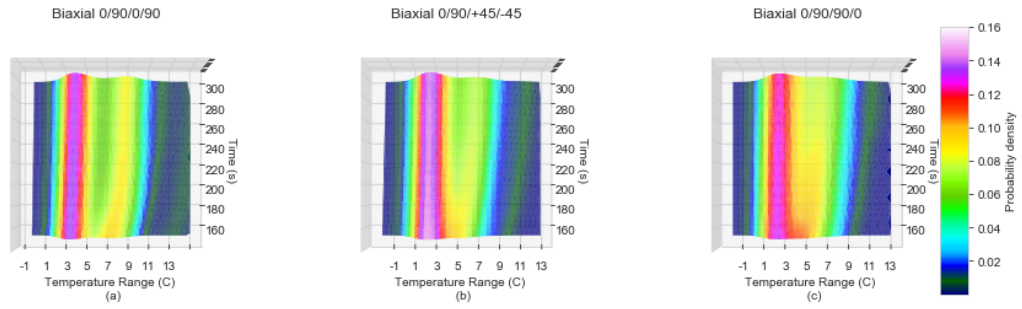


Figure 4.14: Kernel Density Estimate line plots shown as tri-surface plots for temperature ranges -3°C to 13°C , colour map denotes probability density. Sample run 001 for ply profile lay ups between 150-300 s with histograms (a) Biaxial 0/90/0/90 (b) Biaxial 0/90/+45/-45 (c) Biaxial 0/90/90/0.

The results obtained for the three panels are shown Figure 4.14. The horizontal axis represents the temperature difference in $^{\circ}\text{C}$, the vertical axis, the time from $t_{ref} = 150\text{s}$ to 300 s, and the colours represent the frequency at which the temperature is experienced on the sensing surface. For all samples, the ΔT is between -3 and 13°C .

A high degree of differentiation between the panels can be seen by viewing the three dimensional graphs from a different angle as shown in Figure 4.15. Furthermore, the graphs shown the median density profile across time and it is clear that each of these panels provides a distinct signature owing to the interactions between layers. For instance, the first panel contains two modes (peaks) in the median distribution, while for the second panel the higher mode becomes less pronounced (shifts towards the main mode) and even less pronounced for the third panel.

Interpreting the results between Figure 4.14 and Figure 4.15 for panel biaxial 0/90/+45/-45 and 0/90/90/0, the temporal behaviour starts as a distribution with a single mode and progressively develops to a bimodal distribution. On the other hand, the biaxial 0/90/0/90 starts from the beginning as a bimodal distribution, indicating that there is a difference in convection speed between the x and y directions.

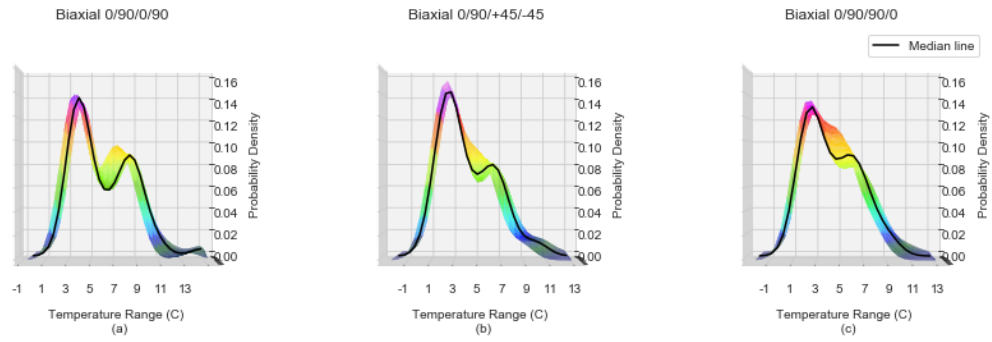


Figure 4.15: Kernel Density Estimate line plots for temperature ranges -3°C to 13°C in sample run 003 for ply profile lay ups between 150-300 s with median line (a) Biaxial 0/90/0/90 (b) Biaxial 0/90/+45/-45 (c) Biaxial 0/90/90/0.

The same behaviour described here with small variations has been observed in all 10 repetitions of the experiment (10 trials for each panel).

4.5.2 Automatic Fibre Orientation Detection Method

A simple but effective approach to automatically detect the fibre orientation of a new panel is to compare its behaviour against the profiles of specimen panels with different fibre orientations as illustrated in Figure 4.16.

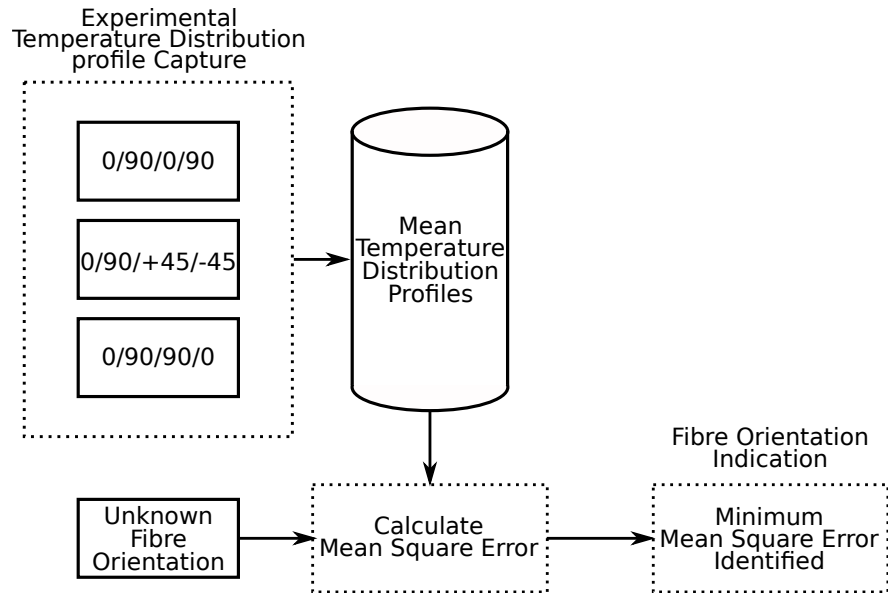


Figure 4.16: Proposed Methodology to Determine Fibre Orientation.

In this study, the database contains profiles for three fibre orientations, biax-

ial 0/90/0/90, 0/90/+45/-45 and 0/90/90/0. To test the approach, 30 experimentally obtained profiles (10 for each panel) are split: 60% used to create the database and 40% for testing the proposed approach.

The 60% of the experiments (i.e., 6 per panel, 18 total) are used to construct a database of 3 profiles one per fibre orientation, which is obtained by averaging the temperature difference distributions over time.

The remaining 40% of the experiments (i.e., 4 per panel, 12 total) are used to test the proposed approach which consists of computing the similarity of the new profile to the 3 in the database. In this case, the Mean Square Error (MSE) metric is used to compute profile similarity and the results show perfect separation between fibre orientations as shown in the confusion matrix Figure 4.17. The process of splitting the 30 trials into training and testing was repeated 5 times in a fashion similar to cross-validation and the results obtained were identical. This indicates that there is a clear separation between fibre orientations leading to 100% accuracy with no false predictions.

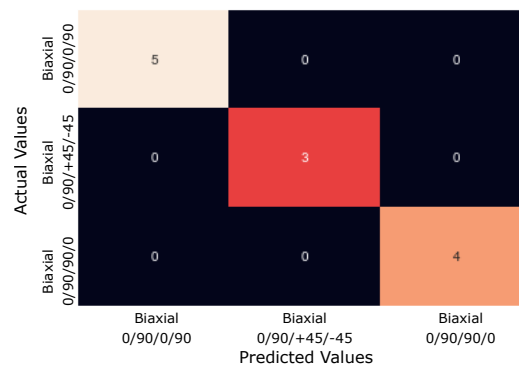


Figure 4.17: Confusion matrix for 12 out of 30 test samples compared to Mean Temperature Distribution Profiles generated from remaining 18 samples.

Although each test sample is classified based on the minimum MSE an additional visualisation can be provided to inspectors to increase confidence as in Figure 4.18. In this visualisation, the black solid line represents the median temperature difference distribution for the test panel overlaid on each of the three specimen profiles in the database along with the MSE for each. In this example, the test panel has biaxial 0/90/0/90 fibre orientation and it is clear that the best match is obtained at the minimum MSE (Figure 4.18). Examples for panels of

biaxial 0/90/+45/-45 and 0/90/90/0 are shown in Figure 4.19 and Figure 4.20, respectively.

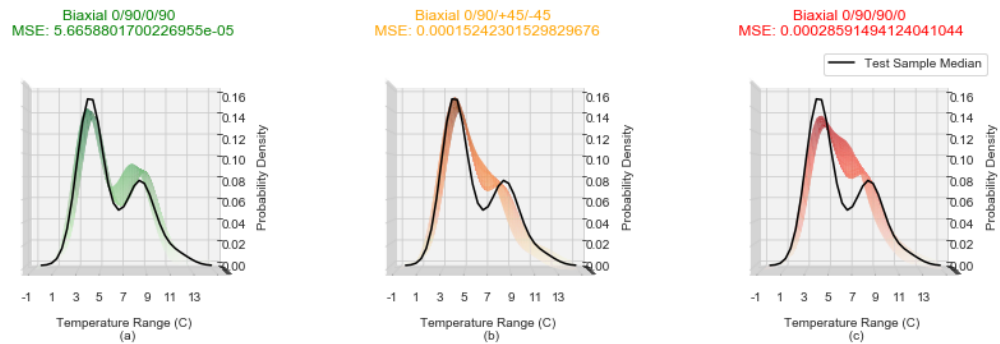


Figure 4.18: A Biaxial 0/90/0/90 correctly classified via a MSE comparison against (a) Biaxial 0/90/90/0 (b) Biaxial 0/90/+45/-45 (c) Biaxial 0/90/0/90.

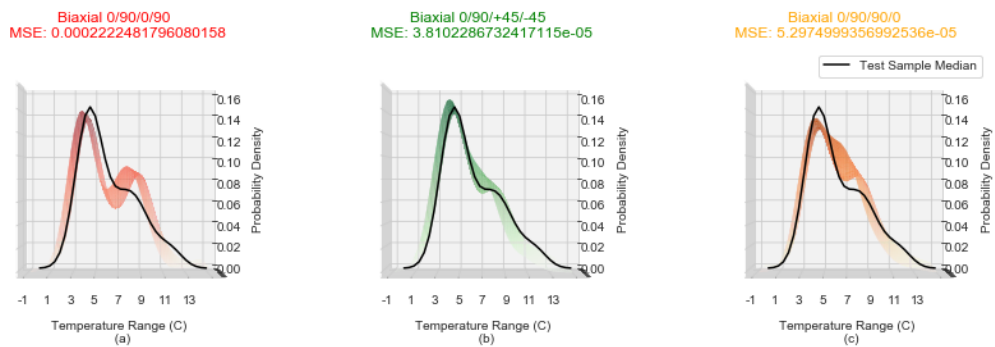


Figure 4.19: A Biaxial 0/90/+45/-45 correctly classified via a MSE comparison against (a) Biaxial 0/90/90/0 (b) Biaxial 0/90/+45/-45 (c) Biaxial 0/90/0/90.

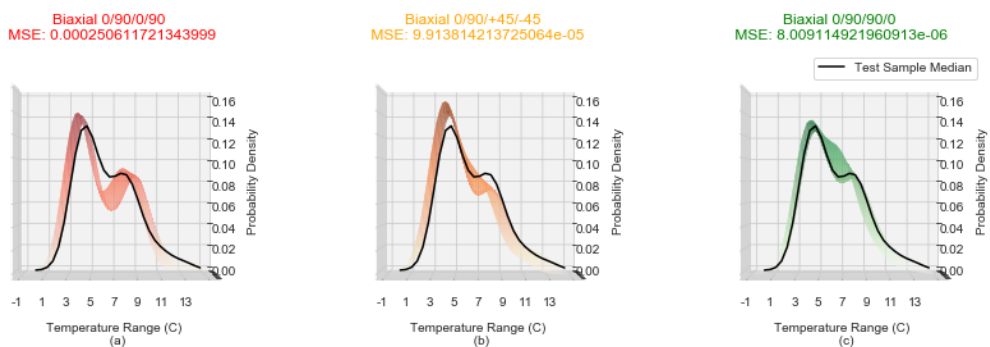


Figure 4.20: A Biaxial 0/90/90/0 correctly classified via a MSE comparison against (a) Biaxial 0/90/90/0 (b) Biaxial 0/90/+45/-45 (c) Biaxial 0/90/0/90.

It is recognised that the test set of 12 trials constitutes a small dataset and experimental results may be affected by noise. To determine the effect and sensi-

tivity to noise, one stratified 60/40% split was obtained and additional data were synthesised for the test set by corrupting each of the temperature probe time with Gaussian (White) noise. Use of synthetic data is a common approach to validate thermography NDT/NDI methods and provide robust validation and testing of methods [200, 201, 202, 203]. In this study, synthesised data were created for various degrees of severity (standard deviation, σ 0.1-0.6 in increments of 0.1) and zero mean $\mathcal{N}(0, \sigma)$. This resulted in a synthetic dataset that contained 6 groups with known degrees of noise. For every of the 12 samples in the test set (40% of 30 trials where each fibre orientation contributes 4 samples in the test set), 100 profiles corrupted by Gaussian Noise were synthesised for each of the 6 degrees of severity (i.e. $12 \times 100 \times 6$) resulting a total 7,200 samples in the synthetic data set.

Evaluating the confusion matrices for each of level of noise yields the performance shown in Table 4.5. The metrics were obtained from individual confusion matrices as for example, the one shown for $\sigma = 0.4$ in Figure 4.21 and are defined as follows:

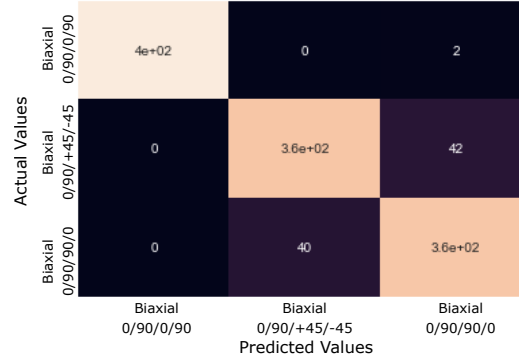


Figure 4.21: Confusion matrix for 1,200 synthetic data sets with Gaussian noise of $\mathcal{N}(0, = 0.4)$.

$$Precision = \frac{tp}{tp + fp} \quad (4.2)$$

$$Recall = \frac{tp}{tp + fn} \quad (4.3)$$

$$F_1score = 2 \cdot \frac{precision \cdot recall}{precision + recall} \quad (4.4)$$

$$Accuracy = \frac{tp + tn}{tp + tn + fp + fn} \quad (4.5)$$

where tp is the number of samples classified correctly, tn number of samples rejected correctly, fp number of samples misclassified in each class and fn the number of samples rejected incorrectly. The F_1score is the harmonic mean of $precision$ and $recall$.

Table 4.5: Classification report for synthetic samples, standard deviations (σ) 0.1 through to 0.6.

σ	Sample	Precision	Recall	F1-score	Accuracy
0.1	Biaxial 0/90/0/90	1.00	1.00	1.00	0.93
	Biaxial 0/90/+45/-45	0.90	0.90	0.90	
	Biaxial 0/90/90/0	0.90	0.90	0.90	
0.2	Biaxial 0/90/0/90	1.00	1.00	1.00	0.93
	Biaxial 0/90/+45/-45	0.90	0.90	0.90	
	Biaxial 0/90/90/0	0.90	0.90	0.90	
0.3	Biaxial 0/90/0/90	1.00	1.00	1.00	0.93
	Biaxial 0/90/+45/-45	0.90	0.90	0.90	
	Biaxial 0/90/90/0	0.90	0.90	0.90	
0.4	Biaxial 0/90/0/90	1.00	0.99	1.00	0.93
	Biaxial 0/90/+45/-45	0.90	0.90	0.90	
	Biaxial 0/90/90/0	0.89	0.90	0.90	
0.5	Biaxial 0/90/0/90	1.00	0.94	0.97	0.88
	Biaxial 0/90/+45/-45	0.89	0.81	0.85	
	Biaxial 0/90/90/0	0.78	0.90	0.84	
0.6	Biaxial 0/90/0/90	1.00	0.91	0.95	0.87
	Biaxial 0/90/+45/-45	0.89	0.80	0.84	
	Biaxial 0/90/90/0	0.76	0.90	0.82	

From Table 4.5 it is clear that the performance remains high for low to moderate levels of noise 0.1-0.4 with overall accuracy 93%. The highest confusion for these noise levels occurs between panels with fibre orientations 0/90/+45/-45 and 0/90/90/0. Separation between the 0/90/0/90 fibre orientation panels is more clear attributed to the perpendicular orientation of the layers in the middle layer. The other panels provide intermediate transitions or completely aligned transitions with the middle layers creating less distinct temperature profiles.

For noise levels of 0.5 and 0.6 the classification performance starts to decrease as the level of corruption is too significant for the MSE discriminator. Levels of noise any higher than 0.6 will result in approximately 32% of the values been altered by more than $\pm 0.6^\circ\text{C}$, according to the 1-Sigma rule (68–95–99.7 rule), which will cause severe shifts to the temperature difference distributions, typically having a range of 14° and hence impacting the MSE estimates.

A further synthetic data set was created to simulate biaxial laminates of double thickness by extending the temperature to time response. The data were generated by inserting a blank time period between each s captured and interpolating the temperature at this time period from the previous and next temperature, in so doing artificially doubling the thermal response time and generating a thermal map representative of laminate plies double the thickness of the experimental samples. Noise from random points of a Gaussian normal process with $\sigma = 0.1$ was applied to generate 1,200 double thickness data points. As before, the synthetic data set was subject to the same MSE comparison as the original experimentally captured test group, against the same specimen profiles for each fibre orientation.

The results for biaxial 0/90/0/90 are comparable to those of the regular thickness samples at $\sigma = 0.3$ as shown in Figure 4.22 and Table 4.6. However, biaxial 0/90/+45/−45 has a reduction in precision from 0.9 to 0.75, due to False Positive identification of the biaxial 0/90/90/0 samples as biaxial 0/90/+45/−45, also reflected within the precision and recall scores of biaxial 0/90/90/0 as 0.88 and 0.7 respectively. Overall, the accuracy between the normal thickness and the double thickness samples with random Gaussian normal noise applied at $\sigma = 0.1$ reduced from 93% in the regular to 87% in the double thickness samples. This reduction in precision and recall is expected due to the double synthetic samples having no mean temperature distribution profile for their specific thickness within the library. However, it is of note that the biaxial 0/90/0/90, which is the most common fibre orientation lay up within the V2500 fan cowl, is still classified with high levels of precision and recall even when thickness increases.

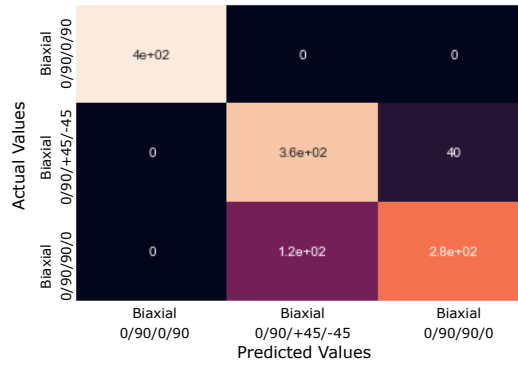


Figure 4.22: Confusion matrix for synthetic double thickness samples with added Gaussian noise $\sigma=0.1$.

Table 4.6: Classification report for synthetic double thickness samples, with added Gaussian noise $\sigma=0.1$.

Bandwidth	Sample	Precision	Recall	F1-score	Accuracy
0.1	Biaxial 0/90/0/90	1.00	1.00	1.00	0.87
	Biaxial 0/90/+45/-45	0.75	0.90	0.82	
	Biaxial 0/90/90/0	0.88	0.70	0.78	

4.6 GUI report presentation

For the Fibre Orientation indication proposed method developed within this chapter, the resultant report is not one of an areal view of the sample under inspection, but in the form of an indication of the closest aligned mean temperature distribution profile outside of the heated area during 150-300 s whilst the sample is at a temperature of 80°C through calculation of the Mean Square Error. As such the proposed method's report is one displaying a prediction of the fibre orientation based on a library of known mean temperature distribution profiles. Figure 4.23 displays the Fibre Orientation indication review screen, where the library of known mean temperature distribution profiles are displayed within the main section of the GUI. As discussed, the MSE of the captured mean temperature distribution of the sample against the library of known fibre orientation ply lay-ups are compared and ranked the lowest MSE to highest. The operator can visually compare the mean temperature distribution profile line of the sample under inspection with the library of mean temperature distribution profiles as well as see the MSE ranking list within the indication box next to the main

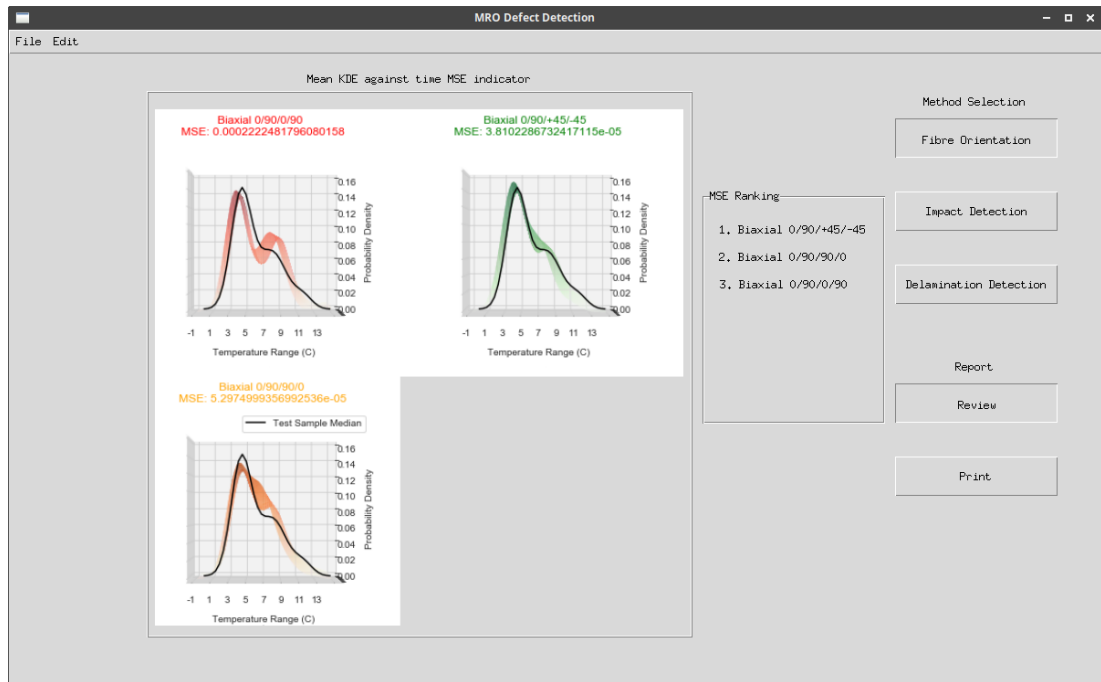


Figure 4.23: Graphical User Interface for operators, Fibre Orientation indication Review screen.

section. A combination of the MSE ranking and operator visual inspection of the generated mean temperature distribution profile can be used to indicate the fibre orientation of the sample under inspection.

4.7 Summary

As demonstrated within this Chapter, it is possible to utilise the transient thermal profiles generated within areas of a CFRP laminate panel not in direct contact with an external heat source to provide indications of the material properties. In particular, this chapter concentrates on inferring fibre orientation of the laminate panels by comparing the thermal response obtained through a heat cycle against a library of known responses. Obtaining the library of responses can either be achieved by Finite Element Analysis methods or through experimental means. Although FEA methods are convenient to obtain, these require high fidelity models which in practise are difficult to construct owing to the complex interaction between fibres, layers in the construction, multi-material interactions

(resin and fibre) and variance in the construction process. Typically, FEA models are constructed for thicker structures which are less sensitive to the local/spatial variation and do not provide accuracy in small scale which are necessary to infer fibre orientation and other defect types. These conclusions have been presented in International Conference on Manufacturing Research ICMR2019 [204].

The second approach in obtaining the library is through experimental data gathering on specimen components, which provides realistic data at the expense of data acquisition effort. Collins Aerospace operates an OEM facility with access to multiple specimen parts, mitigating the challenges of experimental data collection.

Having obtained the library of profiles provides an opportunity for a simple data analysis to identify and visualise fibre orientation. Kernel Density Estimation is used to present the data in a manner that is unambiguous for a human operator and allows for a secondary automated indication of the fibre orientation through minimisation of the Mean Square Error. These results have been presented in the Sensors Journal [18].

This method has been validated using experimental and synthetically generated samples corrupted by Gaussian Noise. For the experimental data, the approach of minimum MSE provides identification with 100% accuracy, however this deteriorates to 93% on the synthetics data for noise levels of $\sigma = 0.1$ to 0.4 and 87% for $\sigma = 0.6$. These synthetic data provides a more diverse representation of possible experimental results. Finally, it is concluded that the discrimination between 0/90/0/90 and 0/90/90/0 is more robust compared to the third intermediate class of 0/90/+45/-45, however this has limited practical implication as this lay-up is not commonly used in aerospace structures, but introduced here as an intermediate orientation.

Finally, a synthetic data set for double thickness lay up is created to demonstrate the ability of the proposed technique to identify fibre orientations and shows an accuracy of 87% at corruption levels of $\sigma = 0.1$ which impressive considering the specimen profiles consist of responses of thin panels.

Chapter 5

Delamination Detection Through Transient Thermal Analysis

As discussed in Chapter 3, one-dimensional thermal conduction profiles can be used to infer defects which cause measurable reductions in in the direction of transmission. However, for defects where the thermal conduction differences in the transmission direction are negligible, such as for inter ply delamination, a modified approach is required. Chapter 4 demonstrates that variations between ply profiles in CFRP laminates can be inferred through the analysis of transient thermal conduction profiles created by heating smaller areas of the sample when compared to the temperature capture area.

Delamination detection has more strict requirements in spatial resolution compared to that of material property detection such as fibre orientation studied previously. Within the V2500 fan cowl, all defects of above 40 mm must be detected by the NDI method [16]. Consequently, interpreting the mean temperature profile across the complete 64×64 sensor array (with dimensions of 300×300 mm) will not provide adequate resolution to infer delaminations.

To mitigate these limitations this chapter combines the temperature profiles from individual probes capturing conduction through the structure (Chapter 3) and the lateral thermal conduction which was utilised to detect fibre orientation (Chapter 4). The proposed approach provides indications of delamination

within a 2 ply CFRP laminate through data analysis and Machine Learning and preliminary results have been presented in the Sensors journal [19].

5.1 Experimental Set up

A sample 300×300 mm panel was manufactured at Collins Aerospace MRO facility (Panel D8) with biaxial 0/90/0/90 two ply lay up consisting of 5 harness pre-impregnated laminate ply, with density 1589 kg m^{-3} . A delamination of 40 mm^2 was artificially introduced between the ply boundary at 55 mm from the top edge and right hand edge of sample. This is achieved through the addition of two PTFE square sheets, of $40 \times 40 \text{ mm}$ in the x and y axis and a thickness of 0.01 mm in the z axis, between the ply laminates during the lay up process while the fabrication of the sample. The D8 panel construction is illustrated in Figure 5.1.

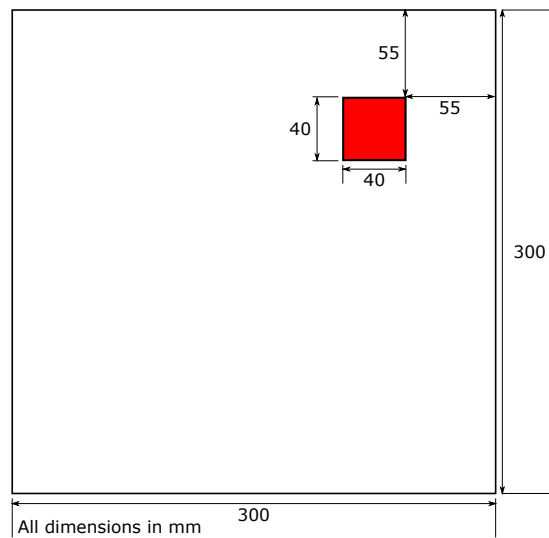


Figure 5.1: Delaminations locations shown in red for sample panel D8.

The NDI process does not only require the ability to detect the presence of a defect but also to provide the location of a defect within the sample under inspection; i.e. the location of the probes that detect the defect must be known. The tool developed in Chapter 3 used throughout the thesis provides an even spacing between temperature sensors and consequently its use is appropriate to

determine the delamination location. Furthermore, the delamination are shallow defects and consequently do not extrapolate clearly when these are directly on the heat transmission path, however, as in the case of fibre orientation, lateral conduction makes them more pronounced. The further away the temperature probes are from the heat source - on the x or y direction - the stronger the temperature profile variations and hence easier to detect. However, as the distance between the defect and heat source increases significantly beyond the point where enough heat is conducted, these signatures become less obvious, hence loosing the ability to detect (the distance effect is discussed in subsequent sections).

To quantify these effects and the ability of the proposed technique to identify delamination defects, the sensing surface is placed on the top of the sample panel, while the heater mat is moved across the bottom surface. This sliding of the heat source across the delamination defect maximises the ability of the proposed algorithms to detect the defects, however, it has practical implications; i.e. it requires multiple heat cycles to be executed, which is time consuming. These practical implications are addressed in Chapter 3 where an alternative tool operation is discussed.

Two sets of experiments are conducted where the sensing surface is either placed directly above the sample (RTD Location 1) and a second set where the sensing surface is shifted to upwards and to the left by 18.75 mm (RTD Location 2) as shown in Figure 5.2 (a) and (c), respectively. These two sets were selected because of the reports in the literature that variations between homogeneous composite regions and defect areas are at their greatest when comparing the centre of the defect and surrounding region [205, 206]. This is justified considering that the heat flux, immediately present at the boundaries of the delaminations, spreads inwards towards the centre point of the delamination [207]. The RTD Location 1 has temperature probes 46, 47, 54 and 55 on the border of the delamination defect, situated 1.25 mm within the delamination edges, both vertical and horizontal and provides temperature profiles for the outer area of the delamination. The RTD Location 2 has only one temperature probe (probe 47) directly over and in the centre of the delamination.

The two RTD locations necessitates different sliding patterns for the heat source. In the first pattern, the heater mat is initially placed on the edge of the panel (Heater Mat Location 1) and shifted by 37.5 mm steps as shown in Figure 5.2 (a) and (c) resulting in Heater Mat Locations 1-5. A second shifting pattern is acquired to ensure that the centre of the heater mat aligns with the edge of the delamination resulting in Locations 6-10 and 11-15 for the two RTD locations Figure 5.2 (b) and (d) respectively. For Heater Mat Locations 6-10 the heater mat is shifted downwards and to the right by 18.75 mm, while for locations 11-15 the same offset it is used but shifted upwards and to the right.

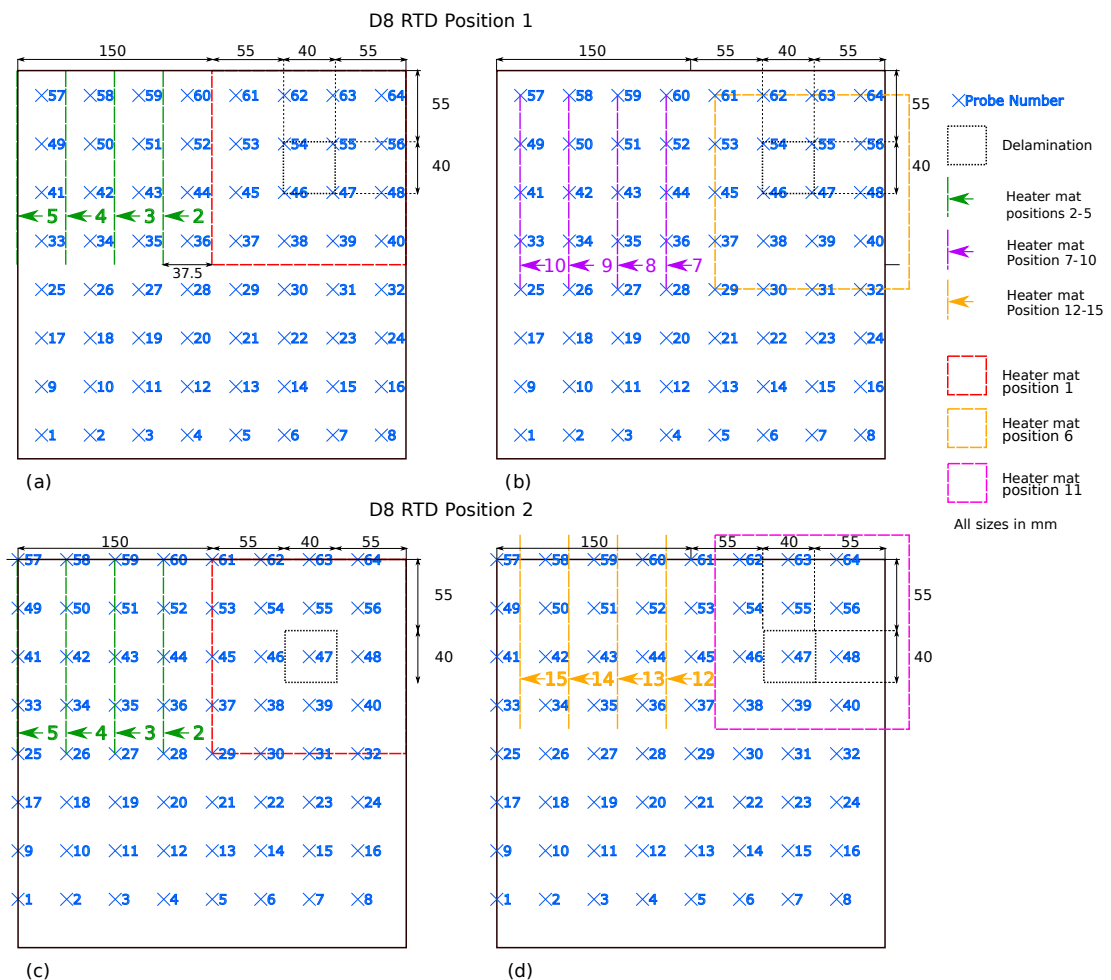


Figure 5.2: Heater mat locations 1-10 for RTD array tool location 1 and 2 for sample D8.

array tool and heat mat locations are known, the introduction of a heat profile to generate temperature against time profiles within the samples is required. Maintaining the maximum 80°C temperature used within the oil drying cycle, a

step heating profile was created for the heater mat (Table 5.1). The temperature against time profile can be seen in Figure 5.3, starting at an ambient temperature for 20 s to ensure no significant deviations from the temperature within the recording environment are present, as this would indicate that the tool has not cooled and is not ready for a cycle. Following the ambient temperature step, there is a 140 second ramp to 80°C at a rate of 0.4°C/s. When 80 °C is reached, it is maintained at this temperature for 160 s in a dwell period. Post the dwell period, the heater mat is allowed to cool to ambient temperature without external cooling for 90 s.

Table 5.1: Step heating profile for heater mat.

Period	Target Temp (°C)	Temperature change rate (°C/s)	Time period (s)
Ambient	Ambient	0	20
Ramp	80	0.4	140
Dwell	80	0	160
Cool	Ambient	-0.1	90

The experimental procedure resulted in 20 RTD and Heater Mat Location combinations and each experiment was repeated 10 times resulting in 200 distinct heat cycles and 12,800 temperature time series.

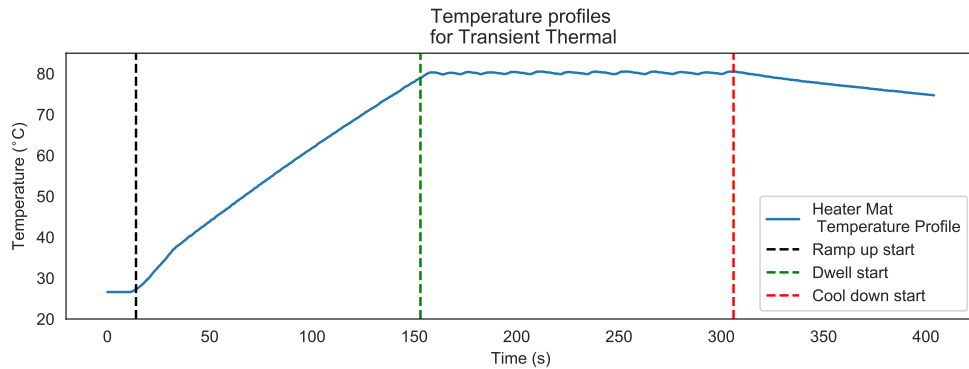


Figure 5.3: Thermal profile for heater mat and step heating profile.

5.2 Methodology

5.2.1 Data Exploration

Given that the temporal and spatial nature of thermal conduction, it is expected that different panel regions will result in variation in the temperature profiles which depends on their distance from the heat source. Considering this observation, temperature probes can be logically grouped based on their x -axis and y -axis distance from the centre of the heater mat; the notation ‘x_heat_dist’ and ‘y_heat_dist’ is used in the remainder of this chapter and signify distance in mm. The experiments conducted in this study only consider heat source movement in 1 dimension (x), while the y -axis distance is invariant for all experiments and results and consequently is not discussed in the rest of the chapter.

Furthermore, the structure below each RTD probe can belong to one of the four following condition:

- 0: Homogeneous Area (HA) under the probe and clear path to the centre of heater mat (Figure 5.4(a)).
- 1: Delamination Edge (DE), the probe located at the edge of the delamination (Figure 5.4(b)).
- 2: Delamination Centre (DC), probe located at the centre of delamination (Figure 5.4(c)).
- 3: Homogeneous Area/Delamination (HA/D) in the thermal conduction path; i.e. there exists a delamination between the probe and the centre of the heater mat (Figure 5.4(d)).

Following the ‘x_heat_dist’ grouping and condition for each probe the temperature profiles are visualised for various distances. Figure 5.5, shows the temperature profile along with the 95% confidence interval for all probe and heater mat combinations, which have 0, 18.75 and 37.5 mm distance from the centre of the heater mat. Note that the 0 and 18.75 mm distances do not contain the condition

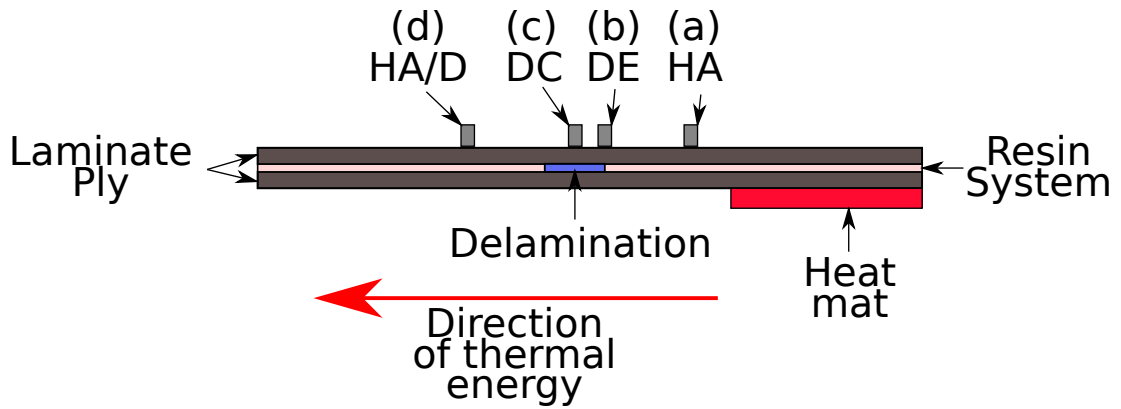


Figure 5.4: Structural conditions of probes in relation to a delamination and the centre of a heat source. (a) Homogeneous Area probe (b) Delamination Edge Probe (c) Delamination Centre Probe (d) Homogeneous Area/Delamination probe.

HA/D since this can not occur due to dimensions of the delamination. From these profiles, there are no consistent distinguishable features to identify the conditions (0-3). This supports the earlier observation that there is no clear differentiation between homogeneous regions and delamination under a transmissive conduction.

Figure 5.6 shows the temperature profiles for probes with distance 56.25 and 75 mm from the centre of the heater mat. For this increased distances, the lateral conduction effects become increasingly prominent because the thermal conduction to the surrounding area of the heater mat gets amplified owing higher temperature differential. This creates a clear differentiation between homogeneous areas (HA and HA/D) and areas with delamination areas (DC, DE). Interestingly, for the 75 mm distance there is a clear difference between HA and HA/D. This was not visible for the 56.25 mm distance most likely because the amount of heat propagated to the probe location is dominated by transmissive conduction rather than lateral conduction (which is the case for 75 mm due to its location on the edge of the heater mat).

Finally, temperature profiles for 93.75 and 112.5 mm are shown in Figure 5.7. For these locations, the probes are entirely outside the heater mat area and the resultant temperature versus time recorded is attributed purely to lateral thermal conduction as the sample tries to reach thermal equilibrium. However, there are no clear distinguishable features to discriminate between conditions.

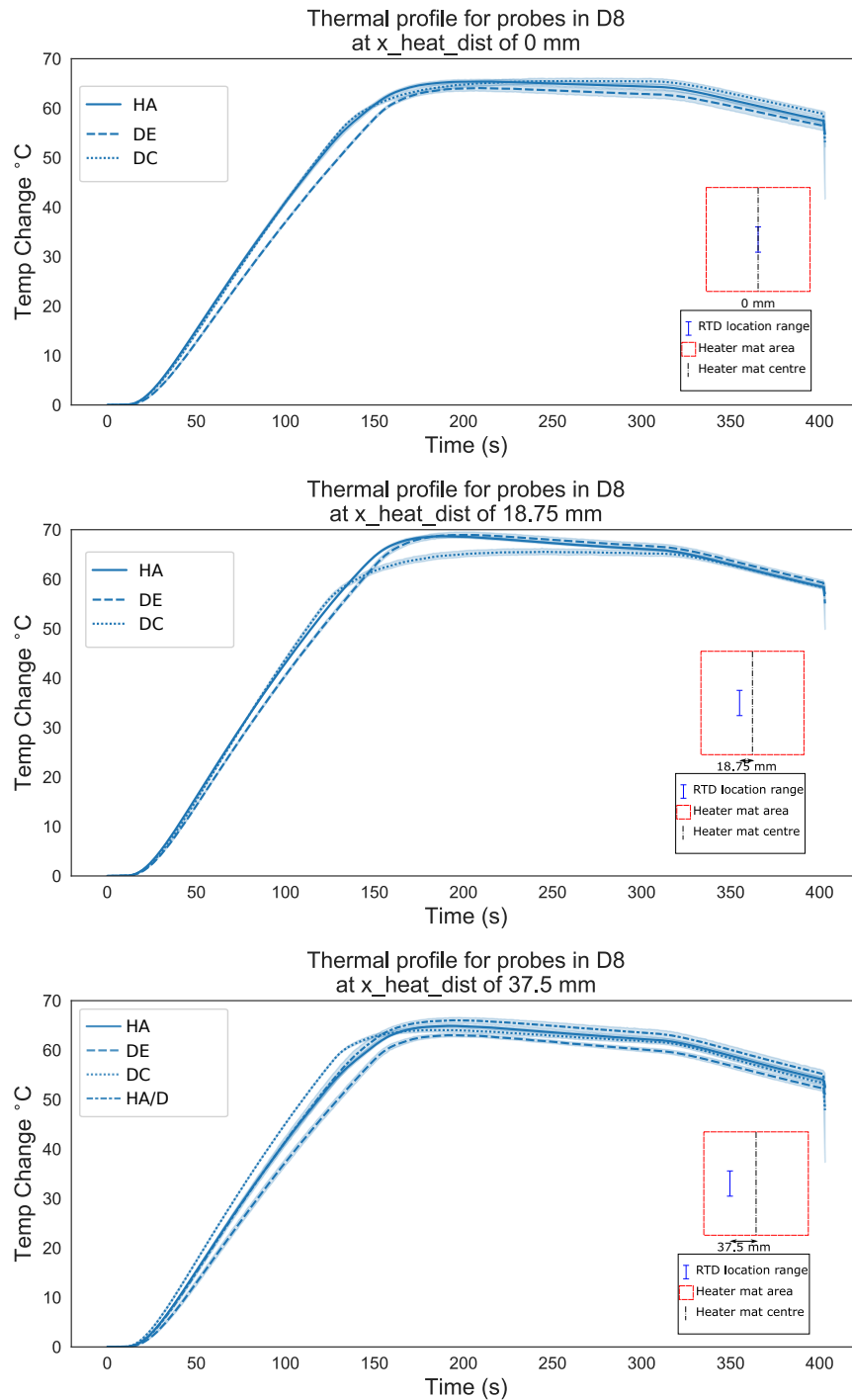


Figure 5.5: Thermal profile for all probes over the centre of the heated area for sample D8 at x_heat_dist of 0, 18.75 and 37.5 mm (top, middle, bottom respectively).

For distances greater than 112.5 mm, the temperature profiles do not rise significantly above the ambient temperature and consequently do not generate enough variation to provide discrimination (Appendix B).

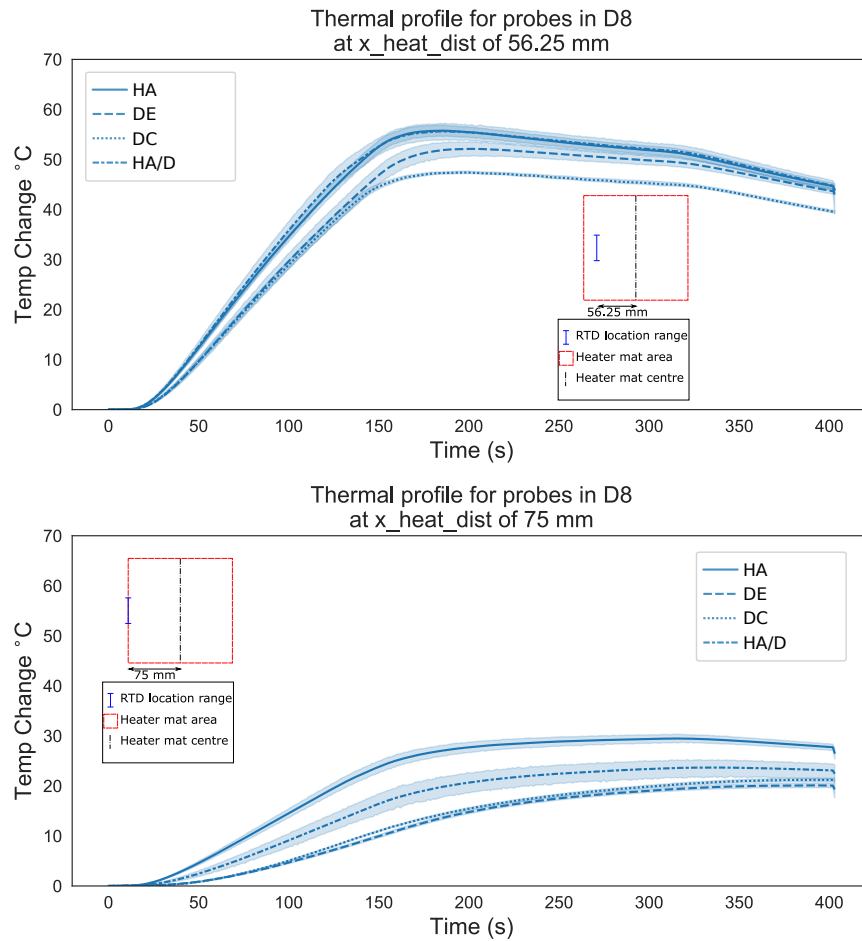


Figure 5.6: Thermal profile for probes in D8 at x_heat_dist of 56.25 and 75 mm (top and bottom respectively).

5.2.2 Pre-processing

Since the experiments conducted concentrate on the top half of the 300×300 mm panel, this results in 32 probe locations of interest for 20 distinct heater mat and RTD location combination with 10 repetitions of each experiment. This would result in 6,400 distinct temperature profiles. However, some of these were discarded either because the RTD sensors were damaged, recorded erroneous data or because there is not enough signal variation to provide meaningful information to the classifier. This is supported by the visualisation shown in the previous section, Figure 5.7 and in particular any probes with 'x_heat_dist' greater than 93.75mm are discarded.

The resultant condition distribution across all the probes is shown in Fig-

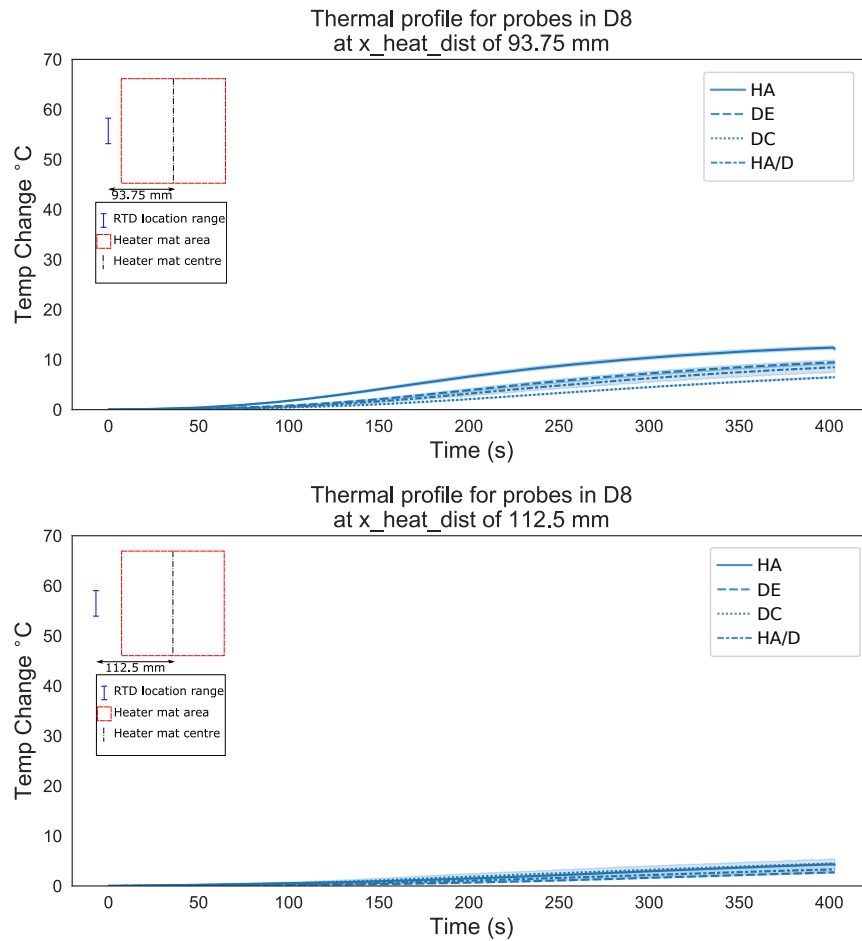


Figure 5.7: Thermal profile for probes in D8 at x_heat_dist of 93.75 and 112.5 mm (top and bottom respectively).

Figure 5.8. As expected, the majority of conditions are Homogeneous (HA) and Homogeneous with a delamination in the path (HA/D) with 3,291 and 225 events, respectively. The delamination observations (both Delamination Edge and Centre) are 238 and 70, respectively. Given there is a high imbalance between conditions, and there is no real benefit from the inspection point of view in the distinction between HA vs HA/D and DE vs DC, it was decided to merge these pairs of classes together resulting in two core conditions; namely ‘Delamination’ and ‘No Delamination’ with distribution, 308 and 3,516, respectively as shown in Figure 5.9. Furthermore, the distribution of ‘x_heat_dist’ in the dataset is shown in Figure 5.10. Any classifiers trained need to be evaluated in a balanced dataset with equal representation of classes and ‘x_heat_dist’. To achieve this initially the total dataset is split into 2 groups for ‘No Delamination’ and ‘Delamination’.

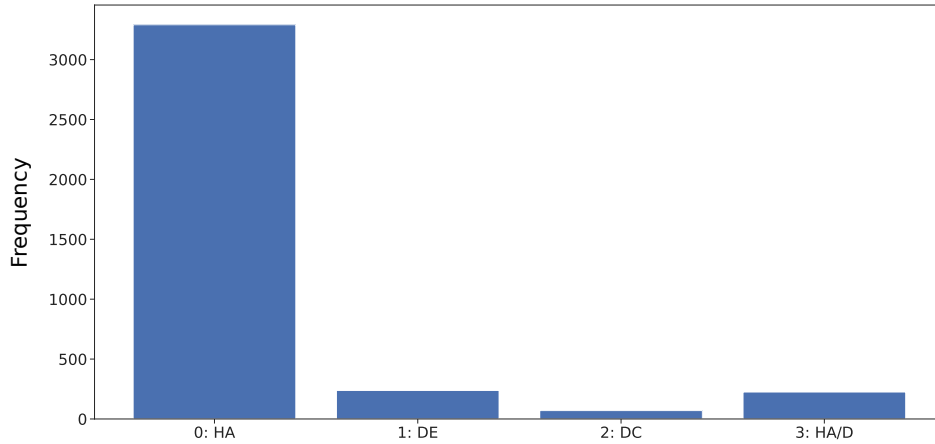


Figure 5.8: Condition distribution within sample D8 data set for HA, DE, DC and HA/D.

For each of group downsampling is performed to ensure that each group contains equal representation of ‘x_heat_dist’ observations (i.e. count all observation for each ‘x_heat_dist’ in each group and obtain the minimum count, then randomly sample for each class and for each ‘x_heat_dist’ equal number of samples). The resultant dataset contains equal number of samples for each ‘x_heat_dist’ and conditions. The final dataset is randomly split to 60% for training and valida-

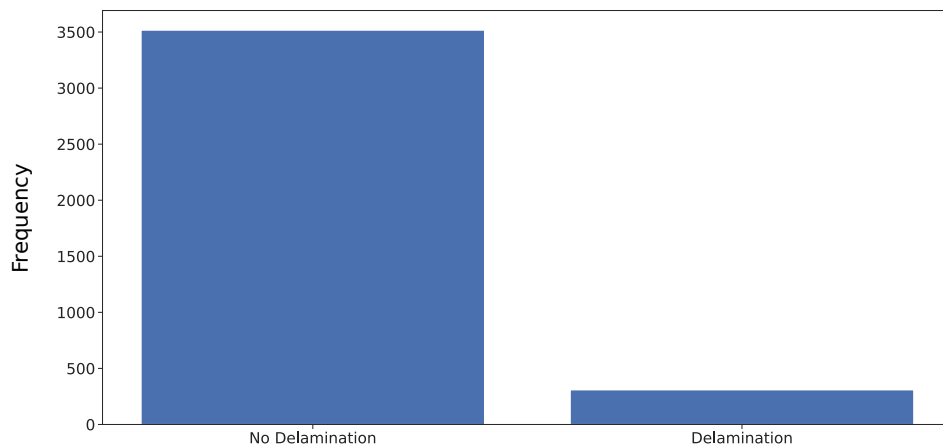


Figure 5.9: Condition distribution within sample D8 data set for No Delamination and Delamination.

tion and 40% for testing. Table 5.2 shows the number of observation for each

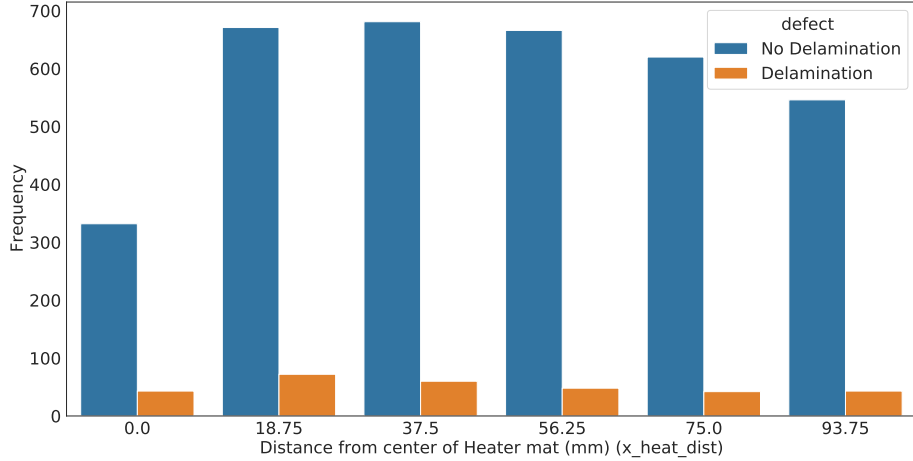


Figure 5.10: All conditions distribution within sample D8 data set for x_heat_dist 0-93.75 mm.

‘x_heat_dist’, each condition and total for each split and the complete dataset.

It is important to note that the 40% test dataset is a keep-out set and never been used for hyperparameter tuning and optimisation, while the 60% training and validation dataset is utilised for k -fold cross-validation. A typical model training/validation cycle consists of shuffling the dataset and splitting it into k folds (where $k = 10$ in this Chapter, unless otherwise stated). Then the model is trained on $k - 1$ folds (compartments) and validated on the remaining fold. The process is repeated k times and the average validation performance is computed. This k -fold cross-validation process is illustrated in Figure 5.11.

	Observations per ‘x_heat_dist’	Observations per Condition	Total Observations
Training & Validation (60%)	50	150	300
Testing (40%)	34	102	204
Complete Dataset	84	252	504

Table 5.2: Number of observation in the training/validation and testing sets.

5.2.3 Feature Extraction

The machine learning models developed in this Chapter aim to classify each of the temperature profiles to one of the two conditions ‘No Delamination’ or ‘Delamination’. To achieve this features must be engineered which will serve as input

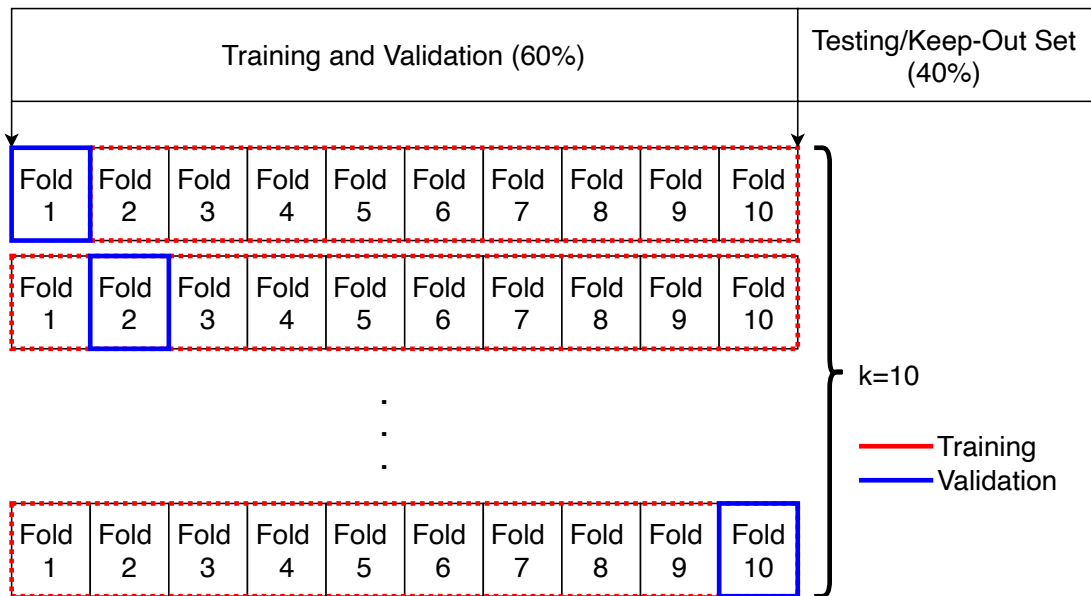


Figure 5.11: Example of k -fold cross-validation with $k = 10$.

to the models. Two approaches are adopted to engineer features: 1) Knowledge Based Feature Engineering and 2) Generic Time Series Feature Extraction. Both approaches are applied across the multiple repetitions of temperature profiles captured.

5.2.3.1 Knowledge Based Feature Engineering

Visualisations of the temperature profiles for probes with various distances from the centre of the heater mat, reveal differences that occur at either the ramp up or dwell phases. The following list of features are extracted for all temperature profiles for both ramp up and dwell phases resulting in the following 18 features:

1. Mean
2. Median
3. Minimum
4. Maximum
5. Standard Deviation
6. Skewness

7. Kurtosis
8. Compute the best fit line and obtain:
 - (a) Rate
 - (b) Intercept

A 19th feature is computed, which is the mean temperature difference between the probe and panel median temperature at every point in time.

5.2.3.2 Generic Time Series Feature Extraction

A number of time series extraction Python software libraries are available, such as FATS [208], CESIUM [209], TSFRESH [210] and TSFEL [211]. These libraries extract generic time series features from the temporal, statistic and spectral domains. The features extracted are similar and the libraries differ in terms of their implementation and the software features they provide, for instance, CESIUM includes a web front end to increase user friendliness, while TSFEL provides estimates on the computation time it requires to compute the features, TSFRESH provides a feature filtering through hypothesis testing. Overall, there is no significant difference in terms of the feature set computed between these libraries and in this study TSFRESH was selected for subsequent characterisation. In particular, the TSFRESH library extracts 111 features which can be grouped in 3 categories:

- Summary statistics – Example features: minimum, maximum, standard deviation, skewness, kurtosis
- Characteristics of sample distribution – Example features: Absolute Energy, Binned Entropy, Number of points above Median, and etc.
- Features derived from observed dynamics – Example features: ARIMA Coefficients, Continuous Wavelet Coefficients, Fast Fourier Transform Coefficients, and etc.

Each of these feature groups may consist of coefficients; for instance, Fast Fourier Transform used 100 frequency bins and each frequency bin has a real, imaginary magnitude and angle, resulting to 400 total features.

Furthermore, the features were extracted separately for the ramp up period and dwell as these phases contain distinct signatures as evident during data visualisation. The resultant total number of features for both periods is 1,118.

5.2.4 Feature Selection

One of the critical steps in the success of the machine learning model is selecting features which are appropriate for the classification task. High dimensional inputs, lead to a well known problem of ‘Curse of Dimensionality’ [212]. In the context of Machine Learning, as the dimensions of the input space increases, so does the volume of the space leading to data being sparsely distributed in the volume. As a result, models tend to overfit the training dataset and perform poorly on validation and testing. A variety of approaches exist to mitigate against high dimensionality categorised as shown in Figure 5.12.

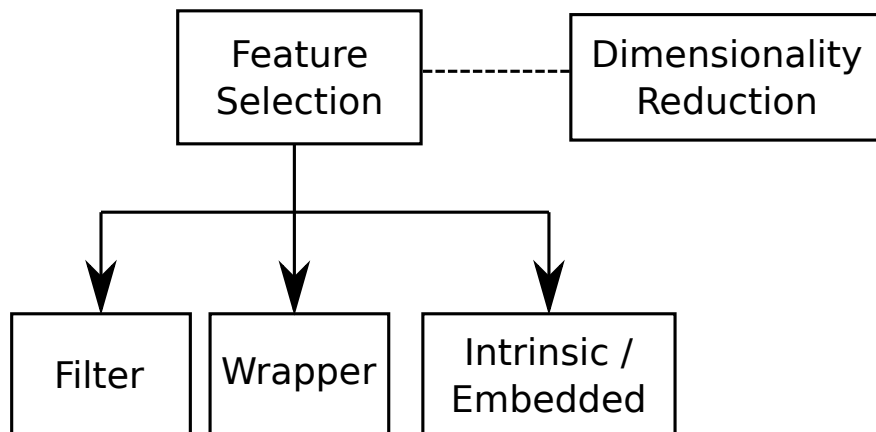


Figure 5.12: Feature Selection overview.

One approach is to reduce the space dimensions by re-projecting the sample data to a lower dimensional space. For instance, Principle Component Analysis [213] and variants, transforms the original feature space to an equal number of orthogonal dimensions (Principle Components) and subsequently utilises a subset of the Principle Components to use on the Machine Learning Model (the subset

is selected based on the percentage of variance maintained in the original feature space). Other approaches to dimensionality reduction exist, such as Non-negative matrix factorization [213] and Neural Network Autoencoders, among others.

An alternative approach to reduce the number of dimensions is through feature selection (also known as variable selection). These approaches do not transform or reproject the original feature space but rather select a subset of the features. A number of well-established feature selection approaches have been developed in the literature which can be categorised as:

- **Filter:** These methods rank features and their association with the output label, based on a score derived from a particular metric. Subsequently, the model can consider only a subset of all features. Common metrics for scoring features are information gain, correlation coefficient, χ^2 statistic, ANOVA F-value, among others. Given that the output of the model is a categorical variable, in this chapter, Mutual Information is considered which for an input feature X and output Y is given by:

$$\mathbb{I}(X; Y) = \sum_x \sum_y \log \frac{p(x, y)}{p(x) \cdot p(y)} \quad (5.1)$$

The mutual information metric yields a value between 0 and 1 where 0 indicates independence between the feature X and the output Y , while higher values of \mathbb{I} indicate higher dependence.

Ideally, the features selected to train a model should have high dependence with the output Y , but low dependence between each other. The drawback of filter methods is that it does not consider the relationship between input features and any redundancy they contain. For instance consider two features X and $2 \cdot X$, these score highly when filter methods are utilised but are highly correlated with each other. The filter methods will select both features as they do not examine the relationship between features. One of the positives of filter approaches is that they are relatively inexpensive to compute as it requires to derive a single score per feature.

- **Wrapper:** The wrapper method is an iterative search procedure which trains and evaluates a model (estimator) with a subset of candidate features and then selects the feature set that yielded the best performance. There are two approaches to define each wrapper iteration: 1) Forward Selection or 2) Backward Elimination. Forward Selection starts with an empty set of features and progressively adds features to the candidate list. If the added features improve performance, these are kept otherwise they are removed. Backward Elimination strategy starts with a full set of features and progressively removes features that do not lower the performance. Considering that there is an exponential number of feature subsets, this will require a high number of training/evaluation cycles which is computationally expensive. When considering a high number of features n , all the ways to select k features is the combination $\binom{n}{k}$. In an exhaustive search scenario that requires search for for all subset cardinalities, i.e. for $k = 1 \rightarrow n$. This leads to:

$$N_{iterations} = \sum_{k=1}^n \binom{n}{k} \quad (5.2)$$

For $n = 1,000$ features, this will yield to $1.071e+301$ iterations which is impossible to compute. For that reason, usually wrapper implementations adopt a ‘greedy’ search algorithm which does not reconsider every selection as it moves through the iterations. Such an approach will lead to:

$$N_{iterations} = \sum_{k=1}^n \binom{n-k+1}{1} = n \cdot \binom{n}{1} = n^2 \quad (5.3)$$

For a similar scenario where $n = 1,000$ features, this will lead to $1e+6$ estimators to train, which is significantly lower but still computationally expensive.

One of the key decisions when implementing wrapper feature selection methods is the choice of the model (estimator) which is used to evaluate performance. Choosing a computationally intensive estimator will lead to high computational cost on top of the complexity due to the number of iterations.

Furthermore, the technique does not consider hyperparameter tuning, which can yield further performance improvements.

- **Intrinsic/Embedded:** In these techniques, the feature selection is included as part of the learning algorithm. This is typically available in decision tree algorithms such as Random Forests [214] or Extremely Randomized Trees [215]. The disadvantage of these approaches is that these are model dependent and the selected features may not have the highest predictive power.

There are of course combination of these approaches. For instance use of the filter method to perform initial feature reduction followed by wrapper approaches to determine the most appropriate features. Another hybrid approach is Recursive Feature Elimination, which trains an Intrinsic/Embedded model first with all features and reduces the features in groups following a wrapper approach.

5.3 Machine Learning Models

5.3.1 Support Vector Machine

An algorithm suited to binary classification of data points is that of a Support Vector Machine (SVM) algorithm [216, 217]. This is achieved through the use of hyperplanes to separate data points. The SVM algorithm will look for a hyperplane that exists between different classifications, within an n dimensional space where n is equal to the number of features used to train the algorithm [218, 219, 220]. These hyperplanes in turn act as decision boundaries to classify the data points. Controlling the degree of error that is permissible in classification of data points when identifying hyperplanes for SVM algorithms is achieved through modification of a ‘C’ value. The ‘C’ value provides a soft margin, by increasing the ‘C’ value a higher number of incorrect classifications by the algorithm are permitted in exchange for an overall better performing decision boundary. Figure 5.13 provides an example of this for a two feature, 2 dimensional classification hyperplane.

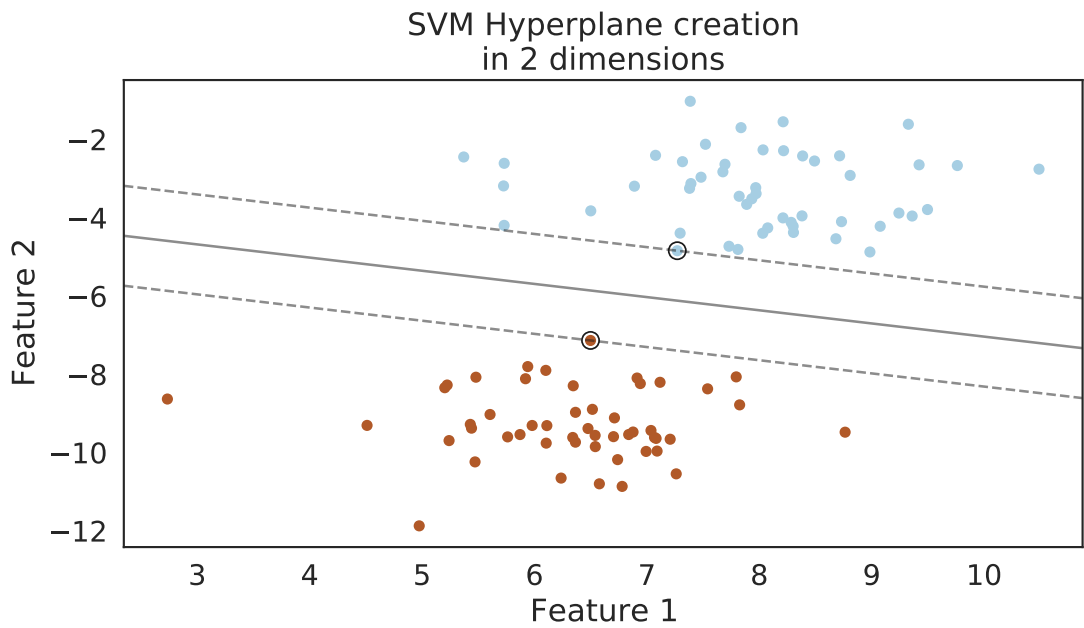


Figure 5.13: Example of an SVM hyperplane between two features in a 2 dimensional space.

Although the SVM algorithm classifies data points based within an n dimensional space it is still in essence a linear boundary used to classify points. As such SVM algorithms are susceptible to reduced performance when used in conjunction with noisy data sets, such as those captured from experimental methods [221].

One method used successfully to mitigate the performance issues associated with noisy datasets in SVM is through the use of a kernel trick, such as those available within the Support Vector Clustering (SVC) algorithm, this builds upon the hyperplane boundary classification method of the SVM algorithm [222]. The SVC version of the SVM algorithm also uses hyperplanes to identify boundaries for classification, and the ‘C’ value to set a soft margin, however, it can also introduce other values into the algorithm to modify the boundary in the form of new features created from transformations of the existing features via kernels. Modifying the boundary in this way allows for non-linear decision boundaries to be created. One such kernel option is Radial Basis Function (RBF), where a new feature is created based on the distance of all data points against a selected data point. The impact of these generated features on the creation of the decision boundary can be controlled by the variable ‘ γ ’. A higher ‘ γ ’ value results in a

high impact on the decision boundary profile, a lower ‘ γ ’ value results in low impact to the decision boundary profile.

5.3.2 Random Forest Classification

Random Forrest (RF) Classifiers are a machine learning algorithm consisting of multiple decision trees, the trees within the Random Forest are each trained on random sub sets of the available training data, with results averaged out across the forest. Trees within the RF consist of leafs and branches, the leafs contain samples and the branches conjunctures which leads to the next leaf. The decision tree will follow the path of conjunctures while it remains true or reaches a classification. For example, Figure 5.14 presents a decision tree for the classification of fruit, it can be seen that the conjectures are logic statements to separate samples of the leafs. Provided that the logic statements remain true, the decision tree should classify a fruit correctly as one of the 5 known fruits within the tree. However, it can be seen within the example of Figure 5.14 that a green

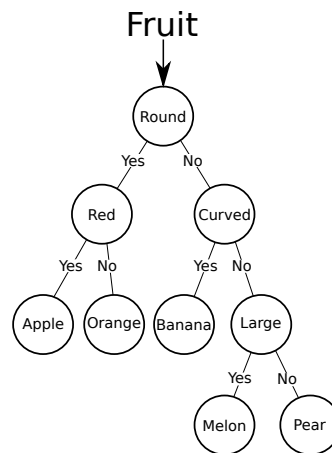


Figure 5.14: Decision Tree example for classification of one of 5 fruit types.

apple would be classified incorrectly as an orange within this particular decision tree. As the decision tree in essence follows logic statements (if true, else), discrete classification values are required, working best with Boolean classification. The number of trees within the forest can be controlled (n estimators) and in turn the maximum depth of each tree (Max Depth).

Once trained, classification is achieved through determining the majority classification of each tree within the RF, Figure 5.15 displays this visually for a RF classifier with n Trees providing an example classification of a green value over a red value. This ‘majority’ voting style of the algorithm is described as an En-

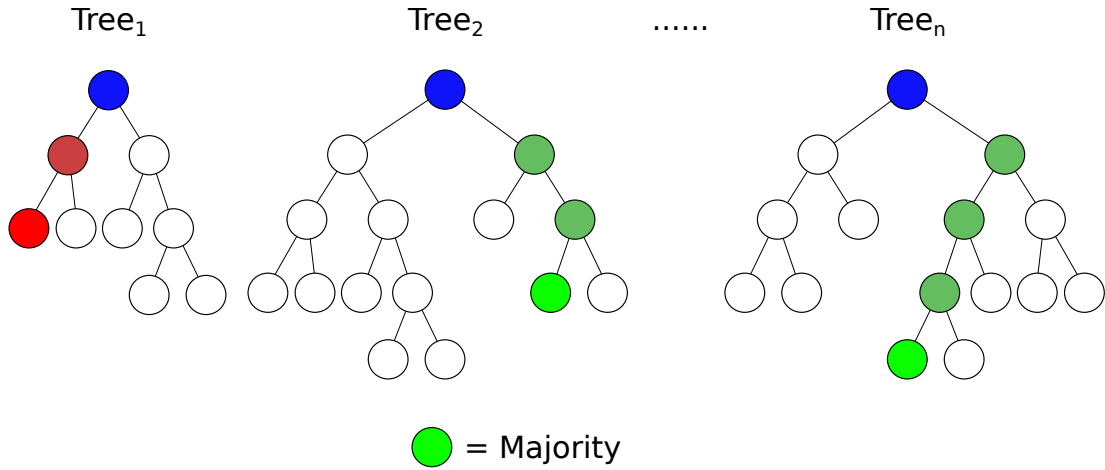


Figure 5.15: Random Forest Classifier of n Trees.

semble Learning classifier [223]. By controlling the portion size of data available within the subsets (Max Features), the averaging of these results within the forest helps in limiting overfitting of the training data, and improves accuracy [224].

As shown in Chapter 2 the use of NN has also shown success in the classification of defects. However Chapter 2 also highlights the requirement for certification of inspection methods within Aerospace, and as such this thesis will concentrate on the use of RF and SVM methods due to their transparency.

5.4 Application of ML

Utilising the complete dataset, two machine learning models were built based on Support Vector Machines (SVM) and Random Forest (RF) to test the effectiveness of Knowledge Based Feature Engineering and the Generic Time Series Feature Extraction described in Sections 5.2.3.1 and 5.2.3.2 respectively. The complete methodology is demonstrated in Figure 5.16 which shows the the complete pipeline for dataset creation, feature extraction and selection, scaling, training/validation and testing and hyperparameter selection.

Figure 5.16(e) highlights the use of a Standard Scaler, which is again utilised within the Application of Model. As the features obtained from feature extraction vary in units and range, large variations can result in imbalanced features. Such imbalances can lead to bias between features within a ML model. A Standard Scaler, normalises the data within each feature relative to that feature to produce unit-less data for each feature where $\mu=0$ and $\sigma=1$, providing equal balance between all features.

$$z = \frac{x - \mu}{\sigma} \quad (5.4)$$

Where z is the standardisation, μ is the mean of the training sample and σ the standard deviation of the training samples.

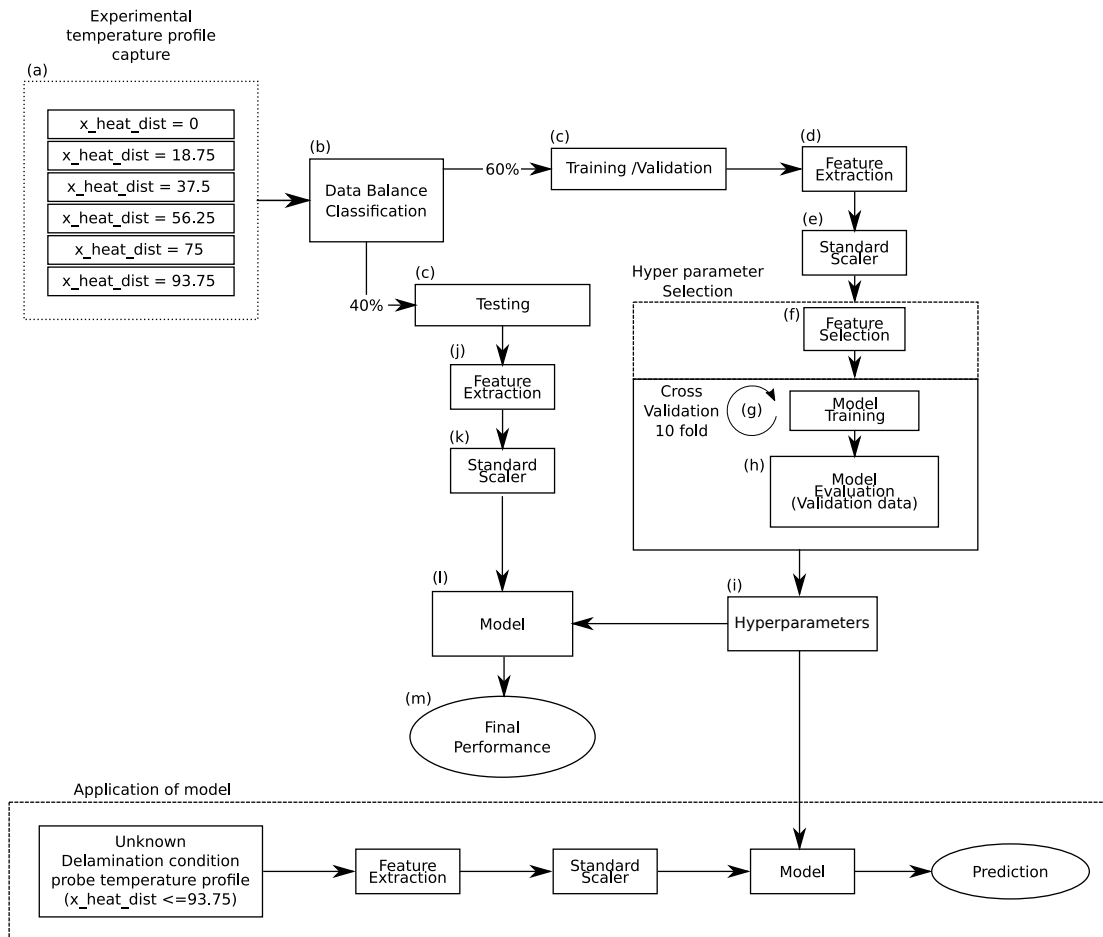


Figure 5.16: ML algorithm pipeline for training/validation and classification of unknown temperature profiles.

5.4.1 Results for Knowledge-Based Feature

Initial experiments were conducted utilising the 19 features extracted based on engineering knowledge and the visualisation performed on the temperature profiles for probes at various distances and defect types. Using the balanced dataset obtained in Section 5.2.2, Support Vector Machine and Random Forest Classifiers were trained and evaluated. To identify the most suitable hyperparameters for both models Grid Search was performed with 10-fold cross-validation to exhaustively search the parameter space. Given that the final dataset is balanced across ‘x_heat_dist’ and classes, the accuracy score was used to rank the models with different hyperparameters.

Fundamentally, the SVM classifier is a linear model separating data into classes and non-linear classifications are facilitated through the use of the kernel trick to transform the features from the original space to a nonlinear space. The most common kernel for SVM classifiers is the Radial Basis Function (RBF). Preliminary experiments where no kernel trick is used yielded low performance and consequently only SVM classifiers that utilise RBF kernels are considered in the hyperparameter search. Two main hyperparameters were considered for the SVM classifier are the regularisation parameter C and the RBF kernel coefficient γ which varied as shown in Table 5.3, resulting in 420 combinations. The resulting average validation accuracy across all 10-folds, for all C and γ combinations are shown in Figure 5.17. As γ increases from 0.05 to 0.2 there is general increase in accuracy but for values above 0.2 the performance starts to drop. The best performance is achieved for $C = 20$ and $\gamma = 0.15$ and the average accuracy across all folds is approximately 71% for both classes ‘No Delamination’ and ‘Delamination’.

Using the hyperparameters identified from the exhaustive Grid Search, a new model is trained utilising the complete training/validation dataset for performance evaluation on the keep-out test set. The normalised confusion matrix for the test set is shown in Figure 5.18. Out of all homogeneous regions, 74% of them are correctly identified by the model with 26% misclassified as delamination. When a true delamination is present, this is identified 85% of the time and

15% of the time the delamination is missed. Table 5.4 show the performance in terms of F1 score, Precision and Recall for each class individually and combined.

Parameter	Range	Step
C	1-20	1
γ	0.05-1	0.05

Table 5.3: Hyperparameters for SVM.

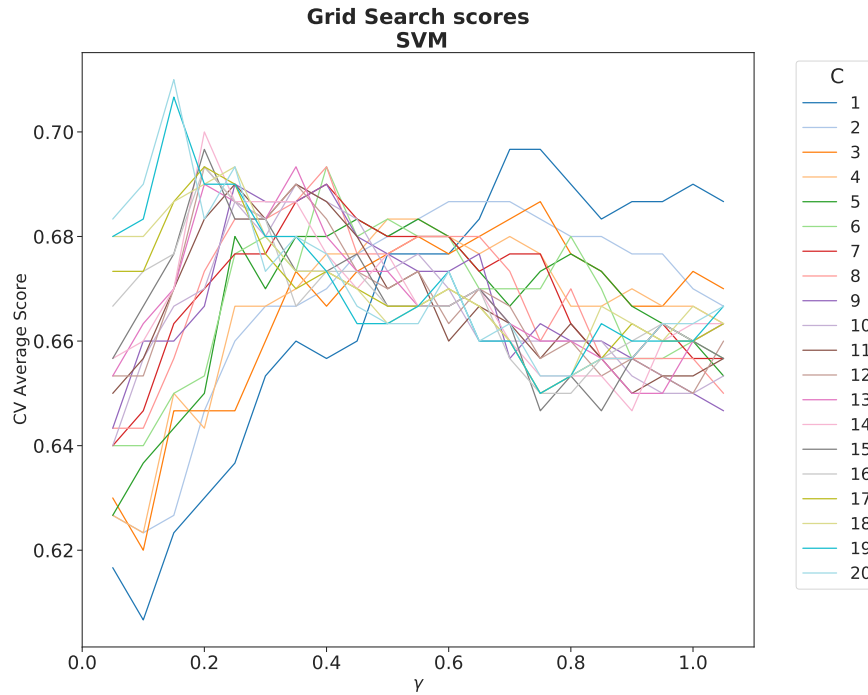


Figure 5.17: Average Cross Validation (CV) Accuracy for all combination of C and γ for sample D8 dataset.

In a similar fashion to the SVM, hyperparameter tuning was performed for the RF classifier. The hyperparameters considered are the number of trees in the forest (`n_estimators`), the maximum depth (`max_depth`) each tree is allowed to develop, and the maximum number of features (`max_features`) considered per tree. The summary of all parameters searched are shown in Table 5.5.

The parameters created 275 combinations for each of the 10 folds (2750 total fits), plotted in Figure 5.19. It can be seen that across all `max_depth` and `n_estimators`, an increase in accuracy is achieved when `max_depth` increases from 2 to 8, at which point 80% accuracy is achieved. This is maintained as `max_depth` increases to 10.

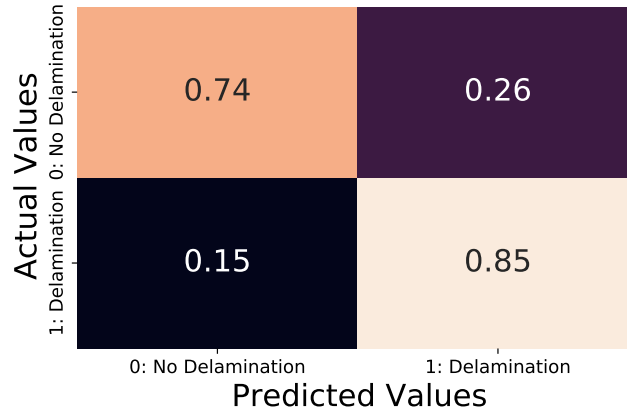


Figure 5.18: SVM Confusion Matrix for the test set for SVM algorithm utilising knowledge based features, $C=20$, $\gamma=0.15$ for sample D8 dataset.

	Precision	Recall	F1-score	Support
Delamination	0.83	0.74	0.78	102
No Delamination	0.76	0.85	0.81	102
Average (both classes)	0.79	0.79	0.79	204
Accuracy	0.79			

Table 5.4: Classification Report of test data set for SVM algorithm utilising knowledge based features, $C=20$, $\gamma=0.15$ for sample D8 dataset.

Parameter	Range	Step
n_estimators	50-1,050	50
max_depth	2-10	2
max_features	2-10	2

Table 5.5: Hyperparameters for Random Forest.

The parameters resulting in the highest accuracy are identified from the exhaustive Grid Search as $n_estimators=150$, $max_depth = 8$, and $max_features = 4$, resulting average accuracy of 80% for both classes ‘No Delamination’ and ‘Delamination’. As for the SVM, an RF model with the identified hyperparameters was trained on the complete training/validation to perform performance evaluation on the keep-out test set, resulting in the confusion matrix shown in Figure 5.20. The performance evaluation resulted in correct identification of 83% of the homogeneous regions of the sample, misclassifying 17% as delaminations. In the instance of true delaminations, a correct classification is achieved for 94%, and incorrect classifications for 6%. The overall performance in terms of F1 score, Precision and Recall and accuracy for both classifications individually and

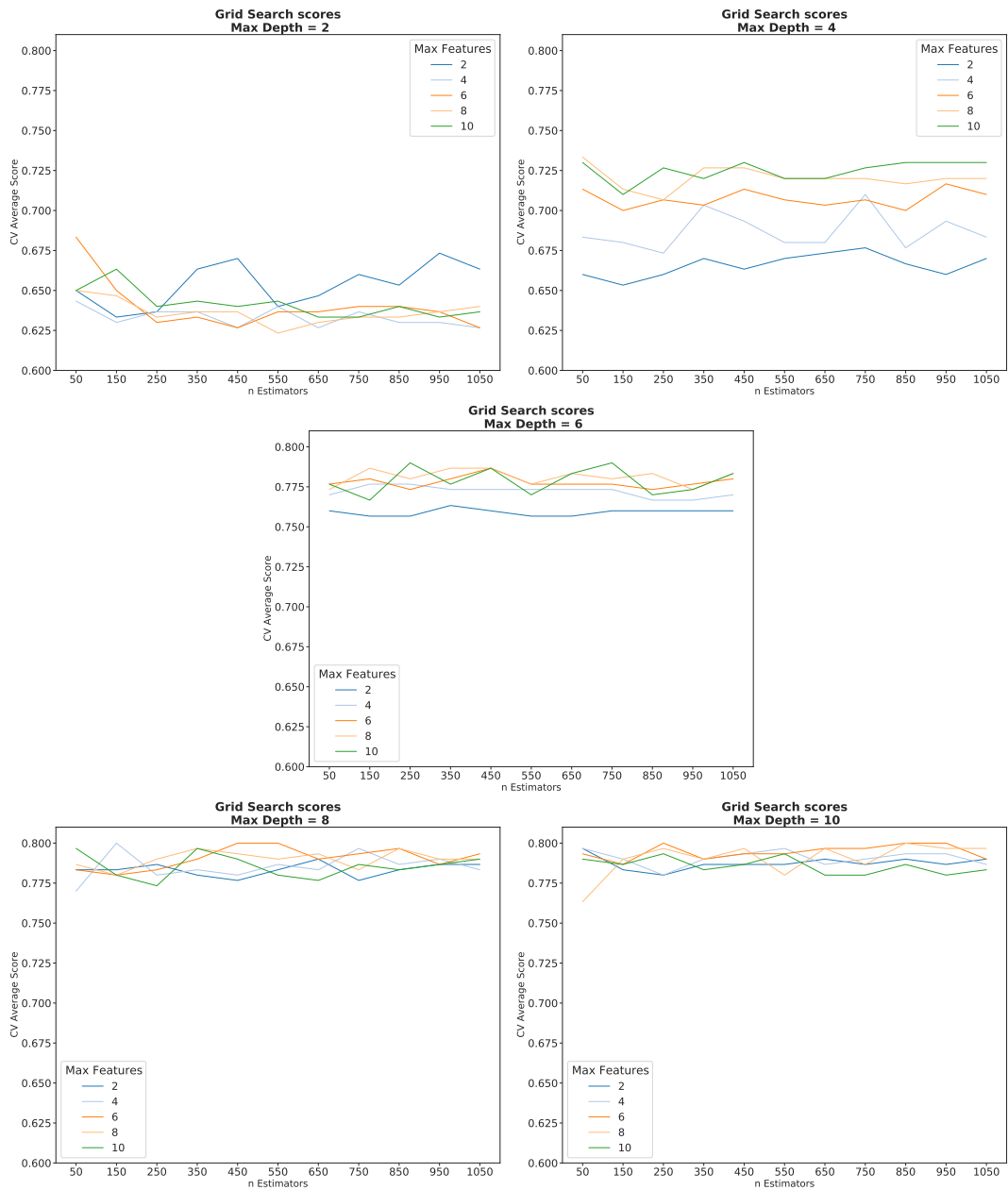


Figure 5.19: Random Forest training/validation Max Depth against Mean Test score for number of features = [50 to 1050] in Max Features = [2 to 10], for sample D8 data set.

combined is presented in the classification report in Table 5.6.

5.4.2 Results for Generic Time Series Features

The total number of Generic Time Series features extracted in Section 5.2.3.2 is 1,118. Clearly, the dimensionality of the input is too high for the size of the data

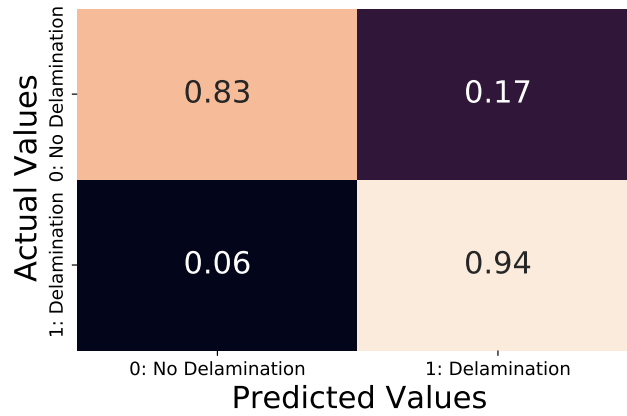


Figure 5.20: Random Forest training/validation confusion matrix for sample D8 data set, `max_depth=8`, `max_features=4`, `n_estimators=150`, for knowledge based features.

Table 5.6: Classification Report of training/validation data set for RF algorithm, `max_depth = 8`, `max_features = 4` and `n_estimators = 150`.

	Precision	Recall	F1-score	Support
Delamination	0.93	0.83	0.88	102.00
No Delamination	0.85	0.94	0.89	102.00
Average (both classes)	0.89	0.89	0.89	204.00
Accuracy	0.89			

set available and consequently, feature selection must be performed. Applying filtering feature selection with Mutual Information scoring provides the features that contain most relevant information to the output. The features are ranked as shown in Figure 5.21. In this graph, there is no obvious knee point or other peculiarities to indicate what is an appropriate number of features to select for the model training. Consequently, this can be treated as a hyperparameter and determined using the exhaustive Grid Search cross-validation.

For both SVM and RF models, the parameters searched are identical to those listed in Tables 5.3 and 5.5 with the only additional parameter added being the number of top-ranked features selected from the filter ranking utilising Mutual Information score. The number of top-ranked features is varied from 5 up to 1,118 in steps of 25. For SVM and RF, the best cross-validation accuracy against the number of selected features is shown in Figure 5.22.

For the SVM, as the number of features increases from 5 to approximately

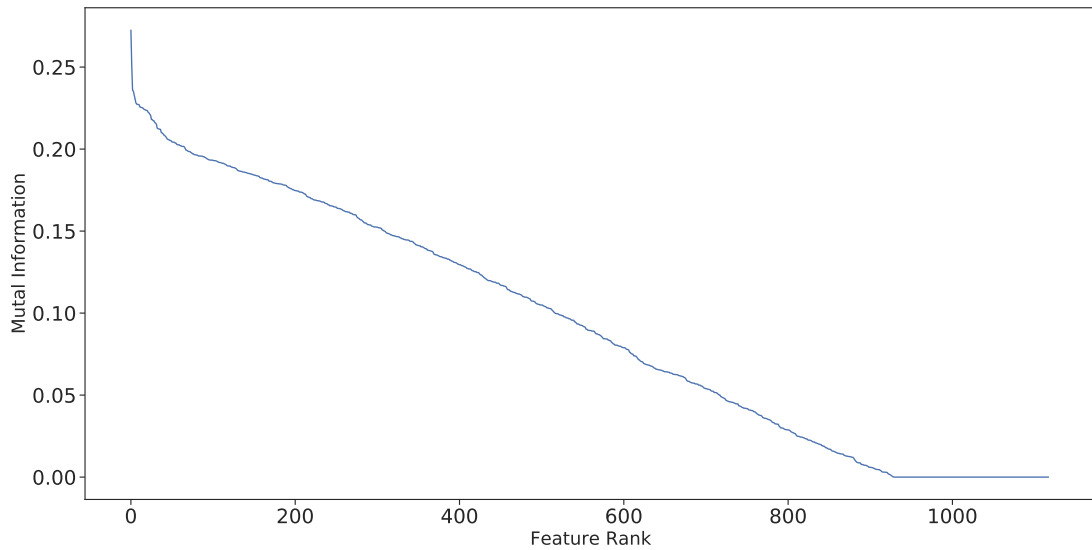


Figure 5.21: Feature Rank against Mutual Information.

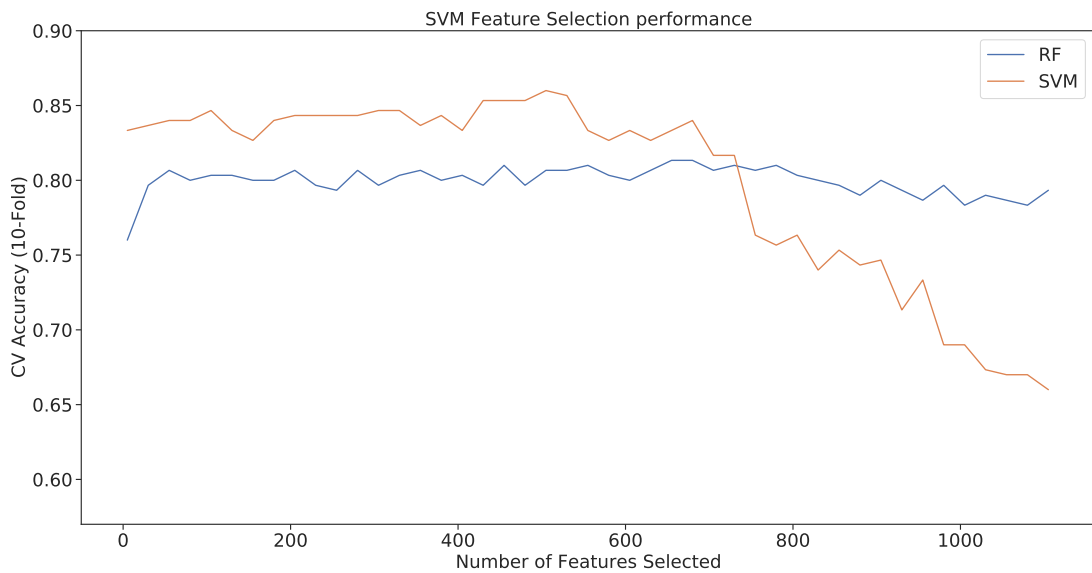


Figure 5.22: Cross-validation Accuracy for SVM and RF models against number of top-ranked features.

730, the average cross-validation accuracy fluctuates around $\tilde{84}\%$ after which the accuracy starts to decrease. This is attributed to ‘curse of dimensionality’; as the number of features increases beyond 730 the space becomes sparse leading to overfitting. The best model performance is achieved for the 505 top-ranked features with $C = 4$ and $\gamma = 0.15$ leading to an average cross-validation accuracy of 86%. The performance of this best model on keep-out test set is shown in Table 5.7 and the corresponding confusion matrix is shown in Figure 5.23. It is

notable that the performance increased to 90% using this model and the generic time series features compared to 79% obtained using the knowledge-based features in Section 5.4.1. More importantly, the missed delamination (i.e., delamination undetected) dropped from 15% to 6%.

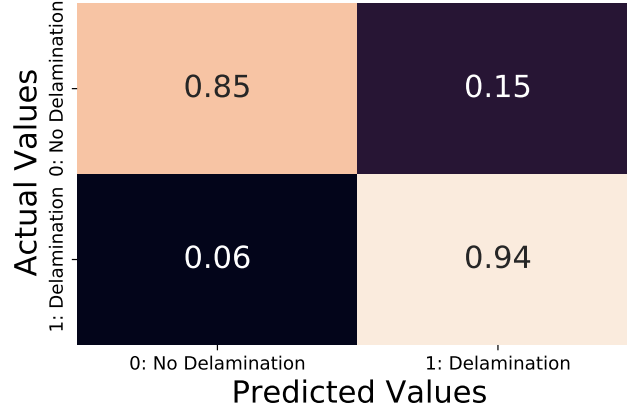


Figure 5.23: SVM test confusion matrix for sample D8 data set, 505 top-ranked features, $C=4$, $\gamma=0.15$.

Table 5.7: Classification Report of test data set for SVM algorithm, 505 top-ranked features, $C=4$, $\gamma=0.15$.

	Precision	Recall	F1-score	Support
Delamination	0.94	0.85	0.89	102.00
No Delamination	0.86	0.94	0.90	102.00
Average (both classes)	0.90	0.90	0.90	204.00
Accuracy	0.90			

The RF does not show large accuracy variations as the number of features increased, with the overall average cross-validation accuracy fluctuating around 80%. This is unlike the SVM which suffered from performance decreases due to the ‘curse of dimensionality’. This is attributed to the ability of the RF deal with large number of features by employing the bagging and max_features per estimator, making the classifier less sensitive to dimensionality bottlenecks. The only noticeable in the RF performance is between 5 and 30 top-ranked features where the performance increases from 76% to 79.6%. The best model is achieved for 655 top-ranked features with n_estimators, max_depth and max_features equal to 650, 8, and 8 respectively, with an average cross-validation accuracy of 81.3%.

The classification performance for the best model and corresponding confusion matrix are shown in Table 5.8 and Figure 5.24 (a) respectively. The classification accuracy on the keep-out test dataset is 85% which is lower than that achieved by the knowledge-based features (89%) in Section 5.4.1. However, the number of missed delaminations remains the same between the knowledge based and the generic time series features 6% with an increase false positive rate of 24% instead of 17%.

The average cross-validation accuracy of the 55 top-ranked features model is 80.6% which is not significantly lower to the best model identified by the exhaustive Grid search. The significantly lower number of features of this model will lead to lower model complexity and this motivates its evaluation in the keep-out test. The test performance and confusion matrix are shown in Table 5.9 and Figure 5.24 (b), respectively. The performance of the lower complexity model shows average accuracy of 83% instead of 85% with a slight increase in the missed delamination of 10% instead of 6%.

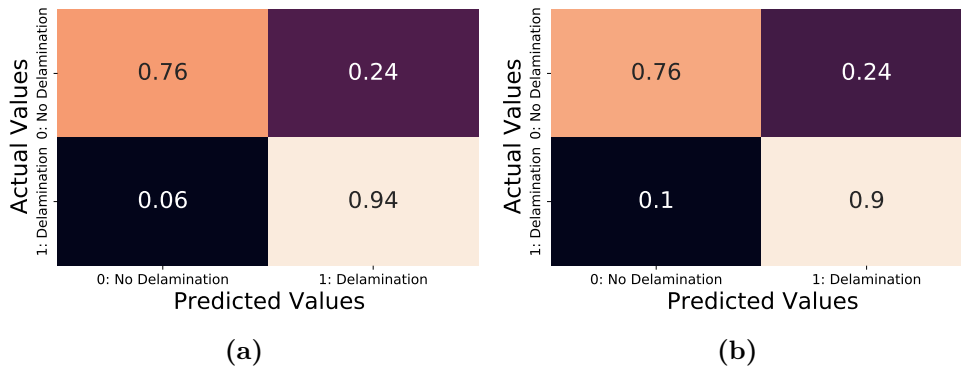


Figure 5.24: RF test confusion matrix for sample D8 data set, (a) 655 top-ranked features, $n_estimators=650$, $max_depth=8$, $max_features=8$, $n_estimators=650$, (b) 55 top-ranked features, $n_estimators=250$, $max_depth=8$, $max_features=6$.

Although there is comparable performance in classifying delaminations correctly between the RF algorithm utilising 655 top-ranked feature and that of the SVM utilising 505 top-ranked features of 94%, the SVM algorithm performs with a higher degree of accuracy overall (90% compared to 85%) and as such is the obvious choice if a single ML algorithm has to be selected.

Table 5.8: Classification Report of test data set for RF algorithm for 655 top-ranked features `n_estimators=650`, `max_depth=8`, `max_features=8`.

	Precision	Recall	F1-score	Support
Delamination	0.93	0.76	0.84	102.00
No Delamination	0.80	0.94	0.86	102.00
Average (both classes)	0.86	0.85	0.85	204.00
Accuracy	0.85			

Table 5.9: Classification Report of test data set for RF algorithm for 55 top-ranked features `n_estimators=250`, `max_depth=8`, `max_features=6`.

	Precision	Recall	F1-score	Support
Delamination	0.89	0.76	0.82	102.00
No Delamination	0.79	0.90	0.84	102.00
Average (both classes)	0.84	0.35	0.83	204.00
Accuracy	0.83			

5.5 GUI report presentation

The proposed method for delamination detection using transient thermal conduction due to structural dissipation within this chapter, provides classifications from probes within 93.75 mm of the centre of a 150×150 mm heat source. By moving the heat source in 75 mm increments through the x -axis it is possible to produce readings for each probe for both transmissive and conductive capture, twice for each. To present this data in a visual manner, the RTD tool array probes are arranged into a heat map which is representative of the probes location within the RTD tool array in the x and y axes. Utilising the SVM model developed in Section 5.4.2 (505 top ranked features, $C = 4$ and $\gamma = 0.15$). The percentage of classification of ‘Delamination’ of the 4 classification results for each probe is then calculated and the result presented within the corresponding RTD tool array probe location upon the heat map.

Figure 5.25 shows a representation of this report indicating a delamination across 5 probes, with a Gaussian filter applied within the main display section of the GUI. It can be seen here that next to the main display section, the operator is provided with two ‘View Selection’ options of ‘Inspection View’ and ‘Score View’. Figure 5.25 displays the default selection of ‘Inspection View’, which is intended

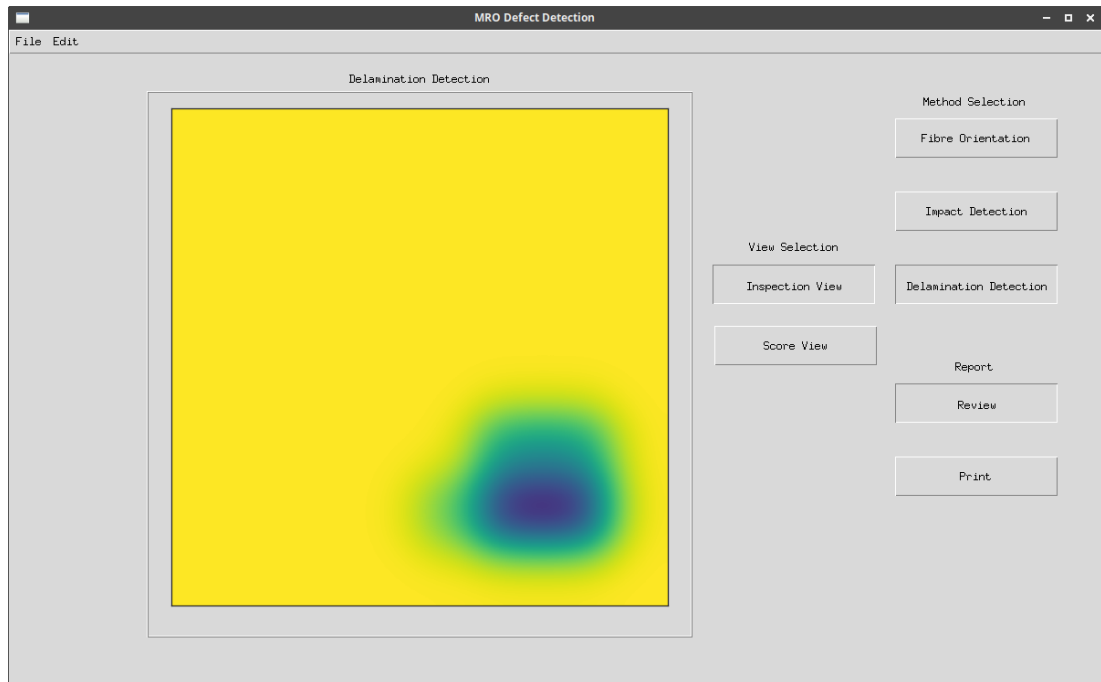


Figure 5.25: Graphical User Interface for operators, Delamination Detection indication Review screen.

to present a visual report that can be quickly interpreted by an operator. Dark areas within this report are indicative of a delamination or area of interest and yellow areas are indicative of a homogeneous area. For more details regarding the performance of the RTD probes classification of ‘No Delamination’, the Operator can select the ‘Score View’ from the ‘View Selection’ option. This presents the same heat map without a Gaussian interpolation, which is overlaid with the count of ‘Delamination’ percentages for each probe, with the value of 1 being representative of 100%. Within the example displayed in Figure 5.26 it can be seen that 2 probes provide a delamination indication of 100%, 2 provide an indication of 50% and the last probe provides an indication of 25%. The expectation is that the indication of delamination will be used by the operator to guide their certified Non-Destructive Testing in order to quantify the delamination within the area.

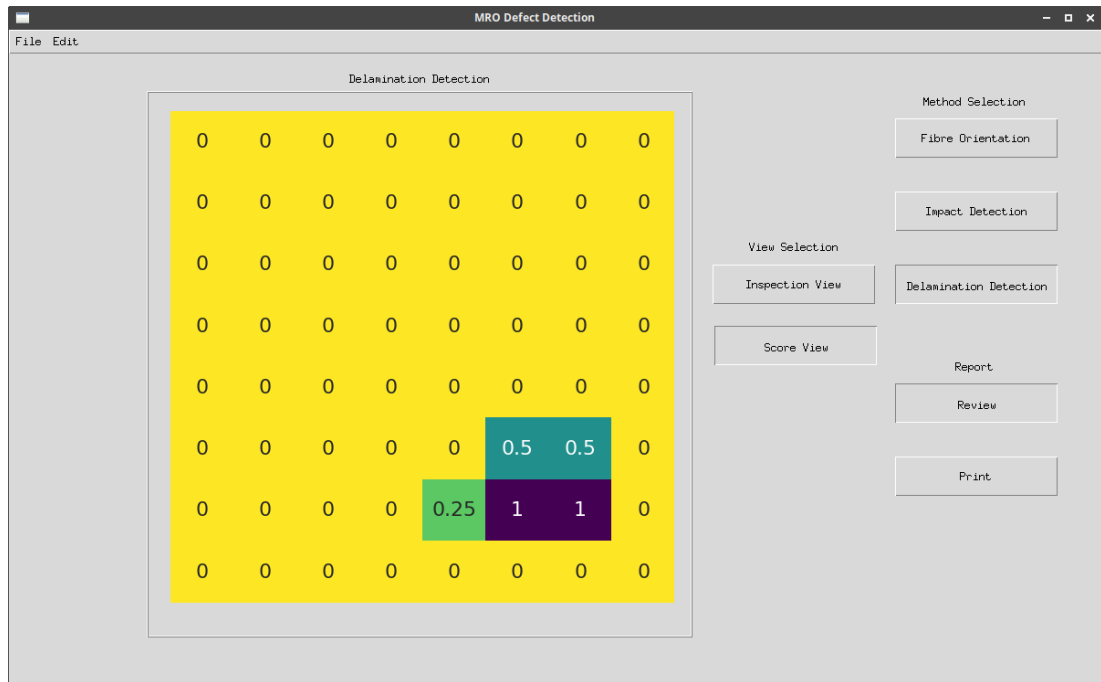


Figure 5.26: Graphical User Interface for operators, Delamination Detection indication with scores Review screen.

5.6 Summary

The Chapter proposes a novel framework for panel inspection utilising heat and temperature sensing surfaces. It has been demonstrated that by introducing a heating cycle that is typically used for drying components and recording the temperature change profiles on the sensing surface it is possible to detect delaminations utilising machine learning algorithms. Two approaches to engineer features from the capture data were evaluated; one extracting features based on engineering knowledge and a second approach where generic time series features are extracted. Both feature sets were evaluated using Support Vector Machine and Random Forest classifiers. For the case of generic time series features, a hybrid feature selection approach was used to initially filter top-ranked features, followed by an exhaustive grid hyperparameter search to determine the appropriate number of features and best model parameters.

The classifiers were trained using 10-fold cross-validation and evaluated on a keep-out test set with a balanced representation of conditions and distances from the centre of the heater mat to allow appropriate evaluation. It is interesting to

note that in all cases the test performance achieved was higher than that on the validation test. This has been attributed to the fact that the final model used for testing is retrained on the complete training/validation dataset to maximise performance.

The SVM classifier suffers from ‘curse of dimensionality’ when all generic time series features are used, but when an appropriate number of features is selected, it performs better compared to knowledge-based features. The RF classifier is insensitive to the increased number of features owing to bagging and the maximum number of features that are used per tree to combat overfitting and ‘curse of dimensionality’. However, the performance did not increase relative to a Random Forest trained on knowledge-based features.

Overall, the best classification scores were obtained utilising the SVM with generic time series features with an overall accuracy of 90% and more importantly, with a low misclassification rate for delamination of 6%. When compared to the existing method of manual tap testing, where defect detection accuracy for similar sized defects is 73% and 81% for Airbus and Boeing respectively [225] this is a notable improvement.

Chapter 6

Conclusion

6.1 Thesis Summary

The objectives set out within this Thesis were to develop methods which are able to detect defects in the form of disbonds and delaminations as well as provide inter-laminate material details regarding fibre orientation utilising a transmission-based heated tool surface designed to remove fluids during a vacuum-assisted low temperature (80°C) drying cycle. The methods were required to function without a direct line of sight to the component surface due to the consumables required to conduct the drying cycle. This allow the proposed methods to realise time savings by avoiding the requirement of removing drying cycle consumables for manual tap test inspection. The thesis technical chapters can be summarised as follows:

- Within Chapter 3 the creation of a two-part thermal transmission tool capable of heating one surface of a component and measuring the resultant thermal transmission from the opposing surface was described. The tool was capable of sustaining a temperature of 80°C as was required for a low temperature drying cycle, as well as having a temperature detection method which was compatible with the vacuum-assisted drying process in the form of an array of RTD probes applied directly to the component surface. It was

shown that the tool can capture temperature data directly from the component surface while the component was set-up for a low temperature drying cycle while alleviating the issues associated with direct line of sight typically required by non-contact NDT/NDI methods such as IR Thermography.

In this chapter the tool was used to indicate disbond locations within a CFRP sandwich panel, in the form of impact damage. This was achieved while the component and the tool are both within the vacuum set-up required for a low temperature drying cycle. The indicative method utilised the principles of Fourier's law of thermal transmission, where changes to the physical condition of a structure directly impacts thermal conduction. Furthermore, the chapter proposes a framework for execution and visualisation of NDI using the methods proposed in the thesis and allows for ease of use, intuitive interpretation, and minimal operator training.

- The effect of transient thermal conduction within a laminate sample was investigated in Chapter 4 to assess if the temperature readings collected can be utilised and determine fibre orientation of a CFRP laminate structure. The analysis was conducted utilising the temperature profiles of the laminates that are heated only through transient thermal conduction while only requiring a cycle with 150 s dwell period at 80°C. The proposed method is based on a comparison between the mean temperature distribution profiles against a library of known thermal responses obtained from sound parts undergoing the same heating cycle, that are routinely available from the OEM business unit. For the purposes of this comparison the mean distribution profiles are compared utilising the Mean Square Error metric. The MSE is computed between all components in the library and the component under test; the fibre orientation of the component under test is assumed to be identical to that of the specimen component that yields the minimum error. The final result is again integrated in the proposed visualisation and execution framework of Chapter 3 to allow an operator to assess the similarities. The proposed method is semi-autonomous in classifying the fibre

orientation and requires minimal training of an operator.

- Continuing exploring the effects of transient thermal conduction due to structural dissipation within a CFRP laminate, Chapter 5 employs machine learning approaches on the temperature profile data to identify locations affected by delamination. The temperature profile data are processed utilising knowledge-base features and generic time series for the training of Support Vector Machine and Random Forest classifiers. Each model is hyperparameter tuned to obtain the most optimal parameters given the corresponding feature sets. The performance of each model and feature set is extensively evaluated. The final model utilises 505 generic time series features with a SVM classifier to achieve an overall accuracy of 90% and more importantly a misclassification rate for delamination of 6%. For the practical implementation of the technique, an incrementally stepped heating source can be adopted to cover the complete area and accumulate additional evidence of affected locations. Consequently, this is expected to yield increased performance by taking advantage of the multiple consecutive heating cycles provided by each step.

6.2 Thesis Contributions

The thesis contributions can be summarised as follows:

- i Develop a versatile contact-based thermography tool that can be used for a variety of NDI tasks.
- ii Proposed and developed contact-based thermography technique that utilises the tool to assess impact damage [17], by visually displaying areas of interest.
- iii Creation and validation of fibre orientation mean temperature response library, to identify fibre orientation of a part of unknown origin and history by

comparing its thermal response to that of the mean temperature response library [18].

- iv Proposed and developed contact-based thermography model to detect delamination utilising incremental step heating [19].

6.3 Further Work

This Section discusses further work which should be conducted to realise the full potential of the proposed inspection methods:

- Multi-Zonal Heated Surface Tooling: It has been discussed in Chapter 3 that a multi-zonal controlled heated surface is required which will work in tandem with the developed sensing array tool. One thread of future work is investigating the direct application of heat within a tooling surface that is compatible with the CFRP thermal properties while it is also able to withstand the MRO environment. For instance, the use of fibre doping with graphite to improve control of the electrical resistance within a CFRP tooling surface could be explored, along with the introduction of other compatible conductive fibres either woven within the CFRP laminates or used as a laminate layer.

Further investigation into the optimum area size of heated zones to maximise the use of the developed methods could be explored. A fully functional zonal heating system capable of producing independent heating profiles will enable maximum benefit from the proposed methods, realising their full potential.

- Certification of Machine Learning Based Non Destructive Testing Methods: It is discussed in Chapter 1 that there is clear difference between a Non-Destructive Testing method and a Non-Destructive Inspection methods. NDT provides certification of the condition of the structure examined, and NDI provides an indication as the condition of the structure examined. Part

of this certification relies on the NDT method being conducted by a qualified operator, who uses experience and training to identify defects based on the captured data. As the proposed methods within this Thesis utilise automated data analysis and Machine Learning to produce indications of defects within the examined structure, they currently can not be certified as NDT methods. Exploration should be carried out into the legal, moral, and technical challenges faced in regard to the certification of Machine Learning methods to that of NDT within the aerospace industry.

Successful certification could allow for faster and more detailed reporting of defects to be realised, with the opportunity to incorporate NDT methods into live condition monitoring sensor systems, in theory, providing NDT reporting of the extent of damage as it occurs.

- Fibre Orientation, Complex Structures: Chapter 4 proposes a method of fibre orientation indication through the holistic examination of a CFRP laminate panel thermal profile. However, the approach has been demonstrated on thin laminates. Sandwich CFRP laminate structures, which consist of two laminates, honeycomb core and two adhesive layers, will have a complex thermal response making the identification of fibre orientation more challenging. Particular interest should be paid to the variation of fibre orientation between the two laminates present within a sandwich structure (inner and outer skin), as the ability to identify fibre orientation of both laminates prevents the possible requirement of removing either the outer or inner skin to determine fibre orientation. Future work could also consider any modification to the capture method. The proposed approach focused on temperature profiles outside the heated area, however, the complexity of the two laminate in the heat propagation does not allow attribution on whether the deviations are caused by the inner or outer laminate. One approach will be to locate the heated and sensing surface on the same side implementing reflective thermography instead of transmissive.
- Finite Element Analysis Model Refinement: Within Chapter 4, it is high-

lighted that due to the complex interactions occurring within composite sandwich panel structures at each boundary (e.g. inter-laminate boundaries, laminate to adhesive boundary, adhesive to core) it can prove difficult to successfully model thermal response within an FE model. Further work could consider the use of test samples, representative of the material lay up of composite sandwich panels, and their experimentally captured thermal response to produce a pipeline approach at refining FE models. This would be of particular interest within the MRO aerospace environment where accurate FE modeling of proposed repairs is of significant importance.

Bibliography

- [1] G. Busse, D. Wu, and W. Karpen, “Thermal wave imaging with phase sensitive modulated thermography,” *Journal of Applied Physics*, 1992.
- [2] N. Avdelidis, D. Almond, A. Dobbinson, B. Hawtin, C. Ibarra-Castanedo, and X. Maldague, “Aircraft composites assessment by means of transient thermal NDT,” *Progress in Aerospace Sciences*, vol. 40, pp. 143–162, apr 2004.
- [3] C. Maierhofer, P. Myrach, M. Reischel, H. Steinfurth, M. Röllig, and M. Kunert, “Characterizing damage in CFRP structures using flash thermography in reflection and transmission configurations,” *Composites Part B: Engineering*, 2014.
- [4] J. P. Fielding, *Introduction to aircraft design*, vol. 11. Cambridge University Press, 2017.
- [5] P. C. Herrmann Axel S. and Zahlen and Z. Ichwan, “Sandwich Structures Technology in Commercial Aviation,” in *Sandwich Structures 7: Advancing with Sandwich Structures and Materials* (E. Thomsen O.T. and Bozhevolya and L. A, eds.), (Dordrecht), pp. 13–26, Springer Netherlands, 2005.
- [6] V. Dattoma, R. Marcuccio, C. Pappalettere, and G. M. Smith, “Thermographic investigation of sandwich structure made of composite material,” *NDT and E International*, 2001.
- [7] T. Malmivirta, J. Hamberg, E. Lagerspetz, and X. Li, “Hot or Not ? Robust and Accurate Continuous Thermal Imaging on FLIR cameras,” in *2019*

IEEE International Conference on Pervasive Computing and Communications (PerCom), pp. 1–9, IEEE, 2019.

- [8] Z. Fawaz, “Quality control and testing methods for advanced composite materials in aerospace engineering,” in *Advanced Composite Materials for Aerospace Engineering*, pp. 429–451, Woodhead Publishing, 2016.
- [9] BS EN 4179:2017, “Aerospace series. Qualification and approval of personnel for non-destructive testing,” 2017.
- [10] UK National Aerospace NDT Board, “UK NANDTB 18 NDT METHOD OR TECHNIQUE-TRAINING AND CERTIFICATION GUIDANCE,” 2015.
- [11] Civil Aviation Authority, “Safety and Airspace Regulation Group Mandatory Requirements for Airworthiness,” 2017.
- [12] EN 473, “Non-destructive testing-Qualification and certification of NDT personnel,” 2008.
- [13] PayScale, “Aircraft Maintenance Services Wages, Hourly Wage Rate — PayScale United Kingdom,” 2018.
- [14] P. Cawley and R. Adams, “The mechanics of the coin-tap method of non-destructive testing,” *Journal of Sound and Vibration*, vol. 122, pp. 299–316, apr 1988.
- [15] J. Gryzagoridis and D. Findeis, “Tap testing vs. Thermography,” in *54th Annual British Conference of Non-Destructive Testing, NDT 2015*, 2015.
- [16] Goodrich, “V2500 Structural Repair Manual Distribution,” 2018.
- [17] D. I. Gillespie, A. W. Hamilton, R. C. Atkinson, X. Bellekens, C. Michie, I. Andonovic, and C. Tachtatzis, “Defect Detection in Aerospace Sandwich Composite Panels Using Conductive Thermography and Contact Sensors,” *Sensors*, vol. 20, p. 6689, nov 2020.

- [18] D. I. Gillespie, A. W. Hamilton, E. J. McKay, B. Neilson, R. C. Atkinson, I. Andonovic, and C. Tachtatzis, “Non-Destructive Identification of Fibre Orientation in Multi-Ply Biaxial Laminates Using Contact Temperature Sensors,” *Sensors*, vol. 20, p. 3865, jul 2020.
- [19] D. I. Gillespie, A. W. Hamilton, R. C. Atkinson, X. Bellekens, C. Michie, I. Andonovic, and C. Tachtatzis, “Composite Laminate Delamination Detection Using Transient Thermal Conduction Profiles and Machine Learning Based Data Analysis,” *Sensors*, vol. 20, p. 7227, dec 2020.
- [20] E. Jasiūnienė, L. Mažeika, V. Samaitis, V. Cicėnas, and D. Mattsson, “Ultrasonic non-destructive testing of complex titanium/carbon fibre composite joints,” *Ultrasonics*, vol. 95, no. December 2017, pp. 13–21, 2019.
- [21] P. He, “Measurement of acoustic dispersion using both transmitted and reflected pulses,” *The Journal of the Acoustical Society of America*, vol. 107, no. 2, pp. 801–807, 2000.
- [22] K. Ono, “A Comprehensive Report on Ultrasonic Attenuation of Engineering Materials, Including Metals, Ceramics, Polymers, Fiber-Reinforced Composites, Wood, and Rocks,” *Applied Sciences*, vol. 10, no. 7, p. 2230, 2020.
- [23] H. Jaffe and D. A. Berlincourt, “Piezoelectric Transducer Materials,” *Proceedings of the IEEE*, vol. 53, no. 10, pp. 1372–1386, 1965.
- [24] D. E. W. Stone and B. Clarke, “Ultrasonic attenuation as a measure of void content in carbon-fibre reinforced plastics,” *Non-Destructive Testing*, vol. 8, no. 3, pp. 137–145, 1975.
- [25] D. K. Hsu, “Experimental analysis ultrasonic attenuation in carbon composites,” *Ultrasonics*, vol. 33, no. 3, pp. 195–203, 1995.
- [26] Y. Ishii, S. Biwa, and A. Kuraishi, “Influence of porosity on ultrasonic wave velocity , attenuation and interlaminar interface echoes in compos-

- ite laminates : Finite element simulations and measurements,” *Composite Structures*, vol. 152, no. September, pp. 645–653, 2016.
- [27] S. J. Jin, X. C. He, J. Chen, S. Q. Shi, and L. Lin, “Recurrence quantitative analysis for porosity characterization of CFRP with complex void morphology,” *Composite Structures*, vol. 229, no. September, 2019.
- [28] Y. D. Khaletskiy, “Effectiveness of Combined Aircraft Engine Noise Suppressors,” *Acoustical Physics*, vol. 58, no. 4, pp. 510–515, 2012.
- [29] P. Theobald, B. Zeqiri, and J. Avison, “Couplants and their influence on AE sensor sensitivity,” *Journal of acoustic emission*, vol. 26, pp. 91–97, 2008.
- [30] M. Castaings, P. Cawley, R. Farlow, and G. Hayward³, “Single Sided Inspection of Composite Materials Using Air Coupled Ultrasound,” *Journal of Nondestructive Evaluation*, vol. 17, no. 1, pp. 37–45, 1998.
- [31] J. Peters, “Non-Contact Inspection of Composites Using Air-Coupled Ultrasound,” in *AIP Conference Proceedings*, vol. 657, pp. 973–980, AIP, 2003.
- [32] R. S. Panda, P. Rajagopal, and K. Balasubramaniam, “Rapid guided wave inspection of complex stiffened composite structural components using non-contact air-coupled ultrasound,” *Composite Structures*, vol. 206, pp. 247–260, dec 2018.
- [33] H. Cho, S. Ogawa, and M. Takemoto, “Non-contact laser ultrasonics for detecting subsurface lateral defects,” *NDT & E International*, vol. 29, oct 1996.
- [34] K. Zhang, Z. Zhou, and J. Zhou, “Application of laser ultrasonic method for on-line monitoring of friction stir spot welding process,” *Applied Optics*, vol. 54, no. 25, p. 7483, 2015.
- [35] J. Spytek, A. Ziaja-Sujdak, K. Dziedziech, L. Pieczonka, I. Pelivanov, and L. Ambrozinski, “Evaluation of disbonds at various interfaces of adhesively

- bonded aluminum plates using all-optical excitation and detection of zero-group velocity Lamb waves,” *NDT & E International*, vol. 112, jun 2020.
- [36] L. Ambrozinski, J. Mrowka, M. O’Donnell, and I. Pelivanov, “Detection and imaging of local ply angle in carbon fiber reinforced plastics using laser ultrasound and tilt filter processing,” *Composites Part A: Applied Science and Manufacturing*, vol. 126, nov 2019.
- [37] I. Pelivanov, T. Buma, J. Xia, C.-W. Wei, and M. O’Donnell, “A new fiber-optic non-contact compact laser-ultrasound scanner for fast non-destructive testing and evaluation of aircraft composites,” *Journal of Applied Physics*, vol. 115, mar 2014.
- [38] D. Datta and N. N. Kishore, “Features of ultrasonic wave propagation to identify defects in composite materials modelled by finite element method,” *NDT and E International*, vol. 29, no. 4, pp. 213–223, 1996.
- [39] I. Pelivanov, A. Shtokolov, C. W. Wei, and M. O’Donnell, “A 1 kHz a-scan rate pump-probe laser-ultrasound system for robust inspection of composites,” *IEEE Transactions on Ultrasonics, Ferroelectrics, and Frequency Control*, vol. 62, no. 9, pp. 1696–1703, 2015.
- [40] Z. Zhang, M. Liu, Q. Li, and Y. Ang, “Visualized characterization of diversified defects in thick aerospace composites using ultrasonic B-scan,” *Composites Communications*, vol. 22, no. May, p. 100435, 2020.
- [41] T. Hasiotis, E. Badogiannis, and N. G. Tsouvalis, “Application of ultrasonic C-scan techniques for tracing defects in laminated composite materials,” *Strojniski Vestnik/Journal of Mechanical Engineering*, vol. 57, no. 3, pp. 192–203, 2011.
- [42] Y. O. Kas and C. Kaynak, “Ultrasonic (C-scan) and microscopic evaluation of resin transfer molded epoxy composite plates,” *Polymer Testing*, vol. 24, no. 1, pp. 114–120, 2005.

- [43] R. Růžek, R. Lohonka, and J. Jironč, “Ultrasonic C-scan and shearography NDI techniques evaluation of impact defects identification,” *NDT and E International*, vol. 39, no. 2, pp. 132–142, 2006.
- [44] W. Zouaghi, M. D. Thomson, K. Rabia, R. Hahn, V. Blank, and H. G. Roskos, “Broadband terahertz spectroscopy: Principles, fundamental research and potential for industrial applications,” *European Journal of Physics*, vol. 34, no. 6, 2013.
- [45] C. H. Ryu, S. H. Park, D. H. Kim, K. Y. Jhang, and H. S. Kim, “Nondestructive evaluation of hidden multi-delamination in a glass-fiber-reinforced plastic composite using terahertz spectroscopy,” *Composite Structures*, vol. 156, pp. 338–347, 2016.
- [46] Q. Wang, X. Li, T. Chang, J. Zhang, L. Liu, H. Zhou, and J. Bai, “Non-destructive imaging of hidden defects in aircraft sandwich composites using terahertz time-domain spectroscopy,” *Infrared Physics and Technology*, vol. 97, no. January, pp. 326–340, 2019.
- [47] M. Zhong, B. Liu, C. Li, Z. Wang, D. Wei, B. Zhou, X. Dai, and Y. Xu, “Terahertz Spectroscopy and Imaging Detection of Defects in Civil Aircraft Composites,” *Journal of Spectroscopy*, vol. 2020, 2020.
- [48] H. Park, “Investigation on low velocity impact behavior of sandwich composite and monolithic laminate plates using FEM analysis,” *Composite Structures*, vol. 220, no. October 2018, pp. 842–846, 2019.
- [49] R. Knibbs and J. Morris, “The effects of fibre orientation on the physical properties of composites,” *Composites*, vol. 5, pp. 209–218, sep 1974.
- [50] D. K. Hsu, “Characterization of a graphite/epoxy laminate by electrical resistivity measurements,” *Plenum Publishing Corporation*, pp. 1219–1228, 1985.
- [51] K. W. Tse, C. A. Moyer, and S. Araj, “Electrical conductivity of graphite

- fiber-epoxy resin composites,” *Materials Science and Engineering*, vol. 49, no. 1, pp. 41–46, 1981.
- [52] J. Zhang, C. Shi, Y. Ma, X. Han, W. Li, T. Chang, D. Wei, C. Du, and H.-L. Cui, “Spectroscopic study of terahertz reflection and transmission properties of carbon-fiber-reinforced plastic composites,” *Optical Engineering*, vol. 54, no. 5, p. 054106, 2015.
- [53] J. W. Park, K. H. Im, D. K. Hsu, J. A. Jung, and I. Y. Yang, “Terahertz spectroscopy approach of the fiber orientation influence on CFRP composite solid laminates,” *Journal of Mechanical Science and Technology*, vol. 26, no. 7, pp. 2051–2054, 2012.
- [54] K. H. Im, D. K. Hsu, C. P. Chiou, D. J. Barnard, S. K. Kim, S. J. Kang, Y. T. Cho, J. A. Jung, and I. Y. Yang, “Influence of terahertz waves on unidirectional carbon fibers in CFRP Composite Materials,” *Medziagotyra*, vol. 20, no. 4, pp. 457–463, 2014.
- [55] P. Lopato, T. Chady, and R. Sikora, “Testing of composite materials using advanced NDT methods,” *COMPEL - The International Journal for Computation and Mathematics in Electrical and Electronic Engineering*, vol. 30, no. 4, pp. 1260–1270, 2011.
- [56] J. Zhang, W. Li, H. L. Cui, C. Shi, X. Han, Y. Ma, J. Chen, T. Chang, D. Wei, Y. Zhang, and Y. Zhou, “Nondestructive evaluation of carbon fiber reinforced polymer composites using reflective terahertz imaging,” *Sensors (Switzerland)*, vol. 16, no. 6, 2016.
- [57] J. B. J. baron Fourier, *The Analytical Theory of Heat*. The University Press, 1878.
- [58] S. J. Blundell and K. M. Blundell, *Concepts in thermal physics*. OUP Oxford, 2009.
- [59] T. Eisele, “Direct biohydrometallurgical extraction of iron from ore,” tech. rep., Michigan Technological Univ., Houghton, MI (United States), 2005.

- [60] T. S. Kuhn, *Black-body theory and the quantum discontinuity, 1894-1912*. University of Chicago Press, 1987.
- [61] M. Planck, “The theory of heat radiation, translated by m,” *Masius, P. Blackiston’s Son & Co, Philadelphia, reprinted by Kessinger*, 1914.
- [62] V. Vavilov, “Thermal NDT: Historical milestones, state-of-the-art and trends,” *Quantitative InfraRed Thermography Journal*, vol. 11, no. 1, pp. 66–83, 2014.
- [63] A. Rogalski, “Terahertz detectors and focal plane arrays,” *Opto-Electronics Review*, vol. 18, no. 2, pp. 121–136, 2010.
- [64] W. M. van der Aalst, “Data scientist: The engineer of the future,” in *Proceedings of the I-ESA Conferences*, vol. 7, pp. 13–26, Springer International Publishing, 2014.
- [65] C. Ibarra-Castanedo, J. M. Piau, S. Guilbert, N. Avdelidis, M. Genest, A. Bendada, and X. P. Maldague, “Comparative study of active thermography techniques for the nondestructive evaluation of honeycomb structures,” *Research in Nondestructive Evaluation*, vol. 20, no. 1, pp. 1–31, 2009.
- [66] W. B. Larbi, C. Ibarra-Castanedo, M. Klein, A. Bendada, and X. Maldague, “Experimental comparison of lock-in and pulsed thermography for the non-destructive evaluation of aerospace materials,” in *6 th International Workshop, Advances in Signal Processing for Non Destructive Evaluation of Materials (IWASPND E)*, Ontario, Canada. Citeseer, Citeseer, 2009.
- [67] A. Dragomir, M. Adam, M. Andrusca, and A. Munteanu, “Aspects concerning the influence of environmental factors in infrared monitoring of electrical equipment,” in *Proceedings of the 2016 International Conference and Exposition on Electrical and Power Engineering, EPE 2016*, pp. 133–138, Institute of Electrical and Electronics Engineers Inc., dec 2016.
- [68] C. D. Wen and I. Mudawar, “Modeling the effects of surface roughness on

- the emissivity of aluminum alloys,” *International Journal of Heat and Mass Transfer*, vol. 49, pp. 4279–4289, nov 2006.
- [69] P. Cawley, “The rapid non-destructive inspection of large composite structures,” *Composites*, vol. 25, no. 5, pp. 351–357, 1994.
- [70] X. Li, N. Tao, J. G. Sun, C. Zhang, and Y. Zhao, “Thickness measurement by two-sided step-heating thermal imaging,” *Review of Scientific Instruments*, vol. 89, p. 014902, jan 2018.
- [71] H. S. Carslaw and J. C. Jaeger, *Conduction of heat in solids: Oxford Science Publications*. Oxford, England, 1959.
- [72] W. J. Parker, R. J. Jenkins, C. P. Butler, and G. L. Abbott, “Flash method of determining thermal diffusivity, heat capacity, and thermal conductivity,” *Journal of Applied Physics*, 1961.
- [73] C. Berggreen, K. Branner, J. F. Jensen, and J. P. Schultz, “Application and analysis of sandwich elements in the primary structure of large wind turbine blades,” *Journal of Sandwich Structures and Materials*, 2007.
- [74] X.-l. Li, J. Sun, N. Tao, L. Feng, J.-l. Shen, Y. He, C. Zhang, and Y.-j. Zhao, “An Effective Method to Inspect Adhesive Quality of Wind Turbine Blades Using Transmission Thermography,” *Journal of Nondestructive Evaluation*, vol. 37, p. 19, feb 2018.
- [75] G. Giorleo and C. Meola, “Comparison between pulsed and modulated thermography in glass–epoxy laminates,” *NDT and E International*, vol. 35, pp. 287–292, jul 2002.
- [76] D. L. Balageas and J. M. Roche, “Common tools for quantitative time-resolved pulse and step-heating thermography - Part I: Theoretical basis,” *Quantitative InfraRed Thermography Journal*, vol. 11, no. 1, pp. 43–56, 2014.

- [77] J. M. Roche and D. L. Balageas, “Common tools for quantitative pulse and step-heating thermography - Part II: Experimental investigation,” *Quantitative InfraRed Thermography Journal*, vol. 12, no. 1, pp. 1–23, 2015.
- [78] R. Marani, D. Palumbo, V. Renò, U. Galietti, E. Stella, and T. D’Orazio, “Modeling and classification of defects in CFRP laminates by thermal non-destructive testing,” *Composites Part B: Engineering*, vol. 135, pp. 129–141, feb 2018.
- [79] C. Maierhofer, M. Röllig, K. Ehrig, D. Meinel, and G. Céspedes-Gonzales, “Validation of flash thermography using computed tomography for characterizing inhomogeneities and defects in CFRP structures,” *Composites Part B: Engineering*, vol. 64, pp. 175–186, aug 2014.
- [80] M. Barus, H. Weleman, F. Collombet, M. L. Pastor, A. Cantarel, L. Crouzeix, Y. H. Grunevald, and V. Nassiet, “crossmark,” *NDT and E International*, vol. 85, no. May 2016, pp. 27–33, 2017.
- [81] R. Steinberger, “International Journal of Fatigue Infrared thermographic techniques for non-destructive damage characterization of carbon fibre reinforced polymers during tensile fatigue testing,” *International Journal of Fatigue*, vol. 28, no. 10, pp. 1340–1347, 2006.
- [82] I. Amenabar, A. Mendikute, A. López-arraiza, M. Lizaranzu, and J. Aurrekoetxea, “Composites : Part B Comparison and analysis of non-destructive testing techniques suitable for delamination inspection in wind turbine blades,” *Composites Part B*, vol. 42, no. 5, pp. 1298–1305, 2011.
- [83] M. Moradi and M. S. Safizadeh, “Edge disbond detection of carbon / epoxy repair patch on aluminum using thermography,” *Composites Science and Technology*, vol. 179, no. April, pp. 41–53, 2019.
- [84] M. Wang, B. Gao, T. Wu, B. Hu, and L. Liu, “Defect depth retrieval method based on nonlinear transformation for pulsed thermographic inspection,”

International Journal of Thermal Sciences, vol. 149, no. November 2019, p. 106196, 2020.

- [85] D. Herzog, M. Schmidt-lehr, M. Canisius, M. Oberlander, J.-p. Tasche, and C. Emmelmann, “Laser cutting of carbon fiber reinforced plastic using a 30 kW fiber laser,” *JOURNAL OF LASER APPLICATIONS*, vol. 27, no. February, 2015.
- [86] H. Zhang, U. Hassler, M. Genest, H. Fernandes, F. Robitaille, C. Ibarra-Castanedo, S. Joncas, and X. Maldague, “Comparative study on submillimeter flaws in stitched T-joint carbon fiber reinforced polymer by infrared thermography, microcomputed tomography, ultrasonic c-scan and microscopic inspection,” *Optical Engineering*, vol. 54, no. 10, p. 104109, 2015.
- [87] H. Zhang, H. Fernandes, F. B. Djupkep Dizeu, U. Hassler, J. Fleuret, M. Genest, C. Ibarra-Castanedo, F. Robitaille, S. Joncas, and X. Maldague, “Pulsed micro-laser line thermography on submillimeter porosity in carbon fiber reinforced polymer composites: experimental and numerical analyses for the capability of detection,” *Applied Optics*, vol. 55, no. 34, p. D1, 2016.
- [88] T. Li, D. P. Almond, and D. A. Rees, “Crack imaging by scanning laser-line thermography and laser-spot thermography,” *Measurement Science and Technology*, vol. 22, no. 3, 2011.
- [89] H. Fernandes, H. Zhang, C. Ibarra-Castanedo, and X. Maldague, “Fiber orientation assessment on randomly-oriented strand composites by means of infrared thermography,” *Compos Sci Technol*, vol. 121, pp. 25–33, dec 2015.
- [90] H. Zhang, L. Yu, U. Hassler, H. Fernandes, M. Genest, F. Robitaille, S. Joncas, W. Holub, Y. Sheng, and X. Maldague, “An experimental and analytical study of micro-laser line thermography on micro-sized flaws in stitched carbon fiber reinforced polymer composites,” *Composites Science and Technology*, vol. 126, pp. 17–26, 2016.

- [91] J. Guo, X. Gao, E. Toma, and U. Netzelmann, “NDT and E International Anisotropy in carbon fiber reinforced polymer (CFRP) and its effect on induction thermography,” *NDT and E International*, vol. 91, no. October, pp. 1–8, 2017.
- [92] H. Kim, S. Yarlagadda, J. W. Gillespie, B. Nicholas, B. K. Fink, H. Kim, S. Yarlagadda, and J. W. Gillespie, “A study on the induction heating of carbon fiber reinforced thermoplastic composites,” *Advanced Composite Materials*, vol. 11, no. 1, pp. 71–80, 2012.
- [93] R. Rudolf, P. Mitschang, and M. Neitzel, “Induction heating of continuous carbon-fibre-reinforced thermoplastics,” *Composites: Part A*, vol. 31, pp. 1191–1202, 2000.
- [94] E. T. Thostenson and T. W. Chou, “Microwave processing: fundamentals and applications,” *Composites Part A: Applied Science and Manufacturing*, vol. 30, no. 9, pp. 1055–1071, 1999.
- [95] Y. He, R. Yang, H. Zhang, D. Zhou, and G. Wang, “Volume or inside heating thermography using electromagnetic excitation for advanced composite materials,” *International Journal of Thermal Sciences*, vol. 111, pp. 41–49, 2017.
- [96] J. A. Menéndez, A. Arenillas, B. Fidalgo, Y. Fernández, L. Zubizarreta, E. G. Calvo, and J. M. Bermúdez, “Microwave heating processes involving carbon materials,” *Fuel Processing Technology*, vol. 91, no. 1, pp. 1–8, 2010.
- [97] I. Meccanica and P. Bari, “Quantitative InfraRed Thermography New data analysis to evaluate defects in composite materials using microwaves thermography,” in *11th International Conference on Quantitative InfraRed Thermography*, 2012.
- [98] A. Foudazi, S. Member, M. T. Ghasr, S. Member, and K. M. Donnell, “Application of Active Microwave Thermography to Inspection of Carbon

- Fiber Reinforced Composites,” in *AUTOTESTCON, International Automatic Testing Conference*, pp. 318–322, IEEE, 2014.
- [99] H. Zhang, R. Yang, Y. He, A. Foudazi, L. Cheng, and G. Tian, “A Review of Microwave Thermography Nondestructive Testing and Evaluation,” *Sensors*, vol. 17, p. 1123, may 2017.
- [100] A. Mendioroz, R. Celorrio, and A. Salazar, “Ultrasound excited thermography: An efficient tool for the characterization of vertical cracks,” *Measurement Science and Technology*, vol. 28, no. 11, 2017.
- [101] J. Segers, S. Hedayatrasa, E. Verboven, G. Poelman, W. Van Paepegem, and M. Kersemans, “In-plane local defect resonances for efficient vibrothermography of impacted carbon fiber-reinforced polymers (CFRP),” *NDT and E International*, vol. 102, no. October 2018, pp. 218–225, 2019.
- [102] F. C. Smith, L. D. Moloney, F. L. Matthews, and J. Hodges, “Fabrication of woven carbon fibre/polycarbonate repair patches,” *Composites Part A: Applied Science and Manufacturing*, vol. 27, no. 11, pp. 1089–1095, 1996.
- [103] L. R. Pickard, K. Smith, J. Kratz, and K. Potter, “Tracking the evolution of a defect, characteristic of AFP layup, during cure with in-process micro-CT scanning,” in *ICCM International Conferences on Composite Materials*, no. August, pp. 20–25, 2017.
- [104] T. E. Saliba, D. Hofmann, and P. Smolinski, “Development of an in situ Hall-effect sensor for on-line monitoring of thickness and compaction during composite curing,” *Composites Science and Technology*, vol. 51, no. 1, pp. 1–9, 1994.
- [105] C. J. Keulen, E. Akay, F. F. Melemez, E. S. Kocaman, A. Deniz, C. Yilmaz, T. Boz, M. Yildiz, H. S. Turkmen, and A. Suleman, “Prediction of fatigue response of composite structures by monitoring the strain energy release rate with embedded fiber Bragg gratings,” *Journal of Intelligent Material Systems and Structures*, vol. 27, pp. 17–27, jan 2016.

- [106] V. Dewynter-Marty, P. Ferdinand, E. Bocherens, R. Carbone, H. Beranger, S. Bourasseau, M. Dupont, and D. Balageas, “Embedded Fiber Bragg Grating Sensors for Industrial Composite Cure Monitoring,” *Journal of Intelligent Material Systems and Structures*, vol. 9, pp. 785–787, oct 1998.
- [107] H.-K. Kang, D.-H. Kang, C.-S. Hong, and C.-G. Kim, “Simultaneous monitoring of strain and temperature during and after cure of unsymmetric composite laminate using fibre-optic sensors,” *Smart Materials and Structures*, vol. 12, pp. 29–35, feb 2003.
- [108] R. Montanini and L. D’Acquisto, “Simultaneous measurement of temperature and strain in glass fiber/epoxy composites by embedded fiber optic sensors: I. Cure monitoring,” *Smart Materials and Structures*, vol. 16, pp. 1718–1726, oct 2007.
- [109] P. Feraboli, “Composite materials strength determination within the current certification methodology for aircraft structures,” *Journal of Aircraft*, vol. 46, no. 4, pp. 1365–1374, 2009.
- [110] W. Ballout, B. Coulon, Y.-A. Janssens, P. Van Velthem, M. Sclavons, D. Magnin, T. Pardoën, and C. Bailly, “Quantitative characterization of interdiffusion at the resin-resin and resin-prepreg interphases of epoxy systems processed by model SQ-RTM,” *Polymer Engineering & Science*, vol. 56, pp. 1061–1069, sep 2016.
- [111] J. A. Becker, C. B. Green, and G. L. Pearson, “Properties and uses of thermistors — Thermally sensitive resistors,” *Electrical Engineering*, vol. 65, pp. 711–725, jul 1946.
- [112] A. Feteira, “Negative Temperature Coefficient Resistance (NTCR) Ceramic Thermistors: An Industrial Perspective,” *Journal of the American Ceramic Society*, vol. 92, pp. 967–983, may 2009.
- [113] M. Hosseini, “Effect of cation composition on the electrical properties and

- aging of Mn-Co-Ni thermistors,” *Ceramics International*, vol. 26, pp. 245–249, apr 2000.
- [114] P. R. N. Childs, J. R. Greenwood, and C. A. Long, “Review of Temperature measurements,” *Review of Scientific Instruments*, vol. 71, p. 2959, 2000.
- [115] T. J. Claggett, R. W. Worrall, and B. G. Liptak, “Thermocouples,” *Instrument engineers’ handbook. Process measurement and analysis*, 1999.
- [116] R. P. Benedict and R. J. Russo, “A note on grounded thermocouple circuits,” *Journal of Fluids Engineering, Transactions of the ASME*, vol. 94, no. 2, pp. 377–380, 1972.
- [117] P. A. Kinzie and L. G. Rubin, “Thermocouple Temperature Measurement,” *Physics Today*, vol. 26, pp. 52–55, nov 1973.
- [118] R. W. Powell, R. P. Tye, and M. J. Woodman, “Thermal Conductivities and Electrical Resistivities of the Platinum Metals,” *Platinum Metals Review*, vol. 6, no. 4, pp. 138–143, 1962.
- [119] R. D. Baxter and P. J. Freud, “Thin film resistance thermometer device with a predetermined temperature coefficient of resistance and its method of manufacture,” 1983.
- [120] H. Preston-Thomas, “The International Temperature Scale of 1990 (ITS-90),” *Metrologia*, vol. 27, pp. 3–10, jan 1990.
- [121] International Electrotechnical Commission, “Industrial platinum resistance thermometers and platinum temperature sensors,” standard, International Electrotechnical Commission, Geneva, CH, jul 2008.
- [122] RS-Components, “Platinum Resistance Thermometer (PRT) Selection Guide.”
- [123] K. O. Hill and G. Meltz, “Fiber Bragg grating technology fundamentals and overview,” *Journal of Lightwave Technology*, vol. 15, pp. 1263–1276, aug 1997.

- [124] G. Luyckx, E. Voet, N. Lammens, and J. Degrieck, “Strain Measurements of Composite Laminates with Embedded Fibre Bragg Gratings: Criticism and Opportunities for Research,” *Sensors*, vol. 11, pp. 384–408, dec 2010.
- [125] B. De Pauw, S. Goossens, T. Geernaert, D. Habas, H. Thienpont, and F. Berghmans, “Fibre Bragg Gratings in Embedded Microstructured Optical Fibres Allow Distinguishing between Symmetric and Anti-Symmetric Lamb Waves in Carbon Fibre Reinforced Composites,” *Sensors*, vol. 17, p. 1948, aug 2017.
- [126] D. C. Betz, G. Thursby, B. Culshaw, and W. J. Staszewski, “Advanced layout of a fiber Bragg grating strain gauge rosette,” *Journal of Lightwave Technology*, vol. 24, pp. 1019–1026, feb 2006.
- [127] D. Gifford, “Distributed fiber-optic temperature sensing using Rayleigh backscatter,” in *31st European Conference on Optical Communications (ECOC 2005)*, no. CP502, pp. v3–511–v3–511, IEE, 2005.
- [128] S. T. Kreger, D. K. Gifford, M. E. Froggatt, B. J. Soller, and M. S. Wolfe, “High resolution distributed strain or temperature measurements in single- and multi-mode fiber using swept-wavelength interferometry,” in *Optical Fiber Sensors*, p. ThE42, Optical Society of America, 2006.
- [129] A. Samuel, “Some Studies in Machine Learning Using the Game of Checkers,” *IBM Journal of Research and Development*, vol. 3, no. 3, pp. 210–229, 1959.
- [130] J. H. Lee, J. Shin, and M. J. Realff, “Machine learning: Overview of the recent progresses and implications for the process systems engineering field,” *Computers and Chemical Engineering*, 2018.
- [131] S. B. Kotsiantis, I. Zaharakis, and P. Pintelas, “Supervised machine learning: A review of classification techniques,” *Emerging artificial intelligence applications in computer engineering*, vol. 160, no. 1, pp. 3–24, 2007.

- [132] M. Cunningham Pádraig and Cord and D. S. Jane, “Supervised Learning,” in *Machine Learning Techniques for Multimedia: Case Studies on Organization and Retrieval* (P. Cord Matthieu and Cunningham, ed.), pp. 21–49, Berlin, Heidelberg: Springer Berlin Heidelberg, 2008.
- [133] Z. Ghahramani, “Unsupervised Learning,” in *Advanced Lectures on Machine Learning: ML Summer Schools 2003, Canberra, Australia, February 2 - 14, 2003, Tübingen, Germany, August 4 - 16, 2003, Revised Lectures* (U. Bousquet Olivier and von Luxburg and R. Gunnar, eds.), pp. 72–112, Berlin, Heidelberg: Springer Berlin Heidelberg, 2004.
- [134] R. S. Sutton and A. G. Barto, *Reinforcement Learning, second edition: An Introduction*. Adaptive Computation and Machine Learning series, MIT Press, 2018.
- [135] J. K. Lancaster, “The effect of carbon fibre reinforcement on the friction and wear of polymers,” *J Phys D: Appl Phys*, vol. 1, no. 5, p. 549, 1968.
- [136] V. D. Azzi and S. W. Tsai, “Anisotropic strength of composites,” *Exp Mech*, vol. 5, pp. 283–288, sep 1965.
- [137] H. Fernandes, H. Zhang, A. Figueiredo, F. Malheiros, L. H. Ignacio, S. Sfarra, C. Ibarra-Castanedo, G. Guimaraes, and X. Maldague, “Machine Learning and Infrared Thermography for Fiber Orientation Assessment on Randomly-Oriented Strands Parts,” *Sensors*, vol. 18, p. 288, jan 2018.
- [138] H. Fernandes, H. Zhang, and X. Maldague, “An active infrared thermography method for fiber orientation assessment of fiber-reinforced composite materials,” *Infrared Physics & Technology*, vol. 72, pp. 286–292, sep 2015.
- [139] V. P. Vavilov and X. P. Maldague, “Dynamic thermal tomography: new promise in the IR thermography of solids,” in *Proceedings of SPIE - The International Society for Optical Engineering*, 1992.
- [140] X. Maldague and S. Marinetti, “Pulse phase infrared thermography,” *Journal of Applied Physics*, 1996.

- [141] N. Rajic, "Principal component thermography for flaw contrast enhancement and flaw depth characterisation in composite structures," *Composite Structures*, 2002.
- [142] N. Otsu, "A Threshold Selection Method from Gray-Level Histograms," *IEEE Transactions on Systems, Man, and Cybernetics*, vol. 9, pp. 62–66, jan 1979.
- [143] X. Maldague, Y. Largouët, and J.-P. Couturier, "A study of defect depth using neural networks in pulsed phase thermography: modelling, noise, experiments," *Revue Générale de Thermique*, vol. 37, pp. 704–717, sep 1998.
- [144] A. Darabi and X. Maldague, "Neural network based defect detection and depth estimation in TNDE," *NDT and E International*, vol. 35, no. 3, pp. 165–175, 2002.
- [145] D. Trias, R. García, J. Costa, N. Blanco, and J. E. Hurtado, "Quality control of CFRP by means of digital image processing and statistical point pattern analysis," *Composites Science and Technology*, 2007.
- [146] T. Bhattacharjee, J. Wade, and C. Kemp, "Material Recognition from Heat Transfer given Varying Initial Conditions and Short-Duration Contact," in *Robotics: Science and Systems XI*, 2015.
- [147] T. Bhattacharjee, A. Kapusta, J. M. Rehg, and C. C. Kemp, "Rapid categorization of object properties from incidental contact with a tactile sensing robot arm," in *IEEE-RAS International Conference on Humanoid Robots*, 2015.
- [148] R. A. Russell, "Thermal sensor for object shape and material constitution," *Robotica*, 1988.
- [149] E. Kerr, T. M. McGinnity, and S. Coleman, "Material classification based on thermal properties - A robot and human evaluation," in *2013 IEEE International Conference on Robotics and Biomimetics, ROBIO 2013*, pp. 1048–1053, IEEE Computer Society, 2013.

- [150] J. F. Florez-Ospina and H. Benitez-Restrepo, "Toward automatic evaluation of defect detectability in infrared images of composites and honeycomb structures," *Infrared Physics & Technology*, vol. 71, pp. 99–112, jul 2015.
- [151] B.-K. Kwon, J.-S. Won, and D.-J. Kang, "Fast defect detection for various types of surfaces using random forest with vov features," *International Journal of Precision Engineering and Manufacturing*, vol. 16, no. 5, pp. 965–970, 2015.
- [152] N. Shipway, T. Barden, P. Huthwaite, and M. Lowe, "Automated defect detection for fluorescent penetrant inspection using random forest," *NDT & E International*, vol. 101, pp. 113–123, 2019.
- [153] M. Chi, R. Feng, and L. Bruzzone, "Classification of hyperspectral remote-sensing data with primal svm for small-sized training dataset problem," *Advances in space research*, vol. 41, no. 11, pp. 1793–1799, 2008.
- [154] R. Samsudin, A. Shabri, and P. Saad, "A comparison of time series forecasting using support vector machine and artificial neural network model," *Journal of applied sciences*, vol. 10, no. 11, pp. 950–958, 2010.
- [155] D. Castelvechi, "Can we open the black box of ai?," *Nature News*, vol. 538, no. 7623, p. 20, 2016.
- [156] A. Bandyopadhyay and A. Sengupta, "A Review of the Concept, Applications and Implementation Issues of Terahertz Spectral Imaging Technique," *IETE Technical Review (Institution of Electronics and Telecommunication Engineers, India)*, vol. 0, no. 0, pp. 1–19, 2021.
- [157] D. Miyagi, A. Sai, N. Takahashi, N. Uchida, and K. Ozaki, "Improvement of zone control induction heating equipment for high-speed processing of semiconductor devices," *IEEE Transactions on Magnetics*, vol. 42, pp. 292–294, feb 2006.
- [158] H. Fujita, N. Uchida, and K. Ozaki, "A New Zone-Control Induction Heating System Using Multiple Inverter Units Applicable Under Mutual

- Magnetic Coupling Conditions,” *IEEE Transactions on Power Electronics*, vol. 26, pp. 2009–2017, jul 2011.
- [159] H. N. Pham, H. Fujita, K. Ozaki, and N. Uchida, “Dynamic Analysis and Control for Resonant Currents in a Zone-Control Induction Heating System,” *IEEE Transactions on Power Electronics*, vol. 28, pp. 1297–1307, mar 2013.
- [160] R. Joven, R. Joven, R. Das, A. Ahmed, P. Roozbehjavan, and B. Minaie, “Thermal properties of carbon fiber-epoxy composites with different fabric weaves Prediction of residual stresses and distortion in carbon fiber-epoxy composite parts due to curing process.,” in *SAMPE International Symposium Proceedings at Charleston, SC 2012*, 2012.
- [161] S. Enoki, K. Iwamoto, R. Harada, K. Tanaka, and T. Katayama, “Heating properties of carbon fibers by using direct resistance heating,” *WIT Transactions on the Built Environment*, vol. 124, pp. 239–248, 2012.
- [162] S. A. Hayes, A. D. Lafferty, G. Altinkurt, P. R. Wilson, M. Collinson, and P. Duchene, “Direct electrical cure of carbon fiber composites,” *Advanced Manufacturing: Polymer & Composites Science*, vol. 1, pp. 112–119, apr 2015.
- [163] K. Tanaka, R. Habe, M. Tanaka, and T. Katayama, “Carbon Fiber Reinforced Thermoplastics Molding by Using Direct Resistance Heating to Carbon Nanofilaments Grafted Carbon Fiber,” *Journal of Composites Science*, vol. 3, p. 14, feb 2019.
- [164] C. Joseph and C. Viney, “Electrical resistance curing of carbon-fibre/epoxy composites,” *Composites Science and Technology*, vol. 60, pp. 315–319, feb 2000.
- [165] S. Liu, Y. Li, Y. Shen, and Y. Lu, “Mechanical performance of carbon fiber/epoxy composites cured by self-resistance electric heating method,”

The International Journal of Advanced Manufacturing Technology, vol. 103, pp. 3479–3493, aug 2019.

- [166] RS-Components, “RS PRO Silicone Heater Mat, 100 W, 150 x 150 (square)mm, 240 V ac — RS Components.”
- [167] X. Maldague, F. Galmiche, and A. Ziadi, “Advances in pulsed phase thermography,” *Infrared Physics & Technology*, vol. 43, no. 3-5, pp. 175–181, 2002.
- [168] J. Wingfield, “Treatment of composite surfaces for adhesive bonding,” *International Journal of Adhesion and Adhesives*, vol. 13, pp. 151–156, jul 1993.
- [169] J. Meyer and C. A. Smith, “Effect of Silicone Contamination on Assembly Processes,” 2012.
- [170] D. Markatos, K. Tserpes, E. Rau, S. Markus, B. Ehrhart, and S. Pantelakis, “The effects of manufacturing-induced and in-service related bonding quality reduction on the mode-I fracture toughness of composite bonded joints for aeronautical use,” *Composites Part B: Engineering*, vol. 45, pp. 556–564, feb 2013.
- [171] Airtech Europe, “Airpad HTX Data Sheet,” 2018.
- [172] Airtech Europe, “Airpad Data Sheet,” 2019.
- [173] Y. Zhao and F. Ansari, “Embedded fiber optic sensor for characterization of interface strains in FRP composite,” *Sensors and Actuators A: Physical*, vol. 100, pp. 247–251, sep 2002.
- [174] C. A. Coronado and M. M. Lopez, “Sensitivity analysis of reinforced concrete beams strengthened with FRP laminates,” *Cement and Concrete Composites*, vol. 28, pp. 102–114, jan 2006.

- [175] G. Ramesh, R. Gettu, and B. H. Bharatkumar, “Bond Behaviour of Externally Bonded FRP Under Cyclic Loading,” in *Recent Advances in Structural Engineering, Volume 2* (A. R. M. Rao and K. Ramanjaneyulu, eds.), (Singapore), pp. 783–795, Springer Singapore, 2019.
- [176] Y. Wang, G. Chen, B. Wan, G. Cai, and Y. Zhang, “Behavior of circular ice-filled self-luminous FRP tubular stub columns under axial compression,” *Construction and Building Materials*, vol. 232, p. 117287, jan 2020.
- [177] R. Stewart, “New mould technologies and tooling materials promise advances for composites,” *Reinforced Plastics*, vol. 54, pp. 30–36, may 2010.
- [178] M. Georges, C. Srajbr, P. Menner, J. Koch, and A. Dillenz, “Thermography and Shearography Inspection of Composite Hybrid Sandwich Structure Made of CFRP and GFRP Core and Titanium Skins,” *Proceedings*, vol. 2, no. 8, p. 484, 2018.
- [179] C. Ibarra-Castanedo, J. R. Tarpani, and X. P. Maldague, “Nondestructive testing with thermography,” *European Journal of Physics*, vol. 34, no. 6, 2013.
- [180] A. Bogdanovich and K. Friedrich, “Initial and progressive failure analysis of laminated composite structures under dynamic loading,” *Composite structures*, vol. 27, no. 4, pp. 439–456, 1994.
- [181] N. Naik and Y. C. Sekher, “Damage in laminated composites due to low velocity impact,” *Journal of Reinforced Plastics and Composites*, vol. 17, no. 14, pp. 1232–1263, 1998.
- [182] W. Shen, “Dynamic response of rectangular plates under drop mass impact,” *International journal of impact engineering*, vol. 19, no. 3, pp. 207–229, 1997.
- [183] D. Palumbo and U. Galietti, “Damage Investigation in Composite Materials by Means of New Thermal Data Processing Procedures,” *Strain*, vol. 52, pp. 276–285, aug 2016.

- [184] F. Ciampa, P. Mahmoodi, F. Pinto, and M. Meo, “Recent advances in active infrared thermography for non-destructive testing of aerospace components,” 2018.
- [185] C. E. Jones, A. W. Hamilton, P. J. Norman, A. Cleary, S. J. Galloway, R. Atkinson, G. M. Burt, C. Michie, I. Andonovic, and C. Tachtatzis, “A novel methodology for macro-scale, thermal characterisation of carbon fibre reinforced polymer for integrated aircraft electrical power systems,” *IEEE Transactions on Transportation Electrification*, pp. 1–1, 2019.
- [186] F. Nosrat-Nezami, T. Gereke, C. Eberdt, and C. Cherif, “Characterisation of the shear–tension coupling of carbon-fibre fabric under controlled membrane tensions for precise simulative predictions of industrial preforming processes,” *Composites Part A: Applied Science and Manufacturing*, vol. 67, pp. 131–139, dec 2014.
- [187] S. V. Lomov, D. S. Ivanov, I. Verpoest, M. Zako, T. Kurashiki, H. Nakai, and S. Hirosawa, “Meso-FE modelling of textile composites: Road map, data flow and algorithms,” *Composites Science and Technology*, vol. 67, pp. 1870–1891, jul 2007.
- [188] P. Boisse, B. Zouari, and A. Gasser, “A mesoscopic approach for the simulation of woven fibre composite forming,” *Composites Science and Technology*, vol. 65, pp. 429–436, mar 2005.
- [189] FLUKE, “Ti90, Ti95 Ti100, Ti105, Ti110, Ti125 TiR105, TiR110, TiR125,” 2014.
- [190] R. Misra, A. Dixit, and H. S. Mali, “Finite Element (FE) Shear Modeling of Woven Fabric Textile Composite,” *Procedia Materials Science*, 2014.
- [191] Y. C. Zhang and J. Harding, “A numerical micromechanics analysis of the mechanical properties of a plain weave composite,” *Computers and Structures*, 1990.

- [192] M. Schuller, L. Peel, C. A. Silva, E. E. Marotta, and M. O’Neill, “In-Plane Thermal Conductivity in Thin Carbon Fiber Composites,” *Journal of Thermophysics and Heat Transfer*, 2007.
- [193] J. Zeman and M. Šejnoha, “Numerical evaluation of effective elastic properties of graphite fiber tow impregnated by polymer matrix,” *Journal of the Mechanics and Physics of Solids*, 2001.
- [194] N. Boyard, D. Delaunay, M. Thomas, L. Perez, and Y. Jarny, “Representative volume element of anisotropic unidirectional carbon–epoxy composite with high-fibre volume fraction,” *Composites Science and Technology*, 2008.
- [195] D. Trias, J. Costa, A. Turon, and J. E. Hurtado, “Determination of the critical size of a statistical representative volume element (SRVE) for carbon reinforced polymers,” *Acta Materialia*, 2006.
- [196] Z. Fang, M. Li, S. Wang, Y. Li, X. Wang, Y. Gu, Q. Liu, J. Tian, and Z. Zhang, “Geometrical Effect on Thermal Conductivity of Unidirectional Fiber-Reinforced Polymer Composite along Different In-plane Orientations,” *Applied Composite Materials*, 2018.
- [197] D. Gillespie, A. Hamilton, C. Tachtatzis, and I. Andonovic, “Data for:” non-destructive identification of fibre orientation in multi-ply biaxial laminates using contact temperature sensors” [data set],” 2020.
- [198] M. A. Pedder, “Interpolation and filtering of spatial observations using successive corrections and Gaussian filters,” *Monthly Weather Review*, vol. 121, pp. 2889–2902, oct 1993.
- [199] M. Florek and H. Hauser, “Quantitative data visualization with interactive KDE surfaces,” in *Proceedings of the 26th Spring Conference on Computer Graphics - SCCG ’10*, (New York, New York, USA), p. 33, ACM Press, 2010.
- [200] J. A. Schroeder, T. Ahmed, B. Chaudhry, and S. Shepard, “Non-destructive testing of structural composites and adhesively bonded composite joints :

- pulsed thermography,” *Composites Part A: Applied Science and Manufacturing*, vol. 33, no. 11, pp. 1511–1517, 2002.
- [201] N. Saeed, M. A. Omar, and Y. Abdulrahman, “Infrared Physics & Technology Regular article A neural network approach for quantifying defects depth , for nondestructive testing thermograms,” *Infrared Physics and Technology*, vol. 94, no. June, pp. 55–64, 2018.
- [202] N. Saeed, Y. Abdulrahman, S. Amer, and M. A. Omar, “Experimentally validated defect depth estimation using arti fi cial neural network in pulsed thermography,” *Infrared Physics and Technology*, vol. 98, no. March, pp. 192–200, 2019.
- [203] J. E. Siegel, M. F. Beemer, and S. M. Shepard, “Automated non-destructive inspection of Fused Filament Fabrication components using Thermographic Signal Reconstruction,” *Additive Manufacturing*, vol. 31, no. July 2019, p. 100923, 2020.
- [204] D. I. Gillespie, A. W. Hamilton, T. Kruckenberg, B. Neilson, R. C. Atkinson, I. Andonovic, and C. Tachtatzis, “Geometrical Thermal Analysis as a Form of Finite Element Analysis Enhancement,” in *Advances in Manufacturing Technology XXXIII: Proceedings of the 17th International Conference on Manufacturing Research, incorporating the 34th National Conference on Manufacturing Research, 10-12 September 2019, Queen’s University, Belfast* (Y. Jin and P. M., eds.), pp. 187–192, IOS Press, sep 2019.
- [205] N. P. Avdelidis, B. C. Hawtin, and D. P. Almond, “Transient thermography in the assessment of defects of aircraft composites,” *NDT and E International*, vol. 36, no. 6, pp. 433–439, 2003.
- [206] E. Kuhn, E. Valot, and P. Herve, “A comparison between thermosonics and thermography for delamination detection in polymer matrix laminates,” *Composite Structures*, vol. 94, no. 3, pp. 1155–1164, 2012.

- [207] P. Jiang and X. Guo, “Detectability of pulsed infrared thermography of delaminations in carbon fiber composites,” in *The 9th International Symposium on NDT in Aerospace*, pp. 1–11, 2017.
- [208] I. Nun, P. Protopapas, B. Sim, M. Zhu, R. Dave, N. Castro, and K. Pichara, “Fats: Feature analysis for time series,” 2015.
- [209] B. Naul, S. van der Walt, A. Crellin-Quick, J. S. Bloom, and F. Pérez, “cesium: Open-source platform for time-series inference,” 2016.
- [210] M. Christ, A. W. Kempa-Liehr, and M. Feindt, “Distributed and parallel time series feature extraction for industrial big data applications,” *arXiv e-prints*, p. arXiv:1610.07717, Oct. 2016.
- [211] M. Barandas, D. Folgado, L. Fernandes, S. Santos, M. Abreu, P. Bota, H. Liu, T. Schultz, and H. Gamboa, “Tsfel: Time series feature extraction library,” *SoftwareX*, vol. 11, p. 100456, 2020.
- [212] C. C. Aggarwal, A. Hinneburg, and D. A. Keim, “On the surprising behavior of distance metrics in high dimensional space,” in *Database Theory — ICDDT 2001* (J. Van den Bussche and V. Vianu, eds.), (Berlin, Heidelberg), pp. 420–434, Springer Berlin Heidelberg, 2001.
- [213] K. Murphy, *Machine Learning: A Probabilistic Perspective*. Adaptive Computation and Machine Learning series, MIT Press, 2012.
- [214] L. Breiman, “Random forests,” *Mach. Learn.*, vol. 45, p. 5–32, Oct. 2001.
- [215] P. Geurts, D. Ernst, and L. Wehenkel, “Extremely randomized trees,” *Machine Learning*, vol. 63, pp. 3–42, 2006.
- [216] D. Bzdok, M. Krzywinski, and N. Altman, “Machine learning: supervised methods,” *Nature Methods*, vol. 15, pp. 5–6, jan 2018.
- [217] S. Suthaharan, “Support Vector Machine,” in *Machine Learning Models and Algorithms for Big Data Classification: Thinking with Examples for Effective Learning*, pp. 207–235, Boston, MA: Springer US, 2016.

- [218] N. H. Farhat, "Photonit neural networks and learning machines the role of electron-trapping materials," *IEEE Expert-Intelligent Systems and their Applications*, vol. 7, no. 5, pp. 63–72, 1992.
- [219] J. C. Platt, "A Fast Algorithm for Training Support Vector Machines," tech. rep., Microsoft, 1998.
- [220] A. Kulkarni and N. Kulkarni, "Fuzzy Neural Network for Pattern Classification," *Procedia Computer Science*, vol. 167, no. 1, pp. 2606–2616, 2020.
- [221] H. X. Li, J. L. Yang, G. Zhang, and B. Fan, "Probabilistic support vector machines for classification of noise affected data," *Information Sciences*, vol. 221, pp. 60–71, 2013.
- [222] A. Ben-Hur, D. Horn, H. T. Siegelmann, and V. Vapnik, "Support Vector Clustering," *J. Mach. Learn. Res.*, vol. 2, pp. 125–137, mar 2002.
- [223] M. F. Amasyali and O. K. Ersoy, "Classifier Ensembles with the Extended Space Forest," *IEEE Transactions on Knowledge and Data Engineering*, vol. 26, pp. 549–562, mar 2014.
- [224] M. Pal, "Random forest classifier for remote sensing classification," *International Journal of Remote Sensing*, vol. 26, pp. 217–222, jan 2005.
- [225] F. A. Administration, "A quantitative assessment of conventional and advanced nondestructive inspection techniques for detecting flaws in composite honeycomb aircraft structures," tech. rep., New Jersey, 2016.

Appendices

Appendix A

RTD Airpad Array creation curing data

Collins Aerospace (UTC Aerospace Systems legacy) Research and Development request for non-production item. The below is the routing for curing of the RTD airpad array.



UTC Aerospace Systems

Prestwick Service Centre



**RESEARCH & DEVELOPMENT
REQUEST FOR
NON-PRODUCTION ITEM**

PSC0226

RTD test array airpad cure

Delivery Date:

Enter when delivery of item is expected

<u>DEPARTMENT</u>	<u>NAME</u>	<u>SIGNATURE</u>	<u>DATE</u>
R&D REQUESTER	David Gillespie		26/MAY/19
APPROVAL	Paul Guthrie	 DAVID BROWN	24/MAY/19

1. GENERAL INSTRUCTIONS

Purpose

The purpose of this R&D request is to cure a test array of Resistance Temperature Detectors (RTD) for use in data capture of temperature against time of test samples.

Specimen Details

Carbon Fibre Reinforced Polymer (CFRP) Airpad (HTX) for housing RTD array.

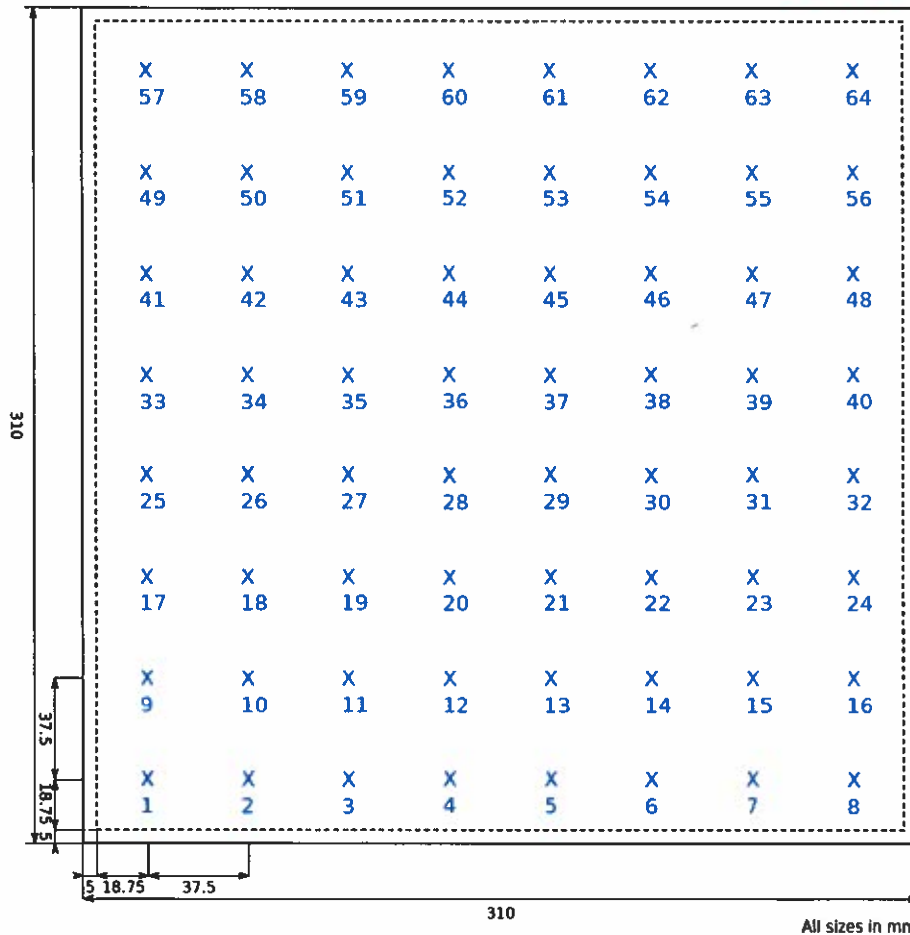


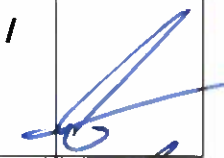
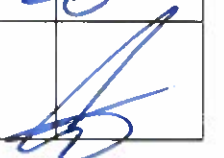
Figure 1 RTD locations within Airpad Array tool

2. EQUIPMENT & MATERIALS:

 Please book all hours to **Project Code 161323700 Operation Number 0010**

A. Standard equipment		
autoclave, TC		
B. Special Tools		
N/A		
C. <u>Materials</u>	<u>Qty</u>	<u>Units</u>
Prepared test array on composite panel ready for cure	01	EA

R&D USE ONLY NON-PRODUCTION MATERIAL

		The action has been completed as described
3.	<p align="center"><u>WARNING</u></p> <p>BEFORE YOU USE CHEMICALS / HAZARDOUS SUBSTANCES, READ, UNDERSTAND, AND OBEY ALL SAFETY INSTRUCTIONS FOR THE CHEMICALS / HAZARDOUS SUBSTANCES. THESE INSTRUCTIONS INCLUDE INSTRUCTIONS FROM THE MANUFACTURER, THE MATERIAL SAFETY DATA SHEET (MSDS), AND GOVERNMENT REGULATIONS.</p> <p>CHEMICALS / HAZARDOUS SUBSTANCES MAY CAUSE INJURY TO YOU OR MAKE YOU SICK WHEN SAFETY INSTRUCTIONS ARE NOT OBEYED. AN MSDS GIVES INSTRUCTIONS ON HOW YOU MUST SAFELY USE, KEEP, AND DISCARD CHEMICALS / HAZARDOUS SUBSTANCES. GET INSTRUCTIONS FROM YOUR EMPLOYER ON HOW YOU MUST SAFELY USE, KEEP, AND DISCARD CHEMICALS / HAZARDOUS SUBSTANCES.</p> <p>ALL CHEMICALS / HAZARDOUS SUBSTANCES CALLED UP IN THIS DOCUMENT ARE HIGHLIGHTED BY USE OF THE FOLLOWING STATEMENT:</p> <p><u>WARNING : SEE (MATERIAL NAME) MSDS FOR THIS MATERIAL BEFORE USE</u></p> <p><u>WARNINGS FOR MATERIALS</u></p> <p>A. To ensure that the R&D materials are segregated from the production materials please ensure that the following is followed:</p> <ul style="list-style-type: none"> • Small R&D materials are kept in the lidded box until they are being worked with • If working outwith the R&D work space, e.g. shop floor work bay or clean room, then use a clear bench with R&D sign indicating that all materials are non-production • Materials are always clearly labelled in some way, R&D tags, labelled sealable bags, chinograph marking on composite, handwritten label on vacuum bag etc. • Unless otherwise stated dispose of excess materials in accordance with RB201 Waste Disposal <p>If there are any queries regarding how to ensure the separation of a particular part ask the R&D engineer responsible for the manufacture</p>	N/A
4.	<p>Cure prepared test Array i.a.w. GRAMRO-SP0012 Method 4 (355 ° F) / 35 PSI Autoclave cure</p> <p>After curing is complete print cure profile</p>	
5.	<p>Debug</p> <p>Remove bagging materials</p>	

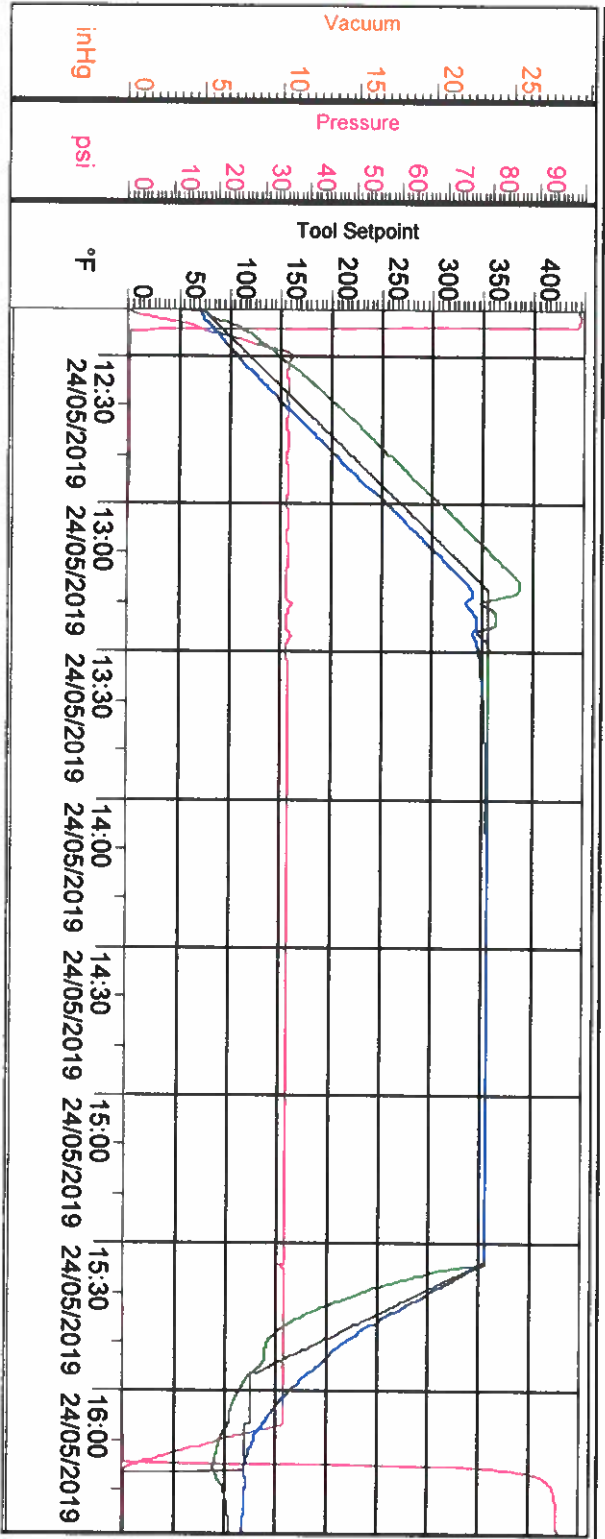
Cure Details: Cure Reference BFG-03498 History File BFG-03498.his
 Description 350F @ 35psi, 120 Minutes
 Autoclave AC2
 Profile 340 - 365 F\35 psi\Gramro SP0012 Method 4.pfl - 350F @ 35psi, 120 Minutes
 Started 12:20 on 24/05/2019 By STUART
 Ended 16:28 on 24/05/2019 Duration 04:08 hh:mm

Load and Part Details

Load 1 Load No: 161323700
 Load Description: RTD TEST ARRAY AIRPAD CURE
 Vacs Used: [7]

Parts

Part No: PSC 0226
 Order No: OP 0010
 Description: R&D
 TCS Used: [7]



Legend

Tool Setpoint	°F
Air Temperature	°F
Pressure Setpoint	psi
Pressure	psi
Load Hottest	°F
Load Coldest	°F
Vacuum Res	inHg
Max Vacuum	inHg
Min Vacuum	inHg
Operator Pause	
Program in Hold	
Cure Checker	
"Hold Time"	256 min
"Cumulative Time"	257 min
"Peel Ply Exposure"	257 min
Max above Critical Press.	36.0 psi
Min above Critical Press.	120.0 psi

Appendix B

Temperature against time thermal profiles for Sample D8

This appendix contains Figures for 'x_heat_dist' values of 131.25 mm and greater of sample D8, generated within Chapter 5. Figure B.1 and Figure B.2 display

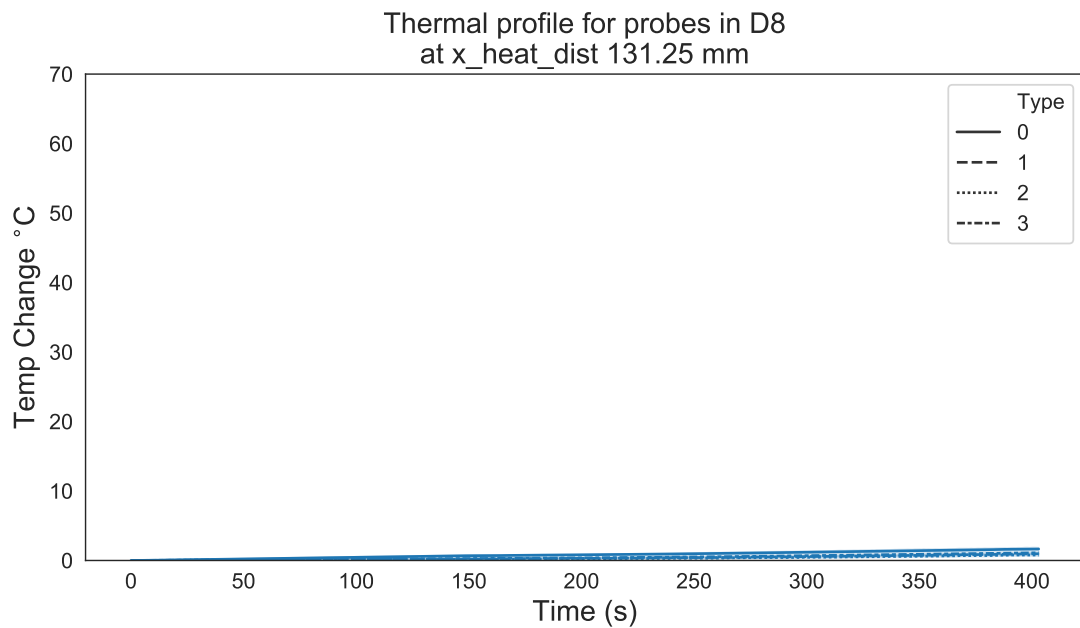


Figure B.1: Thermal profile for probes in D8 at y_heat_dist of ≤ 37.5 mm and x_heat_dist of 131.25 mm

the 400 s period of heating and show that the RTD probes are still detecting some increase in temperature. However all 4 types of defects are within the

confidence interval of each other. As 'x_heat_dist' reaches 168.75 mm, defect

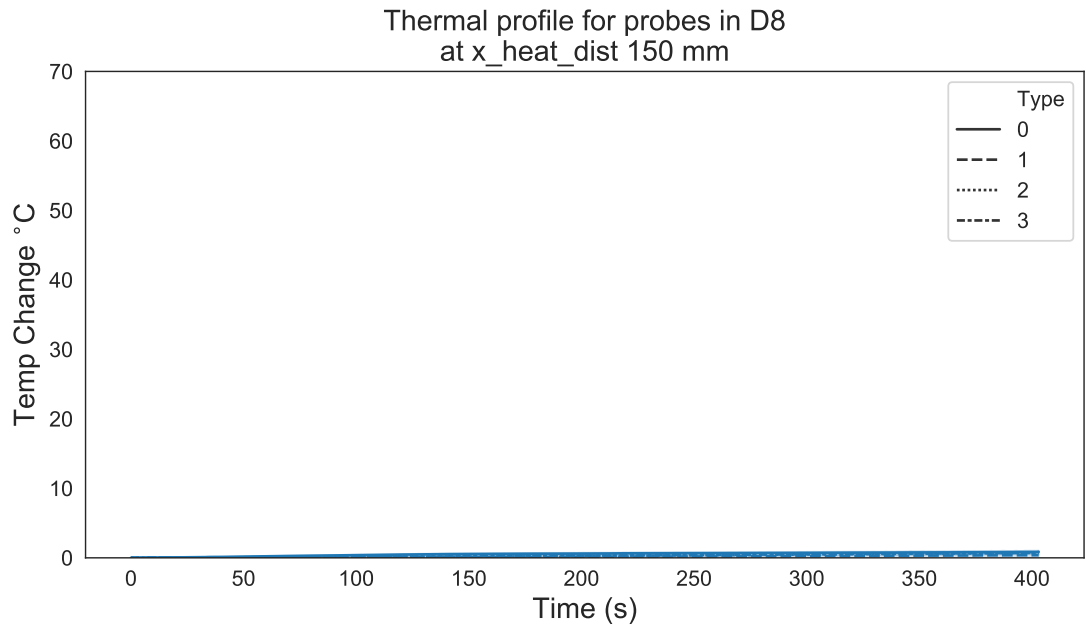


Figure B.2: Thermal profile for probes in D8 at y_heat_dist of ≤ 37.5 mm and x_heat_dist of 150 mm

types 0,1, and 3 are present only. Again the confidence interval between these plots when compared to those closer to the centre of the heater mat makes it visually difficult to differentiate between defect types. As the probes location increases in distance from the centre of the heater mat and 'x_heat_dist' reaches 187.5 mm, only homogeneous regions are now present. Figure B.4 and Figure B.5 display the temperature against time for 187.5 and 206.25, respectively, where the homogeneous defect types 0 and 3 are present only. Such is the overlap of the confidence interval for both profiles, once again that if individually presented, it would prove difficult to distinguish either from the other.

Distances of 225 and 243.75 mm contain only defect type 0 (Figure B.6 Figure B.7). As no other defect type is present at this distance, their value as training or testing data is minimal regardless of temperature profile. It can be seen, however, that at these distances that some transient thermal conduction is still detected.

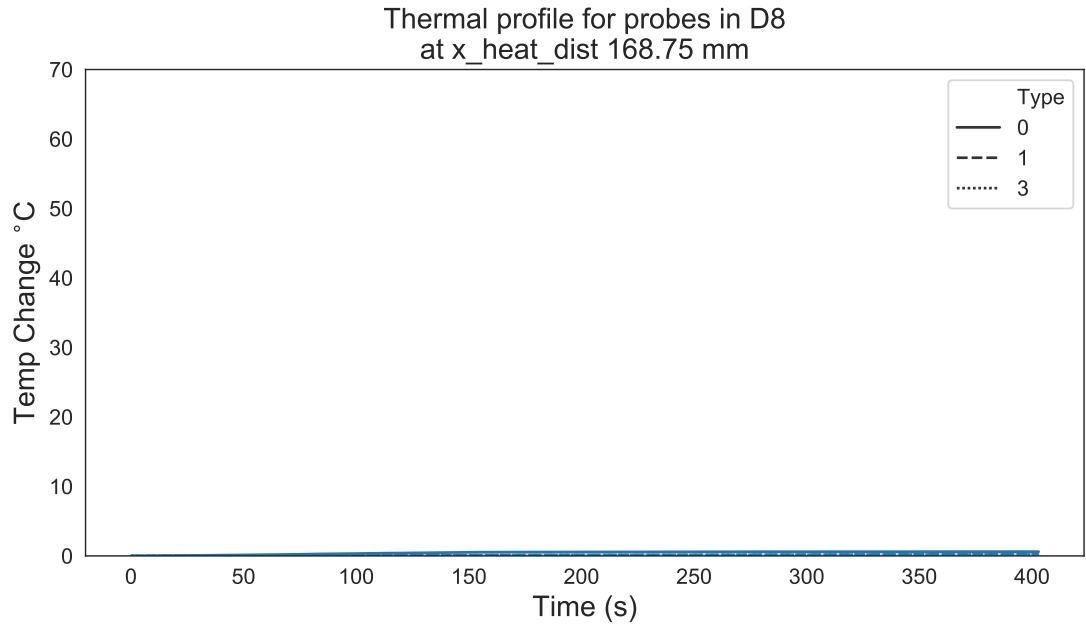


Figure B.3: Thermal profile for probes in D8 at y_heat_dist of ≤ 37.5 mm and x_heat_dist of 168.75 mm

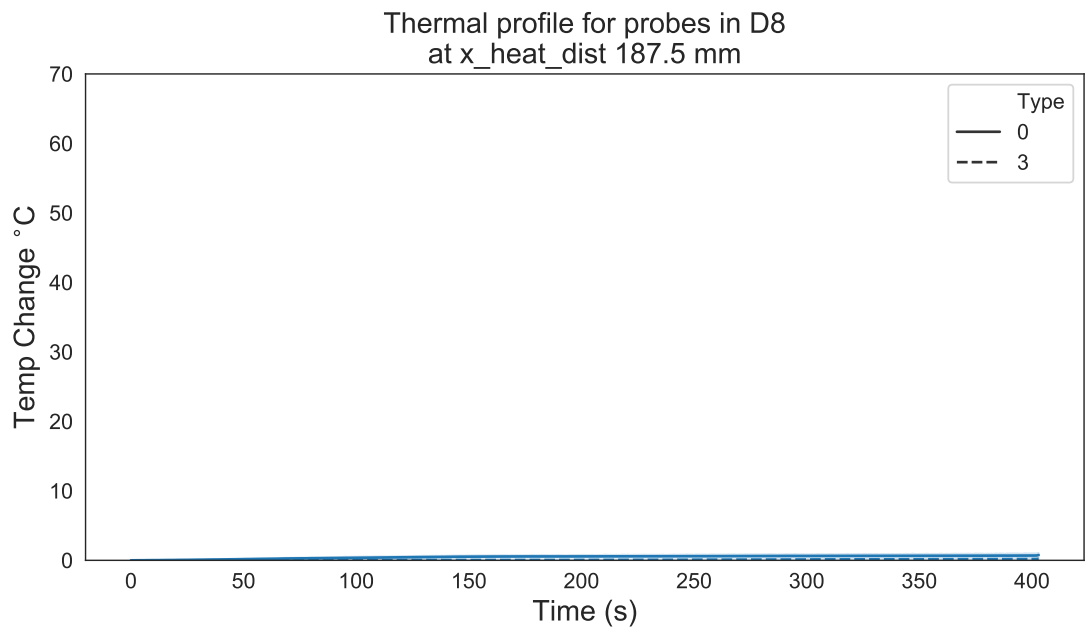


Figure B.4: Thermal profile for probes in D8 at y_heat_dist of ≤ 37.5 mm and x_heat_dist of 187.5 mm

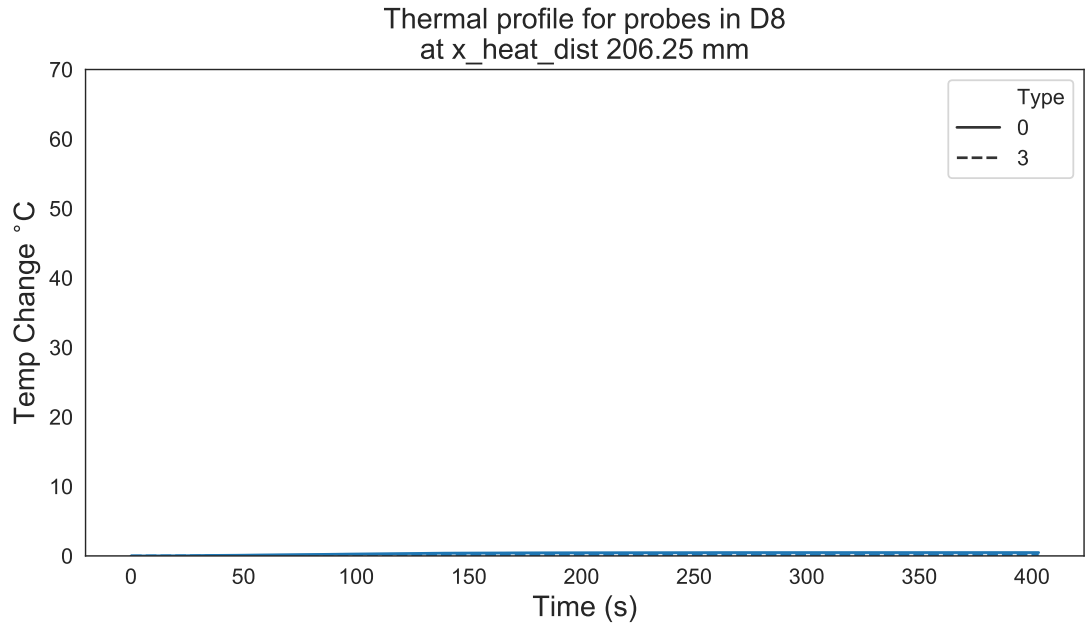


Figure B.5: Thermal profile for probes in D8 at y_heat_dist of ≤ 37.5 mm and x_heat_dist of 206.25 mm

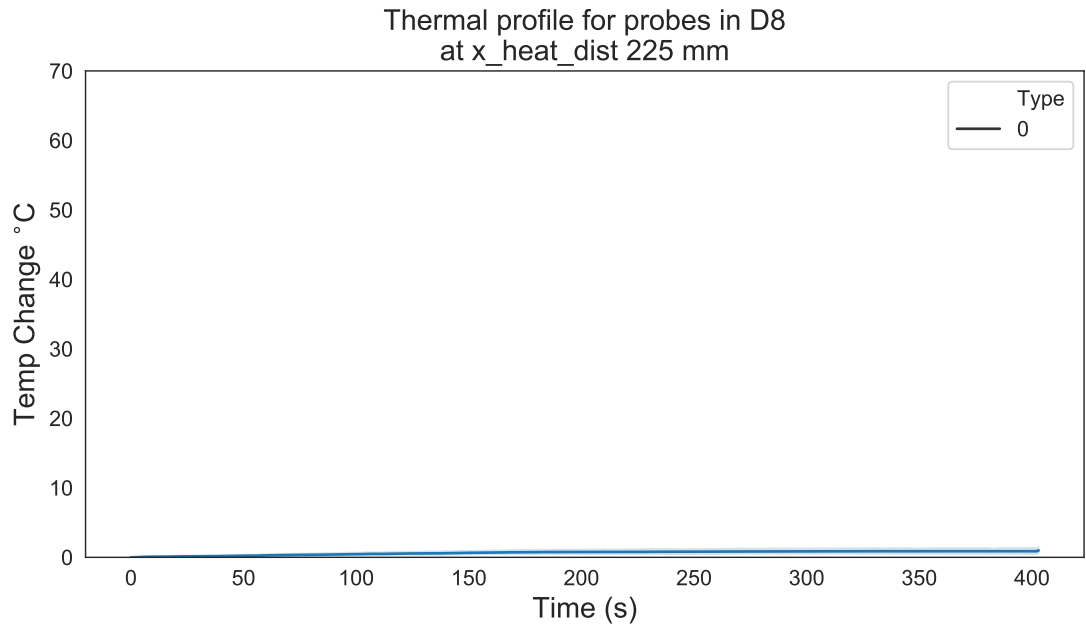


Figure B.6: Thermal profile for probes in D8 at y_heat_dist of ≤ 37.5 mm and x_heat_dist of 225 mm

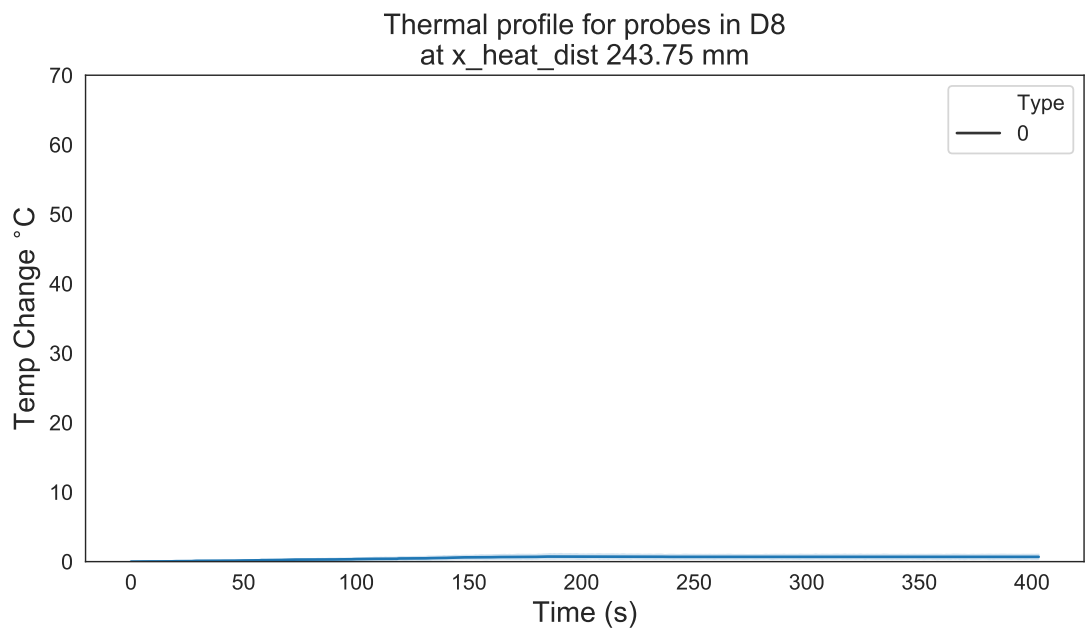


Figure B.7: Thermal profile for probes in D8 at y_heat_dist of ≤ 37.5 mm and x_heat_dist of 243.75 mm